Thermal evolution of massive strange compact objects in a SU(3) chiral Quark Meson Model

- Dissertation -

von

Andreas Zacchi

Goethe Universität Frankfurt

März 2017

Erstbetreuer: **Prof. Dr. Jürgen Schaffner-Bielich**
Zweitbetreuer: **Prof. Dr. Carsten Greiner**

.

Dissertation
zur
Erlangung des
Doktorgrades der Naturwissenschaften

vorgelegt beim Fachbereich Physik
der Johann Wolfgang Goethe Universität
in
Frankfurt am Main von

Andreas Zacchi
aus Dreieichenhain

Frankfurt am Main, den 01.03.2017
(D30)

Dekan:	Prof. Dr. R. Reifarth
Gutachter:	Prof. Dr. Jürgen Schaffner-Bielich Prof. Dr. Carsten Greiner
Datum der Disputation:	04 Juli 2017

vom Fachbereich Physik der Johann Wolfgang Goethe Universität als Dissertation angenommen.

Contents

1 Introduction and motivation

The interplay between particle physics and astronomy is one of the most fascinating aspects in modern science. Current theories are formulated such that they are consistent with relativity and quantum mechanics[1].

Einsteins postulates of special relativity tells us, that the laws of physics should be the same in all inertial frames[2] and that the speed of light in vacuo is a constant[3], called **c**. In a burdensome but in the end magnificent work during 1905-1916 he formulated a much more general theory of relativity, which deals with accelerated frames and its connection to gravity. In this theory not a force mediates interactions between to massive bodies, but rather the curvature of spacetime. The theory of **general relativity** (GR) will be illuminated in chapter 2.

The importance of *fields* for the understanding of fundamental processes in

[1] For the references and further literature we refer to the corresponding chapters.

[2] Which is actually not that innovative, since it was already known in classical mechanics, he *merely* expanded it for all known theories

[3] The speed of light ist: $299.792.458 \frac{m}{s}$

nature was one of the main discoveries in the 20^{th} century. According to the very succesful **Standard Model** of particle physics, the basic constituents of matter are *quarks* and *leptons*, of which six of each are known to exist. An interesting fact of quarks is that that they appear not to exist as free particles, the force *glueing* them together is so strong, that a single quark cannot be extracted from a bound system. This feature is called *quark-confinement*. The particles transmitting this force are consequentially called gluons. On the other side quarks can act as free particles in short time intervals inside such a bound system[4], this is what is meant by *asymptotic freedom*. Each quark has three internal degrees of freedom, called *colour*. The theory of the strong interaction, **Quantum Chromodynamics** (QCD), describes how these coloured quarks and gluons interact. Quarks and leptons have spin $\frac{1}{2}$, and thus are fermions, which means, they obey the Pauli exclusion principle. The particles mediating the strong interaction, the gluons, are Bosons and thus are particles with integer spin. Elementary particle physics and the theory of the strong interaction will be discussed in greater detail in chapter 3 in section 3.2.

Strongly interacting matter as described by QCD plays a major role in the understanding of astrophysical scenarios such as the Big Bang, Supernova explosions and the inner structure and general properties of compact stellar objects. To date there is no unified theory describing the interaction at large scales (GR) and very small scales (QCD) combined, therefore a physical description which connects general relativity and Quantum Chromodynamics is still missing.
The properties of hadrons in ultradense and ultrahot matter and the search for the deconfinement and chiral phase transition is pivotal for understanding yet unclear key phenomena of the strong interaction. The possibility to study matter for such large temperatures appearing under these extreme conditions is possible within high-energy relativistic heavy ion collisions, performed at the Large Hadron Collider at CERN and the Relativistic Heavy Ion Collider at the Brookhaven National Laboratory, and future experiments

[4] A bound system would be a proton or a neutron for instance

at the Facility for Antiproton and Ion Research at GSI will be designed to study matter at high densities.
The use of effective models is however a way to achieve results which are believed to be very close to what nature provides, i.e. what can be observed or experimentally verified. The main topic of this thesis connects a chiral effective model, describing fundamental particles, to astrophysical phenomena, mainly compact stars, but also the subject of Supernovae explosions and compact star merger is discussed.
The study of an equation of state within an effective model and the search for these phase transitions is fundamental to explore and understand the properties of an exploding star (Supernova) and its remnant, i.e. of ultradense compact stellar objects within the theory of the strong interaction, because the inner regions of the most massive compact stellar objects might be occupied by a deconfined phase of quarks. Scenarios of possibility are either hybrid stars, i.e. compact objects with an outer layer composed of nuclear matter and with a core consisting of quark matter, or even pure strange quark stars[5].
The observations of the massive pulsars PSR J1614-2230 and of PSR J0348+0432 with about two solar masses imply that the equation of state constructing such relativistic stellar models has to be constrained respecting these new limits.

To generate an appropriate equation of state an alternative framework to the commonly used MIT bag model [1, 2] is the chiral Quark Meson model [3, 4, 5], which is based upon the linear-σ model and both are well established and respect important properties such as chiral symmetry breaking patterns of QCD. The bosonic sector of the Quark Meson model contains scalar- and vector fields, which serve as stationary mediators to model the quark-quark interaction. That is, only thermal fluctuations of quarks are considered.
In this thesis we go beyond the so called mean field approximation by considering not only the vacuum fluctuations of quarks, but even thermal and

[5]The subject of pure strange stars has been discussed in great detail in my Master thesis.

vacuum fluctuations of the corresponding boson fields. This has been carried out in the SU(2) chiral Quark Meson model to full extend in chapter 4, where we also study a combined renormalized approach.

Based on the results obtained, we find that the meson contributions are negligible in the SU(3) expansion, but renormalization needs to be taken into account. The implementation of the divergent vacuum term in the SU(3) approach will be discussed and presented in chapter 5. Calculations for $T \neq 0$ (Supernova equation of state[6]), applicable for compact star merger and for new born proto neutron stars, can be found at the end of chapter 5 in section 5.8. The results obtained look promising and are hence auspicious for future works concerning such extreme astrophysical phenomena.

Calculations at $T = 0$ on the other side provide an equation of state for the compact star sector, discussed in chapter 6. Because of the Pauli exclusion principle, the particles- and fields energies are far larger than the temperature the star might still have, so that a $T \to 0$ approach is justified. The corresponding equation of state serves then as an input to solve the TOV equations (chapter 2), whose solutions are the mass-radius relations of the corresponding compact objects. Chapter 6 deals furthermore with the variety of compact star types the SU(3) Quark Meson equation of state is able to deliver and, apart from the $2M_{\odot}$ constraint, several constraints which also need to be fulfilled. As for the technical part concerning chapter 4 and 5, the thermodynamical properties have been calculated via the grand potential, which itself will be derived from an effective Lagrangian using the path integral formalism[7]. From the grand potential all physically relevant quantities, among them the equation of state, can be derived.

[6] Supernova matter formed prior to the formation of a compact stellar object, can be found in the QCD phase diagram at high temperatures and densities, while compact star matter is usually located at $T = 0$.

[7] This is commonly the more difficult way, but, due to Lorentz invariance compared to an approach via second quantization, preferrable.

2

Main features of General Relativity

This introduction is based upon works from [6, 7, 8, 9, 10, 11, 12, 13]. A more detailled introductional discussion on general relativity can be found in (nearly) every textbook concerning general relativity. Nonetheless it will be quoted were certain expressions have their origin.

Albert Einstein's theory of general relativity is the basis to understand and describe compact objects, which are among the main topics of this thesis. White dwarfs, neutron stars and black holes owe their existence to this very theory of spacetime, geometry and gravitation. Its foundations arise from a few simple questions with important consequences.

i.) Why are we not happy with Newtons classical description of gravity?

ii.) If all bodies, no matter of what composed, suffer the same acceleration, i.e. fall in gravitational fields in precisely the same way, then their motion has nothing to do with their nature, but rather with the geometry of spacetime?

iii.) What is the exact connection between gravity and acceleration?

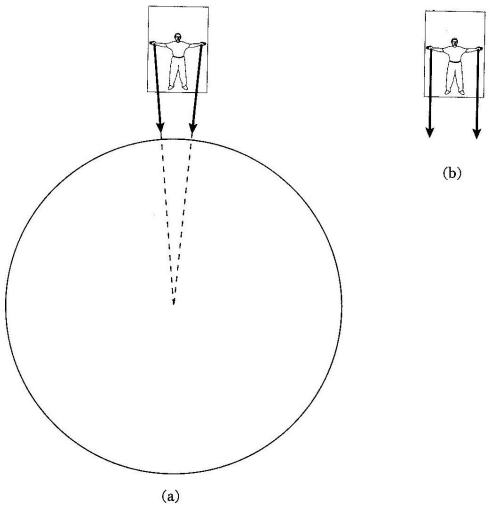

Figure 2.1: *Non-uniform gravitational field and uniform acceleration, [11]*

A decisive investigation of these questions is the basis to understand Einsteins theory of gravity.

First of all, Newtons theory is not Lorentz invariant, postulating an action at a distance and an instantaneous propagation of the gravitational field to every point in space. That implies that the speed of light (i.e. transmission of information) $c = \infty$, which is (strangely enough) known to be a finite quantity ($c = 299792459$ m/s). Einstein found that Newtons theory of gravity is a very special case of a much more *general* theory. According to special relativity mass is just another form of energy: The famous $E = mc^2$ equation. In a relativistic invariant theory, gravity would also couple to energy (see section 2.1.1).

It is important that the inertial mass of a body is equal to its gravitational mass[1]. Einstein concluded that there must be a close relation between inertia and gravity itself. This is the famous idea of the falling elevator in a gravitational field, say the earths one, when accelerated leading to the immagination of being in an uniform gravitational field: One can not distinguish between acceleration and gravity. Beware, that this is only valid

[1]Usually paraphrased as: All bodies fall at the same rate in a gravitational field.

locally, since the earths gravitational field is (nearly) spherically symmetric (see figure 2.1). In a non-uniform gravitational field the effects of gravity cannot be eliminated by changing to a free falling coordinate system. Based on this, Einstein formulated a generalized *equivalence principle*, which roughly states, that physics in a free falling frame in a gravitational field is the same as in an inertial frame in Minkowski space in the absence of acceleration. There is no experiment that can distinguigh a uniform acceleration from a uniform gravitational field. Two immediate consequences of this are

- Clocks run slower in a gravitational field than in the abscence of gravity.
- Light is deflected by a gravitational field just like matter is.

To understand the first statement, one can immagine two observers at the top and the bottom of an elevator, sending light signals to each other. Once the elevator accelerates upwards the observer at the bottom will receive the signals at a higher rate than his counterpart. His interpretation will be, that his clock runs slower than the upper located clock. The equivalence principle states that one should observe the same situation in a gravitational field at different altitudes[2].

To see the inevitability of the second assertion, imagine a light ray entering the elevator horizontally through a window on the left hand side and exiting again at the same height through a window on the right. Now imagine that the elevator accelerates upwards, or according to the equivalence principle, being put in a gravitational field. Then clearly the light ray that enters on the left will exit at a lower point of the elevator than on the right. It follows immediately that in a gravitational field the light ray is deflected downwards (see section 2.1.2).

Einsteins approach to find a modificated theory was to revsit the equivalence principle of special relativity, the relation between inertial and gravitational mass, and its relation to special relativity and accelerations. This key insight led him to the realization that gravity should be described and understood not as a physical external force like most of the other forces in nature, but

[2]The first statement can also be understood via the twin paradox of special relativity.

rather as a manifestation of the geometry and curvature of space-time itself (see section 2.1.3).
Einstein suggested three tests to verify his theory of a curved spacetime:

i.) Gravitational redshift

ii.) Deflection of light near masive bodies (Eddington 1919)

iii.) Perihelion shift of mercury

Einstein calculated the theoretical predictions for these effects, which have been verified with enormous accuracy. All these tests have in common that they are carried out in empty space, with gravitational fields that are to an excellent aproximation stationary and isotropic, i.e. time independent and spherically symmetric. The first aim of this chapter will be to motivate and solve the vacuum Einstein equations under the simple assumptions of stationarity and isotropy (see section 2.2).
It might be interesting, that other tests have also been suggested and performed, for example the time delay of radar echos passing the sun, which is known as the Shapiro effect.

2.1.
From Special- to General Relativity

The need for a general relativistic theory of gravity is motivated by describing how and when Newtonian physics leads to no suitable results. As a mathematical doorway for this thesis this section will provide a short review of the Lorentz covariant formulation of special relativity, mainly to set the notation and conventions that will be used throughout this thesis. This is followed by a section on curvature and the need for tensor-like equations leading eventually to the Einstein field equations.

2.1.1.
Lorentz transformations

Based on the experimental results of Michelson and Morley the Einstein postulates tell us that

i.) The laws of physics are the same in all inertial frames of reference.

ii.) The speed of light in free space has the same value c in all inertial frames of reference.

The *first* postulate is already known from classical mechanics, Einstein merely expanded it to all known physical theories.
The *second* one is crucial, since it states that the speed of light does not change, neither when moving towards the source of light or moving away from it. The outcome of this is, that the Galilei transformation is not the correct one describing two systems of inertia. We can therefore expect to learn something about the effects of gravitation by transforming the laws of nature from an inertial cartesian coordinate system to other coordinates. The correct transformation is called the Lorentz transformation, which leaves invariant the proper time[3] in Minkowski spacetime.
The principle of relativity states, that the proper time $d\tau^2$ is invariant, because the speed of light in vacuo is a constant.

$$d\tau^2 = c^2dt^2 - dx^2 - dy^2 - dz^2 \tag{2.1}$$

Now, a general Lorentz transformation contains rotation in space and a boost, say in z-direction. Rotationally invariant laws can be written as vectors, for instance Newtons law of force, $\vec{F} = m\vec{a}$, or the centrifugal force, $\vec{F} = m\vec{\omega} \times (\vec{\omega} \times \vec{r})$. The proper time can then be written as

$$d\tau^2 = g_{\mu\nu}dx^\mu dx^\nu \tag{2.2}$$

[3]Sometimes also called the invariant interval or line element

where

$$g_{\mu\nu} = g^{\mu\nu} = \begin{pmatrix} 1 & 0 & 0 & 0 \\ 0 & -1 & 0 & 0 \\ 0 & 0 & -1 & 0 \\ 0 & 0 & 0 & -1 \end{pmatrix} \tag{2.3}$$

is the Minkowski metric and $x^\mu = (x^0, x^1, x^2, x^3)^T = (t, \vec{r})^T$ a Lorentz 4-vector. A Lorentz 4-vector transforms under a change of reference frame in the same way as the coordinates do.

$$x'^\mu = \Lambda^\mu_\nu x^\nu \tag{2.4}$$

where

$$\Lambda^\mu_\nu = \begin{pmatrix} \gamma & 0 & 0 & -\beta\gamma \\ 0 & 1 & 0 & 0 \\ 0 & 0 & 1 & 0 \\ -\beta\gamma & 0 & 0 & \gamma \end{pmatrix} \tag{2.5}$$

is the boost matrix and $\gamma = \frac{1}{\sqrt{1-\frac{v^2}{c^2}}} = \frac{1}{\sqrt{1-\beta^2}}$ the Lorentz-gamma factor. The condidition of invariance then is

$$d\tau^2 = g_{\mu\nu} dx^\mu dx^\nu = g_{\alpha\beta} dx'^\alpha dx'^\beta = g_{\alpha\beta} \Lambda^\alpha_\mu \Lambda^\beta_\nu dx^\mu dx^\nu \tag{2.6}$$

A boost matrix Λ^μ_ν must satisfy the relationship assuring the invariance of proper time (equation (2.2)), since this is valid for any dx^α.

2.1.2.

From the equivalence principle to the equations of motion

What consequences arise from the equality of inertial and gravitational mass? If all bodies suffer the same acceleration, gravity would be a pseudo- or fictional force, such as the centrifugal force. This is weird, since mass, creating a gravitational field, is responsible for this. The solution to this will be, that

masses distort spacetime itself instead of acting through forces.
According to Newton, where $x = vt$ and $z(x) = -\frac{gt^2}{2}$ with $g \simeq 9.81$ m/s^2

$$z(x) = -\frac{gx^2}{2v^2} \tag{2.7}$$

deriving twice

$$\ddot{z}(x) = -\frac{g}{v^2} \tag{2.8}$$

Classically it is therefore not possible that gravity equates curvature, since the trajectory of an arbitrary particle would depend on an initial condition: it's velocity.
According to Einstein then, all pseudoforces can be recognized as gravitational forces, i.e. they just depend on a nearby mass distribution. Then objects move forceless along the straightest line, a so called **geodesic**. In general relativity the shortest connection between two points is no longer a straight line, but a *bended path*. The equations of general relativity need to respect that massive bodies generate curvature, i.e. a distortion of spacetime. In a locally inertial frame the relativistic approach for a particles trajectory along the coordinates ξ^A is

$$\frac{d^2}{d\tau^2}\xi^A = 0 \tag{2.9}$$

$$\frac{d^2}{d\tau^2}\xi^A = \frac{\partial\xi^A}{\partial x^\mu}\frac{d^2x^\mu}{d\tau^2} + \frac{\partial\xi^A}{\partial x^\nu}\frac{\partial\xi^A}{\partial x^\lambda}\frac{dx^\nu}{d\tau}\frac{dx^\lambda}{d\tau} = 0 \tag{2.10}$$

$$\frac{d^2}{d\tau^2}\xi^A = \frac{\partial\xi^A}{\partial x^\mu}\left[\frac{d^2x^\mu}{d\tau^2} + \frac{\partial x^\mu}{\partial\xi^A}\frac{\partial\xi^A}{\partial x^\nu}\frac{\partial\xi^A}{\partial x^\lambda}\cdot\frac{dx^\nu}{d\tau}\frac{dx^\lambda}{d\tau}\right] = 0 \tag{2.11}$$

$$\frac{d^2}{d\tau^2}\xi^A = \frac{d^2x^\mu}{d\tau^2} + \frac{\partial x^\mu}{\partial\xi^A}\frac{\partial\xi^A}{\partial x^\nu}\frac{\partial\xi^A}{\partial x^\lambda}\cdot\frac{dx^\nu}{d\tau}\frac{dx^\lambda}{d\tau} = 0 \tag{2.12}$$

$\frac{\partial\xi^A}{\partial x^\mu}$ models the transformation from inertial- to accelerated system and cannot be equal zero. Thus we see that indeed the equations of motion for a massive particle in an arbitrary gravitational field are

$$\ddot{x}^\mu + \Gamma^\mu_{\nu\lambda}\dot{x}^\nu\dot{x}^\lambda = 0 \tag{2.13}$$

where the abbrevations

$$\frac{\partial x^\mu}{\partial \xi^A}\frac{\partial \xi^A}{\partial x^\nu}\frac{\partial \xi^A}{\partial x^\lambda} = \Gamma^\mu_{\nu\lambda} \tag{2.14}$$

$$\frac{d^2x^\mu}{d\tau^2} = \ddot{x}^\mu \tag{2.15}$$

$$\frac{dx^\nu}{d\tau}\frac{dx^\lambda}{d\tau} = \dot{x}^\nu \dot{x}^\lambda \tag{2.16}$$

were used. $\Gamma^\mu_{\nu\lambda}$ is called Christoffel symbol[4], which is symmetric in its lower indices. They are not tensor quantitative, since they spoil the transformation laws[5]. The Christoffel symbols can be expressed in terms of the metric and its derivatives.

$$\Gamma^\lambda_{\nu\mu} = \frac{1}{2}g^{\lambda\kappa}\left(\frac{\partial g_{\nu\kappa}}{\partial x^\mu} + \frac{\partial g_{\kappa\mu}}{\partial x^\nu} - \frac{\partial g_{\mu\nu}}{\partial x^\kappa}\right) \tag{2.17}$$

These objects describes the pseudoforce in accellerated reference frames. The path described by equation (2.13) is called *geodesic*, the extremal path in the spacetime of an arbitrary gravitational field.

2.1.3.

Riemann curvature tensor

To derive Einsteins field equations the knowledge of how curvature is relativistically defined, is required. The so called Riemann tensor, equation (2.18) describes curvature and is constructed by the metric and its first and second derivatives, see [8], [9] or [14] for a more detailled derivation.

$$\begin{aligned}\mathcal{R}_{\alpha\beta\gamma\delta} &= \left(\frac{\partial^2 g_{\alpha\gamma}}{\partial x^\beta \partial x^\delta} + \frac{\partial^2 g_{\beta\delta}}{\partial x^\alpha \partial x^\gamma} - \frac{\partial^2 g_{\beta\gamma}}{\partial x^\alpha \partial x^\delta} - \frac{\partial^2 g_{\alpha\delta}}{\partial x^\beta \partial x^\gamma}\right) \\ &+ g_{\rho\sigma}\left(\Gamma^\rho_{\gamma\alpha}\Gamma^\sigma_{\beta\delta} - \Gamma^\rho_{\delta\alpha}\Gamma^\sigma_{\beta\gamma}\right)\end{aligned} \tag{2.18}$$

To get in touch with such formulae, a two dimensional example (the curvature of a sphere) has been calculated in detail in [5], however contraction leads to

[4] Sometimes also called affine connection.

[5] A more physical explanation is that due to the equivalence principle the local graviational field can be switched off by going to a free falling inertial system.

the following quantities of $\mathcal{R}_{\alpha\beta\gamma\delta}$

$$g^{\alpha\gamma}\mathcal{R}_{\alpha\beta\gamma\delta} = \mathcal{R}_{\beta\delta} \tag{2.19}$$

is known as *Ricci*-tensor and

$$g^{\beta\delta}\mathcal{R}_{\beta\delta} = \mathcal{R} \tag{2.20}$$

is known as *curvature scalar*.
Note that for $\mathcal{R}_{\alpha\beta\gamma\delta} = 0$ a cartesian coordinate frame (a flat space) exists, else the geometry is distorted.

2.2. Einstein's Field Equations

The equations of Newton already tell us what possible path a particles takes and how mass acts as a source of the gravitational field [9].

$$m\frac{dr^2}{dt^2} = -m\vec{\nabla}\phi(\vec{r}) \qquad \text{and} \qquad \vec{\nabla}\phi(\vec{r}) = 4\pi G\rho(\vec{r}) \tag{2.21}$$

where $G \simeq 6.67 \cdot 10^{-11}$ m^3/kgs^2 is the gravitational constant. From special relativity it is known that energy and mass are equivalent [11]. That means that energy is also a source of a gravitational field. The equations have to become tensorical: The field $\phi(\vec{r}) \to g_{\mu\nu}$ and the corresponding counterpart on the other side of the equation is the energy momentum tensor $T_{\mu\nu}$.
The field equations can be derived via the metric $g_{\mu\nu}$, which models the gravitational potential, and the Christoffel symbols, which model the pseudoforce (remember section 2.1.2). The two contractions of Riemann, equation (2.19) and equation (2.20) model the curvature and are themself derivatives of the Christoffel symbols.

$$G_{\mu\nu} = \mathcal{R}_{\mu\nu} - \frac{1}{2}g_{\mu\nu}\mathcal{R} = \frac{8\pi G}{c^4}T_{\mu\nu} \tag{2.22}$$

To ensure energy and momentum conservation, $T_{\mu\nu}$ has to be divergenceless. Note that the Ricci tensor, equation (2.19), is not divergenceless. Therefore the Einstein equations contain a *correction* in form of a product of the metric and the Ricci scalar, eq. (2.20). A brief examination of equation (2.22) tells us, that indeed curvature equals a mass- and/or energy distribution.

> *Matter tells space how to curve. Space tells matter how to move.*
> John A. Wheeler [7]

Matter, energy and spacetime influence each other, therefore Einsteins field equations are highly non-linear and exceedingly complicated to solve. There are but a few solutions in closed form, of which one the most famous *Schwarzschild solution* is. The Schwarzschild solution describes the metric outside a sperically symmetric and static star and will briefly derived in section (2.2.1). For the interior structure of a spherically symmetric static star, the *Tolman-Oppenheimer-Volkoff*[6] equations, described in section (2.2.2), need to be solved. The TOV equations are in particular interesting within this thesis.
Another possible solution of the Einstein field equations is for instance the Kerr metric, descibing rotating stars, but not discussed within this introduction since beyond the scope of this thesis.

2.2.1. Schwarzschild solution

The Schwarzschild solution has been the first solution of the Einstein field equations. The solution has been found by the german astrophysicist Karl Schwarzschild during his service in the first world war in 1916 and describes a non-rotating, spherically symmetric mass in abscence of mass or energy, i.e.: $T_{\mu\nu} = 0$, a so called vacuum solution.
The Minkowski line element in spherical coordiantes reads

$$ds^2 = dt^2 - dr^2 - r^2\left(d\theta + \sin^2\theta d\phi^2\right) \tag{2.23}$$

[6] Usually abbreviated as TOV equations.

Because of its radial symmetry every term can be multiplicated by a space dependent function

$$ds^2 = A(r)dt^2 - B(r)dr^2 - C(r)r^2\left(d\theta + \sin^2\theta d\phi^2\right) \tag{2.24}$$

A boundary condition is, that for $r \to \infty$ the metric has to become the Minkowski metric, meaning $\lim_{r\to\infty} A(r) = \lim_{r\to\infty} B(r) = 1$, so that A and B can be replaced by exponentials.
The metric then reads

$$g_{\mu\nu} = \begin{pmatrix} e^{\nu(r)} & 0 & 0 & 0 \\ 0 & -e^{\lambda(r)} & 0 & 0 \\ 0 & 0 & -r^2 & 0 \\ 0 & 0 & 0 & -r^2\sin^2\theta \end{pmatrix} \tag{2.25}$$

To solve the field equations 2.22 the next step is to calculate the thirteen non-vanishing Christoffel symbols, which are "hidden" in the Ricci tensor.

$$\Gamma^r_{rr} = \frac{1}{2}g^{rr}\left(\frac{\partial g_{rr}}{\partial x^r} + \frac{\partial g_{rr}}{\partial x^r} - \frac{\partial g_{rr}}{\partial x^r}\right) = \frac{1}{2}g^{rr}\partial_r g_{rr} = \frac{\lambda'}{2} \tag{2.26}$$

The others are

$$\Gamma^r_{\theta\theta} = -re^{-\lambda} \tag{2.27}$$

$$\Gamma^r_{tt} = \frac{\nu' e^{\nu-\lambda}}{2} \tag{2.28}$$

$$\Gamma^r_{\phi\phi} = -r\sin^2\theta e^{-\lambda} \tag{2.29}$$

$$\Gamma^\theta_{\theta r} = \Gamma^\theta_{r\theta} = \Gamma^\phi_{r\phi} = \Gamma^\phi_{\phi r} = \frac{1}{r} \tag{2.30}$$

$$\Gamma^t_{tr} = \Gamma^t_{rt} = \frac{\nu'}{2} \tag{2.31}$$

$$\Gamma^\theta_{\phi\phi} = -\sin\theta\cos\theta \tag{2.32}$$

$$\Gamma^\phi_{\theta\phi} = \Gamma^\phi_{\phi\theta} = \cot\theta \tag{2.33}$$

The Ricci tensor is

$$\mathcal{R}^{\lambda}_{\mu\lambda\nu} = \mathcal{R}_{\mu\nu} = \partial_\lambda \Gamma^{\lambda}_{\mu\nu} - \partial_\nu \Gamma^{\lambda}_{\mu\lambda} + \Gamma^{\lambda}_{\lambda\rho}\Gamma^{\rho}_{\mu\nu} - \Gamma^{\lambda}_{\nu\rho}\Gamma^{\rho}_{\mu\lambda} \tag{2.34}$$

obeying the symmetries

$$\mathcal{R}_{r\theta} = \mathcal{R}_{r\phi} = \mathcal{R}_{t\theta} = \mathcal{R}_{t\phi} = \mathcal{R}_{\theta\phi} = 0$$

then applying

$$\Gamma^{\mu}_{\mu\lambda} = \partial_\lambda \ln\sqrt{|g|} \tag{2.35}$$

and the Ricci Tensor finally becomes

$$\mathcal{R}_{\mu\nu} = \frac{\partial^2}{\partial x^\mu \partial x^\nu} \ln\sqrt{|g|} - \partial_\lambda \Gamma^{\lambda}_{\nu\mu} + \Gamma^{\lambda}_{\nu\alpha}\Gamma^{\alpha}_{\lambda\mu} - \Gamma^{\alpha}_{\nu\mu}\partial_\alpha \ln\sqrt{|g|} \tag{2.36}$$

After a non enlightening application of algebra one obtains the following

$$\mathcal{R}_{tt} = -\frac{2}{2}e^{\nu-\lambda}\left(\nu'' + \frac{v'^2}{2} - \frac{\nu'\lambda'}{2} + \frac{2\nu'}{r}\right) \tag{2.37}$$

$$\mathcal{R}_{rr} = -\frac{1}{2}\left(\nu'' + \frac{v'^2}{2} - \frac{\nu'\lambda'}{2} + \frac{2\lambda'}{r}\right) \tag{2.38}$$

$$\mathcal{R}_{\phi\phi} = -1 + e^{-\lambda}\left(1 + \frac{(\nu'-\lambda')r}{2}\right) \tag{2.39}$$

$$\mathcal{R}_{\theta\theta} = \sin^2\theta \mathcal{R}_{22} \tag{2.40}$$

$$\mathcal{R}_{\mu\nu} = 0 \tag{2.41}$$

The calculation of the Ricci scalar is a restorative calculation compared to the calculation of the Ricci Tensor, however

$$\mathcal{R} = g^{\mu\nu}\mathcal{R}_{\mu\nu} = -\frac{2}{r^2}\mathcal{R}_{\phi\phi} \tag{2.42}$$

Since $\mathcal{R}_{\mu\nu}$ and $g_{\mu\nu}$ are diagonal, $\mathcal{G}_{\mu\nu}$ is too. Recalling that the Schwarzschild solutions are vacuum solutions, i.e. $T_{\mu\nu} = 0$, the Einstein equations eventu-

ally read:

$$\mathcal{G}_{tt} = -\frac{\lambda'}{r} + \frac{1}{r^2} - \frac{e^\lambda}{r^2} = 0 \tag{2.43}$$

$$\mathcal{G}_{rr} = \frac{\nu'}{r} - \frac{1}{r^2} + \frac{e^\lambda}{r^2} = 0 \tag{2.44}$$

$$\mathcal{G}_{\phi\phi} = \nu'' + \frac{\nu'^2}{2} - \frac{\nu'\lambda'}{2} + \frac{\nu' - \lambda'}{r} = 0 \tag{2.45}$$

$$\mathcal{G}_{\theta\theta} = \sin^2\theta \mathcal{R}_{22} \tag{2.46}$$

$$\mathcal{G}_{\mu\nu} = 0 \tag{2.47}$$

Integration of equation 2.43 yields $re^{-\lambda} - r = const = -r_s$ and the functions reduce to $e^{-\lambda(r)} = 1 - \frac{r_s}{r} = e^{\nu(r)}$ so that the line element finally reads

$$ds^2 = \left(1 - \frac{r_s}{r}\right) c^2 dt^2 - \left(1 - \frac{r_s}{r}\right)^{-1} dr^2 - r^2(d\theta^2 + \sin^2\theta d\phi^2) \tag{2.48}$$

which satisfies the condition for an asymptotically flat space as required. This equation describes the space outside a mass distribution[7] and is only valid for $r_s < r$, else time and space twist their character. The integration constant r_s is derived by comparison with the Newtonian potential for $r >> 1$

$$\phi(r) = -\frac{GM}{r} \simeq \frac{c^2}{2}(g_{00} - 1) \tag{2.49}$$

$$\phi(r) = \frac{c^2}{2}(e^\nu - 1) \tag{2.50}$$

$$\phi(r) = -\frac{c^2 r_s}{2r} \tag{2.51}$$

$$\rightarrow r_s = \frac{2GM}{c^2} \tag{2.52}$$

where r_s is the famous *Schwarzschild radius*. Table 2.1 shows different values of r_s for different atronomical objects.

[7] This is due to $T_{\mu\nu} = 0$, for an inner solution $T_{\mu\nu} \neq 0$, which will be discussed in the following section 2.2.2

Object	$M/M_\odot$	Radius [km]	Schwarzschildradius [km]
Earth	$3 \cdot 10^{-6}$	6400	$9 \cdot 10^{-6}$
Sun	1.0	$7 \cdot 10^5$	3
White dwarf	1.2	10.000	3.6
Compact star	2.0	12	6

Table 2.1: *General relativistic corrections of different objects in the Schwarzschild metric*

2.2.2.
The Tolman-Oppenheimer-Volkoff equations

To determine the inner solutions of spherically symmetric astrophysical objects $T_{\mu\nu} \neq 0$. The solutions of the field equations 2.22 are then used to describe compact stars, and are called the *Tolman-Oppenheimer-Volkoff* equations (TOV). An "ordinary" star is born due to the gravitational collapse of a interstellar cloud of gas. The thermal pressure counterbalances gravity and the star reaches a stable configuration for a relatively long time. The conditions for the stability of a nonrotating spherically symmetric ("ordinary") star are

$$dp = \frac{dF}{A} = \frac{dF}{4\pi r^2} \qquad \text{where} \qquad dF = -\frac{G \cdot dm \cdot m(r)}{r^2} \tag{2.53}$$

These considerations lead to

$$\frac{dp}{dr} = -\frac{G\rho(r)m(r)}{r^2} \tag{2.54}$$

$$\frac{dm}{dr} = 4\pi r^2 \rho(r) \tag{2.55}$$

The above derived equations describe non relativistic Newtonian stars.
After the star has consumed all its nuclear fuel it eventually explodes in a SN Type II, assuming it was massive[8] enough. The remnant is called a **com-**

[8] $M_{star} \geq 8M_\odot$

pact star[9]. Compact stars have to be described by general relativity due to their enormous effects on the surrounding spacetime. The TOV equations have first been derived in 1939 by Tolman, Oppenheimer and Volkoff [15]. Unlike as in the Schwarzschild solutions the energy momentum tensor will be considered finite. For isotropic, static and spherically symmetric mass distributions and metric $T_{\mu\nu}$ adopts the hydrodynamical form, since the matter within a compact star can be treated as a relativistic fluid[10].

$$T_{\mu\nu} = \left(\rho + \frac{p}{c^2}\right) u_\mu u_\nu - p g_{\mu\nu} \tag{2.56}$$

For the star to be in hydrodynamical equilibrium: $u^\mu = (u^0, \vec{0})$ and $g_{00}(u^0)^2 = c^2$, fron which follows that $(u_0)^2 = c^2 g_{00}$. The energy momentum tensor then reads

$$T_{\mu\nu} = \left(\rho + \frac{p}{c^2}\right) c^2 g_{00}\delta_{\mu 0}\delta_{\nu 0} - p g_{\mu\nu} = \begin{pmatrix} \rho_0 c^2 e^{\nu(r)} & 0 & 0 & 0 \\ 0 & p e^{\lambda(r)} & 0 & 0 \\ 0 & 0 & p r^2 & 0 \\ 0 & 0 & 0 & p r^2 \sin^2\theta \end{pmatrix}$$

The condition for hydrodynamic equilibrium requires that the covariant derivative of the enery momentum tensor vanishes

$$D^\mu T_{\mu\nu} = \frac{1}{2}\vec{\nabla}\ln(g_{00}) + \frac{1}{\rho c^2 + p}\vec{\nabla} p = 0 \tag{2.57}$$

After rearranging the terms

$$\frac{dp}{dr} = -\frac{1}{2}\nu'(r)\left(\rho(r)c^2 + p(r)\right) \tag{2.58}$$

This equation is already in similar shape as 2.54, only $v'(r)$ has to be determined by the Einstein equations 2.22. The procedure is similar to the Schwarzschild case and shall therefore be presented abbreviated. Main differences compared to 2.43, 2.44 and 2.45 are that the right-hand side of these

[9] See chapter 6 for a more detailled description of a stars life and death.
[10] Note that no electrical or magnetical fields are considered.

equations is, unlike as in the Schwarzschild case, finite:

$$G_{tt} = e^{\nu-\lambda}\left(-\frac{\lambda'}{r}+\frac{1}{r^2}\right)-\frac{e^{\nu}}{r^2}=-\frac{8\pi G}{c^4}\rho e^{\nu} \tag{2.59}$$

$$G_{rr} = -\frac{\nu'}{r}-\frac{1}{r^2}+\frac{e^{\lambda}}{r^2}=-\frac{8\pi G}{c^4}pe^{\lambda} \tag{2.60}$$

$$G_{\phi\phi} = -\frac{1}{2}r^2e^{-\lambda}\left(\nu''+\frac{\nu'\lambda}{2}-\frac{\nu'\lambda'}{2}+\frac{\nu'-\lambda'}{r}\right)=-\frac{8\pi G}{c^4}pr^2 \tag{2.61}$$

Furthermore, $G_{\theta\theta}$ yields exactly the same as in the Schwarzschild case (see eq. 2.46) and can hence be adopted. Solving for ν' and substituting into equation 2.58 yields

$$\frac{dp}{dr}=-\frac{(\rho c^2+p)\left[m(r)+\frac{4\pi G}{c^4}p(r)r^3\right]}{r^2-2m(r)r} \tag{2.62}$$

It can be seen that for $m(r) << r$ and $p << \rho c^2$ the equation reproduces the Newtonian limit, namely equation 2.54 and can therefore be considered as a correct general relativistic generalization. Mass conservation, equation 2.55, is valid without any corrections. Rearranging expression 2.62 gives

$$\frac{dp}{dr}=-\frac{G\epsilon(r)m(r)}{(cr)^2}\left(1+\frac{p(r)}{\epsilon(r)}\right)\left(1+\frac{4\pi r^3p(r)}{m(r)c^2}\right)\left(1-\frac{2Gm(r)}{c^2r}\right)^{-1} \tag{2.63}$$

where the three general relativistic correction factors can be distinguished from the Newtonian case:

The first correction factor implies that gravity does not only act upon a energy-mass distribution but also on its pressure.

The second one tells that not only the mass, but every single entry from $T_{\mu\nu}$ contributes to the gravitational field, i.e. energy is a source of gravity, so that pressure generates even more pressure.

The third one reflects the difference between Newtonian gravity and the gravitational "force" due to general relativity. This accounts for the additional factor in the denominator.

Note that the right-hand side of the equations 2.62 and 2.63 is negative so to assure the pressure inside the star decreases as one moves to larger values of the objects radius r. These equations, together with mass conservation, equation 2.55, can be solved numerically with an appropriate equation of state, typically given by a relation between pressure and energydensity.
The solutions of the TOV equations are determined by different equations of state, and the entire collection of masses and corresponding radii is called the mass-radius relation of compact stars. For each equation of state, $p(\epsilon) = p(\epsilon(r))$, where p is the pressure and ϵ the corresponding energy density at a given radius r, exists a solution which is parametrized by p_c, the central pressure of the star.

3

Elementary Particles and fundamental interactions

This introduction is based upon works from [16, 17, 18, 19, 20, 21, 22, 23]. A more detailled introductional discussion on elementary particles and their respective interactions can be found in (nearly) every textbook concerning the topic. Nonetheless it will be quoted were certain expressions have their origin.

At the beginning of the 20^{th} century the theory of special relativity (remember section 2.1) along with *Quantum-mechanics* revolutionized our understanding of nature. Since Quantum mechanics is a nonrelativistic theory, the development of a theory combining both, relativistic effects and elementary particles, has been lacked. During the 1920's and 1930's the most competent and capable physicists developed the idea of a *Quantum field theory*. A Quantum field theory treats particles as excited states of a corresponding physical field, so called field quanta, where quantum mechanical interactions between particles are described by interaction terms between the correspond-

ing underlying quantum fields.

3.1.
Elementary particle physics

Elementary particle physics addresses the question: "'What is the matter made of?"'. At the smallest scale of size there is a zoo of particles which can be found, some stable[1] ($\tau_{1/2} = 30$ years) and some not ($\tau_{1/2} = 10^{-20}$ seconds). These particles are then replicated in astronomical size to form all the matter around us. A theoretical framework to describe decays is therefore important in Quantum Field Theory. However the smallest particles to be found are quarks. Particles containing quarks are known as **hadrons**. Hadrons have to be color singletts, i.e. an appropriate combination of either color-anticolor, or three colors to make a *colorless* state (see section 3.6.2). Since a colored quark-state has never been solely detected in nature, quarks are *confined* within a hadron. Another important feature of quarks is, that for large temperature or density they behave *asymptotically free*. However, hadrons are classified into two groups: *mesons*, with integer spin[2], and *baryons* with half integer spin. The force between two quarks is mediated by the exchange of gluons, which are responsible for binding quarks together to make hadrons, and indirectly for holding protons and neutrons together. This feature is described by the theory of the strong interaction, quantum chromodynamics (see section 3.2). As we shall see, gluons carry a combination of color- and the appropriate anticolor. Murray Gell-Mann introduced the *eightfold way*, which arranges the baryons and mesons in weird geometrical patterns, according to their charge and strangeness. An understanding of the *eightfold* way came in 1964, when Gell-Mann and Zweig proposed that all hadrons are in fact composed of quarks, which themselfes come in three types of flavours (see table 3.1), forming a triangular pattern. In the 1960's and 1970's a theory emerged that described all the known elementary

[1] Stable on a cosmological timescale so to speak.
[2] Spin up $\uparrow$, Spin down $\downarrow$

generation	flavour	charge (e)	mass (MeV)
first	**u** (up)	$\frac{2}{3}$	2.3 ± 0.6
	d (down)	$-\frac{1}{3}$	4.8 ± 0.5
second	**s** (strange)	$-\frac{1}{3}$	95 ± 5
	c (charm)	$\frac{2}{3}$	1275 ± 25
third	**b** (bottom)	$-\frac{1}{3}$	4180 ± 30
	t (top)	$\frac{2}{3}$	1735 ± 70

Table 3.1: *The six quark flavours with spin* $\frac{1}{2}$ *and a few of their properties*

particle interactions, except gravity: It is incorporating Quantum electrodynamics and called *Glashow Weinberg Salam theory* of electroweak processes. Together with quantum chromodynamics (QCD) this theory has come to be called the *Standard Model*. The Standard Model is based upon two families of elementary particles: quarks and leptons[3] (and mediators) and can be derived by one general principle: The requirement of local gauge invariance, to be discussed in section 3.5.2.

3.2. Quantum chromodynamics

The theory of the strong interaction is the so called *quantum chromodynamics*. It describes the interaction between quarks and gluons. Due to the electric charge of the quarks, the electromagnetic force also plays but a subdominant part, this is due to the fact that the electromagnetic coupling constant is two orders of magnitude smaller $\alpha_{em} \sim \frac{1}{137}$ than the strong coupling in vacuum $\alpha_s \sim 1$. By exchanging weak bosons, quarks can also interact weakly, this mechanism is responsible for the β-decay of nucleons, which themselves consist of quarks. The range of the strong interaction is about 10^{-15} m. In the framework of the standard model, color[4] plays the role

[3] Recall that leptons do not carry color, so they do not participate in the strong interaction

[4] Usually red, green and blue, and the appropriate anticolors for antiquarks

of charge, and the fundamental process is $q \to q + g$, see figure 3.1. Two or more such *primitive* vertices can be combined to represent more complicated processes. The concept of color as charge will be enlightened in section 3.6.2.

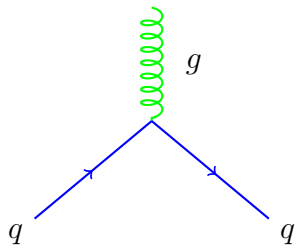

Figure 3.1: *Feynman diagram of the process $q \to q + g$. In this fundamental process, the color of the quark q may change, but not its flavour. They interact via a gluon g, which carries away the difference in charge. For instance: $r \to b + r\bar{b}$.*

Before dealing and discussing quantum chromodynamics in greater detail, a few preliminary considerations are derived to an extend required to understand not only the need for an effective model, but also topic and results of this thesis, and are therefore crucial.

3.3. Lagrangians

A particle is a localized entity. In classical mechanics we are interested in calculating its position as a function of time $\vec{x}(t)$. A field, on the other hand, occupies some region of space, so our concern is to calculate functions of position and time $\phi_i(t, \vec{x})$. In classical mechanics the Lagrangian was a function of the coordinates q_i and its derivatives $\dot{q}_i$. The starting point in a quantum field theoretical approach is a Lagrangian density[5] $\mathcal{L}$, which is an expansion of the Lagrange function of classical mechanics to field theory[6].

[5] Often just called Lagrangian

[6] The considered object will be replaced by a field with ∞ degrees of freedom.

Note that in classical mechanics the Lagrange function is derived, in field theory $\mathcal{L}$ is axiomatic.

3.3.1. Euler-Lagrange equation

The used Lagrangian $\mathcal{L}$, which models the properties of any given problem in field theories, usually depends on the fields themselves and it's first derivatives $\mathcal{L} = \mathcal{L}(\phi, \partial_\mu \phi)$. A small displacement in the fields ϕ causes

$$\delta S = \int d^4x (\mathcal{L}(\phi', \partial_\mu \phi') - \mathcal{L}(\phi, \partial_\mu \phi)) \tag{3.1}$$

S being the action, which is required to vanish. Expanding in Taylor series

$$\delta S = \int d^4x \left(\mathcal{L}(\phi, \partial_\mu \phi) + \frac{\partial \mathcal{L}}{\partial \phi} \delta\phi + \frac{\partial \mathcal{L}}{\partial(\partial_\mu \phi)} \delta(\partial_\mu \phi) - \mathcal{L}(\phi, \partial_\mu \phi) \right) = 0 \tag{3.2}$$

so that

$$\delta S = \int d^4x \left(\frac{\partial \mathcal{L}}{\partial \phi} \delta\phi + \frac{\partial \mathcal{L}}{\partial(\partial_\mu \phi)} \delta(\partial_\mu \phi) \right) = 0 \tag{3.3}$$

Using the product rule the second expression in the brackets can be rewritten to

$$\delta S = \int \delta\phi \left(\frac{\partial \mathcal{L}}{\partial \phi} - \partial_\mu \frac{\partial \mathcal{L}}{\partial(\partial_\mu \phi)} \right) = 0 \tag{3.4}$$

Since $\delta\phi$ is arbitrary the term in the brackets has to vanish

$$\frac{\partial \mathcal{L}}{\partial \phi} - \partial_\mu \frac{\partial \mathcal{L}}{\partial(\partial_\mu \phi)} = 0 \tag{3.5}$$

Equation (3.5) is known as *Euler-Lagrange* equation and is the field theoretical expansion of the well know Lagrange equation from classical mechanics.

3.4.
Particles with integer Spin

3.4.1.
The Klein Gordon equation

The *Klein Gordon* equation describes particles with spin 0. It is a relativistic generalization of the Schrödinger equation. When the *Klein Gordon* equation was first derived it was first rejected since its interpretation was not clear at first. This is due to her second order time character. Later it could be interpreted as the equation describing spin 0 particles. The Lagrangian describing boson fields ϕ reads

$$\mathcal{L} = \frac{1}{2}(\partial_\mu \phi)(\partial^\mu \phi) - \frac{1}{2}m^2\phi^2 \tag{3.6}$$

Using the Euler-Lagrange equation (3.5)

$$-\frac{\partial(\mathcal{L})}{\partial(\phi)} + \partial_\mu\left(\frac{\partial(\mathcal{L})}{\partial(\partial_\mu\phi)}\right) = 0 \tag{3.7}$$

the Lagrangian becomes

$$\frac{\partial(\mathcal{L})}{\partial(\phi)} = -m^2\phi \qquad \text{and} \qquad \frac{\partial(\mathcal{L})}{\partial(\partial_\mu\phi)} \to \frac{1}{2}(\partial_\mu\phi)(\partial^\mu\phi) \tag{3.8}$$

We will treat ∂_μ in the second expression in equation (3.7) afterwards

$$\begin{aligned}
\frac{\partial(\mathcal{L})}{\partial(\partial_\mu\phi)} &= \frac{\partial}{\partial(\partial_\mu\phi)}\left(\frac{1}{2}g^{\alpha\beta}(\partial_\alpha\phi)(\partial_\beta\phi)\right) \qquad (3.9)\\
&= \frac{1}{2}g^{\alpha\beta}\frac{\partial}{\partial(\partial_\mu\phi)}\left((\partial_\alpha\phi)(\partial_\beta\phi)\right) = \frac{1}{2}g^{\alpha\beta}\left(\frac{\partial\partial_\alpha\phi}{\partial(\partial_\mu\phi)}\partial_\beta\phi + \partial_\alpha\phi\frac{\partial\partial_\beta\phi}{\partial(\partial_\mu\phi)}\right)\\
&= \frac{1}{2}g^{\alpha\beta}\left(g^\mu_\alpha\partial_\beta\phi + \partial_\alpha\phi g^\mu_\beta\right) = \frac{1}{2}g^{\alpha\beta}\partial_\mu\left(g^\mu_\alpha\partial_\beta\phi + \partial_\alpha\phi g^\mu_\beta\right)\\
&= \frac{1}{2}g^{\alpha\beta}\left(\partial_\alpha\partial_\beta\phi + \partial_\alpha\partial_\beta\phi\right) = \partial_\alpha\partial^\alpha\phi
\end{aligned}$$

The equation of motion for spin 0 particles finally reads

$$\Box\phi + m^2\phi = 0 \tag{3.10}$$

3.4.2. The Proca equation

For the sake of completeness the Proca equation shall be mentioned. When dealing with spin 1 bosons, one defines a vector A^ν and an arbitrary mass m. The field equation becomes

$$\partial_\mu F^{\mu\nu} + mA^\nu = 0 \tag{3.11}$$

If the notation reminds you of electrodynamics: This is no incident, since the electromagnetic field is a massless[7] vector field with spin 1.

3.5. Particles with half integer spin

3.5.1. Dirac equation

The Dirac Lagrangian describing fermions[8] with half integer spin is

$$\mathcal{L} = \bar{\Psi}(i\not{\partial} - \hat{m})\Psi \tag{3.12}$$

with the shorthand $\not{\partial} = \gamma_\mu\partial^\mu$ and the Dirac matrices

$$\gamma_0 = \begin{pmatrix} \mathbb{1}_2 & 0 \\ 0 & -\mathbb{1}_2 \end{pmatrix} \gamma_i = \begin{pmatrix} 0 & \hat{\tau}_i \\ -\hat{\tau}_i & 0 \end{pmatrix} \tag{3.13}$$

[7] Set $m = 0$ and you are left with the Maxwell equations for empty space
[8] Such as the neutron or proton

and τ_i being the Pauli matrices,

$$\tau_1 = \begin{pmatrix} 0 & 1 \\ 1 & 0 \end{pmatrix} \tau_2 = \begin{pmatrix} 0 & -i \\ i & 0 \end{pmatrix} \tau_3 = \begin{pmatrix} 1 & 0 \\ 0 & -1 \end{pmatrix} \tag{3.14}$$

The Dirac equation can be obtained by applying the Euler Lagrange equation 3.5 to the Dirac Lagrangian, yielding

$$(\gamma^\mu p_\mu - m)\,\Psi = 0 \tag{3.15}$$

$$(\gamma^\mu p_\mu + m)\,\bar{\Psi} = 0 \tag{3.16}$$

which is the equation of motion for particles 3.15 and antiparticles 3.16 with spin $\pm 1/2$.

3.5.2. Gauge invariance and covariant derivative

$\mathcal{L}$ from equation 3.12 is invariant under a global phase transition $\Psi \to \Psi' = \Psi e^{i\Theta}\Psi$ where Θ is a constant, but not invariant under a local phase transition, when $\Theta(x^\mu)$ itself is a function, i.e different at different space-time points, then

$$\Psi \to \Psi' = \Psi e^{i\Theta(x^\mu)}\Psi \tag{3.17}$$

The Lagrangian then has an additional term

$$\begin{aligned}
\mathcal{L} &= ie^{-i\Theta(x^\mu)}\bar{\Psi}\not{\partial}e^{i\Theta(x^\mu)}\Psi - \hat{m}e^{i\Theta(x^\mu)}\bar{\Psi}e^{-i\Theta(x^\mu)}\Psi \\
&= ie^{-i\Theta(x^\mu)}\bar{\Psi}\gamma^\mu\left((\partial_\mu\Psi)e^{i\Theta(x^\mu)} + (\partial_\mu(i\Theta(x^\mu)))e^{i\Theta(x^\mu)}\Psi\right) - \hat{m}\bar{\Psi}\Psi \\
&= ie^{-i\Theta(x^\mu)}\bar{\Psi}\gamma^\mu\partial_\mu\Psi e^{i\Theta(x^\mu)} \\
&- ie^{-i\Theta(x^\mu)}\bar{\Psi}\gamma^\mu(\partial_\mu(\Theta(x^\mu))e^{i\Theta(x^\mu)}\Psi - \hat{m}\bar{\Psi}\Psi \\
&= i\bar{\Psi}\not{\partial}\Psi - \hat{m}\bar{\Psi}\Psi - \bar{\psi}\gamma^\mu\partial_\mu(\Theta(x^\mu)) \\
&= \bar{\Psi}(i\not{\partial} - \hat{m})\Psi - \bar{\psi}\gamma^\mu\partial_\mu(\Theta(x^\mu))
\end{aligned} \tag{3.18}$$

With $\lambda(x^\mu) = -\frac{1}{q}\Theta(x^\mu)$, where q is the charge of the particle involved, then the Lagrangian can be written as

$$\mathcal{L} = \mathcal{L} + q\bar{\Psi}\not{\partial}\lambda(x^\mu)\Psi \tag{3.19}$$

The extra term resulting from the derivative has to be soaked up for the whole Lagrangian to be invariant. Suppose

$$\mathcal{L} = i\bar{\Psi}\not{\partial}\Psi - \hat{m}\bar{\Psi}\Psi - q\bar{\Psi}\gamma^\mu\Psi A_\mu \tag{3.20}$$

where A_μ is an additional field, which transforms according to

$$A_\mu \rightarrow A'_\mu = A_\mu + \partial_\mu\lambda \tag{3.21}$$

This *improved* Lagrangian is locally invariant, since

$$\begin{aligned} \mathcal{L} &= i\bar{\Psi}\not{\partial}\Psi - \hat{m}\bar{\Psi}\Psi - q\bar{\Psi}\gamma^\mu\Psi A_\mu - q\bar{\Psi}\gamma^\mu\Psi\partial_\mu\Psi + q\bar{\Psi}\gamma^\mu\Psi\partial_\mu\Psi & (3.22)\\ &= i\bar{\Psi}\not{\partial}\Psi - \hat{m}\bar{\Psi}\Psi - q\bar{\Psi}\gamma^\mu\Psi A_\mu & (3.23)\end{aligned}$$

The price to pay therefore is to introduce a new massless vector field which couples to Ψ, called **gauge field**. In case of QED this is the well known photon field, as will be described in section (3.6.1). The difference between global and local phase transitions occurs when calculating derivatives of the fields

$$\partial_\mu\Psi \rightarrow e^{i\lambda}(\partial_\mu + iq\partial_\mu\lambda)\Psi \tag{3.24}$$

Instead of a simple phase factor, $\partial_\mu\lambda$ has to be introduced. If now every derivative in $\mathcal{L}$ will be replaced by the so called *covariant derivative*

$$\mathcal{D}_\mu \equiv \partial_\mu - iqA_\mu \tag{3.25}$$

the gauge transformation of A_μ, equation 3.21, will cancel the offending term, and $\mathcal{L}$ is finally invariant under a local phase transition. With equations 3.17,

3.21, 3.25 and the abbreviation $\Theta(x^\mu) = \Theta$

$$\begin{aligned}
\mathcal{D}\Psi \to \mathcal{D}'\Psi' &= (\partial_\mu - iqA'_\mu)e^{i\Theta} && (3.26)\\
&= (\partial_\mu - iqA_\mu - iq\partial_\mu\Theta)e^{iq\Theta}\Psi && (3.27)\\
&= (\partial_\mu - iqA_\mu + iq\partial_\mu\Theta - iq\partial_\mu\Theta)e^{iq\Theta}\Psi && (3.28)\\
&= (\partial_\mu - iqA_\mu)e^{iq\Theta}\Psi = e^{iq\Theta}\mathcal{D}\Psi && (3.29)
\end{aligned}$$

The Dirac Lagrangian finally transform then according to

$$\begin{aligned}
\bar{\Psi}(i\not{\mathcal{D}} - \hat{m})\Psi &\to \bar{\Psi}'(i\not{\mathcal{D}}' - \hat{m})\Psi' && (3.30)\\
&= e^{-iq\Theta}\bar{\Psi}(i\not{\mathcal{D}}'\Psi' - \hat{m}\Psi') && (3.31)\\
&= e^{-iq\Theta}\bar{\Psi}(ie^{iq\Theta}\not{\mathcal{D}}\Psi - \hat{m}e^{iq\Theta}\Psi) && (3.32)\\
&= \bar{\Psi}i\not{\mathcal{D}}\Psi - \bar{\Psi}\hat{m}\Psi && (3.33)\\
&= \bar{\Psi}(i\not{\mathcal{D}}\Psi - \hat{m})\Psi && (3.34)
\end{aligned}$$

and hence is locally invariant.
Using the example of QED, we shall see in a following section (3.6.1) how the field strenght tensor, including the respective gauge field, transforms.

3.6. Unitary symmetries and symmetry breaking

Symmetries play an important role in the description of the fundamental interactions. Before describing the model used in this work a much simpler example of an underlying symmetry is discussed. Eventually the QCD Lagrangian will be examined. This should be beheld as a base for further investigations in the (chiral) **quark meson model**, which in detail will be discussed in chapter 4 and is among the main parts in this thesis.

3.6.1.

U(1) symmetry of Quantumelectrodynamics

Quantum **E**lectro **D**ynamics is the oldest and most successful of the dynamical theories, the others are self-consciously modeled on it, so that this section is not only a historical, but also a decisive necessity for the discussion of certain symmetries of quantum chromodynamics.
It describes the theory of electromagnetism as an interaction between electrons and photons, see figure 3.2.
The Lagrangian of QED in natural units reads

$$\mathcal{L} = -\frac{1}{4}F^{\mu\nu}F_{\mu\nu} + \bar{\Psi}(i\not{D} - m)\Psi \tag{3.35}$$

with $F^{\mu\nu} = \partial^\mu A^\nu - \partial^\nu A^\mu$ as the field strenght tensor of the electromagnetic field including A^μ as gauge field, Ψ represents the spinor of the electron, m their mass and $D_\mu = \partial_\mu - ieA_\mu$ being the covariant derivative as discussed in section (3.5.2). Equation (3.35) is invariant under a U(1) gauge transformation of the form

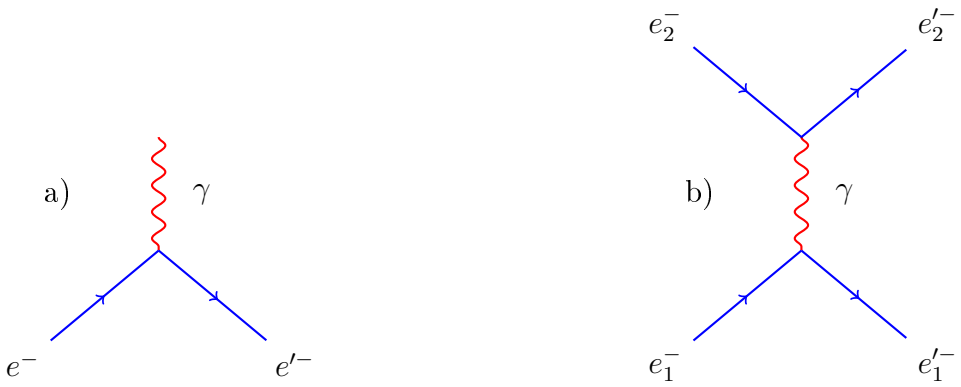

Figure 3.2: *Feynman diagram of quantum electrodynamics. a) reads that a charged electron e^- enters, emits (or either absorbs) a photon γ and exits as e'^-. In case b) two electrons, e_1^- and e_2^- enter, a photon passes between them and two (primed) electrons exit. As shortly mentioned in section 3.2, more complicated processes can be described by combining more primitive vertices.*

$$\Psi \to \Psi' = \hat{U}\Psi \tag{3.36}$$

$$A_\mu \to A'_\mu = \hat{U}A_\mu\hat{U}^{-1} - \frac{i}{e}(\partial_\mu\hat{U})\hat{U}^{-1} \tag{3.37}$$

where $\hat{U} = e^{ie\Theta(x)}$ is the space-time dependend phase.
In the U(1) case equation (3.37) simplifies to equation (3.21). Following equation (3.31) one can see immediately that the term describing matter, in case of QED the electrons, is locally invariant. So is the field strenght tensor including the gauge field A^μ, since

$$F^{\mu\nu} \to F'^{\mu\nu} = \partial^\mu(A^\nu + \partial^\nu\Theta) - \partial^\nu(A^\mu + \partial^\mu\Theta) = F^{\mu\nu} \tag{3.38}$$

The gauge field in QED is the photon-field, describing the electromagnetic interaction via an exchange of photons.

3.6.2.
SU(3) color symmetry of Quantumchromodynamics

The main goal of any physical model is to describe processes in nature in a most approximativley way. The necessity of an additional degree of freedom called color for quarks arises from the Pauli principle. Following the eightfold way, a proton[9] is a state containing two up quarks and one down quark. Its spin-flavour wave function can be written as

$$|p> = \frac{1}{\sqrt{3}}\left(|u_\uparrow u_\uparrow d_\downarrow> + |u_\uparrow u_\downarrow d_\uparrow> + |u_\downarrow u_\uparrow d_\uparrow>\right) \tag{3.39}$$

In 1965 a baryon with charge 2e and spin 3/2 has been discovered, which could only be described by up quarks, but only if the Pauli exclusion principle was violated. The particle was labelled Δ^{++} and its spin-flavour wave

[9] For the neutron just replace $u \to d$

function had to be

$$|\Delta^{++}>=|u_\uparrow u_\uparrow u_\uparrow> \tag{3.40}$$

The solution to this paradox was to introduce another additional degree of freedom: color.
The feature of color has even been verified experimentally. The π^0 decays into 2γ and the standard model determines the corresponding decay width [24] to

$$\Gamma_{\pi^0\to 2\gamma} = \frac{\alpha^2 m_\pi^3}{64\pi^2 f_\pi^2}\left(\frac{N_c}{3}\right)^2 \equiv 7.73\text{eV}\left(\frac{\mathrm{N_c}}{3}\right)^2 \tag{3.41}$$

where N_c denotes the number of colors and f_π being the pion decay constant (which plays an important role in the forthcoming). The experimental value was found to be $\Gamma^{exp}_{\pi^0\to 2\gamma} = 7.83 \pm 0.37$ eV and can only be described by the standard model if $N_c = 3$ [25].
However, to construct a Lagrangian which contains either the flavour and the colour degrees of freedom, the SU(3) gauge symmetry needs to be utilized. The Lagrangian requires invariance under rotations in color space[10]. A quark field in the fundamental representation transforms as

$$q_f \to q'_f = e^{-i\Theta^\alpha(x)\hat{T}_\alpha}\cdot q_f = \hat{U}q \tag{3.42}$$

where $\hat{T}_\alpha$ denotes the eight generators $\hat{T}_\alpha = \frac{\hbar}{2}\hat{\lambda}_\alpha$ of the group, also known as Gell-Mann matrices. Θ^a are the parameters of the group. Analogous to the Dirac Lagrangian for fermions, a locally SU(3) symmetric Lagrangian for quarks can be constructed.

$$\mathcal{L}_q = \bar{q}(i\gamma^\mu D_\mu - m_f)q \tag{3.43}$$

where the sum over the different quark flavors f is implied and $D_\mu = \partial_\mu - igA_\mu$ is the covariant derivative with the eight gauge fields A_μ of the SU(3) group, representing the gluon fields. Under the SU(3) group the gluon fields

[10] Generally spoken, the Lagrangian needs to be Poincarre-invariant

transform similar to the QED gauge field

$$A_\mu \to A'_\mu = U A_\mu U^\dagger - \frac{i}{g}(\partial_\mu U)U^\dagger \tag{3.44}$$

The theory of the strong interaction is then characterized by the following Lagrangian

$$\mathcal{L} = \bar{\Psi}(i\not{\mathcal{D}} - \hat{m})\Psi - \frac{1}{4}(\mathcal{F}^{\mu\nu}\mathcal{F}_{\mu\nu}) \tag{3.45}$$

where $\mathcal{F}^{\mu\nu} = F^{\mu\nu}\hat{T}_\alpha$ is the gauge-field term. Ψ is the Dirac-4-spinor of the quarks with the mass matrix $\hat{m}$. Ψ is not just a spinor, but also a 3-vector in color-space. The more, there are six quark flavors, so that $\hat{m}$ is actually a 72-component matrix. The relationship to the QED-Lagrangian is highly visible.

The main difference between QED and QCD is, that in QCD eight field strenght tensors $F^{\mu\nu}\hat{T}_\alpha$, corresponding to eight colors of the gluon fields, exist. Its 4-potential $\mathcal{A}^\mu \equiv A^\mu_\alpha \hat{T}_\alpha$ then represent the gluons.

Since $\mathcal{F}_{\mu\nu}$ is defined as a commutator of two covariant derivatives, additional terms in the field-strenght tensor arise.

$$F^{\mu\nu}\hat{T}_\alpha = \partial^\mu A^\nu_\alpha - \partial^\nu A^\mu_\alpha + g f_{abc} A^\mu_b A^\nu_c \tag{3.46}$$

where f_{abc} are the antisymmetric structure constants, i.e commutation relations for Gell-Mann matrices. This non-abelian nature of QCD leads to 3- and 4 gluon interaction terms, which makes QCD such hard to calculate. Nontheless is equation (3.45) locally gauge invariant. This is one of the reasons[11] why quarks and gluons can be arranged in multiplets of SU(3). Quarks and gluons only transform into each other, but never among themselves. A coupling of a triplett and an antitriplett $[\bar{3}] \otimes [3] = [1] \oplus [8]$ generates a singlett and an octett. These patterns then represent the gluons[12], which in this picture can be understood as a combination of color and anticolor, see figure 3.3.

[11] The other reasons will be discussed in section (3.6.3)

[12] The same is possible for mesons and baryons.

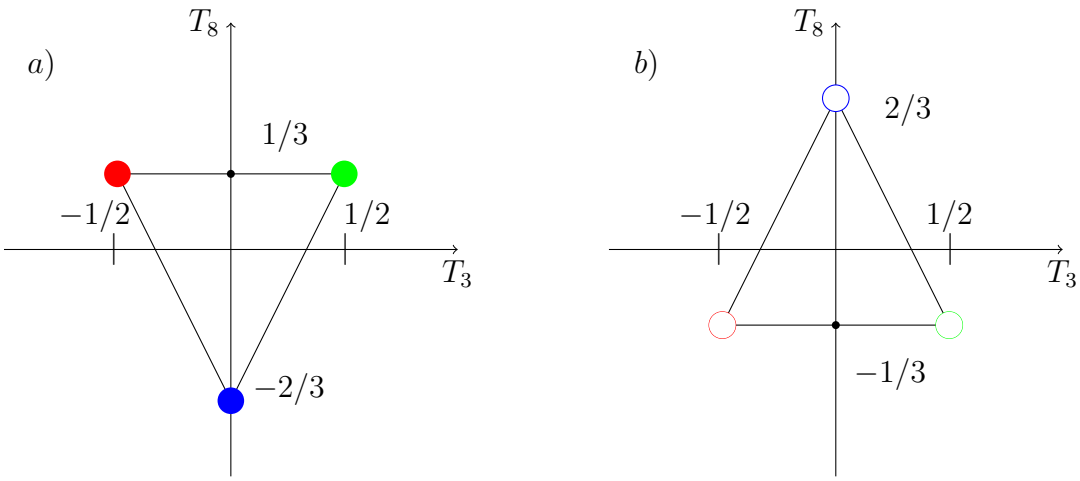

Figure 3.3: *The triplett in fundamental representation: a) displays the colors, b) the respective anticolors. The T_3 axis is the color's spin, whereas the T_8 axis labels the hypercharge. Since anti particles have opposite sign in charge, this has even to be the case for the color (Remember: color is a charge). Therefore is b) the corresponding antitriplett.*

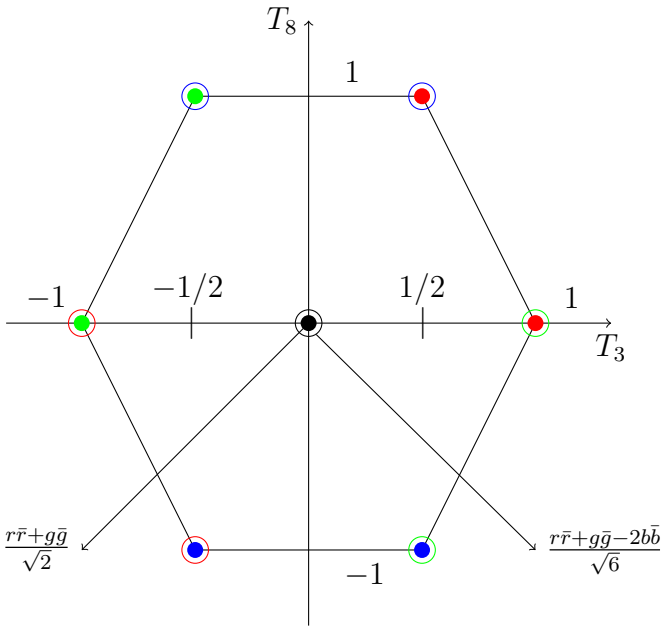

Figure 3.4: *The eight gluons occupy states in the adjoint representation of the octett. Due to* $[\bar{3}] \otimes [3] = [1] \oplus [8]$ *are gluons a combination of colors and anticolors. Confinement requires that all naturally occuring particles be color singlets, this explains why the octett gluons never appear as free particles, hence there is no singlett state, because if there was, it would appear as a free particle. The centered states are combinations of colors and anticolors according to the Clebsch-Gordan coefficients.*

3.6.3.

SU(3) flavor symmetry of Quantumchromodynamics

In case of massless QCD left- and righthanded fields decouple. Even if quarks are not massless, the mass of the up and down quark is relatively small (see table (3.1)) on a hadronic scale (nucleon≅ 1GeV). Using the projectors

$$\Psi_L = (\mathbb{1} - \gamma_5)\Psi \tag{3.47}$$

$$\Psi_R = (\mathbb{1} + \gamma_5)\Psi \tag{3.48}$$

and splitting the Lagrangian from equation (3.12) up into $\mathcal{L} = \mathcal{L}_L + \mathcal{L}_R$

$$\mathcal{L} = \bar{\Psi}(i\not{\partial} - \hat{m})\Psi \tag{3.49}$$
$$\mathcal{L} = (\bar{\Psi}_L + \bar{\Psi}_R)(i\not{\partial} - \hat{m})(\Psi_L + \Psi_R) \tag{3.50}$$

Yielding

$$\begin{aligned}\mathcal{L} = i\bar{\Psi}_L\not{\partial}\Psi_L + i\bar{\Psi}_R\not{\partial}\Psi_R - m(\bar{\Psi}_L\Psi_R + \bar{\Psi}_R\Psi_L)\\ +i\bar{\Psi}_L\not{\partial}\Psi_R + i\bar{\Psi}_R\not{\partial}\Psi_L - m(\bar{\Psi}_L\Psi_L + \bar{\Psi}_R\Psi_R)\end{aligned} \tag{3.51}$$

The Dirac matrices satisfy $\{\gamma^\mu, \gamma^\nu\} = 2g^{\mu\nu}$ so that $g_{\mu\nu}p^\mu p^\nu = \frac{1}{2}\{\gamma^\mu, \gamma^\nu\}p^{\mu\nu} = \gamma^\mu m_\mu \gamma^\nu m_\nu$. Using equation (3.13) and

$$\gamma_5 \equiv i\gamma_0\gamma_1\gamma_2\gamma_3 = \begin{pmatrix} 0 & \mathbb{1} \\ \mathbb{1} & 0 \end{pmatrix} \tag{3.52}$$

such as

$$\gamma_5^2 = \mathbb{1} \tag{3.53}$$
$$\{\gamma_5, \gamma_\mu\} = 0 \quad \forall\mu = 0, 1, 2, 3 \tag{3.54}$$

and $\bar{\Psi} = \Psi^\dagger\gamma^0$, the left hand product of the fields gives

$$\bar{\Psi}_L\Psi_L = \frac{1}{4}\Psi^\dagger(\mathbb{1} - \gamma_5)\gamma^0(\mathbb{1} - \gamma_5)\Psi \tag{3.55}$$
$$= \frac{1}{4}\Psi^\dagger(\gamma^0 + \gamma^0\gamma_5)(\mathbb{1} - \gamma_5)\Psi \tag{3.56}$$
$$= \frac{1}{4}\bar{\Psi}(\mathbb{1} + \gamma_5)(\mathbb{1} - \gamma_5)\Psi = 0 \tag{3.57}$$

Analoguous for the right handed fields $\bar{\Psi}_R \Psi_R = 0$.
With the abbreviation $\not{p} = \partial_\mu \gamma^\mu$ and using equation (3.54)

$$\begin{aligned} \not{p}\Psi_R &= \frac{1}{2}\partial_\mu \gamma^\mu (\mathbb{1} + \gamma_5)\Psi && (3.58) \\ &= \frac{1}{2}(\gamma^\mu + \gamma^\mu \gamma_5)\partial_\mu \Psi && (3.59) \\ &= \frac{1}{2}(\mathbb{1} - \gamma_5)\gamma^\mu \partial_\mu \Psi && (3.60) \\ &= \frac{1}{2}(\mathbb{1} - \gamma_5)\not{p}\Psi && (3.61) \end{aligned}$$

Adding $\bar{\Psi}_L$

$$\begin{aligned} \bar{\Psi}_L \not{p} \Psi_R &= \frac{1}{2}\Psi^\dagger (\mathbb{1} - \gamma_5)\gamma^0 \frac{1}{2}(\mathbb{1} - \gamma_5)\not{p}\Psi && (3.62) \\ &= \frac{1}{4}\bar{\Psi}(\mathbb{1} + \gamma_5)(\mathbb{1} - \gamma_5)\not{p}\Psi = 0 && (3.63) \end{aligned}$$

and from equation (3.51) everything but

$$\mathcal{L} = i(\bar{\Psi}_L \not{p} \Psi_L + \bar{\Psi}_R \not{p} \Psi_R) - m(\bar{\Psi}_L \Psi_R + \bar{\Psi}_R \Psi_L) \qquad (3.64)$$

cancels.
In case $m = 0$ both fields decouple, so that eventually $\mathcal{L} = \mathcal{L}_L + \mathcal{L}_R$.
This property is called *chiral* symmetry. Note that a mass term m breaks chiral symmetry explicitely. This feature shall be enlightened in section 3.6.6. The conserved quantities however are the vector current, i.e. the *isospin*, and the axialvector current, which is only partially conserved [20]. Conservation of isospin and strangeness are mainly responsible for the arrangement in multiplets. Mesons and baryons can be (for instance) arranged due to $[\bar{3}] \otimes [3] = [1] \oplus [8]$ into a *singlett*- and an *oktett* state (see figure 3.5), similar as the colors combine to make gluons (see figure 3.4). Only mesons and baryons consist of quarks and antiquarks.

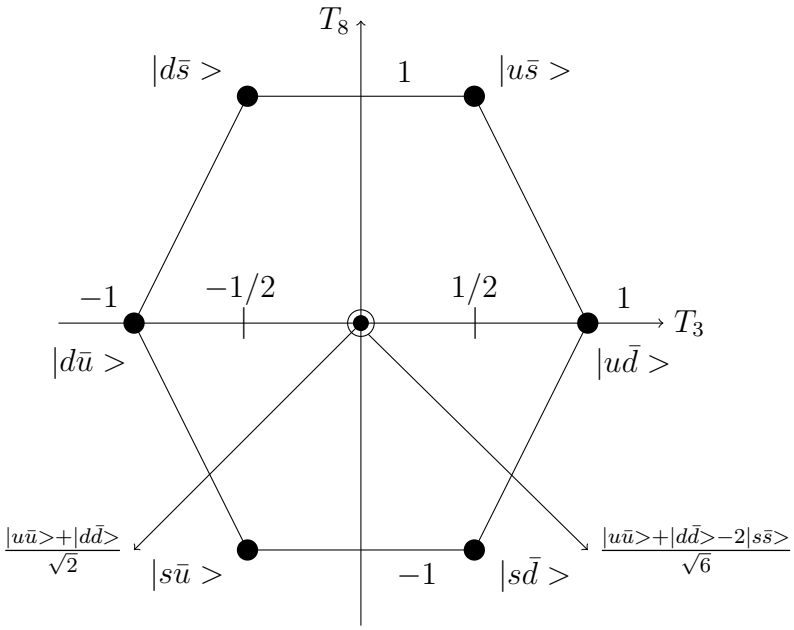

Figure 3.5: *The meson octett and the respective flavour content. One can then distinguish between scalar, pseudoscalar, vector and axialvector mesons. The $|u\bar{s}>$ state for instance represents different Kaon states. The centered states are combinations of quarks and antiquarks according to the Clebsch-Gordan coefficients. The singlett is not shown here.*

3.6.4.

Symmetries and conserved quantities

The Noether theorem known from classical mechanics combines symmetries with conserved quantities, see table 3.2. This holds also for fields. Mathematically a symmetry is a variation of the field or respectively the Lagrangian, leaving the appropriate equation of motion invariant. Two of the most fundamental conservation laws in physics, conservation of energy and momentum, are due to a symmetry that results from a small displacement in spacetime. Variation of $x^\mu \rightarrow x^{\mu'} = x^\mu + a^\mu$, where a^μ is a small and arbitrary parameter,

leads to a change in the fields to

$$\phi(x) \to \phi(x+a) = \phi(x) + a^\mu \partial_\mu \phi \tag{3.65}$$

The fields then can be described as $\phi \to \phi + \delta\phi$ where

$$\delta\phi = a^\mu \partial_\mu \phi = \partial_\mu \phi a^\mu \tag{3.66}$$

Let us now consider a variation of an arbitrary Lagrangian $\mathcal{L}$, which usually depends on the field and its first derivatives

$$\delta\mathcal{L} = \frac{\partial\mathcal{L}}{\partial\phi}\delta\phi + \frac{\partial\mathcal{L}}{\partial(\partial_\mu\phi)}\delta(\partial_\mu\phi) \tag{3.67}$$

With the Euler-Lagrange equations (3.5) $\frac{\partial\mathcal{L}}{\partial\phi}$ can be replaced.
Furthermore $\delta(\partial_\mu\phi) = \partial_\mu(\delta\phi)$. Finally

$$\delta\mathcal{L} = \partial_\mu\left(\frac{\partial\mathcal{L}}{\partial(\partial_\mu\phi)}\right)\delta\phi + \frac{\partial\mathcal{L}}{\partial(\partial_\mu\phi)}\partial_\mu(\delta\phi) \tag{3.68}$$

Using the product rule

$$\delta\mathcal{L} = \partial_\mu\left(\frac{\partial\mathcal{L}}{\partial(\partial_\mu\phi)}\delta\phi\right) \tag{3.69}$$

Now we can use equation (3.66) and

$$\delta\mathcal{L} = \partial_\mu\left(\frac{\partial\mathcal{L}}{\partial(\partial_\mu\phi)}\partial_\nu\phi\right)a^\nu = \delta^\mu_\nu\partial_\mu(\mathcal{L})a^\nu \tag{3.70}$$

so that

$$\partial_\mu\left(\frac{\partial\mathcal{L}}{\partial(\partial_\mu\phi)}\partial_\nu\phi - \delta^\mu_\nu\mathcal{L}\right)a^\nu = 0 \tag{3.71}$$

Since a^ν is arbitrary, the term in the brackets has to vanish

$$\partial_\mu\left(\frac{\partial\mathcal{L}}{\partial(\partial_\mu\phi)}\partial_\nu\phi - \delta^\mu_\nu\mathcal{L}\right) = 0 \tag{3.72}$$

The quantity in the brackets is of tremendous importance, so it has its own name:
The **energy-momentum tensor**

$$T^{\mu}_{\nu} = \frac{\partial \mathcal{L}}{\partial(\partial_{\mu}\phi)}\partial_{\nu}\phi - \delta^{\mu}_{\nu}\mathcal{L} \tag{3.73}$$

We end up with

$$\partial_{\mu}T^{\mu}_{\nu} = 0 \tag{3.74}$$

Assuming the Lagrangian does not change under a spacetime variation one gets the following expression

$$\partial_{\mu}\left(\frac{\partial \mathcal{L}}{\partial(\partial_{\mu}\phi}\delta\phi\right) = \partial_{\mu}J^{\mu} = 0 \tag{3.75}$$

The important statement of equation (3.74) and of (3.75) is, that for every continuous symmetry, which leaves the Lagrangian invariant, a conserved quantity exists. In case of equation (3.74) those would be *energy* with the energy density T^0_0 and *momentum* with the momentum density T^0_i, where i denotes the spacial components.

Operation	conserved quantity
space-translation	conservation of momentum
time-translation	conservation of energy
rotation	conservation of angular momentum

Table 3.2: *Transformations and conserved quantities*

3.6.5.

Spontaneous symmetry breaking

An example of a Lagrangian that is invariant under the transformation $\phi \to -\phi$ is the Lagrangian from ϕ^4-theory.

$$\mathcal{L} = \partial_\mu \phi \partial^\mu \phi - \frac{m^2}{2}\phi^2 - \frac{\lambda}{4}\phi^4 = \partial_\mu \phi \partial^\mu \phi - V(\phi) \tag{3.76}$$

for some mass m and an arbitrary coupling λ. In many cases a system that has some symmetry in the corresponding Lagrangian, may have a ground state which does not satisfy the same symmetry.

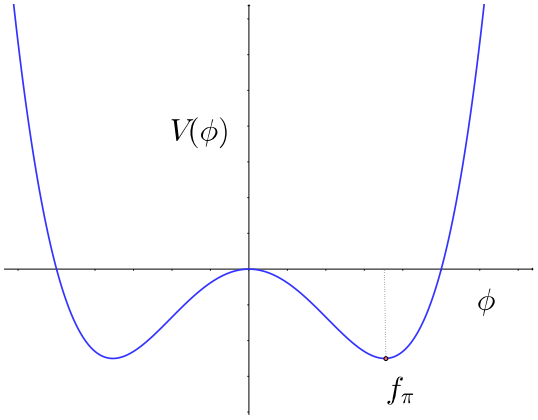

Figure 3.6: *The potential $V(\phi)$ in arbitrary units described by $\mathcal{L}$ from equation 3.76. The true ground state would be located at the vacuum expectation value f_π.*

This is the case for $\mathcal{L}$ from equation 3.76 for $\lambda < 0$. Immagine an upside down bowl placed on flat ground and place a particle[13] on top of it. The system is symmetric, from every point of view around the bowl.
But: The system is actually unstable, since the slightest perturbation would cause the marble to roll down[14]. Now suppose the marble comes to rest on the flat ground:

[13] In this case a marble would suit best.
[14] The analogy to quantum field theory is that the particle in the ground state is unstable.

The perturbation has *sponteaneously* broken the symmetry, i.e. the particle was not really in its ground state, the state of minimal potential energy, see figure 3.6.
Now the minima of the potential for (a more realistic) positive coupling λ can be expressed in terms of $m^2 > 0$ and $m^2 < 0$.

$$\frac{\partial V(\phi)}{\partial \phi} = \phi(m^2 + \lambda\phi^2) \tag{3.77}$$

The case $\phi = 0$ represents a scalar field of mass m and corrresponds to $m^2 > 0$. When the ground state is at $\phi = 0$, it obviously satisfies the symmetry present in $\mathcal{L}$.
The other minima correspond to $\phi = \pm\sqrt{\frac{-m^2}{\lambda}} = \pm\mu$. In order to represent a real field $m^2 < 0$. This case corresponds to the particle sitting on top of the bowl, i.e. the unstable point. The ground state would be to break the symmetry by choosing either $\pm\mu$. An importatnt feature of spontaneously broken symmetries is the appearence of a massless mode, a so called *Goldstone*-boson[15]. However, a perturbative expansion around $\pm\mu$ allows for the Feynman rules, since the calculations converge.

3.6.6.
Explicit symmetry breaking

Remembering the discussion in section 3.6.3 we learned that a mass term breaks chiral symmetry explicitely. For QCD this is indeed the case since quarks have a finite mass. The quantity of breaking is comparatively small for the up and down quark due to their small mass, see table 3.1, so that QCD exhibits an approximatively SU(2) flavour symmetry[16].
In case of an explicit breaking already the Lagrangian is unsymmetric:

$$\mathcal{L} = \partial_\mu\phi\partial^\mu\phi - \frac{m^2}{2}\phi^2 - \frac{\lambda}{4}\phi^4 + H\phi \tag{3.78}$$

[15] This can be shown by using the Noether theorem, but shall not be performed here.
[16] Also called: Isospin symmetry

where H breaks the symmetry explicitely.
This implies that the potential is not invariant under rotations anymore, see figure 3.7. As long as the explicit breaking is small, we expect spontaneous breaking to be the dominant feature.

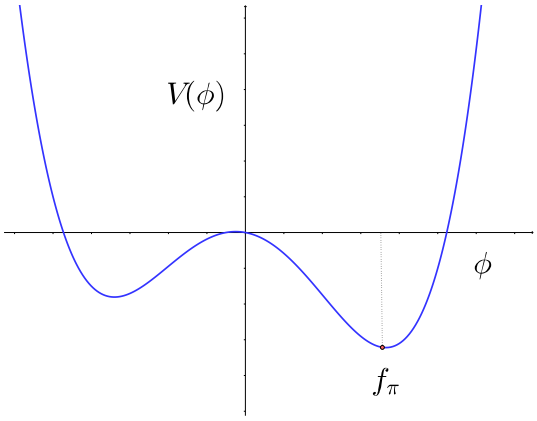

Figure 3.7: *The potential $V(\phi)$ in arbitrary units described by $\mathcal{L}$ from equation 3.78 with explicit symmetry breaking term. The true ground state would be located at the vacuum expectation value f_π.*

Explicit symmetry breaking is nonetheless an important issue, because radial exitations do cost energy, i.e. mass: The appearing Goldstone bosone becomes massive. In the SU(2) case this feature is responsible for the π to have a finite mass. Within this picture it can be simply understood what the derivatives of the the potential with respect to the fields represent: The extremum of $V(\phi)$ correlates to the state the particle actually sits in and the second derivative correlates to its mass.

4

Finite temperature field theory - SU(2) case

As discussed in the previous sections (3.6.2) and (3.6.3) the QCD Lagrangian possesses an exact color symmetry and an approximate flavor symmetry. For sufficiently low temperature and density, quarks and gluons are confined inside colourless hadrons. Since QCD is non-perturbative in the low energy regime, effective theories and models based on the QCD Lagrangian and its properties have to be utilized. In the low energy regime it is predominantly chiral symmetry which determines hadronic interactions, whereas in the high energy dominion quarks are expected to behave asymptotically free.
The *linear sigma model* is an effective theory which contains hadrons as degree of freedom instead of quarks and gluons and where chiral symmetry is realized. It has been first developed in 1960 by Gell-Mann and Levy to describe the interaction of nucleons via the exchange of pions [26]. Generally speaking, the interaction can be modelled by the transmission of either scalar-, pseudoscalar- and vector[1] mesons. If one adopts the linear sigma model for

[1] pseudovector mesons are in most approaches not crucial

quark interactions, it is referred to as the chiral *Quark Meson* model [27, 20, 3, 4, 28]. Its great advantage in comparison to other chiral models like the Nambu-Jona-Lasinio model lies in its renormalizability. Renormalizability takes into account the (in most works neglected) contribution of vacuum fluctuations, which within this thesis is among the main topics.
A SU(2) approach refers to the light quark sector, i.e. up- and down quark being considered. The first part of this chapter deals with the purely mesonic treatment, whereas the following sector respects only quark interactions and treats the mesonic fields as stationary background. Both approaches will be treated without vacuum polarization and then, after performing the so called *dimensional regularization* scheme, the vacuum contributions will be included. The final discussion is a combination of both sectors neglecting and eventually including vacuum fluctuations.

4.1. Thermodynamics

Before analyzing independently the SU(2) Quark Meson model for the mesonic- and the quark sector, a brief repetition on the relevant thermodynamics shall be given, which is valid for both sectors and also for the combined approach[2]. The starting point for the determination of thermodynamic quantities is the identification of the pressure as the negative of the effective thermodynamical potential, normalized such that it vanishes in the vacuum [29]

$$p(T,\mu) = -\Omega(T,\mu) + \Omega_0(T=\mu=0) \tag{4.1}$$

The entropy density s and the quark flavour densities n_f can be derived from the effective potential by the Gibbs-Duhem relations

$$s = -\frac{\partial\Omega}{\partial T}\bigg|_{\mu_f=\text{const.}} \quad \text{and} \quad n_f = -\frac{\partial\Omega}{\partial\mu_f}\bigg|_{T=\text{const.}} \tag{4.2}$$

[2]These equations also hold for the SU(3) case to be discussed in Chapter 5.

The energy density is consequently given as

$$\epsilon = Ts + \Omega + \mu_f n_f \tag{4.3}$$

and the Stefan-Boltzmann limit of the quark meson model is [30, 31, 29, 32]

$$\frac{p^{SB}}{T^4} = \xi \left[\frac{7\pi^2}{180} + \frac{1}{6}\left(\frac{\mu}{T}\right)^2 + \frac{1}{12\pi^2}\left(\frac{\mu}{T}\right)^4 \right] \tag{4.4}$$

$$\frac{s^{SB}}{T^3} = 4\xi \left[\frac{7\pi^2}{180} + \frac{1}{12}\left(\frac{\mu}{T}\right)^2 \right] \tag{4.5}$$

$$\frac{n_f^{SB}}{T^3} = \frac{\xi}{3} \left[\left(\frac{\mu}{T}\right) + \frac{1}{\pi^2}\left(\frac{\mu}{T}\right)^3 \right] \tag{4.6}$$

Here $\xi = N_c N_f$ with $N_c = 3$ and $N_f = 2$.
It will prove, that the second expression for the mesonic case in equation 4.2 to be discussed below is always zero, because mesons do not possess any chemical potential. Due to this feature we consider $\mu_f = 0$ for the quark case likewise.
We present our thermodynamical results in the Stefan-Boltzmann limit (SB limit, eqs. 4.4 and 4.5), where the pressure of a single fermionic degree of freedom at $\mu = 0$ is

$$p^{SB}_{fermion} = \xi_f T \int \frac{d^3\vec{k}}{(2\pi)^3} \ln\left(1 + \mathrm{e}^{-\beta \mathrm{k}}\right) = \xi_{\mathrm{f}} \frac{7}{8} \frac{\pi^2}{90} \mathrm{T}^4 \tag{4.7}$$

and the pressure of a single bosonic degree of freedom is

$$p^{SB}_{boson} = \xi_m T \int \frac{d^3\vec{k}}{(2\pi)^3} \ln\left(1 - \mathrm{e}^{-\beta \mathrm{k}}\right) = \xi_{\mathrm{m}} \frac{\pi^2}{90} \mathrm{T}^4 \tag{4.8}$$

where $\xi_{f,m}$ connotes the relevant degrees of freedom within the respective sector. The entropy density limit can be obtained by utilizing the Gibbs-Duhem relation, eq. 4.2.

4.2.
The formalism in terms of propagators

In this short section we present the formalism of the theory in terms of propagators and the functional derivatives. The reason is that it can easily be seen that our approach is in any case considered thermodynamically consistent. A general ansatz for the effective action $\Gamma[\phi, G, Q]$ according to [33, 34, 35, 36] is

$$\begin{aligned}\Gamma[\phi, G, Q] &= I[\phi] \\ &- \frac{1}{2}\mathrm{Tr}\left(\ln \mathrm{G}^{-1}\right) - \frac{1}{2}\mathrm{Tr}\left(\mathrm{D}^{-1}\mathrm{G} - 1\right) \\ &+ \mathrm{Tr}\left(\ln \mathrm{Q}^{-1}\right) + \mathrm{Tr}\left(\mathrm{S}^{-1}\mathrm{Q} - 1\right) \\ &+ \Gamma_2[\phi, G, Q]\end{aligned} \tag{4.9}$$

where ϕ represents the fields involved, $I[\phi]$ is the classical action or the tree-level potential, see equation 4.16 and figure 4.1. G is the full propagator, equation 4.32, and D^{-1} is the inverse tree level propagator for the mesons, equation 4.31. Q represents the full propagator-, and S^{-1} the inverse tree level propagator for the quarks respectively. $\Gamma_2[\phi, G, Q]$ is the contribution from the two-particle irreducible diagrams, which in our case only depends on the fields and the full propagator of the mesons, i.e. $\Gamma_2[\phi, G]$, see equation 4.33 and figure 4.4.

For vanishing sources the stationary conditions read

$$\begin{aligned}\frac{\delta\Gamma[\phi, G, Q]}{\delta\phi} &= \frac{\delta I[\phi]}{\delta\phi} - \frac{1}{2}\mathrm{Tr}\left(\frac{\delta \mathrm{D}^{-1}}{\delta\phi}\mathrm{G}\right) \\ &+ \mathrm{Tr}\left(\frac{\delta \mathrm{S}^{-1}}{\delta\phi}\mathrm{Q}\right) + \frac{\delta\Gamma_2[\phi, \mathrm{G}]}{\delta\phi} = 0 \end{aligned} \tag{4.10}$$

$$\frac{\delta\Gamma[\phi, G, Q]}{\delta G} = -\frac{1}{2}D^{-1} + \frac{1}{2}G^{-1} + \frac{\delta\Gamma_2[\phi, G]}{\delta G} = 0 \tag{4.11}$$

$$\frac{\delta\Gamma[\phi, G, Q]}{\delta Q} = -G^{-1} + S^{-1} = 0 \tag{4.12}$$

Since no contribution from $\Gamma_2[\phi, G]$ to the stationary conditions occurs when deriving with respect to the quark propagator Q, no diagrams containing a quark propagator within a meson loop appears within our approach. Hence it is justified to evaluate the potentials independently and the respective gap equations in the combined sector are consequently additive[3].

4.3. Mesonic interactions within the 2PI formalism

A generic Lagrangian [37, 34][4] containing meson fields in case of two flavours reads

$$\mathcal{L} = \frac{1}{2}\partial_\mu \vec{\phi}\partial^\mu \vec{\phi} - \frac{\lambda}{4}(\vec{\phi}^2 - v^2)^2 + H\sigma \tag{4.13}$$

where

$$\vec{\phi} = \begin{pmatrix} \sigma \\ \vec{\pi} \end{pmatrix} \tag{4.14}$$

λ is the coupling to the fields, v^2 being a general paramter approaching the vacuum expectaion value f_π, if the explicit symmetry breaking term H approaches zero, see the discussion in 3.6.6. Equation 4.13 can hence be written as

$$\mathcal{L} = \frac{1}{2}\left(\partial_\mu\sigma\partial^\mu\sigma + \partial_\mu\vec{\pi}\partial^\mu\vec{\pi}\right) - U(\sigma, \vec{\pi}) \tag{4.15}$$

with the linear sigma potential

$$U(\sigma, \vec{\pi}) = \frac{\lambda}{4}((\sigma^2 + \vec{\pi}^2) - v^2)^2 - H\sigma \tag{4.16}$$

$$= \frac{\lambda}{4}(\sigma + \vec{\pi})^4 + \frac{m^2}{2}(\sigma + \vec{\pi})^2 + \frac{\lambda v^4}{4} - H\sigma \tag{4.17}$$

shown in figure 4.1.

[3] The same argumentation holds for the SU(3) case.

[4] See also section 5 for the motivation of the terms involved in the Lagrangian.

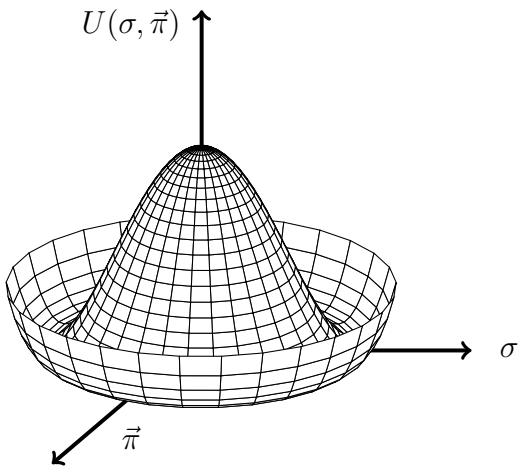

Figure 4.1: *The potential $U(\sigma, \vec{\pi})$ without explicit symmetry breaking term, i.e. $H = 0$ (Also called mexican hat potential). For the case of $H \neq 0$ the whole "hat" would be shifted to the right, so that the pion would have to climb up the inner circle. This means the pion gains a mass.*

Note, that in some cases one uses a mass term instead of v^2, then $m^2 = -\lambda v^2$. Figure 4.2 shows the corresponding Feynman diagrams resulting from the kinetic terms in the Lagrangian from equation 4.15.

Figure 4.2: *Left: A propagating sigma meson without any interaction, right: a propagating pion.*

At finite temperature perturbative expansion in powers of the coupling constant breaks down and an approach via the path integral formalism leads consequently to difficulties. At low momentum spontaneous symmetry breaking for instance leads to quasi particle exitations with imaginary energies [34, 38, 39]. These difficulties can be circumvented utilizing the Cornwall-Jackiw-Toumboulis (CJT) [33] formalism, which can be understood as a relativistic generalization of the Luttinger Ward formalism [40, 41]. The CJT (often refered to as the 2PI-formalism: Two particle irreducible formalism)

formalism can be viewed as a prescription for computing the effective action of a theory, where the stationary conditions are the Greens functions[5]. The *in-medium* masses of the σ and the $\vec{\pi}$ can then be solved self-consistently [34, 38]. The grandcanonical potential can be derived via the generating functional for the respective Greens functions, which, in the presence of the two sources J and K, is given as

$$Z[J,K] = e^{\mathcal{W}[J,K]} = \int \mathcal{D}\phi e^{(I[\phi]+\phi J+\frac{1}{2}\phi K\phi)} \tag{4.18}$$

with $\mathcal{W}[J,K]$ as the generating functional for the connected Greens functions with the sources

$$\phi J \equiv \int_x \phi(x)J(x) \tag{4.19}$$

$$\phi K\phi \equiv \int_{x,y} \phi(x)K(x,y)\phi(y) \tag{4.20}$$

with $I[\phi] = \int_x \mathcal{L}$ as the classical action. The expectation values are

$$\frac{\delta\mathcal{W}[J,K]}{\delta J(x)} \equiv \bar{\phi}(x) \tag{4.21}$$

$$\frac{\delta\mathcal{W}[J,K]}{\delta K(x,y)} \equiv \frac{1}{2}\left(G(x,y)+\bar{\phi}(x)\bar{\phi}(y)\right) \tag{4.22}$$

To obtain the effective action a double Legendre transformation needs to be performed leading to

$$\Gamma[\bar{\phi},G] = \mathcal{W}[J,K] - \bar{\phi}J - \frac{1}{2}\bar{\phi}K\bar{\phi} - \frac{1}{2}GK \tag{4.23}$$

[5]Note that this approach works due to a symmetry reason: For translational invariant systems the effective action corresponds to the effective potential, which is the finally achieved quantity.

and $GK \equiv \int_{x,y} G(x,y)K(y,x)$. Thus

$$\frac{\delta\Gamma[\bar{\phi},G]}{\delta\bar{\phi}} = J(x) - \int_y K(x,y)\phi(y) \tag{4.24}$$

$$\frac{\delta\Gamma[\bar{\phi},G]}{\delta G(x,y)} = -\frac{1}{2}K(x,y) \tag{4.25}$$

For vanishing sources the stationary conditions then read

$$\left.\frac{\delta\Gamma[\bar{\phi},G]}{\delta\bar{\phi}}\right|_{\bar{\phi}=\varphi,G=\mathcal{G}} = 0 \tag{4.26}$$

$$\left.\frac{\delta\Gamma[\bar{\phi},G]}{\delta G(x,y)}\right|_{\bar{\phi}=\varphi,G=\mathcal{G}} = 0 \tag{4.27}$$

and the effective action according to [33] is

$$\Gamma[\bar{\phi},G] = I[\bar{\phi}] - \frac{1}{2}\mathrm{Tr}(\ln \mathrm{G}^{-1}) - \frac{1}{2}\mathrm{Tr}(\mathrm{D}^{-1}\mathrm{G} - 1) + \Gamma_2[\bar{\phi},\mathrm{G}] \tag{4.28}$$

where

$$D^{-1}(x,y,\bar{\phi}) \equiv -\left.\frac{\delta^2 I[\phi]}{\delta\phi(x)\delta\phi(y)}\right|_{\phi=\bar{\phi}} \tag{4.29}$$

is the inverse tree level propagator and $\Gamma_2[\bar{\phi},G]$ is the sum of all two particle irreducible diagrams where all lines represent full propagators G. For constant fields $\bar{\phi}(x) = \bar{\phi}$ and homogenous systems, the effective potential is [33, 34]

$$\Omega[\bar{\phi},G] = U(\bar{\phi}) + \frac{1}{2}\int_k \ln G^{-1}(k) + \frac{1}{2}\int_k \left[D^{-1}(k,\bar{\phi})G(k) - 1\right] + \Omega_2 \tag{4.30}$$

where

$$D^{-1}(k,\bar{\phi}) = -k^2 + U''(\bar{\phi}) \tag{4.31}$$

is the inverse tree level propagator and

$$G_{\sigma,\pi}(k) = \frac{1}{-k^2 + \bar{m}^2_{\sigma,\pi}} \tag{4.32}$$

is the full (or dressed) propagator. In equation 4.30 $\Omega_2 \equiv -T\Gamma_2[\bar{\phi},G]/V$, and V being the 3-volume of the system.

The CJT potential is obtained from equation 4.30 and reads

$$\begin{aligned}\Omega(\phi, G_{\sigma,\pi}) &= \frac{1}{2}m^2\phi^2 + \frac{1}{4}\lambda\phi^4 - H\phi \\ &+ \frac{1}{2}\int_k \left[\ln \mathrm{G}_\sigma^{-1}(\mathrm{k}) + \mathrm{D}_\sigma^{-1}(\mathrm{k},\phi)\mathrm{G}_\sigma(\mathrm{k}) - 1\right] \\ &+ \frac{3}{2}\int_k \left[\ln \mathrm{G}_\pi^{-1}(\mathrm{k}) + \mathrm{D}_\pi^{-1}(\mathrm{k},\phi)\mathrm{G}_\pi(\mathrm{k}) - 1\right] \\ &+ \frac{3\lambda}{4}\left[\int_k G_\sigma(k)\right]^2 + \frac{15\lambda}{4}\left[\int_k G_\pi(k)\right]^2 \\ &+ \frac{3\lambda}{2}\left[\int_k G_\sigma(k)\right]\left[\int_k G_\pi(k)\right]\end{aligned} \tag{4.33}$$

The one loop correction to the tree level potential can be computed as the sum of all one particle irreducible diagrams with a single loop and zero external momentum. Each vertex has two external legs, see figure 4.3. The factor 1/2 in certain terms in equation 4.28 and equation 4.30, which is actually the 1 PI contribution to the whole potential, comes from the fact that interchanging the two external lines of the vertex does not change the diagram.

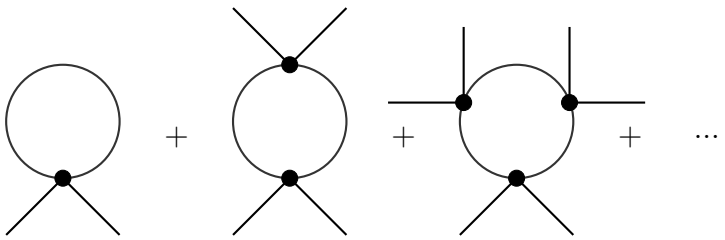

Figure 4.3: *The 1-PI loops contributing to the effective potential in eq. 4.28, i.e. eq. 4.30 (The logarithmic terms modyfied by the factor* 1/2*). The logarithm within the propagator tells to sum up an infinite number of diagrams.*

The terms $D^{-1}_{\sigma,\pi}(k,\phi)G_{\sigma,\pi}(k)$ are corrections to the naked propagating mass of either the sigma or the pion due to corrections from the potential, i.e. the second derivative in equation 4.31. If one furthermore takes into account the double-bubble diagrams in figure 4.4, i.e. Ω_2, one obtains the so called Hartree approximation of the linear sigma model Lagrangian. Note that Ω_1 and Ω_2 contain an infinite number of diagrams. The computation on the

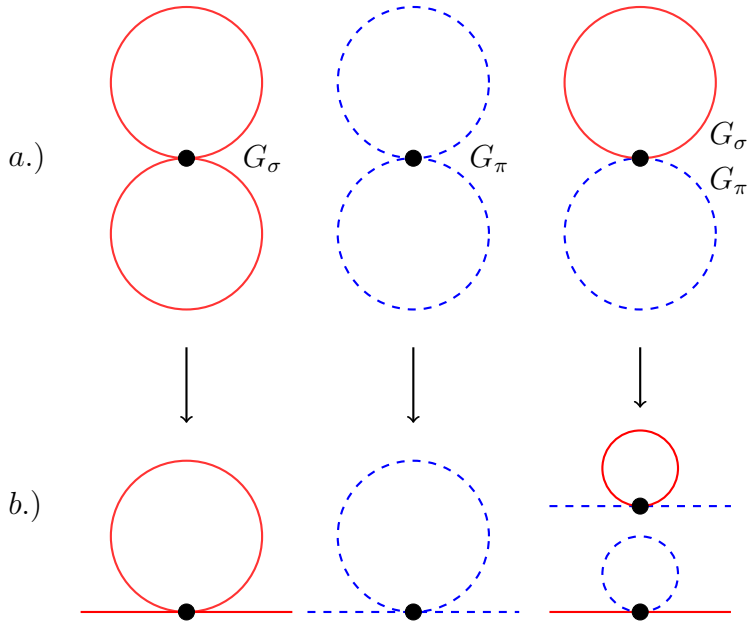

Figure 4.4: *a.) The two loop Hartree contributions to the CJT effective potential (Ω_2). The full red line corresponds to G_σ, whereas the dashed blue line corresponds to G_π. The most right loop correlates to the last term in equation 4.33. The black circle corresponds to the vertex $\sim \lambda$. b.) displays the tadpole contribution to the self energy, obtained by cutting a line. For this self energy the Dyson-Schwinger equation is self consistently solvable, because the internal lines in the tadpole diagrams represent full propagators.*

other hand has to be restricted to a finite number. The stationary conditions with respect to $\Omega[\bar{\phi}, G]$ read

$$\left.\frac{\delta\Omega[\bar{\phi}, G]}{\delta\bar{\phi}}\right|_{\bar{\phi}=\varphi, G=\mathcal{G}} = 0 \tag{4.34}$$

$$\left.\frac{\delta\Omega[\bar{\phi}, G]}{\delta G(k)}\right|_{\bar{\phi}=\varphi, G=\mathcal{G}} = 0 \tag{4.35}$$

The latter can be written

$$\mathcal{G}^{-1}(k) = D^{-1}(k, \varphi) + \Pi(k) \tag{4.36}$$

where

$$\Pi(k) = 2\frac{\delta\Gamma_2[\bar{\phi}, G]}{\delta G(k)}\bigg|_{\bar{\phi}=\varphi, G=\mathcal{G}} \tag{4.37}$$

is the self energy. Since $\Pi(k)$ is in general a functional of $\mathcal{G}$, equation 4.36 represents a Schwinger-Dyson equation for the dressed propagator. Using eq. (4.31) one arrives at the inverse tree level propagators for the sigma and the pion

$$D_\sigma^{-1} = -k^2 + m^2 + \frac{12\lambda}{N}\phi^2 \tag{4.38}$$

$$D_\pi^{-1} = -k^2 + m^2 + \frac{4\lambda}{N}\phi^2 \tag{4.39}$$

At tree level, the parameters of the Lagrangian are fixed, so that the masses agree with the observed masses $m_\sigma = 550$ MeV and $m_\pi = 138$ MeV.

$$m_\sigma^2 = m^2 + 3\lambda f_\pi^2 \tag{4.40}$$

$$m_\pi^2 = m^2 + \lambda f_\pi^2 \tag{4.41}$$

From this the tree level parameters are obtained[6]. The coupling constant is

$$\lambda = \frac{(m_\sigma^2 - m_\pi^2)}{2f_\pi^2} \tag{4.42}$$

where $f_\pi = 92.4$ MeV is the pion decay constant. Solving for the mass term

$$m^2 = -\frac{m_\sigma^2 - 3m_\pi^2}{2} \tag{4.43}$$

leading eventually to $H = m_\pi^2 f_\pi$. These constants are the same as for the quark-quark interaction case, see equations 4.114, 4.115 and 4.116 in section 4.4, and being derived in similar manner. However, the dressed masses $\bar{m}_{\sigma,\pi}$

[6]Note, that the parameters change upon renormalization

are then determined by solving the following Gap equations:

$$H = \phi\left[m^2 + \lambda\left(\phi^2 + 3F(\bar{m}_\sigma, T) + 3F(\bar{m}_\pi, T)\right)\right] \tag{4.44}$$

$$\bar{m}_\sigma = m^2 + \lambda\left[3\phi^2 + 3F(\bar{m}_\sigma, T) + 3F(\bar{m}_\pi, T)\right] \tag{4.45}$$

$$\bar{m}_\pi = m^2 + \lambda\left[\phi^2 + F(\bar{m}_\sigma, T) + 5F(\bar{m}_\pi, T)\right] \tag{4.46}$$

derived by the potential given in eq. (4.33) with respect to the fields. Herein the function

$$\begin{aligned} F(\bar{m}_{\sigma,\pi}, T) &= F_T(\bar{m}_{\sigma,\pi}, T) + F_{vac}(\bar{m}_{\sigma,\pi}, T) \\ &= \int \frac{d^3\vec{k}}{(2\pi)^3} \frac{1}{\sqrt{\vec{k}^2 + \bar{m}^2_{\sigma,\pi}}} \cdot \left[\frac{1}{e^{\beta\sqrt{\vec{k}^2+\bar{m}^2_{\sigma,\pi}}} - 1} + \frac{1}{2}\right] \end{aligned} \tag{4.47}$$

displays the temperature dependence including the vacuum contribution, i.e. the last additive term [34]. Within this section we simply ignore the vacuum term $F_{vac}(\bar{m}_{\sigma,\pi}) = 0$, claiming it to be independent of temperature. The function $F(\bar{m}_{\sigma,\pi}, T) \to F_T(\bar{m}_{\sigma,\pi}, T)$ reduces then to a thermal part only where

$$F_T(\bar{m}_{\sigma,\pi}, T) = \int \frac{d^3\vec{k}}{(2\pi)^3} \frac{1}{\sqrt{\vec{k}^2 + \bar{m}^2_{\sigma,\pi}}} \cdot \left[\frac{1}{e^{\beta\sqrt{\vec{k}^2+\bar{m}^2_{\sigma,\pi}}} - 1}\right] \tag{4.48}$$

The exclusion of the self energy in the mesonic sector is also not negligible, which will be discussed in the following section, where we take into account the corresponding self energy term $F_{vac}(\bar{m}_{\sigma,\pi}, T)$.

4.3.1.

Vacuum fluctuations of mesons

Taking into account vacuum fluctuations needs regularization schemes[7]. To lowest order, the vacuum term is just the one loop effective potential at zero temperature. However, regularization is a method of isolating the divergen-

[7] This section is based upon works from [18, 21, 42] but is nonetheless somewhat more detailled due to carried out calculations.

cies in Feynman integrals, and there are several techniques of regularization. The most intuitive one is to introduce a cut-off parameter Λ in the momentum integrals. To regularize the divergencies of a given theory the most common procedure though is the so called dimensional regularization scheme. The idea behind this scheme is to calculate in dimensions d where the theory is still calculable due to convergent integrals and then reduce to the dimension required for the given problem.
Using dimensional regularization, a new parameter has to be introduced. But since the theory should not depend on heuristic parameters, they have finally to be removed utilizing renormalization. The isolated divergent part can eventually be removed via appropriate counter terms.
The divergent quantity modifying the free particle propagator and contributing to the self energy corresponds in momentum space to

$$\lambda \int \frac{d^4\vec{k}}{(2\pi)^4} \frac{1}{\vec{k}^2 - m^2} \tag{4.49}$$

Since there are four powers in the numerator and only two in the denominator, the integral converges quadratically at large k. The question arises how to find the divergence of a particular graph, i.e. the *superficial degree of divergence*, D. Considering a ϕ^r interaction in d dimensions, then each propagator contributes $\sim k^{-2}$ and each vertex k^d powers, together with a momentum conservating $\delta-$function for each vertex contributing $\sim k^{-d}$. Only one $\delta-$function does not contribute to guarantee d-momentum conservation. The number of loops corresponds to the number of independent momenta. Using the method of power counting with n vertices, I internal lines (propagators), E external lines and L loops, L is given as

$$L = I - n + 1 \tag{4.50}$$

This means that the internal lines correspond to the number of independent d-momentum integrals The superficial degree D of a divergence is then

$$D = dL - 2I \tag{4.51}$$

In ϕ^r-theory every vetrex has r legs and every internal line L is connected to two vertices, yielding

$$D = -\delta n - \left(\frac{d}{2} - 1\right) E + d \tag{4.52}$$

where

$$\delta \equiv d - \left(\frac{d}{2} - 1\right) r \tag{4.53}$$

In Minkowski spacetime $d = 4$ and $E = \text{const.}$, so that D depends on the type of interaction, i.e. the number of fields interacting at a vertex and of course the number of vertices. A case by case analysis gives

1. $\delta < 0$: not renormalizable
2. $\delta = 0$: renormalizable
3. $\delta > 0$: super-renormalizable

Equation 4.52 can be written as

$$D = \left[\left(\frac{r}{2} - 1\right) n - \frac{E}{2} + 1\right] d - rn + E \tag{4.54}$$

The superficial degree of D grows with the number of dimensions. For a 4-point interactive theory (ϕ^4) the calculation has to be carried out in $d < 4$ and, when done, $d \to 4$. The first step is to expand the Lagrangian

$$\mathcal{L} = \frac{1}{2}\partial_\mu\phi\partial^\mu\phi - \frac{m^2}{2}\phi^2 - \frac{\lambda}{4}\phi^4 \tag{4.55}$$

from four to d dimensions. Since ϕ has dimensions $1/2d-1$ and $\mathcal{L}$ dimension d^{-1} (Lenght equates to Λ^d in momentum - remember that the action $s = \int d^dx\mathcal{L}$ is dimensionless). λ is dimensionless in 4 dimensions, the coupling in $d \neq 4$ dimensions is then no longer dimensionless $[\lambda] = \Lambda^\delta = \Lambda^{4-d}$. The 4-point interactive term has to become $\lambda \to \lambda\mu^{4-d}$ to restore the dimensionless coupling λ.

The interaction provides a correction δm^2 to the naked mass m^2, i.e $m_r^2 = m^2 + \delta m^2$, where m_r^2 is called dressed mass (or renormalized mass). Using

the Feynman rules to calculate the order of the one-loop contribution to the free propagator gives

$$\delta m^2 = \frac{i\lambda}{2}\mu^{4-d}\int \frac{d^dk}{(2\pi)^d}\frac{1}{k^2 - m^2 + i\eta} \tag{4.56}$$

which is nothing but a correction to the naked mass of the respective boson. The Feynman integral[8]

$$\begin{aligned}\int_0^1 \frac{dz}{[az + b(1-z)]^2} &= \int_0^1 \frac{dz}{[(a-b)z + b]^2} = -\frac{1}{a-b}\frac{1}{(a-b)z+b}\Big|_0^1 \\ &= -\frac{1}{a-b}\left[\frac{1}{a} - \frac{1}{b}\right] = \frac{1}{ab}\end{aligned} \tag{4.57}$$

can later be used to calculate scattering amplitudes [42], at this point it is given for the sake of completeness. However, realizing that equation 4.56 can be reduced to an integral of such a form

$$I_d(P) = \int d^dk \frac{1}{(k^2 + 2p^\mu k_\mu - M^2 + i\eta)^\alpha} \tag{4.58}$$

and utilizing spherical coordinates

$$d^dk = dk_0 dk k^{d-2} d\Omega_k \tag{4.59}$$

the angle dependence can be treated separately since δm^2 is independent of any angle, i.e.

$$\int d\Omega_k = \frac{2\pi^{(d-1)/2}}{\Gamma\left(\frac{d-1}{2}\right)} \tag{4.60}$$

being the surface of the $d-1$ dimensional unit sphere.
Equation 4.58 is then

$$I_d(P) = \frac{2\pi^{(d-1)/2}}{\Gamma\left(\frac{d-1}{2}\right)}\int_{-\infty}^{\infty} dk_0 \int_{-\infty}^{\infty} dk k^{d-2} \frac{1}{(k_0^2 + 2p_0k_0 - k^2 - M^2 + i\eta)^\alpha} \tag{4.61}$$

[8] Which is an elementary integral for the purpose of writing $1/ab$ in a slighlty more complicated way.

Using the substitute $k_0' = k_0 + p_0$, making use of the binomic formula and eventually renaming $k_0' \to k_0$ leads to

$$I_d(P) = \frac{4\pi^{(d-1)/2}}{\Gamma\left(\frac{d-1}{2}\right)} \int_0^\infty dk_0 \int_{-\infty}^\infty dk k^{d-2} \frac{1}{(k_0^2 - k^2 - (p_0^2 + M^2) + i\eta)^\alpha} \tag{4.62}$$

For the following, the Euler beta function[9] is usefull

$$B(x,y) = \frac{\Gamma(x)\Gamma(y)}{\Gamma(x+y)} = 2\int_0^\infty \frac{t^{2x-1}}{(1+t^2)^{x+y}} dt \tag{4.63}$$

where $\Gamma(x) = \int_0^\infty e^{-u} u^{x-1} du$ is the Gamma function. The next integral has to be solved to see the similarity to equation 4.63

$$\int_0^\infty ds \frac{s^\beta}{(s^2+n^2)^\alpha} \tag{4.64}$$

setting $s = nt \to ds = ndt$, $\beta = 2x - 1 \to x = (1+\beta)/2$ and $\alpha = x + y \to y = \alpha - (1+\beta)/2$ gives

$$\begin{aligned}
\int_0^\infty ndt \frac{(nt)^{2x-1}}{[(nt)^2 + n^2]^{x+y}} &= \int_0^\infty \frac{t^{2x-1}}{(t^2+1)^{x+y}} \frac{n^{2x}}{n^{2(x+y)}} dt && (4.65)\\
&= \int_0^\infty \frac{t^{2x-1}}{(t^2+1)^{x+y}} n^{-2\alpha+1+\beta} dt && (4.66)\\
&= \frac{1}{2} B(x,y) \frac{1}{(n^2)^{\alpha-(1+\beta)/2}} && (4.67)\\
&= \frac{\Gamma\left(\frac{1+\beta}{2}\right)\Gamma\left(\alpha - \frac{1+\beta}{2}\right)}{\Gamma(\alpha)} \frac{1}{2(n^2)^{\alpha-(1+\beta)/2}} && (4.68)
\end{aligned}$$

Identifying $s = k_0$, $n^2 = -k^2 - (p^2 + M^2) + i\eta$ and $\beta = 0$ the integration over k_0 has been carried out and $i\eta$ can be neglected since the remaining q-integral has no singularity. What remains from equation 4.62 is the integral over k

$$I_d(P) = (-1)^{-\alpha+\frac{1}{2}} \frac{2\pi^{(d-1)/2}}{\Gamma\left(\frac{d-1}{2}\right)} \frac{\Gamma\left(\frac{1}{2}\right)\Gamma\left(\alpha - \frac{1}{2}\right)}{\Gamma(\alpha)} \int_0^\infty dk k^{d-2} \frac{1}{(k^2 + p^2 + M^2)^{\alpha-\frac{1}{2}}} \tag{4.69}$$

[9] See Abramowitz and Stegun: Handbook of mathematical functions

which is fortunately of the same form as equation 4.64, and with $s = k$, $\beta = d-2$, $n^2 = p^2 + M^2$ and $\alpha \to \alpha - \frac{1}{2}$, i.e.

$$\int_0^\infty dk k^{d-2} \frac{1}{(k^2+p^2+M^2)^{\alpha-\frac{1}{2}}} = \frac{\Gamma\left(\frac{d-1}{2}\right)\Gamma\left(\alpha-\frac{1}{2}-\frac{(d-1)}{2}\right)}{\Gamma\left(\alpha-\frac{1}{2}\right)} \frac{1}{2(p^2+M^2)^{\alpha-1/2-(d-1)/2}} \tag{4.70}$$

Using $(-1)^{1/2} = i$ and $\Gamma(\frac{1}{2}) = \sqrt{\pi}$ and inserting 4.70 in equation 4.69 gives

$$\begin{aligned} I_d(P) &= (-1)^{-\alpha+\frac{1}{2}} \frac{2\pi^{(d-1)/2}}{\Gamma(\alpha)} \pi^{\frac{1}{2}} \frac{1}{2(p^2+M^2)^{\alpha-1/2-(d-1)/2}} \Gamma\left(\alpha - \frac{1}{2} - \frac{(d-1)}{2}\right) \\ &= -i\pi^{d/2} \frac{\Gamma\left(\alpha-\frac{d}{2}\right)}{\Gamma(\alpha)} \frac{1}{(p^2+M^2)^{\alpha-1/2}} \end{aligned} \tag{4.71}$$

Choosing $p = 0$ and $\alpha = 1$ equation 4.56 then is

$$\delta m^2 = \frac{i\lambda}{2} \mu^{4-d} \int \frac{d^d k}{(2\pi)^d} \frac{1}{k^2 - m^2} \tag{4.72}$$

$$\delta m^2 = \frac{\lambda}{2} \mu^{4-d} \frac{\pi^{d/2}}{(2\pi)^d} \frac{\Gamma\left(1-\frac{d}{2}\right)}{\Gamma(1)(m^2)^{1-d/2}} \tag{4.73}$$

$$\delta m^2 = \frac{\lambda}{2} \frac{\Gamma\left(1-\frac{d}{2}\right)}{(4\pi)^{d/2}} m^2 \left(\frac{\mu^2}{m^2}\right)^{2-d/2} \tag{4.74}$$

It seems like nothing has simplyfied, since the divergence is still hidden within the gamma function, because the gamma function has poles at zero and negative integer values. To isolate the divergencies as poles we need to prove that

$$\Gamma(-n+\epsilon) = \frac{(-1)^n}{n!} \left[\frac{1}{\epsilon} + \Psi_1(n+1) + \mathcal{O}(\epsilon)\right] \tag{4.75}$$

with a Taylor expansion where $\epsilon << 1$. To this purpose we introduce

i.) $z\Gamma(z) = \Gamma(z+1)$

ii.) $\Psi_1(z) = \frac{d \ln \Gamma(z)}{dz} = \frac{\Gamma'(z)}{\Gamma(z)}$

iii.) $\frac{1}{\Gamma(z)} = z e^{\gamma z} \prod_{n=1}^{\infty} \left(1 + \frac{z}{n}\right) e^{-z/n}$

where

i.) can be shown by integration by parts,
ii.) is the Euler Ψ function, and
iii.) is called Weierstrass representation of the Gamma function.
γ is known from theoretical arithmetic to be

$$\gamma = \lim_{n\to\infty}\left(\sum_{r=1}^{n}\frac{1}{r} - \ln n\right) \simeq 0.5772157 \tag{4.76}$$

and called the Euler-Mascheroni constant.
Starting with ii.)

$$\begin{aligned}
\frac{1}{\Gamma(z)} &= ze^{\gamma z}\prod_{n=1}^{\infty}\left(1+\frac{z}{n}\right)e^{-z/n}\Big|\ln \\
\ln\left(\frac{1}{\Gamma(z)}\right) &= \ln(z)+\gamma z+\ln\left(1+\frac{z}{1}\right)-\frac{z}{1}+\ln\left(1+\frac{z}{2}\right)-\frac{z}{2}+... \\
&= \ln(z)+\gamma z+\sum_{n=1}^{\infty}\left[\ln\left(1+\frac{z}{n}\right)-\frac{z}{n}\right]\Big|\frac{d}{dz} \\
-\frac{d\ln(\Gamma(z))}{dz} &= \frac{1}{z}+\gamma+\sum_{n=1}^{\infty}\left(\frac{1}{z+n}-\frac{1}{n}\right) \\
\text{which is} &= -\Psi_1(z)
\end{aligned} \tag{4.77}$$

For $z = n \in \mathbb{N}$

$$\Psi_1(n) = -\gamma + \sum_{r=1}^{n-1}\frac{1}{r} \tag{4.78}$$

The crucial step is to expand Γ in Taylor around ϵ

$$\Gamma(1+\epsilon) = \Gamma(1)+\epsilon\Gamma'(1)+\mathcal{O}(\epsilon^2) \tag{4.79}$$

$$\Gamma(1+\epsilon) = 1+\epsilon\Gamma(1)\Psi_1(1)+\mathcal{O}(\epsilon^2) \tag{4.80}$$

$$\Gamma(1+\epsilon) = 1-\epsilon\gamma+\mathcal{O}(\epsilon^2) \tag{4.81}$$

where $\Psi_1(1) = -\gamma$ and ii.) $\Gamma'(1) = \Gamma(1)\Psi_1(1)$ were used. Recall i.) $\Gamma(\epsilon+1) = \epsilon\Gamma(\epsilon)$ then

$$\Gamma(\epsilon) = \frac{1}{\epsilon} - \gamma + \mathcal{O}(\epsilon) \tag{4.82}$$

Now

$$\Gamma(-1+\epsilon) = -\frac{1}{1-\epsilon}\Gamma(\epsilon) = -\left[\frac{1}{\epsilon}+1-\gamma+\mathcal{O}(\epsilon)\right] \quad (4.83)$$

$$\Gamma(-2+\epsilon) = -\frac{1}{2-\epsilon}\Gamma(\epsilon) = \frac{(-1)^2}{2}\left[\frac{1}{\epsilon}+1+\frac{1}{2}-\gamma+\mathcal{O}(\epsilon)\right] \quad (4.84)$$

$$... \quad (4.85)$$

$$\Gamma(-n+\epsilon) = \frac{(-1)^n}{n!}\left[\frac{1}{\epsilon}+1+\frac{1}{2}+...\frac{1}{n}-\gamma+\mathcal{O}(\epsilon)\right] \quad (4.86)$$

$$\Gamma(-n+\epsilon) = \frac{(-1)^n}{n!}\left[\frac{1}{\epsilon}+\Psi_1(n+1)+\mathcal{O}(\epsilon)\right] \quad (4.87)$$

The Gamma function from equation 4.74 can now be calculated for $d = 4$ using the prooved equation 4.75, i.e. $\epsilon = 4-d \rightarrow d = 4-\epsilon \rightarrow \frac{d}{2} = 2-\frac{\epsilon}{2}$, so that

$$\Gamma\left(1-\frac{d}{2}\right) = \Gamma\left(-1+\frac{\epsilon}{2}\right) = -\left[\frac{2}{\epsilon}-\gamma+1+\mathcal{O}(\epsilon)\right] \quad (4.88)$$

replacing in equation 4.74 yields

$$\delta m^2 = \frac{\lambda}{2}\frac{\Gamma\left(1-\frac{d}{2}\right)}{(4\pi)^{2-\epsilon/2}}m^2\left(\frac{\mu^2}{m^2}\right)^{\epsilon/2} \quad (4.89)$$

$$= \frac{\lambda}{32\pi^2}\left[-\frac{2}{\epsilon}+\gamma-1+\mathcal{O}(\epsilon)\right]m^2\left(\frac{4\pi\mu^2}{m^2}\right)^{\epsilon/2} \quad (4.90)$$

The last term can be expanded again since $x^\epsilon = e^{\epsilon\ln(x)} \simeq 1+\epsilon\ln(x)+\mathcal{O}(\epsilon^2)$, so that

$$\delta m^2 = \frac{\lambda}{32\pi^2}\left[-\frac{2}{\epsilon}+\gamma-1+\mathcal{O}(\epsilon)\right]\left[1+\frac{\epsilon}{2}\ln\left(\frac{4\pi\mu^2}{m^2}\right)+\mathcal{O}(\epsilon^2)\right] \quad (4.91)$$

$$\delta m^2 = -\frac{\lambda m^2}{16\pi^2\epsilon}-\frac{\lambda m^2}{32\pi^2}\ln\left(\frac{4\pi\mu^2 e}{m^2 e^\gamma}\right)+\mathcal{O}(\epsilon^2) \quad (4.92)$$

and remember $-\ln(x)+\gamma = -\ln(x)+\ln(e^\gamma) = \ln\left(\frac{e^\gamma}{x}\right) = -\ln\left(\frac{x}{e^\gamma}\right)$. The first term in equation 4.92 is divergent for $\lim\epsilon \rightarrow 0$, whereas the second term corrects the naked mass of the respective bosons. Unfortuantely the formula still diverges. The loophole is to define the naked mass also divergent, so that eventually the divergence cancels. What remains is the true physical

mass of the particle, the so called *dressed mass*. This procedure is called **renormalization**. The one-loop correction to the mass is

$$m_r^2 = m^2 + \delta m^2 = m^2 \left(1 - \frac{\lambda}{16\pi^2\epsilon} - \frac{\lambda}{32\pi^2} \ln\left(\frac{4\pi\mu^2 e}{m^2 e^\gamma}\right)\right) \tag{4.93}$$

and the corresponding vacuum diagram is shown in figure 4.5 amongst the self energy term for the quark propagator.

Figure 4.5: *Left picture: Vacuum polarization, i.e. the self energy of the respective boson, either the sigma shown here or the pion (which in this thesis is denoted as blue thick dotted line such as in figure 4.2 on the right hand side). Right picure: The corresponding diagram for the respective quark self-interacting due to vacuumfluctuations (to be discussed in section 4.4.1).*

The idea however is to choose the naked mass as such as to cancel the divergence, so that m_r^2 is eventually the physical mass of the corresponding particle. Solving equation 4.93 for m^2 gives

$$m^2 = m_r^2 + \frac{\lambda m^2}{16\pi^2\epsilon} + \frac{\lambda m^2}{32\pi^2} \ln\left(\frac{4\pi\mu^2 e}{m^2 e^\gamma}\right) \tag{4.94}$$

$$m^2 = m_r^2 + \frac{\lambda m_r^2}{16\pi^2\epsilon} + \frac{\lambda m_r^2}{32\pi^2} \ln\left(\frac{4\pi\mu^2 e}{m_r^2 e^\gamma}\right) \tag{4.95}$$

m^2 on the right-hand side can be replaced by m_r^2 since the corrections are of order $\mathcal{O}(\lambda^2)$, even in the logarithmic expression. Now we are free to choose

$$\mu^2 = \frac{m_r^2 e^\gamma}{4\pi e} \tag{4.96}$$

to get rid of the logarithmic term. This is called minimal substraction scheme

[34, 42], however

$$m^2 = m_r^2\left(1+\frac{\lambda}{16\pi^2\epsilon}\right)+\mathcal{O}(\lambda^2) \tag{4.97}$$

$$m_r^2 = \frac{m^2}{1+\frac{\lambda}{16\pi^2\epsilon}}+\mathcal{O}(\lambda^2) \tag{4.98}$$

$$m_r^2 = m^2\left(1+\frac{\lambda}{16\pi^2\epsilon}\right)+\mathcal{O}(\lambda^2) \tag{4.99}$$

where we approximated $1/(1+x)\simeq 1+x$.
Inserting equation 4.97 in equation 4.93 gives $m_r^2 = m_r^2+\mathcal{O}(\lambda^2)$. The divergencies cancel.
One now may ask the question if this whole procedure of dimensional regularization is necessary, because the vacuum contribution from 4.47 is temperature independent anyway. The answer is: Yes, because the field and the masses are affected via the derivations by it. The correction is small, but not negligible. To solve then the Gap equations 4.44, 4.45 and 4.46 incorporating the vacuum contribution leads to modifyed Gap equations where equation 4.47 splits up into a temperature dependent and a vacuum part. To obtain the renormalized gap equations simply replace

$$F(\bar{m}_{\sigma,\pi},T) = F_T(\bar{m}_{\sigma,\pi},T)+F_{dr}(\bar{m}_{\sigma,\pi}) \tag{4.100}$$

where the index dr stands for $d$imensional $r$egularization and the temperature dependent part is

$$F_T(\bar{m}_{\sigma,\pi},T) = \int\frac{d^3\vec{k}}{(2\pi)^3}\frac{1}{\sqrt{\vec{k}^2+\bar{m}_{\sigma,\pi}^2}}\cdot\left[\frac{1}{e^{\beta\sqrt{\vec{k}^2+\bar{m}_{\sigma,\pi}^2}}-1}\right] \tag{4.101}$$

and the renormalized vacuum contribution $F_{vac}(\bar{m}_{\sigma,\pi})\to F_{dr}(\bar{m}_{\sigma,\pi})$ where

$$F_{dr}(\bar{m}_{\sigma,\pi}) = \int\frac{d^3\vec{k}}{(2\pi)^3}\frac{1}{2\sqrt{\vec{k}^2+\bar{m}_{\sigma,\pi}^2}} = -\frac{\bar{m}_{\sigma,\pi}}{16\pi^2}\left[1+\ln\left(\frac{\mu^2}{\bar{\mathrm{m}}_{\sigma,\pi}}\right)\right] \tag{4.102}$$

Now it is important to note that apart from that the renormalization proce-

dure changes the results [42], the renormalization scale can be chosen arbitrary[10]. Here we set $\mu = m_\sigma/\sqrt{e}$ according to the choice of [34, 43] and in order for $F_{dr}(\bar{m}_\sigma)$ to vanish in the vacuum. The renormalized parameters of the Lagrangian are determined to be

$$\lambda_r = \frac{m_\sigma^2 - m_\pi^2}{2\left[f_\pi^2 + F_{dr}(\bar{m}_\sigma) - F_{dr}(\bar{m}_\pi)\right]} \tag{4.103}$$

$$m_r^2 = m_\sigma^2 - 3\lambda_r\left[f_\pi^2 + F_{dr}(\bar{m}_\sigma) - F_{dr}(\bar{m}_\pi)\right] \tag{4.104}$$

$$H_r = m_\pi^2 f_\pi = H \tag{4.105}$$

where the explicit symmetry breaking term remains unaffected by renormalization due to our choice $\mu = m_\sigma/\sqrt{e}$.

4.3.2. Results in the mesonic sector

Figure 4.6 shows the order parameter σ as a function of the temperature for three different initial vacuum sigma meson masses m_σ^{vac}, neglecting (denoted in the figure as "th") and including (denoted in the figure as "th+vac") the self energy of the mesons. We find that with increasing σ meson mass m_σ^{vac} the phase transition in the thermal case becomes more crossover like, i.e. approaching a first order phase transition, up to an area, where all three curves nearly intersect ($T = 230 - 245$MeV at $\sigma = 30 - 33$MeV). That is the area around the phase transition and from this area on the case of the largest value of the initial sigma meson mass approaches the chiral limit at lower temperatures compared to the other cases. This special behaviour has not been observed in the quark case, which is investigated in detail in section 4.4 . The larger the initial m_σ^{vac} in the thermal case, the sooner the chiral limit is approached with increasing temperature, nonetheless not that close as in the quark case.

[10] Within a physically reasonable range.

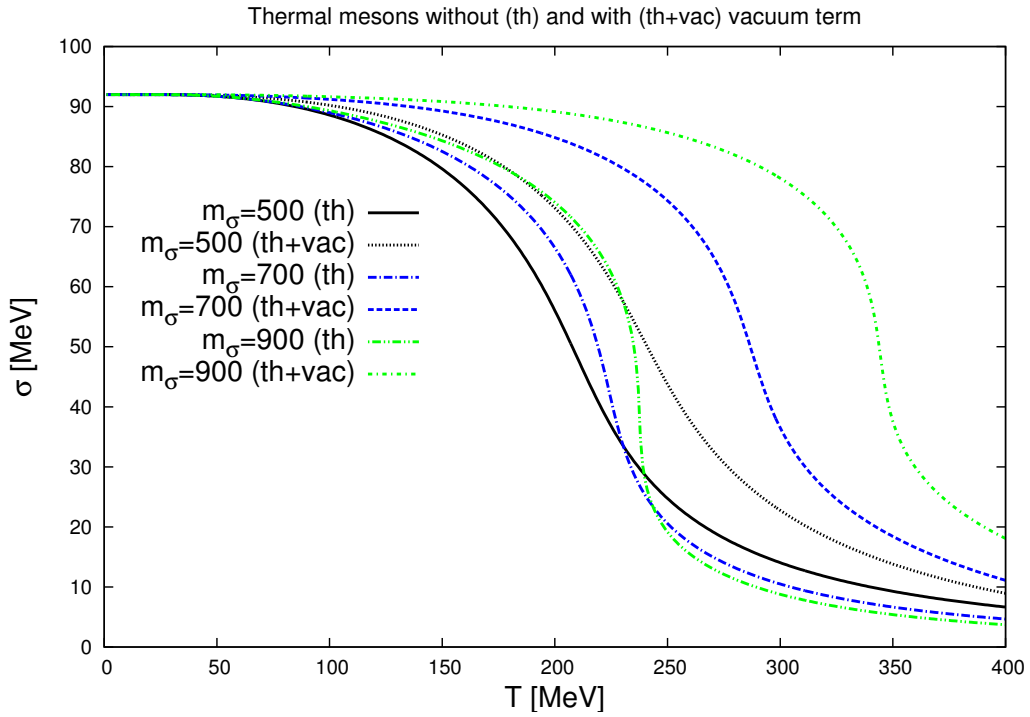

Figure 4.6: *The σ condensate as a function of temperature without (denoted as "th") and with vacuum contribution (denoted as "th+vac") for three different values of the initial vacuo sigma meson mass m_σ^{vac}. The larger m_σ^{vac}, the more crossover like is the behaviour of the "thermal" curves up to a temperature, where the curves intersect. From there on the highest initial vacuo mass of the sigma mesons shows the steepest case of fall with temperature, and approaching the chirally restored phase more rapidly. The vacuum contribution leads to the same behaviour as when increasing the initial value of m_σ. The highest chosen initial vacuo mass and the inclusion of the vacuum contribution leads to a phase transition at very high temperature and the condensate is farthest from being in the chirally restored phase.*

The most crossover like trend from the quark case, i.e. $m_\sigma^{vac} = 900$ MeV with the inclusion of the self energy nearly matches the least crossover like trend in the thermal mesonic sector, that is $m_\sigma^{vac} = 500$ MeV without considering the self energy. These two curves are nearly equal up to $T \sim 210$ MeV. From there on the quark curve approaches the chirally restored phase more steeply.

At $T = 400$ MeV the value of the field reads $\sigma \sim 1.4$ MeV for the former case compared to $\sigma \sim 6.7$ MeV for the latter case. However, all three cases discussed here containing the vacuum contribution do not show an intersection. The inclusion of the vacuum contribution shifts the curves to higher temperatures, whereas the curve with the highest initial sigma meson mass bends down at higher temperatures, steeper than the others. These behaviours have not been observed in the quark cases including or neglecting the vacuum contribution. There, the trends become slightly more crossover like with increasing m_σ^{vac}. For $m_\sigma^{vac} = 500$ MeV the phase transition in the present case neglecting the self energy takes place at $T \sim 230$ MeV, for $m_\sigma^{vac} = 700$ MeV at $T \sim 240$ MeV and for $m_\sigma^{vac} = 900$ MeV at $T \sim 245$ MeV, i.e. for larger initial sigma meson mass m_σ the chiral transition temperatures rise, but not that significantly as in the quark sector. Including the vacuum contributions, for $m_\sigma^{vac} = 500$ MeV the phase transition takes place at $T \sim 260$ MeV, for $m_\sigma^{vac} = 700$ MeV at $T \sim 305$ MeV and for $m_\sigma^{vac} = 900$ MeV at $T \sim 360$ MeV. Comparing the phase transition differences ΔT_c in temperature, the thermal differences, neglecting the vacuum term, are significantly smaller in the mesonic sector when changing the initial value of the sigma meson mass, $230 \leq \Delta pt \leq 245$ MeV for the mesonic case and $130 \leq \Delta pt \leq 205$ MeV for the quark case in section 4.4. Δpt marks the differences around the phase transition. The same behaviour can be observed when including the vacuum term. Here $260 \leq \Delta pt \leq 360$ MeV for the mesonic case and $163 \leq \Delta pt \leq 233$ MeV for the quark case (section 4.4), see also Table 4.1.
The chiral condensate does not vanish entirely, so that there the system is significantly away from a chirally restored phase then compared to the quark sector for temperatures up to 400 MeV.

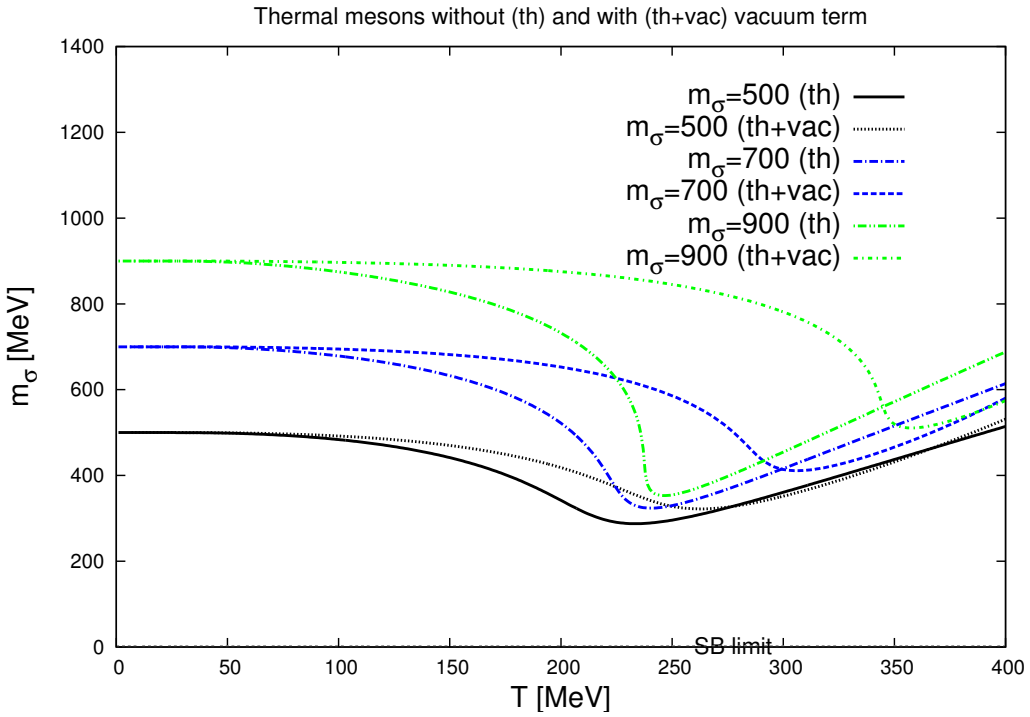

Figure 4.7: *The sigma meson mass m_σ as a function of temperature without (denoted as "th") and with vacuum contribution (denoted as "th+vac") for three different values of the initial vacuo sigma meson mass m_σ.*

Figure 4.7 shows the mass of the sigma mesons as a function of the temperature, neglecting (denoted as "th") and including (denoted as "th+vac") the vacuum term. The value of the minimum in the thermal case (neglecting the self energy) for the initial value of $m_\sigma^{vac} = 500$ MeV reads $T = 230$ MeV and $m_\sigma = 290$ MeV, for $m_\sigma^{vac} = 700$ MeV the temperature is located at $T = 238$ MeV and the sigma meson mass $m_\sigma = 324$ MeV. For $m_\sigma^{vac} = 900$ MeV, $T = 245$ MeV and $m_\sigma = 355$ MeV.
Inclusion of the self energy leads to the values $T = 260$ MeV and $m_\sigma = 320$ MeV for $m_\sigma^{vac} = 500$ MeV, $T = 305$ MeV and $m_\sigma = 414$ MeV for $m_\sigma^{vac} = 700$ MeV and $T = 360$ MeV and $m_\sigma = 510$ MeV for $m_\sigma^{vac} = 900$ MeV. Studying the thermal case, the minima are quite close together ($230 \leq$ T ≤ 245 MeV and $290 \leq$ m$_\sigma \leq 355$ MeV), whereas the inclusion of the self energy leads to a decisive stretching of the temperature region for varying vacuum

sigma meson masses ($260 \leq \mathrm{T} \leq 360$ MeV and $320 \leq \mathrm{m}_\sigma \leq 510$ MeV). The rise of all curves at high temperatures is clearly less steep then in the quark case (section 4.4).

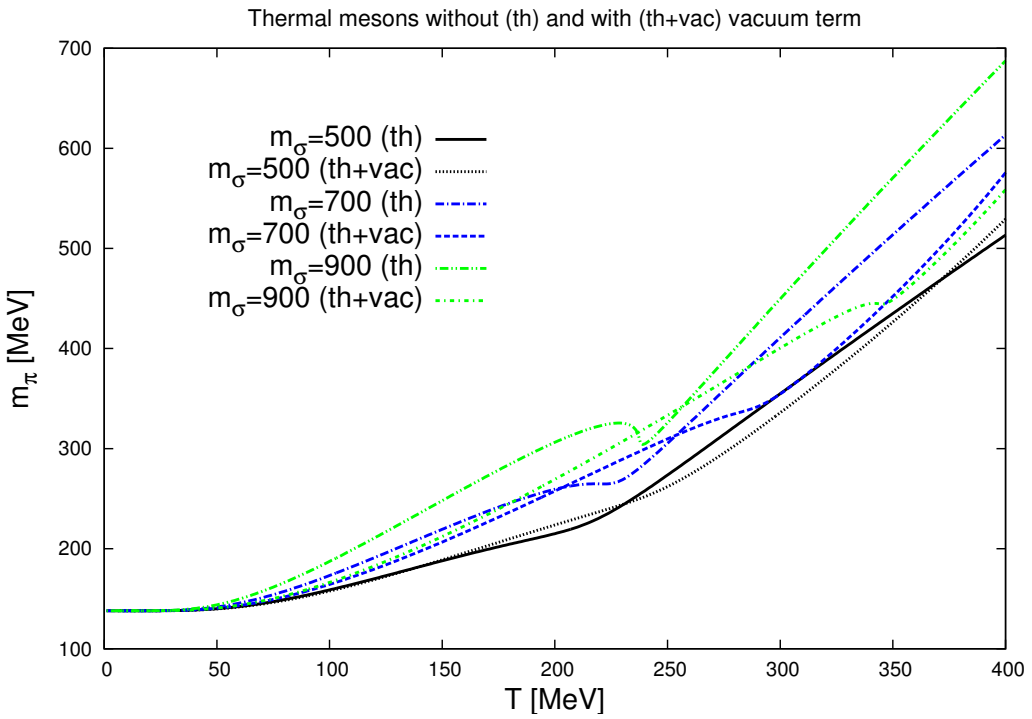

Figure 4.8: *The pion mass m_π as a function of temperature without (denoted as "th") and with vacuum contribution (denoted as "th+vac") for three different values of the initial vacuo sigma meson mass. At $T \sim 50$ MeV the curves start to deviate from the vacuum mass of the pion. Some curves show a minimum, which cannot be back traced to the behaviour of the fields and is rather a feature of the distribution function eq. 4.47.*

Figure 4.8 shows the behaviour of the pion mass for the three different values of the sigma meson m_σ^{vac}, neglecting and including the vacuum contribution of the mesons. Compared to the quark case (section 4.4) all the mesonic pion-mass curves start to deviate from their vacuum value at $T \sim 50$ MeV already before the phase transition takes place, so that this behaviour cannot be backtraced to the trend of the respective fields in fig. 4.6. In contrast to the quark case some of these curves also show a negative slope. For $m_\sigma^{vac} \geq$

700 MeV, the curves clearly show a minimum. This is also the case when including the vacuum fluctuations, at a larger value of the initially chosen sigma meson mass, $m_\sigma^{vac} \sim 900$ MeV. As we shall see, the appearance of a minimum in the pionic mass spectrum influences the thermodynamics in a nontrivial manner. Another important difference to the quark case is that the masses of the degenerate mesons are only half as heavy at high temperatures. Within the 2PI formalism we only reach $500 \leq m_{\pi,\sigma} \leq 600$ MeV, whereas in the quark case masses of ~ 1.2 GeV have been achieved.

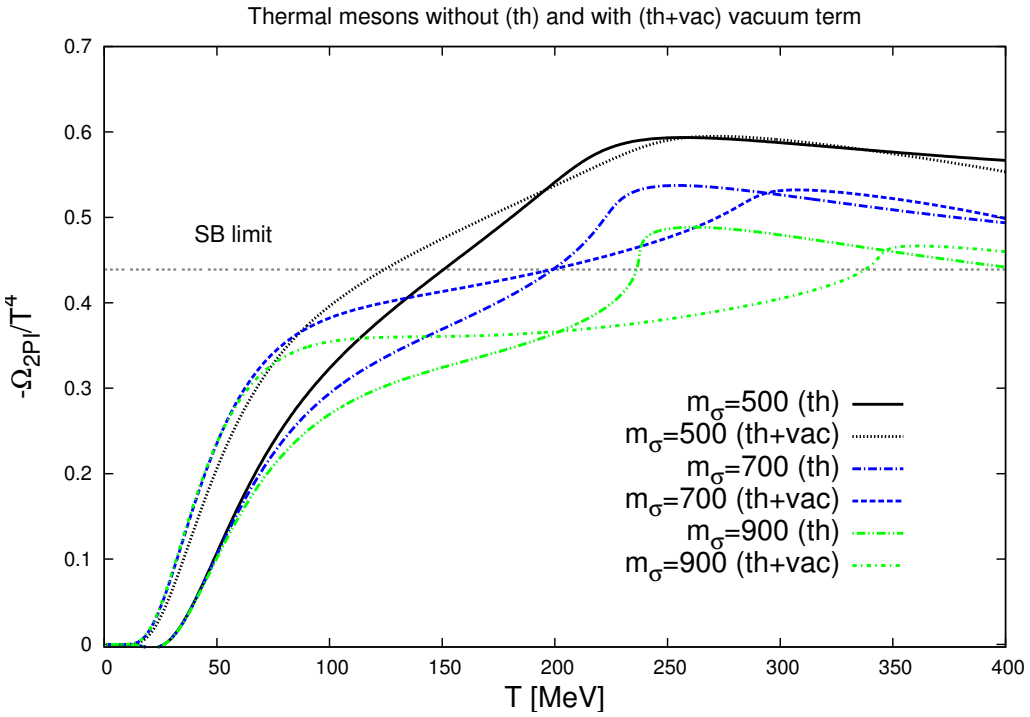

Figure 4.9: *The negative of the potential, i.e. the pressure, divided by T^4 as a function of temperature without (denoted as "th") and with vacuum contribution (denoted as "th+vac") for three different values of the initial vacuo sigma meson mass m_σ^{vac}. The curves show a deviation from the Stefan Boltzmann limit at high temperatures.*

The pressure of the mesonic contribution divided by T^4 provided by the CJT formalism is shown in fig. 4.9. All curves neglecting the self energy start to rise significantly at $T \simeq 30$ MeV, whereas the inclusion of the self

energy causes the pressure to rise at already $T \simeq 20$ MeV. Neglecting the vacuum term, for $m_\sigma^{vac} = 500$ MeV the curve rises nearly monotonically up to $T \simeq 250$ MeV and slowly decreases for higher temperatures failing to approach the Stefan Boltzmann limit (up to 23% deviation), that is eq. 4.7 with $\xi_m = 4$. This is because the field σ does not fully reach the value of a chirally restored phase, see fig. 4.6, and all relevant degrees of freedom aquire a thermal mass. The larger the chosen mass of the sigma meson, the less pressure the system 3 has at a given temperature, which is in accordance with our observation in the quark case (section 4.4), and due to the same reasons discussed in section 4.4.2 reasonable. The deviation from a monotonically trend of the curves for higher chosen mass $m_\sigma^{vac} \geq 500$ MeV goes along with the non-monotonically behaviour of the sigma meson mass shown in fig. 4.7. The higher the vacuum mass of the sigma meson, the more pronounced is the minimum implying a deviation from a monotonically trend of the pressure. Connected to that is the strange behaviour of the pion mass, shown in fig. 4.8. When the mass of the pion starts to rise less steeply, becomes constant or even gets less heavy with rising temperature (this happens around the phase transition), the ratio of p/T^4 is immediately affected via these features. In the quark sector all pressure curves rise monotonically, see fig. 4.18. There the relevant degrees of freedom are obtained around the phase transition. In the mesonic sector the Stefan Boltzmann limit is not reached. Inclusion of the self energy shifts all curves to the left, yielding a higher pressure at given temperature, which is opposite to the feature seen in the quark case (section 4.4). The pressure is found to be closest to the Stefan Boltzmann limit for a higher mass of m_σ^{vac}. Speaking of a chiral limit is, however, doubtful, since all curves show no asymptotic behaviour. The irregularities in the curves are mainly resulting from the odd behaviour of the pion mass, which itself is connected to the sigma mass (remember that the gap equations 4.44, 4.45 and 4.46 are coupled equations). In the quark sector the masses of the mesons are generated by the fields and its coupling, and are independent of temperature, whereas in the mesonic sector the mass term in the distribution function, equation 4.47, itself is dependent on temperature. That is, eq. 4.45 enters in the distribution function, either in the temperature dependent part,

eq. 4.48 and, including the vacuum term, also in the vacuum part eq. 4.102. This also leads to the fact, that for the mesonic case there exists no analytic expression for the entropy density s.

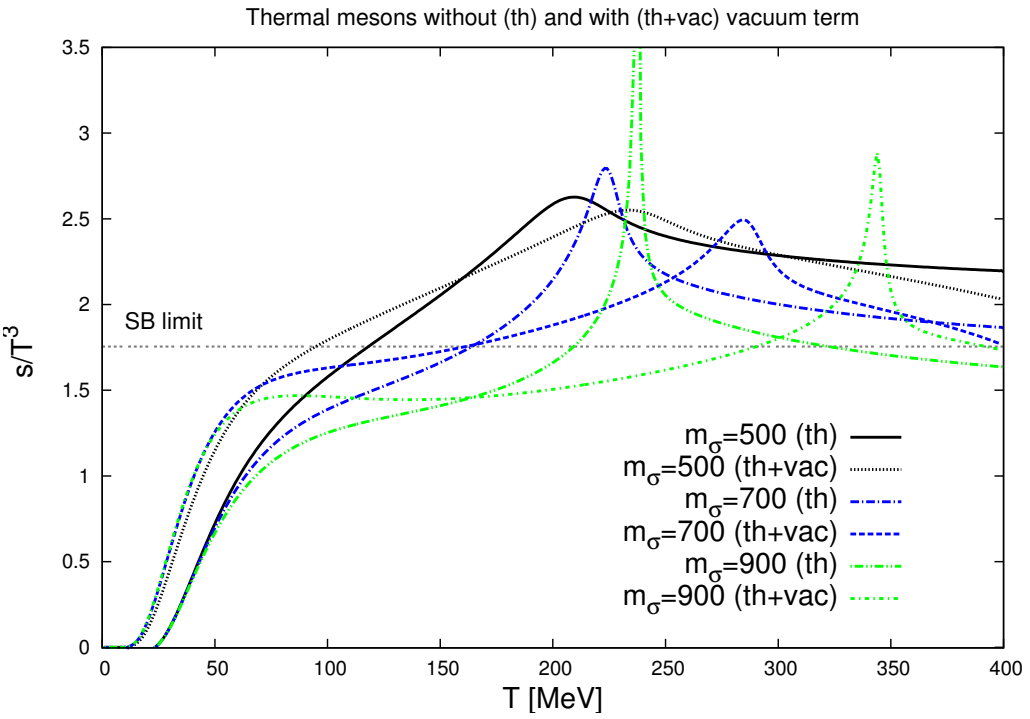

Figure 4.10: *The entropy density s divided by T^3 as a function of temperature without (denoted as "th") and with vacuum contribution (denoted as "th+vac") for three different values of the initial vacuo sigma meson mass m_σ^{vac}. The curves are clearly more distorted then in the quark case (fig. 4.19) and show accentuated maxima within a small region of the temperature.*

The entropy density divided by T^3 is shown in fig. 4.10, related to the derivation of the potential with respect to the temperature, in fig. 4.9, the accentuated maxima for all of these curves can hence be traced back to the odd behaviour of the potential. When the pressure rises disproportional a drastic increase in the entropy density is seen. As soon as the pressure reaches the maximum towards the Stefan Boltzmann limit, the entropy density decreases drastically, too, to eventually saturate towards the Stefan Boltzmann limit. This feature can be explained as follows:

The disorder within the system rises because the sigma meson mass is at its point of inflection. Here the pion mass does not rise anymore, i.e. it nearly stays constant. At the very point of inflection of the sigma meson mass the entropy is maximal. As soon as the mass of the pion rises again to become degenerate with the sigma meson mass, the entropy density approaches asymptotically the Stefan Boltzmann limit. A detailed analysis of the quark case in the next section 4.4 shows the same relation of the meson masses to the entropy. There the effect is not that visible because the mass of the pion rises considerably after the phase transition (and does not remain constant as in the mesonic case), which also leads to the missing of the "spikes" in the entropy to T^3 ratio in the quark sector.

4.4. Quark-quark interactions

A Lagrangian [37][11] with $N_f = 2$ respecting quark fields may be written as

$$\begin{aligned} \mathcal{L} &= \bar{\Psi}\left(i\partial\!\!\!/ - g(\sigma + i\gamma_5 \vec{\tau}\cdot\vec{\pi})\right)\Psi \\ &+ \frac{1}{2}\left(\partial_\mu\sigma\partial^\mu\sigma + \partial_\mu\vec{\pi}\partial^\mu\vec{\pi}\right) - U(\sigma,\vec{\pi}) \end{aligned} \tag{4.106}$$

where g is a Yukawa type coupling to the quark spinors $\Psi, \bar{\Psi}$ and $U(\sigma,\vec{\pi})$ is the same tree level potential as given in equation 4.16. The respective Feynman diagrams resulting from the quark-meson interaction can be seen in figure 4.11.

Instead of using a CJT-type formalism, the quark-quark interaction is derived commonly with the path integral formalism[12] with the mesons as classical background fields.

[11] See section 5 for a more detailled treatment and motivation of the terms involved in the Lagrangian.

[12] A detailled path integral calculation within this thesis is performed for the more lavorious and relevant SU(3) case in section 5. The SU(2) calculation can then easily be retraced.

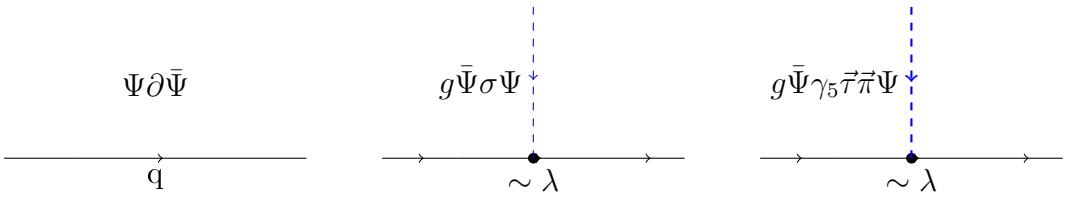

Figure 4.11: *Left picture: A propagating quark without any interaction, so called free propagator. Middle: a propagating quark interacting with a stationary sigma meson field. Right: A propagating quark interacting with a pion. The formulae in the upper middle of each picture depicts how each term in the Lagrangian can be translated into a Feynman diagram. g couples the quarks to the mesons and the vertex is proportional to the coupling λ.*

The grand canonical potential then reads

$$\Omega_{\bar{q}q} = U(\sigma,\vec{\pi}) - N_f N_c T \int_0^\infty \frac{dk^3}{(2\pi)^3}\left[\frac{E_k}{T} + \ln\left[1+e^{-\beta(E_k\pm\mu_f)}\right]\right] \tag{4.107}$$

The thermal contribution to the potential is

$$\Omega^{th}_{\bar{q}q} = \frac{3T}{\pi^2}\int_0^\infty dk k^2 \ln\left[1+e^{-\beta(E_k\pm\mu_f)}\right] \tag{4.108}$$

where the single particle energy

$$E_k = \sqrt{k^2+\tilde{m}_f^2} \qquad \text{with} \qquad \tilde{\mathrm{m}}_\mathrm{f} = \mathrm{g}\sqrt{(\sigma^2+\tilde{\pi}^2)} \tag{4.109}$$

as the effective mass $\tilde{m}_f$ with the Yukawa type coupling $g = \frac{m_{q,vac}}{f_\pi}$ corresponding to the constituent quark mass $m_{q,vac} = 300$ MeV and the already known pion decay constant $f_\pi = 92.4$ MeV, have been introduced. f represents the two quark flavours incorporated in the model and μ_f is the flavour dependent quark chemical potential. The vacuum contribution $\Omega^{vac}_{\bar{q}q} = \int \frac{dk^3}{(2\pi)^3} E_k$ will be treated in the next section 4.4.1. To solve the coupled gap equations at finite T where both particle- and antiparticle states are considered, one needs firstly to fix the vacuum values for λ, H and v^2. To fix these values one needs the derivatives of $\Omega_{\bar{q}q}$ at $T = 0$ with respect to

the fileds σ and $\vec{\pi}$.
The first derivatives read:

$$\left.\frac{\partial\Omega_{\bar{q}q}}{\partial\sigma}\right|_{T=\mu=0} = \left.\frac{\partial U(\sigma,\vec{\pi})}{\partial\sigma}\right|_{\pi=0} = \lambda(\sigma^2-v^2)\sigma - H \tag{4.110}$$

$$\left.\frac{\partial\Omega_{\bar{q}q}}{\partial\pi}\right|_{T=\mu=0} = \left.\frac{\partial U(\sigma,\vec{\pi})}{\partial\vec{\pi}}\right|_{\pi=0} = \lambda(\pi^2+\sigma^2-v^2)\pi \tag{4.111}$$

Note, that the first derivative of Ω with respect to π yields zero. This is reasonable, since the π does not condensate due to parity. The second derivatives are consequently:

$$\begin{aligned}\left.\frac{\partial^2\Omega_{\bar{q}q}}{\partial\sigma^2}\right|_{T=\mu=0} &= \left.\frac{\partial U^2(\sigma,\vec{\pi})}{\partial\sigma^2}\right|_{\pi=0} \\ &= \lambda(3\sigma^2-v^2) = m^2_{\sigma,vac.} = 550\ MeV\end{aligned} \tag{4.112}$$

$$\begin{aligned}\left.\frac{\partial^2\Omega_{\bar{q}q}}{\partial\pi^2}\right|_{T=\mu=0} &= \left.\frac{\partial U^2(\sigma,\vec{\pi})}{\partial\vec{\pi}^2}\right|_{\pi=0} = 0 \\ &= \lambda(\sigma^2-v^2) = m^2_{\pi,vac.} = 135\ MeV\end{aligned} \tag{4.113}$$

i.e. the first derivatives give the minimum of the potential, which actually is the true ground state of a particle (remember the disccussion in section 3.6.5) and the second derivatives yield the respective masses of the particles. Using eqs.: 4.110, 4.112 and 4.113 one can extract the values for

$$H = m_\pi^2 f_\pi \tag{4.114}$$

$$\lambda = \frac{m_\sigma^2 - m_\pi^2}{2f_\pi} \tag{4.115}$$

$$v^2 = f_\pi^2 - \frac{m_\pi^2}{\lambda} \quad \text{or: } v^2 = 3f_\pi^2 - \frac{m_\sigma^2}{\lambda} \tag{4.116}$$

Including the tree level potential and only the thermal contributions from

$\Omega_{\bar{q}q}$ the first derivative with respect to σ is

$$\left.\frac{\partial\Omega^{th}_{\bar{q}q}}{\partial\sigma}\right|_{T,\mu\neq 0} = \lambda(\sigma^2-v^2)\sigma - H + \frac{3g\sigma}{\pi^2}\int_0^\infty dk\frac{k^2}{E_k}\cdot\frac{1}{1+e^{\beta(E_k\pm\mu_f)}} \tag{4.117}$$

The second derivatives including the thermal contribution read

$$\begin{aligned}\left.\frac{\partial^2\Omega^{th}_{\bar{q}q}}{\partial\sigma^2}\right|_{T,\mu\neq 0} &= M_\sigma^2 = \lambda(3\sigma^2-v^2) \\ &+ \frac{3g^2}{\pi^2}\int_0^\infty dk k^2\left(\frac{1}{E_k}-\frac{g^2\sigma^2}{E_k{}^{\frac{3}{2}}}\right) \\ &\times \frac{1}{1+e^{\beta(E_k\pm\mu_f)}} - \frac{g^2\sigma^2 e^{\beta(E_k\pm\mu_f)}}{TE_k{}^2(1+e^{\beta(E_k\pm\mu_f)})^2}\end{aligned} \tag{4.118}$$

$$\begin{aligned}\left.\frac{\partial^2\Omega^{th}_{\bar{q}q}}{\partial\pi^2}\right|_{T,\mu\neq 0} &= M_\pi^2 = \lambda(\sigma^2-v^2) \\ &+ \frac{3g^2}{\pi^2}\int_0^\infty dk k^2\left(\frac{1}{E_k}-\frac{g^2\vec{\pi}^2}{E_k{}^{\frac{3}{2}}}\right) \\ &\times \frac{1}{1+e^{\beta(E_k\pm\mu_f)}} - \frac{g^2\pi^2 e^{\beta(E_k\pm\mu_f)}}{TE_k{}^2(1+e^{\beta(E_k\pm\mu_f)})^2}\end{aligned} \tag{4.119}$$

and yield the masses of the corresponding particles[13].

The equations 4.117, 4.118 and 4.119 represent the gap equations in the thermal quark sector for $N_f = 2$, which are to be solved self-consistently. Note that, due to $<\vec{\pi}>=0$ not all terms contribute to the Integral in equation 4.119. Figure 4.12 shows the values of the σ condensate up to $T = 400$ MeV. At large T chiral symmetry is restored, i.e. the condensate vanishes. The corresponding potential Ω as a function of the order parameter σ can be seen in the figures 4.13 for $\mu = 0$ and in 4.14 for $\mu = 100$ MeV, where the respective minima matches the values in figure 4.12. For small temperature the mexican hat like potential (Remember the discussion in section 3.6.5, i.e. figure 3.6) is clearly to be seen.

[13]This feature can be understood as how much energy is needed to "climb" up the potential wall (Recall that $E = mc^2$) in σ direction.

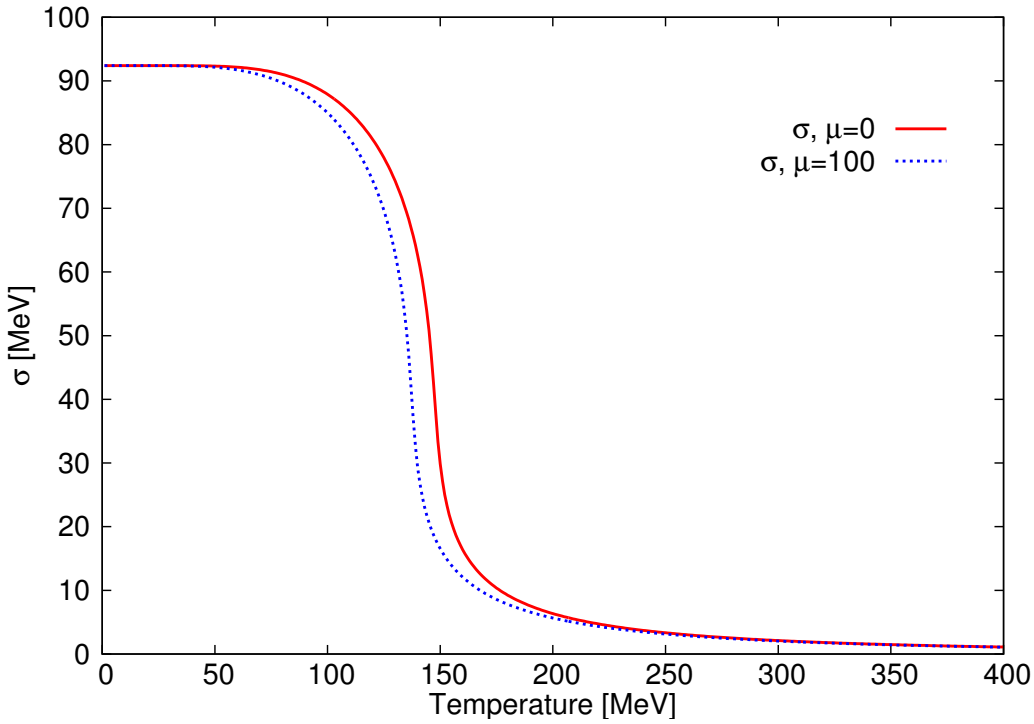

Figure 4.12: *The σ field as function of the Temperature in the SU(2) case considering quark-quark interactions with stationary mesonic background fields at two different values of μ. The respective values $m_{q,vac} = 300$ MeV, $m_\sigma = 600$ MeV, $f_\pi = 92.4$ MeV are the standard values. The curve represents the minimum of the potential at any given T.*

The physical interpretation of the '*mexican hat potential* is that the sigma "lies" in a circle around the origin (see figure 4.1), which is its true ground state. The explicit symmertry breaking term H gives an nonvanishing mass to the pion, see the discussion in section 3.6.6 and also figure 3.7.

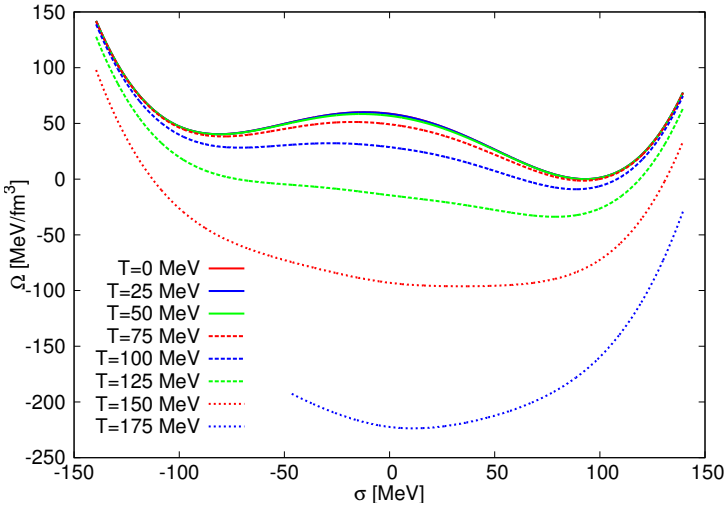

Figure 4.13: *The curves show the minima of the potential at different T for the parameter choice* $m_{q,vac} = 300\ MeV$, $m_\sigma = 600\ MeV$, $f_\pi = 92.4\ MeV$. $\mu = 0$ *in all cases. For a better understanding compare to figs.:* 3.6 *and* 3.7.

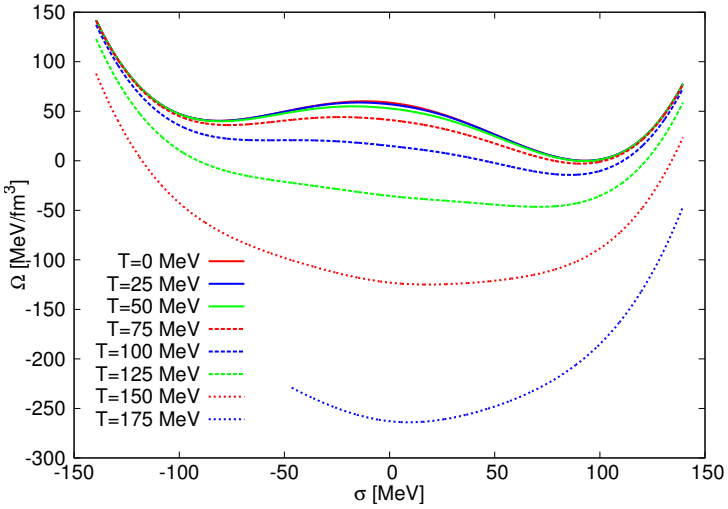

Figure 4.14: *The curves show the minima of the potential at different T for the parameter choice* $m_{q,vac} = 300\ MeV$, $m_\sigma = 600\ MeV$, $f_\pi = 92.4\ MeV$. $\mu = 100\ MeV$ *in all cases. For a better understanding compare to figs.:* 3.6 *and* 3.7.

4.4.1.
Vacuum fluctuations of quarks

Like in the bosonic case in section 4.3.1, a proper renormalisation of the one-loop contribution leads to a fermionic vacuum contribution to the in-medium effective potential, see figure 4.5. Consequently one expects contributions in particular for large chemical potential and high temperatures. So, vacuum terms from both fermionic and bosonic fields can change qualitatively the process of the order parameter and the mass spectrum. The fermion vacuum contribution from equation 4.107 can also be obtained by the dimensional regularization scheme, which for fermions is derived similar as been performed in section 4.3.1 for the mesons. Here only the result shall be given

$$\Omega_{\bar{q}q}^{vac} = \int \frac{dk^3}{(2\pi)^3} E_k \qquad \rightarrow \qquad \Omega_{\bar{q}q}^{dr} = -\frac{N_c N_f}{8\pi^2} \tilde{m}_f^4 \ln\left(\frac{\tilde{m}_f}{\Lambda}\right) \tag{4.120}$$

where Λ is the renormalization scale parameter (corresponding to μ in the mesonic case and not to be messed up with the chemical potential μ). The values of the parameters λ, H and v^2, i.e. equations 4.114, 4.115 and 4.116, then no longer represent vacuum solutions. They have a logarithmic dependence on the renormalization scale Λ and have to be replaced by renormalized ones, which have to be extracted from the derivatives of the whole potential 4.107 (the one including the vacuum contributions). To determine the renormalized parameters the vacuum loop part from equation 4.120

$$\Omega_{\bar{q}q}^{dr} = -\frac{N_c N_f}{8\pi^2} \tilde{m}_f^4 \ln\left(\frac{\tilde{m}_f}{\Lambda}\right)$$

has to be derived with respect to the fields. The equations 4.110, 4.112 and 4.113 then are additive[14]. Defining $\phi_i^2 = \sigma^2 + \vec{\pi}^2$ respresentaive for the two

[14] Analoguous to the considerations on additivity in section 4.2

contributing fields σ and $\vec{\pi}$ and $\tilde{m}_f^2 = g^2\phi_i^2$ the first derivative becomes

$$\begin{aligned}
\frac{\partial\Omega_{\bar{q}q}^{dr}}{\partial\phi_i} &= \frac{\partial\Omega_{\bar{q}q}^{dr}}{\partial\tilde{m}_f^2}\frac{\partial\tilde{m}_f^2}{\partial\phi_i} \\
&= -\frac{N_c N_f}{8\pi^2}\left[2\tilde{m}_f^2\frac{\partial\tilde{m}_f^2}{\partial\phi_i}\ln\left(\frac{\sqrt{\tilde{m}_f^2}}{\Lambda}\right) + (\tilde{m}_f^2)^2\frac{\Lambda}{\sqrt{\tilde{m}_f^2}}\frac{1}{\Lambda}\frac{1}{2\sqrt{\tilde{m}_f^2}}\frac{\partial\tilde{m}_f^2}{\partial\phi_i}\right] \\
&= -\frac{N_c N_f}{8\pi^2}\left[2\tilde{m}_f^2\frac{\partial\tilde{m}_f^2}{\partial\phi_i}\ln\left(\frac{\sqrt{\tilde{m}_f^2}}{\Lambda}\right) + \frac{\tilde{m}_f^2}{2}\frac{\partial\tilde{m}_f^2}{\partial\phi_i}\right] \\
\frac{\partial\Omega_{\bar{q}q}^{dr}}{\partial\sigma} &= -\frac{N_c N_f}{8\pi^2}\left[2g^2\sigma^2 2g^2\sigma\ln\left(\frac{\tilde{m}_f}{\Lambda}\right) + \frac{g^2\sigma^2}{2}2g^2\sigma\right] \\
\frac{\partial\Omega_{\bar{q}q}^{dr}}{\partial\sigma} &= -\frac{N_c N_f}{8\pi^2}g^4\sigma^3\left[4\ln\left(\frac{\tilde{m}_f}{\Lambda}\right) + 1\right] \qquad (4.121)
\end{aligned}$$

Since $\vec{\pi} = 0$, its first derivative vanishes and is hence needless. The second derivatives then are

$$\begin{aligned}
\frac{\partial^2\Omega_{\bar{q}q}^{dr}}{\partial\phi_i^2} &= -\frac{N_c N_f}{8\pi^2}\left[2\tilde{m}_f^2\frac{\partial^2\tilde{m}_f^2}{\partial\phi_i^2}\ln\left(\frac{\tilde{m}_f^2}{\Lambda}\right) + 2\left(\frac{\partial m_f}{\partial\phi_i}\right)^2\ln\left(\frac{m_f}{\Lambda}\right) + \frac{3}{2}\left(\frac{\partial m_f}{\partial\phi_i}\right)^2 + \frac{\tilde{m}_f^2}{2}\frac{\partial^2\tilde{m}_f^2}{\partial\phi_i^2}\right] \\
&= -\frac{N_c N_f}{8\pi^2}\left[\frac{3}{2}\left(\frac{\partial m_f^2}{\partial\phi_i}\right)^2 + \frac{\tilde{m}_f^2}{2}\frac{\partial^2\tilde{m}_f^2}{\partial\phi_i^2} + 2\ln\left(\frac{\tilde{m}_f}{\Lambda}\right)\left[\left(\frac{\partial m_f^2}{\partial\phi_i}\right)^2 + \tilde{m}_f^2\left(\frac{\partial^2\tilde{m}_f^2}{\partial\phi_i^2}\right)\right]\right] \\
\frac{\partial^2\Omega_{\bar{q}q}^{dr}}{\partial\sigma^2} &= -\frac{N_c N_f}{8\pi^2}\left[\frac{3\cdot 4}{2}g^4\sigma^2 + \frac{g^2\sigma^2}{2}2g^2 + 2\ln\frac{g\sigma}{\Lambda}\left(4g^4\sigma^2\right) + 2g^2g^2\sigma^2\right] \\
\frac{\partial^2\Omega_{\bar{q}q}^{dr}}{\partial\sigma^2} &= -\frac{N_c N_f}{8\pi^2}g^4\sigma^2\left[7 + 12\ln\left(\frac{\tilde{m}_f}{\Lambda}\right)\right] \qquad \text{and} \qquad (4.122) \\
\frac{\partial^2\Omega_{\bar{q}q}^{dr}}{\partial\vec{\pi}^2} &= -\frac{N_c N_f}{8\pi^2}\left[\frac{3\cdot 4}{2}g^2\vec{\pi}^2 + \frac{2g^2\left(\sigma^2+\vec{\pi}^2\right)g^2}{2} + 2\ln\left(\frac{\tilde{m}_f}{\Lambda}\right)\left[4g^4\vec{\pi}^2 + 2g^2\left(\sigma^2+\vec{\pi}^2\right)g^2\right]\right] \\
\frac{\partial^2\Omega_{\bar{q}q}^{dr}}{\partial\vec{\pi}^2} &= -\frac{N_c N_f}{8\pi^2}g^4\sigma^2\left[1 + 4\ln\left(\frac{\tilde{m}_f}{\Lambda}\right)\right] \qquad (4.123)
\end{aligned}$$

Combining the vacuum contributions of the linear sigma potential, i.e. equations 4.110, 4.112, 4.113, with 4.121, 4.122 and 4.123, and inserting the corresponding vacuum values for $<\sigma>= f_\pi$, $m_\sigma = 550$ MeV and $m_\pi = 138$ MeV leads to modified renormalized vacuum terms $\lambda \to \lambda_r$, $m^2 \to m_r^2$ and

$H \to H_r$.

$$0 = -\frac{N_c N_f}{8\pi^2} g^4 \sigma^3 \left[4 \ln\left(\frac{\tilde{m}_f}{\Lambda}\right) + 1\right] + \lambda_r f_\pi^3 + m_r^2 f_\pi - H_r \quad (4.124)$$

$$m_\sigma^2 = -\frac{N_c N_f}{8\pi^2} g^4 \sigma^2 \left[7 + 12 \ln\left(\frac{\tilde{m}_f}{\Lambda}\right)\right] + 3\lambda_r f_\pi^2 + m_r^2 \quad (4.125)$$

$$m_\pi^2 = -\frac{N_c N_f}{8\pi^2} g^4 \sigma^2 \left[1 + 4 \ln\left(\frac{\tilde{m}_f}{\Lambda}\right)\right] + \lambda_r f_\pi^2 + m_r^2 \quad (4.126)$$

Substracting 4.126 from 4.125 gives

$$m_\sigma^2 - m_\pi^2 = -\frac{N_c N_f}{8\pi^2} g^4 f_\pi^2 \left[6 + 8 \ln\left(\frac{\tilde{m}_f}{\Lambda}\right)\right] + 2\lambda_r f_\pi^2 \quad (4.127)$$

Solving for λ_r yields

$$\lambda_r = \frac{m_\sigma^2 - m_\pi^2}{2 f_\pi^2} + \frac{N_c N_f}{8\pi^2} g^4 \left[3 + 4 \ln\left(\frac{g f_\pi}{\Lambda}\right)\right] \quad (4.128)$$

Placing equation 4.128 in 4.125 gives[15]

$$m_r^2 = \frac{N_c N_f}{4\pi^2} g^4 f_\pi^2 + \frac{m_\sigma^2 - 3m_\pi^2}{2} \quad (4.129)$$

Putting these values back in 4.124 gives $H_r = m_\pi^2 f_\pi = H$. The explicit symmety breaking term again remains unaffected by renormalization, such as in the bosonic case (equation 4.105). Placing the renormalized values into the whole temperature-independent potential, i.e. eqs. 4.16 and 4.120, the renormalization scale Λ dependence cancels out in λ_r, so that

$$\lambda_r = \frac{m_\sigma^2}{2 f_\pi^2} - \frac{H}{2 f_\pi^3} + \frac{3}{8} \frac{N_c N_f}{\pi^2} g^4 \quad (4.130)$$

[15] It can of course also be placed in 4.126

and after having rearranged the terms, the vacuum part plus the linear sigma part of the potential eventually reads

$$\begin{aligned}\Omega^{dr}_{\bar{q}q} + U(\sigma,\vec{\pi}) &= -\frac{N_c N_f}{8\pi^2}\tilde{m}_f^4 \ln\left(\frac{\tilde{m}_f}{g f_\pi}\right) \\ &+ \frac{\lambda_r}{4}\left(\sigma^2+\vec{\pi}^2\right)^2 + \frac{m_r^2}{2}\left(\sigma^2+\vec{\pi}^2\right) - H\sigma \end{aligned} \tag{4.131}$$

and, including the thermal part, everything together reads

$$\begin{aligned}\Omega_{q\bar{q}} = \Omega^{dr}_{\bar{q}q} + \Omega^{th}_{\bar{q}q} + U(\sigma,\vec{\pi}) &= -\frac{N_c N_f}{8\pi^2}\tilde{m}_f^4 \ln\left(\frac{\tilde{m}_f}{g f_\pi}\right) \\ &- \frac{3T}{\pi^2}\int_0^\infty dk k^2 \ln\left[1+e^{-\beta(E_k \pm \mu_f)}\right] \\ &+ \frac{\lambda_r}{4}\left(\sigma^2+\vec{\pi}^2\right)^2 + \frac{m_r^2}{2}\left(\sigma^2+\vec{\pi}^2\right) - H\sigma \end{aligned} \tag{4.132}$$

The whole potential is independent of any renormalization.
The vacuum contributions to each the thermal gap equation (4.117, 4.118 and 4.119) is additive.

$$\frac{\partial \Omega^{dr}_{\bar{q}q}}{\partial \sigma} = -\frac{N_c N_f g^4 \sigma^3}{8\pi^2}\left[1+4\ln\left(\frac{\sigma}{f_\pi}\right)\right] \tag{4.133}$$

$$\frac{\partial^2 \Omega^{dr}_{\bar{q}q}}{\partial \sigma^2} = -\frac{N_c N_f g^4 \sigma^2}{8\pi^2}\left[7+12\ln\left(\frac{\sigma}{f_\pi}\right)\right] \tag{4.134}$$

$$\frac{\partial^2 \Omega^{dr}_{\bar{q}q}}{\partial \vec{\pi}^2} = -\frac{N_c N_f g^4 \sigma^2}{8\pi^2}\left[1+4\ln\left(\frac{\sigma}{f_\pi}\right)\right] \tag{4.135}$$

4.4.2. Results in the quark sector

Figure 4.15 shows the order parameter σ as a function of the temperature for three different initial vacuo sigma meson masses m_σ^{vac}, neglecting (denoted in the following figures as "th") and including (denoted in the following figures as "th+vac") the vacuum term of the quarks.

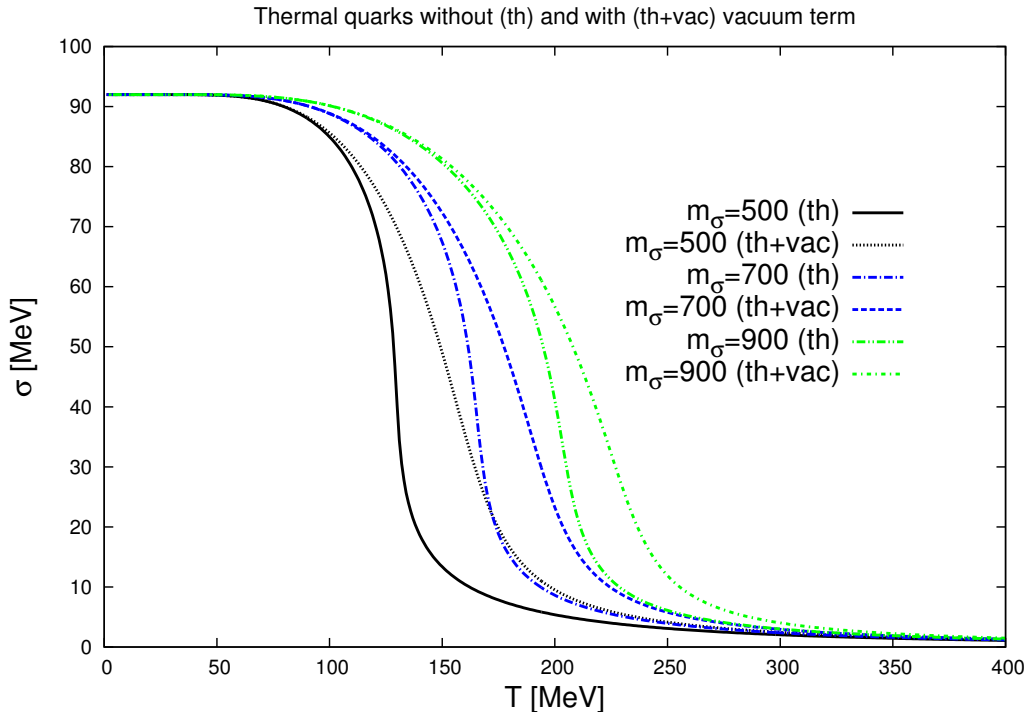

Figure 4.15: *The σ condensate as a function of temperature for zero chemical potential without (denoted as "th") and with vacuum contribution (denoted as "th+vac") for three different values of the vacuo sigma meson mass m_σ^{vac}. A higher value of m_σ^{vac} shifts the phase transition to higher temperatures in the thermal case, and also in the vacuum contributing case. The incorporation of the vacuum term at a given value of m_σ^{vac} leads to a smoother crossover, where the phase transition is located at a higher temperature. Neglecting the vacuum term at the lowest choice of m_σ^{vac} shows a curve where the phase transition is nearly first order, whereas a high vacuo mass m_σ^{vac} accompanied with the inclusion of the vacuum term leads to the smoothest behaviour and the highest transition temperature.*

We find that with increasing vacuo σ meson mass m_σ^{vac} the phase transition in the thermal case is shifted to higher temperatures and becomes slightly more crossover like, whereas smaller values of m_σ^{vac} lead to a behaviour close to first order phase transition, which is not achieved even for our lowest choice of $m_\sigma^{vac} = 500$ MeV. For this choice the phase transition takes place

at $T \sim 130$ MeV, whereas for $m_\sigma^{vac} = 700$ MeV at $T \sim 165$ MeV and for $m_\sigma^{vac} = 900$ MeV at $T \sim 205$ MeV, i.e. the larger the sigma meson mass m_σ^{vac} the higher are the chiral transition temperatures. The curves containing the vacuum contribution show the same behaviour, only the trends are noticeable more crossover like, and shifted to higher transition temperatures with increasing values of m_σ^{vac}. With vacuum contribution and the initial value of $m_\sigma^{vac} = 500$ MeV the phase transition takes place at $T \sim 163$ MeV, for $m_\sigma^{vac} = 700$ MeV at $T \sim 198$ MeV and for $m_\sigma^{vac} = 900$ MeV at $T \sim 233$ MeV. The thermal curve with $m_\sigma^{vac} = 700$ MeV intersects the vacuum contributing curve with $m_\sigma^{vac} = 500$ MeV at $T = 172$ MeV and $\sigma = 22$ MeV.
In summary a lower mass of the sigma meson mass and neglecting the vacuum term leads to a trend close to a first order phase transition at relatively low chiral transition temperatures, whereas a higher m_σ^{vac} and the inclusion of the vacuum term shifts the curves considerably to higher temperatures, i.e. a noticeable smoother behaviour with a higher chiral transition temperatures. Because of the explicit symmetry breaking term H, the thermal quarks without (th) and with (th+vac) vacuum term condensate does not vanish entirely in the restored phase at high temperature, it approaches $\sigma \sim 1$ MeV for all choices of m_σ^{vac}, which is however considerably quite close to the chiral limit. A first order phase transition can be achieved in the chiral limit for $H = 0$ [34, 36].

The behaviour of the order parameter within our parameter range can be translated to the behaviour of the masses as a function of the temperature, see fig. 4.16 for the sigma meson mass spectrum, and fig. 4.17 for the pion mass spectrum. A first order transition would cause the sigma meson mass to vanish at the phase transition point, i.e. at the respective minimum, which is clearly not the case in fig. 4.16, and furthermore cause the pion mass to jump at the transition from a lower mass to a larger one, which is also not the case in figure 4.17.

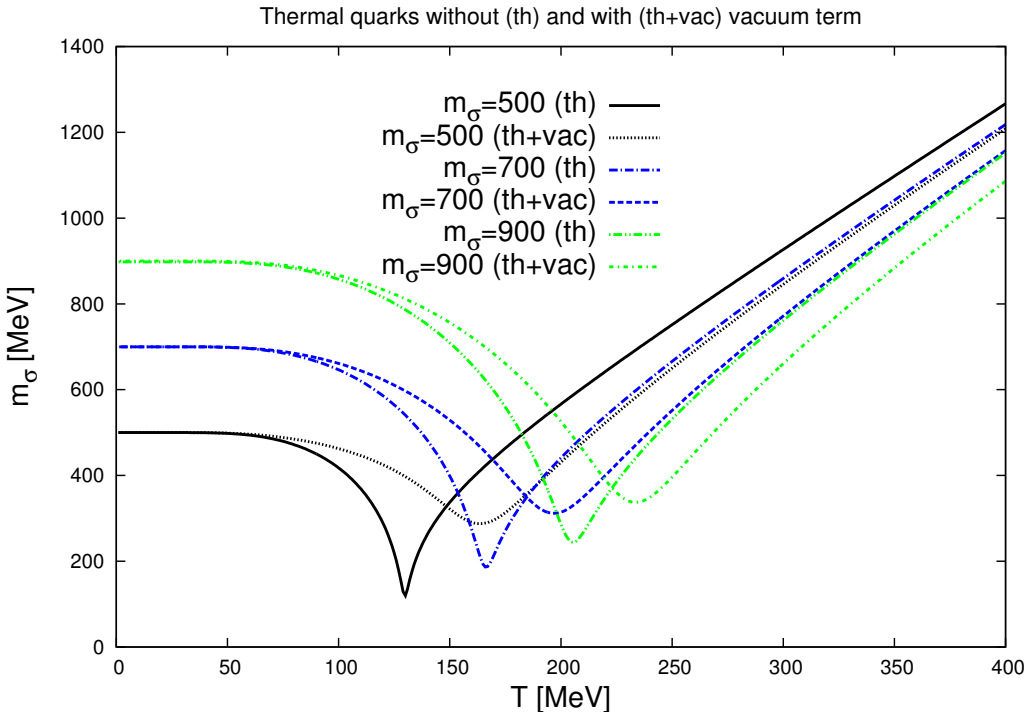

Figure 4.16: *The sigma meson mass m_σ as a function of temperature for zero chemical potential without (denoted as "th") and with vacuum contribution (denoted as "th+vac") for three different values of the vacuo sigma meson mass m_σ^{vac}. The larger the value of m_σ^{vac} the smoother is the behaviour of the thermal mass spectrum, which is shifted to higher temperatures. The thermal curves show a relatively pronounced minimum, which indicates the chiral phase transition point. Inclusion of the vacuum term leads to a less distinctive decrease of the sigma meson mass which is shifted to higher temperatures.*

For $m_\sigma^{vac} = 500$ MeV, when neglecting the vacuum term, both curves for the sigma and the pion mass come (within our chosen parameter range) as close as possible to the chiral limit. That is, the respective minimum in fig. 4.16 is the most spiky one at the lowest attainable mass, $T = 130$ MeV and $m_\sigma = 120$ MeV, and the pion mass nearly jumps vertically in fig. 4.17. Raising the initial value of the vacuum sigma meson mass causes the respective minima to be slightly less spiky and located at higher temperatures and higher sigma meson mass ($T = 165$ MeV, $m_\sigma = 185$ MeV for $m_\sigma^{vac} = 700$ MeV

and $T = 205$ MeV, $m_\sigma = 243$ MeV for $m_\sigma^{vac} = 900$ MeV). The inclusion of the vacuum contribution for all values of the initial vacuo mass m_σ^{vac} leads to a less distinctive decrease of the curve up to the minimum, going along with a clearly less spiky minimum, which is also located at higher temperatures and higher m_σ compared to the respective thermal value, i.e. when neglecting the vacuum term. The minimum values including the vacuum term for $m_\sigma^{vac} = 500$ MeV are $T = 163$ MeV, $m_\sigma = 287$ MeV, for $m_\sigma^{vac} = 700$ MeV the transition temperature is located at $T = 198$ MeV and the sigma meson mass $m_\sigma = 310$ MeV. For $m_\sigma^{vac} = 900$ MeV, $T = 233$ MeV and $m_\sigma = 336$ MeV. Like in the thermal case, the inclusion of the vacuum term causes the phase transition to be at higher temperatures, but also at a higher mass of the sigma meson in medium. For all the chosen initial vacuum masses m_σ^{vac} the minima shift in a similar manner in fig. 4.16.
Note, that all masses increase approximately linear at high temperatures. The initial vacuum mass of the sigma meson m_σ^{vac} is furthermore directly related to the parameters λ, m^2 and H, according to eqs. 4.114, 4.115 and 4.116 for the thermal case, and to eqs. 4.129 and 4.130 including the vacuum contribution [16]. These parameters are mainly responsible for the potentials depth (the case when investigating the potential as a function of the field σ ($\Omega_{\bar{q}q}(\sigma)$) at fixed temperature) and thereby for spontaneous symmetry breaking. The respective minimum of each curve in fig. 4.16 therefore represents the point of the chiral phase transition. From there on the mass of the sigma and the pion start to be degenerate. When the order parameter σ reaches approximately the chiral limit, the quarks become nearly massless and the mesons heavy.

The pion mass as a function of the temperature is shown in fig. 4.17. The curves behave in accordance with the one of the different fields (fig. 4.15) and with the one of the sigma meson mass (fig. 4.16). Increasing m_σ^{vac} in the thermal case causes the pion mass to increase at higher temperatures in combination with a softer rise of the mass around the respective transition

[16] Remember that $H_r = m_\pi^2 f_\pi = H$ and the discussion at the beginning of chapter 4.3 on the relation between λ and the mass term m.

temperature. The inclusion of the self energy causes a softer rise with temperature, so that the the highest chosen m_σ^{vac} including the self energy shows the softest increase of the pion mass spectrum, starting around the highest transition temperature. For the lowest chosen value of $m_\sigma^{vac} = 500$ MeV when neglecting the self energy the curve rises the steepest at the transition.

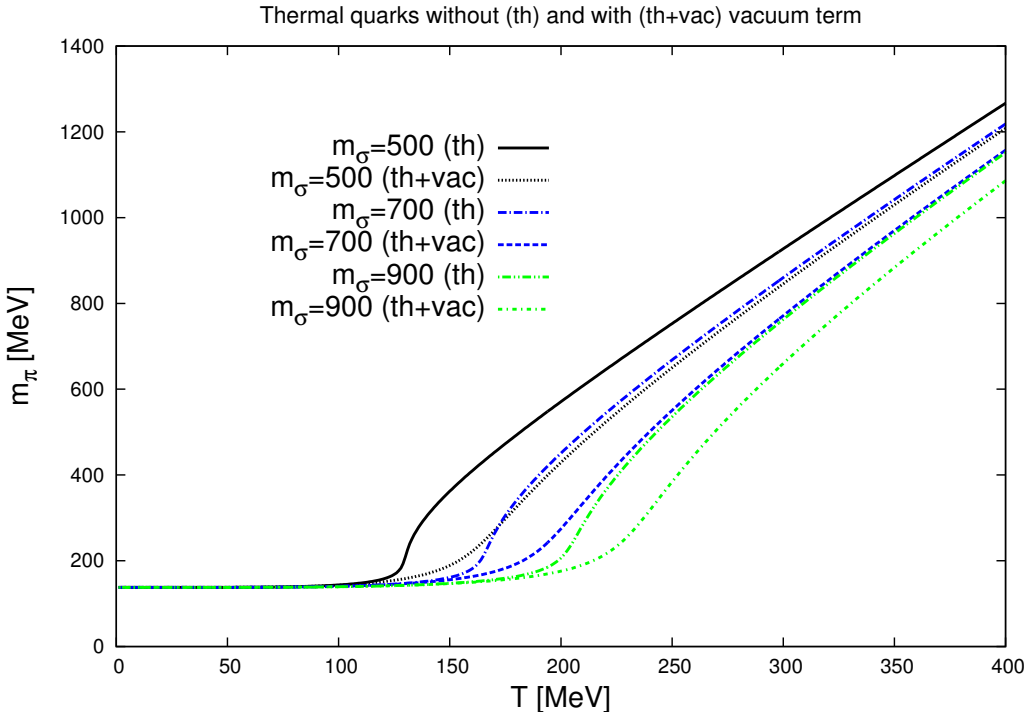

Figure 4.17: *The pion mass m_π as a function of temperature for zero chemical potential without (denoted as "th") and with vacuum contribution (denoted as "th+vac") for three different values of the initial vacuo sigma meson mass m_σ^{vac}. The curves start to deviate from the initial mass of the pion, $m_\pi =$ 138 MeV, becoming larger when the chiral phase transition sets in. These features are directly related to the behaviour of the corresponding fields in fig. 4.15 and furthermore with the respective minimum of the temperature dependent sigma meson mass shown in fig. 4.16.*

From the phase transition point on the mass of the pion becomes equal to the mass of the sigma. At $T = 400$ MeV sigma and pion masses of $\sim$1.2 GeV are achieved. The physical interpretation of this feature is that at high

temperatures the quarks behave more and more like a massless free Fermi gas generating highly massive mesons. The highest masses at $T = 400$ MeV are attained when considering a small initial sigma meson mass and neglecting the self energy, then $m_\sigma = m_\pi = 1.25$ GeV. The inclusion of the self energy and the highest chosen sigma meson mass in vacuo, $m_\sigma^{vac} = 900$ MeV, lead to $m_\sigma = m_\pi = 1.1$ GeV. For all initial vacuum sigma meson masses the inclusion of the vacuum contribution leads to degenerate masses of the sigma and the pion ~ 40 MeV smaller compared to the case when neglecting the vacuum contribution. The pions and the sigmas gain mass with temperature, and become degenerate due to the restoration of chiral symmetry. The conclusion is, that the lighter the initial mass of the sigma, the heavier it gets at high temperatures, which can be observed in figs. 4.16 and 4.17.

Figure 4.18 shows the pressure of the three different initial sigma meson masses including and neglecting the vacuum contributions. All curves rise monotonically, but in the temperature region 100 MeV$\leq T \leq$ 350 MeV the curves separate in a sense that the pressure becomes smaller with increasing value of the initial vacuum sigma meson mass. The inclusion of vacuum fluctuations intensifies this trend at given m_σ^{vac}, so that the pressure within this temperature range is smallest for high m_σ^{vac} and inclusion of the self energy. The higher the initial mass of the sigma, the less pronounced are the effects from the inclusion of the vacuum fluctuations. For high temperatures all curves approach the Stefan Boltzmann limit, i.e. eq. 4.7, where $\xi_f = 4N_cN_f$ (the factor four represents particle- and antiparticle contributions and the corresponding spin of the particle), quite close (up to 99.5%).

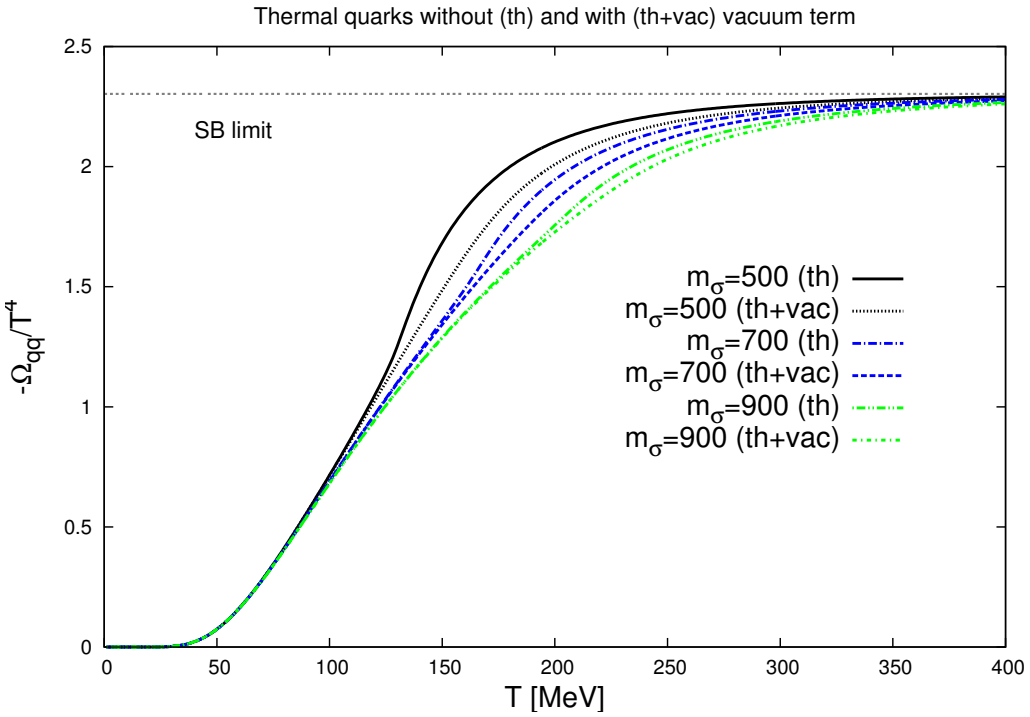

Figure 4.18: *The negative of the potential, i.e. the pressure, divided by* T^4 *as a function of temperature for zero chemical potential without (denoted as "th") and with vacuum contribution (denoted as "th+vac") for three different values of the initial vacuo sigma meson mass* m_σ^{vac}*. The curves are nearly equal to one another up to* $T \sim 100$ *MeV, where they split up to finally saturate at the Stefan Boltzmann limit, eq. 4.7.*

This feature implies, that in each considered case the quarks behave like a nearly massless free fermi gas at very high temperatures with all the considered degrees of freedom involved. For the smallest value of the initial vacuum sigma meson mass $m_\sigma^{vac} = 500$ MeV and neglecting the vacuum contribution, the quarks reach the limit at the lowest temperature, whereas the inclusion of the vacuum contribution at $m_\sigma^{vac} = 500$ MeV pushes down the curve within the temperature region 100 MeV$\leq T \leq$ 350 MeV. This statement is valid for all m_σ^{vac}, and can be understood as an intrinsic property of the self energy. The quarks struggle more to become massless, because the intrinsic self energy rises their own mass. This matches the statement

concerning the respective mass spectrum of the sigma and the pion at high temperature and can also be observed from the behaviour of the σ fields in fig. 4.15. There the inclusion of the self energy causes the field to reach the chiral limit somewhat later. Recalling that the effective mass of the quarks is generated through the coupling g and the fields, see eq. 4.109, in the potential, eq. 4.108, this conclusion is not surprising.

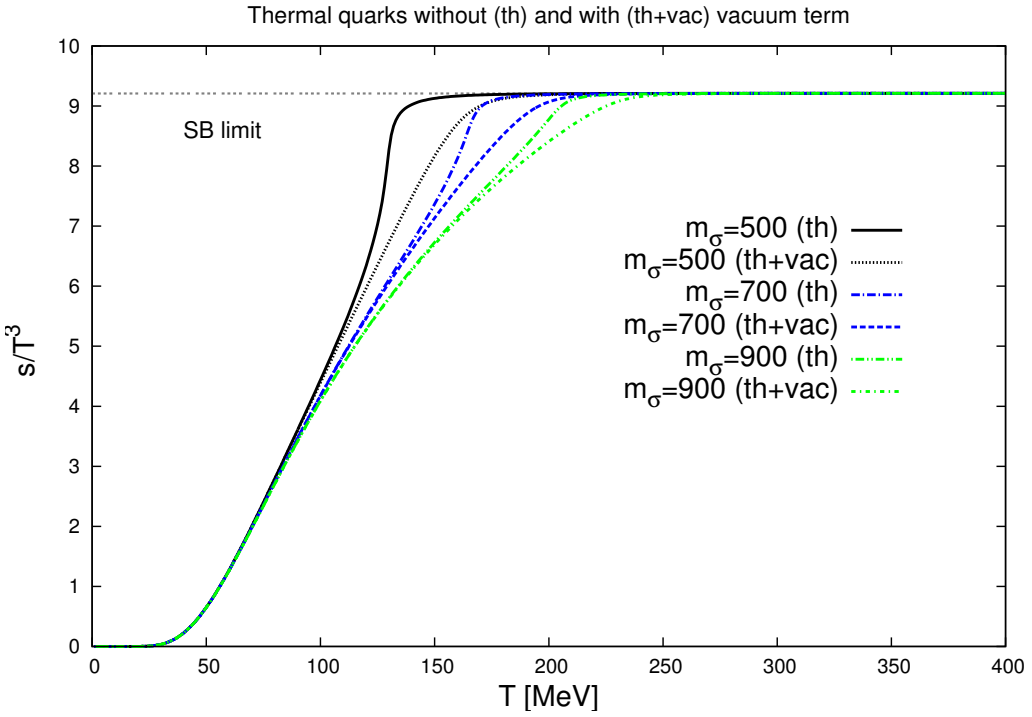

Figure 4.19: *The entropy density s divided by T^3 as a function of temperature for zero chemical potential without (denoted as "th") and with vacuum contribution (denoted as "th+vac") for three different values of the initial vacuo sigma meson mass m_σ^{vac}. The curves are nearly equal to one another up to $T \sim 100$ MeV where they split up to finally saturate at the Stefan Boltzmann limit.*

Figure 4.19 shows the entropy density divided by T^3 of the three different initial sigma meson masses m_σ^{vac} including and neglecting the vacuum contributions. The curves also rise monotonically as the pressure does, and as they should due to the Gibbs-Duhem relation, eq. 4.2. The entropy density

for small m_σ^{vac} and without the vacuum term has higher values at a given temperature compared to the cases with high initial vacuum mass m_σ and the inclusion of the self energy. This feature stems from the fact, that the disorder in the system gets larger, the more freely the quarks are. Remember, that the heavier the initial vacuum value m_σ^{vac}, the later the quarks reach the chiral limit, leading to heavier quarks at given temperature. The inclusion of the self energy term amplifies this effect, for low m_σ^{vac} more significantly than for large m_σ^{vac}. The approach to the Stefan-Boltzmann limit indicates the chiral phase transition, where the system acts with all considered massless degrees of freedom. From the chiral phase transition on, the ratio of the entropy remains approximately constant to T^3, the quarks cannot become lighter than (nearly) massless and the entropy can not increase any further, i.e. no other degrees of freedom than the considered ones can appear.

4.5. Combining interactions between Quarks and Mesons

Since the grand canonical potential is an intensive quantity, it is additive, and so are the respective gap equations of the corresponding previous sections, where we investigated mesonic interactions and quark-quark interactions. This section now combines both approaches to an unified set of equations. Here we will treat the thermal contributions only, whereas the following section includes the vacuum fluctuations of the quark sector. The potential is a sum of the independent potentials, i.e. eq. 4.33 and eq. 4.107 (including only once the tree level potential $U(\sigma, \vec{\pi})$).

$$\Omega_{QAM}^{th} = \Omega_{2PI}(\phi, G_{\sigma,\pi}) + \Omega_{\bar{q}q}^{th} \tag{4.136}$$

Here Ω_{QAM}^{th} is the thermal part of the combined grand canonical potential of quarks and mesons (QAM), where only thermal contributions the mesonic sector, i.e. eq. 4.48 and from the fermionic sector, eq. 4.108, are taken into

account.

The corresponding vacuum parameters are given by eqs. 4.114, 4.115 and 4.116, since the addition of any thermal part does not influence the vacuum parameters at $T = 0$.

As mentioned above, all relevant quantities are additive, and so are the vacuum contributions. Hence there is no need to regularize and renormalize anew[17]. Both equations for the divergent vacuum contributions, equation 4.102 and equation 4.120, can be merged into a single set of gap equations. The potential is the sum of the independent potentials, i.e. equation 4.33 (with both contributions: equations 4.48 and 4.102, i.e. the whole distribution function from the mesonic sector eq. 4.47 needs to be considered for $\Omega_{2PI}(\phi, G_{\sigma,\pi})$), 4.107 (including the tree level potential $U(\sigma, \vec{\pi})$) and 4.120.

$$\Omega_{qam} = \Omega^{th}_{\bar{q}q} + \Omega^{dr}_{\bar{q}q} + \Omega_{2PI}(\phi, G_{\sigma,\pi}) \tag{4.137}$$

Certainly the vacuum parameters λ, m^2 and H change. They are determined to be

$$\lambda = \frac{m_\sigma^2 + m_\pi^2 + \frac{N_c N_f}{8\pi^2} g^4 \sigma^2 \left[6 + 8 \ln\left(\frac{g\sigma}{\Lambda}\right)\right]}{2\left(F_{dr}(\bar{m}_\sigma) - F_{dr}(\bar{m}_\pi) + \sigma^2\right)} \tag{4.138}$$

$$\begin{aligned} m^2 &= \frac{N_c N_f}{8\pi^2} g^4 \sigma^2 \left[7 + 12 \ln\left(\frac{g\sigma}{\Lambda}\right)\right] \\ &- 3\lambda \left(F_{dr}(\bar{m}_\sigma) + F_{dr}(\bar{m}_\pi)\right) + m_\sigma^2 - 3\lambda\sigma^2 \end{aligned} \tag{4.139}$$

$$\begin{aligned} H &= -\frac{N_c N_f}{8\pi^2} g^4 \sigma^3 \left[1 + 4 \ln\left(\frac{g\sigma}{\Lambda}\right)\right] \\ &+ 3\lambda\sigma \left(F_{dr}(\bar{m}_\sigma) + F_{dr}(\bar{m}_\pi)\right) + \sigma(m^2 + \lambda\sigma^2) \end{aligned} \tag{4.140}$$

[17] Remember the discussion on additivity in section 4.2

and the corresponding gap equations read

$$\begin{aligned}
\frac{\partial\Omega_{QAM}}{\partial\sigma} &= -\frac{N_c N_f}{8\pi^2} g^4\sigma^3\left[1+4\ln\left(\frac{g\sigma}{\Lambda}\right)\right] \qquad (4.141)\\
&+ 3\lambda\sigma\left(F(\bar{m}_\sigma)+F(\bar{m}_\pi)\right)+m^2\sigma+\lambda\sigma^3 = H\\
\frac{\partial^2\Omega_{QAM}}{\partial\sigma^2} &= -\frac{N_c N_f}{8\pi^2} g^4\sigma^2\left[7+12\ln\left(\frac{g\sigma}{\Lambda}\right)\right] \qquad (4.142)\\
&+ 3\lambda\left(F(\bar{m}_\sigma)+F(\bar{m}_\pi)\right)+m^2+3\lambda\sigma^2 = m_\sigma^2\\
\frac{\partial^2\Omega_{QAM}}{\partial\pi^2} &= -\frac{N_c N_f}{8\pi^2} g^4\sigma^2\left[1+4\ln\left(\frac{g\sigma}{\Lambda}\right)\right] \qquad (4.143)\\
&+ \lambda\left(F(\bar{m}_\sigma)+F(\bar{m}_\pi)\right)+m^2+\lambda\sigma^2 = m_\pi^2
\end{aligned}$$

Unfortunately these equations leave us with the possibility of having two renormalization scales, one from the quark-quark contribution, Λ, and one hidden in $F(\bar{m}_{\sigma\pi})$, namely μ (see eq. 4.102).
Recall that the chemical potential μ is zero and has so far nothing to do with the renormalization scale μ.

4.5.1. Results in the combined sector 1: Quark vacuum energy

At first we neglect the vacuum contribution from both sectors, which is denoted as (usual) "therm" to eventually include the vacuum contributions from the quark sector only, having the main impact. That is, set $F_{dr}(\bar{m}_{\sigma,\vec{\pi}}) = 0$. Excluding the mesonic vacuum contribution, the dependence on the renormalization scale Λ does not vanish due to the contribution from Ω_{2PI}. We choose a value of $\Lambda = 1033$ MeV due to reasons which will become apparently clear during the next section 4.5.2, where we discuss the dependence on both renormalization scales.

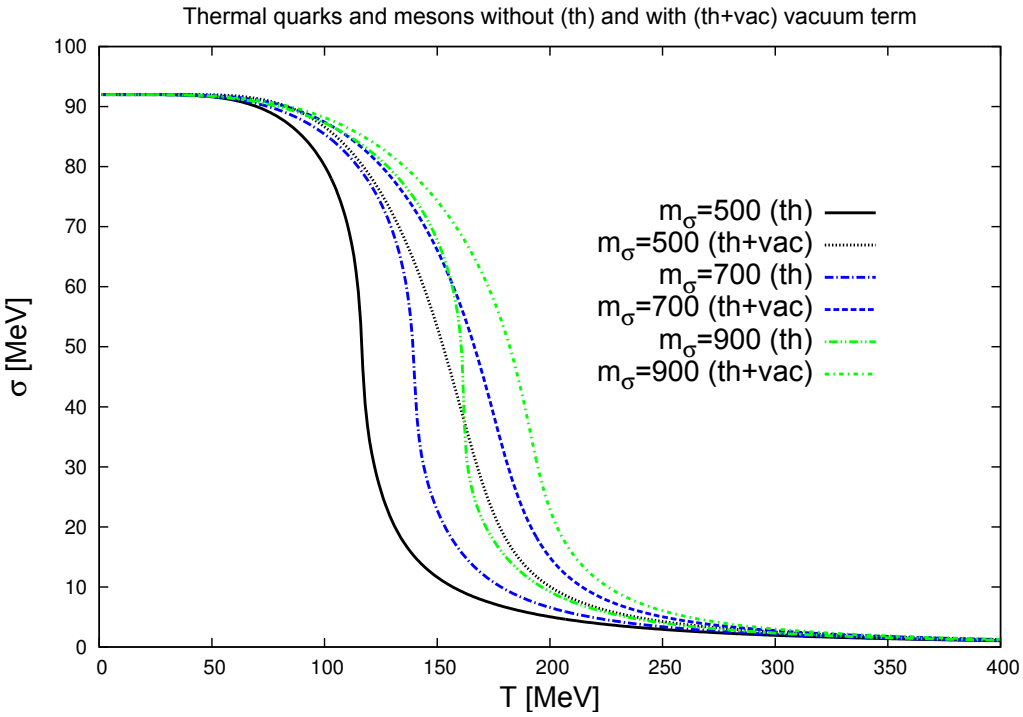

Figure 4.20: *The σ condensate in the combined approach as a function of temperature for zero chemical potential without (denoted as "th") and with quark vacuum contribution (denoted as "th+vac") for three different values of the initial vacuo sigma meson mass m_σ^{vac}. The value of the renormalization scale has been chosen to be $\Lambda = 1033$ MeV. The larger the value of m_σ^{vac} the more the phase transition is shifted to larger temperatures. The vacuum contribution leads to the same behaviour as when raising m_σ^{vac}. All curves are shifted to larger temperature in a similar manner. A high vacuo mass m_σ accompanied with the inclusion of the self energy leads to the highest transition temperature. The thermal curve with $m_\sigma^{vac} = 900$ MeV intersects the vacuum contributing curve with $m_\sigma^{vac} = 500$ MeV at $T = 160$ MeV and $\sigma = 38$ MeV.*

Figure 4.20 shows the order parameter σ as a function of the temperature within the combined approach for the choice of the renormalization scale $\Lambda = 1033$ MeV. The larger the value of m_σ the farther is the curve shifted to higher temperatures. The vacuum contribution leads to the same trend as

when raising the initial value of m_σ^{vac}, so that a high vacuo mass m_σ^{vac} accompanied with the inclusion of the self energy leads to the highest transition temperature. Interesting to note is that all curves are shifted in a similar manner very much alike as in the quark case, see fig. 4.15. The main difference to the quark sector is, that all trends are slightly shifted to the left, i.e. to a smaller transition temperature. This feature is accompanied with a slightly steeper decrease indicating a first order phase transition, which still is not achieved. This can be traced back to the influence of Ω_{2PI} from the mesonic sector. The thermal curve with $m_\sigma^{vac} = 900$ MeV intersects the vacuum contributing curve with $m_\sigma^{vac} = 500$ MeV at $T = 160$ MeV and $\sigma = 38$ MeV. However, neither the thermal nor the vacuum contributing curves show an intersection of the thermal curves from the mesonic sector, see fig. 4.6, which too is an indication that the quarks adopt the dominant role in the combined approach. Comparing the individual features for initial sigma meson mass for quarks, mesons and within the combined approach, the order parameter has been shifted to smaller temperatures and seems to converge towards a first order phase transition, which can be traced back to the influence of the mesonic contribution. Certainly the quarks have a large influence, not only because the curves look much like the ones from fig. 4.15 but also because quarks can gain a large amount of energy through the temperature and can therefore sooner reach the chiral phase transition.

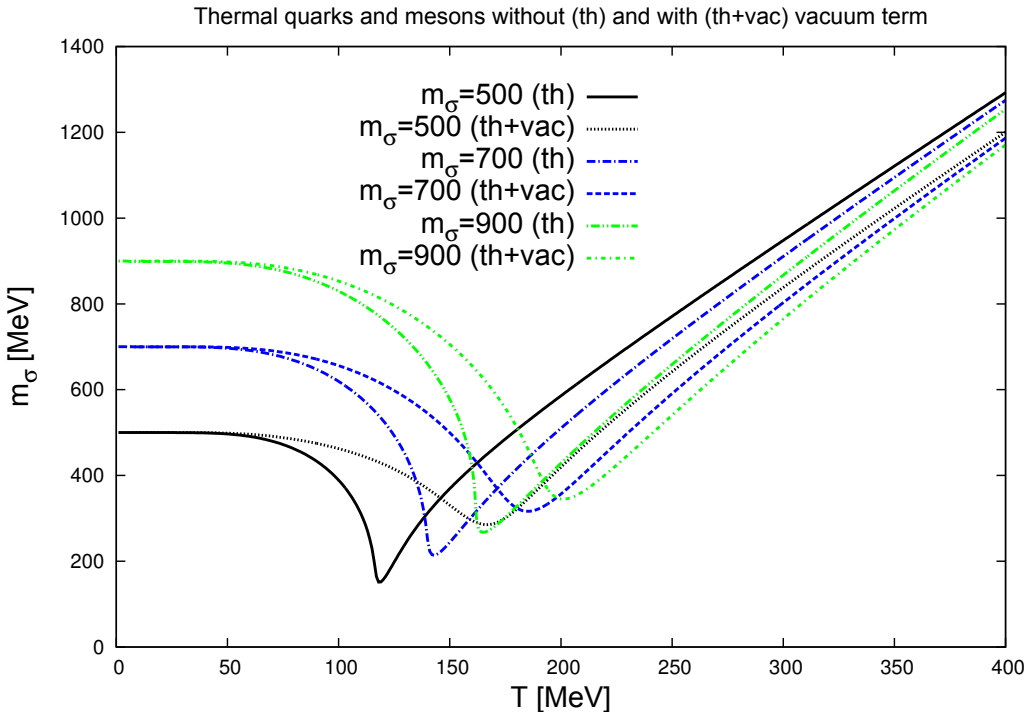

Figure 4.21: *The sigma meson mass m_σ in the combined approach as a function of temperature for zero chemical potential without (denoted as "th") and with quark vacuum contribution (denoted as "th+vac") for three different values of the initial vacuo sigma meson mass m_σ^{vac}. The value of the renormalization scale has been chosen to be $\Lambda = 1033$ MeV. The curves are similar to the curves obtained for the quark case in fig. 4.16, which indicates the dominance of the quark contribution over the mesonic case.*

The sigma meson mass as function of the temperature is plotted in fig. 4.21. The curves are quite similar to the curves obtained for the quark case in fig. 4.16 and the minima are closer to the values from the quark sector then from the mesonic sector, see table 4.1. For $m_\sigma^{vac} = 500$ MeV the values (and the whole curve) are quite similar, but increasing the mass of the initial vacuum mass m_σ^{vac} drives the minima slightly apart, indicating that the meson contribution gains influence.

Table 4.1 shows the minimal value of the sigma meson mass in medium for thermal quarks, thermal mesons and for the combined approach. With or

m_σ^{vac}	TM, section 4.3		TQ, section 4.4		TQM, section 4.5	
	T	m_σ	T	m_σ	T	m_σ
$500_{(th)}$	230	290	130	120	118	150
$500_{(th+vac)}$	260	320	163	187	166	285
$700_{(th)}$	238	324	165	185	143	214
$500_{(th+vac)}$	305	414	198	310	185	316
$900_{(th)}$	245	355	205	243	165	267
$500_{(th+vac)}$	360	510	233	336	201	344

Table 4.1: *The minimal mass for the σ-meson for all three different approaches, i.e. thermal mesons (TM) with and without vacuum term (section 4.3), thermal quarks (TQ) with and without vacuum term (section 4.4) and and thermal quarks and mesons combined (TQM) (section 4.5). All values are given in MeV.*

without the vacuum term the minima of the combined approach are closer to the values of the thermal quarks then to the values for thermal mesons. The impact of the thermal mesons shifts the minima of the combined approach to lower temperatures at similar in medium masses, that is a crossover phase transition at lower temperatures. This feature can also be observed when investigating the order parameter for fixed m_σ^{vac} as a function of the temperature for the three different approaches separately.

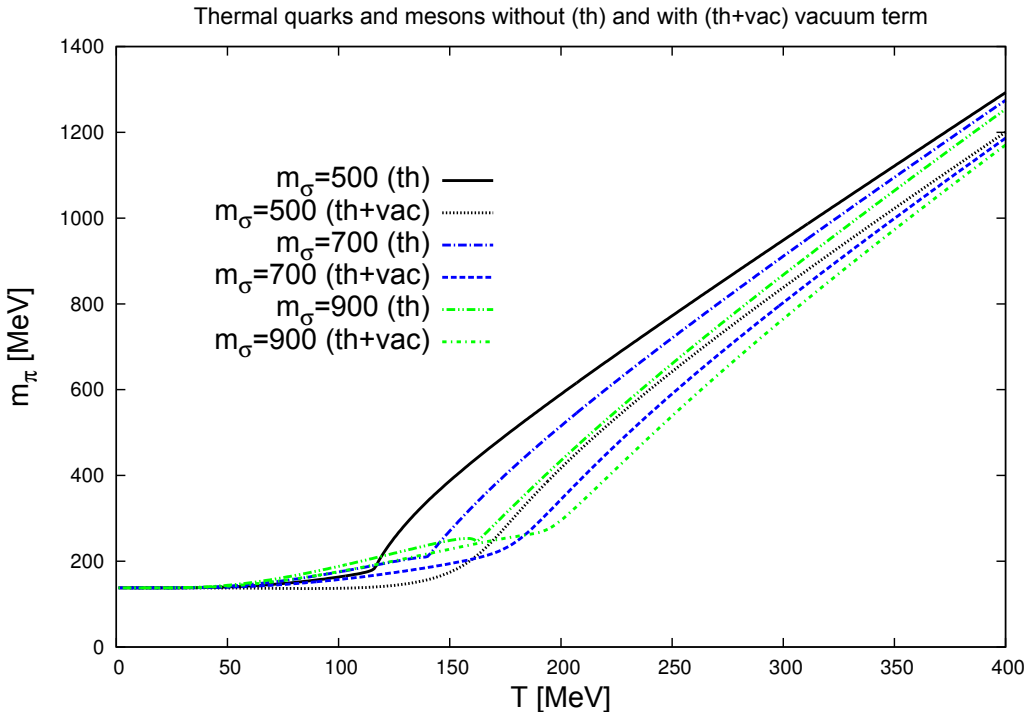

Figure 4.22: *The pion mass m_π in the combined approach as a function of temperature for zero chemical potential without (denoted as "therm.") and with quark vacuum contribution (denoted as "vac.") for three different values of the initial vacuo sigma meson mass m_σ^{vac}. The value of the renormalization scale has been chosen to be $\Lambda = 1033$ MeV. The curves are similar to the curves obtained for the quark case in fig. 4.17, which indicates the dominance of the quarks within the combined approach.*

The behaviour of the pion mass within the combined approach can be seen in fig. 4.22. The curves seem to be a combination of the pion mass spectrum from the quark sector fig. 4.17 and the one from the mesonic sector fig. 4.8, while the quark contribution dominants. For larger chosen initial value of m_σ^{vac} the pion mass starts to increase at lower tempertature, as has been already seen in the mesonic sector. This underlines the statement that for larger sigma meson mass the 2PI formalism gains influence within the combined approach. The explicit symmetry breaking term H in eq. 4.140, which is mainly responsible for the in-medium mass of the pion in combi-

nation with the other two parameters eqs. 4.138 and 4.139 provides a larger in-medium mass of the pion when the value of m_σ^{vac} is rather high. However, both masses, figs. 4.21 and 4.22, reach ∼1.2 GeV at $T = 400$ MeV as is the case in the quark sector.

The pressure of the combined system divided by T^4 provided by the SU(2) Quark Meson model and the CJT formalism is shown in fig. 4.23.

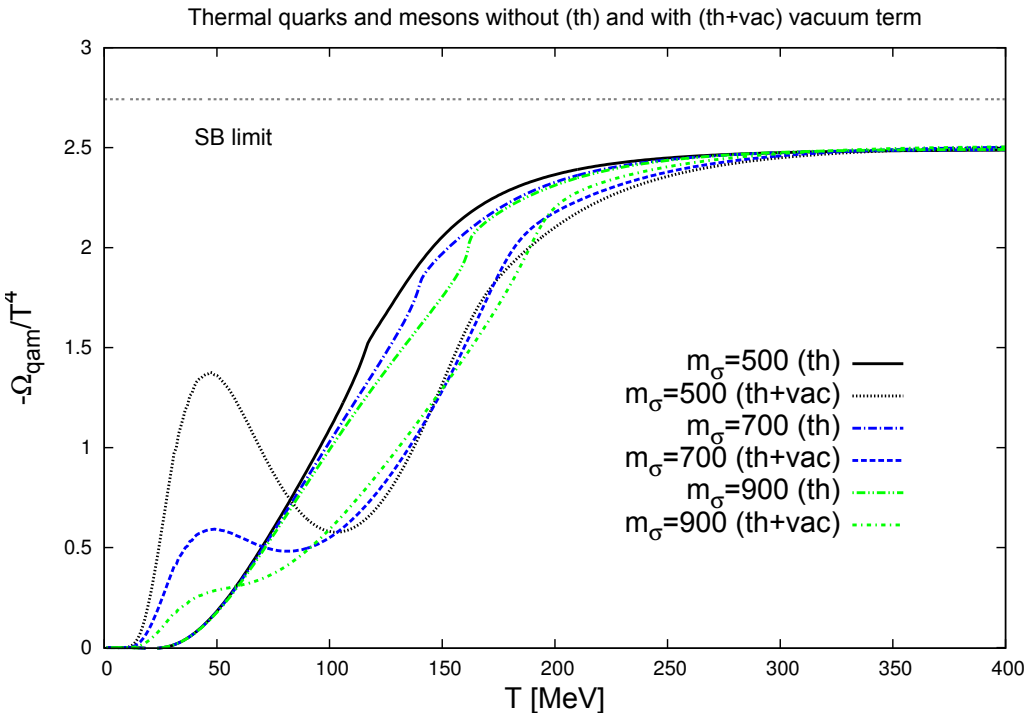

Figure 4.23: *The negative of the potential, i.e. the pressure, divided by T^4 as a function of temperature without (denoted as "therm.") and with vacuum contribution (denoted as "vac.") for three different values of the initial vacuo sigma meson mass m_σ^{vac}. The curves show clearly maxima and minima. The SB limit is given by combining the equations 4.7 and 4.8.*

All cases without the vacuum term start to rise significantly at $T \simeq 30$ MeV, whereas the inclusion of the vacuum term causes the pressure to rise at already $T \simeq 20$ MeV. This behaviour has also been observed in the mesonic case, see fig. 4.9. Neglecting the vacuum contribution, the curves exhibit

a nontrivial behaviour within the temperature range $100 \leq T \leq 180$ MeV. The extrema seen in fig. 4.23 will be important for the discussion of the corresponding entropy density divided by T^3 below. The curves show distinct extrema, less pronounced with larger m_σ^{vac}, located around $T \simeq 45$ MeV. This clearly is correlated to the behaviour of the mesons, where the inclusion of the vacuum term leads to a higher pressure at given temperature compared to the case without the vacuum term, see fig. 4.9. In the combined approach this leads to distinct extrema, indicating the dominance of the meson contribution to the low energy regime. It is important to note that these extrema are not instabilities, since the pressure itself is a monotonically rising function, and so is the entropy density. The curves in fig. 4.23 reflect the behaviour of the relativistic degrees of freedom at given temperature. For quarks eq. 4.7 is valid and approached at high temperature. For the mesons within the 2PI approach the high temperature limit, eq. 4.8, is not reached. In the combined approach a limit is reached for all parameter choices, but it is not the sum relativistic degrees of freedom, eqs. 4.7 and 4.8. It deviates about $\sim 10\%$ from this Stefan Boltzmann limit, which seems to be a result from the mesonic contribution.

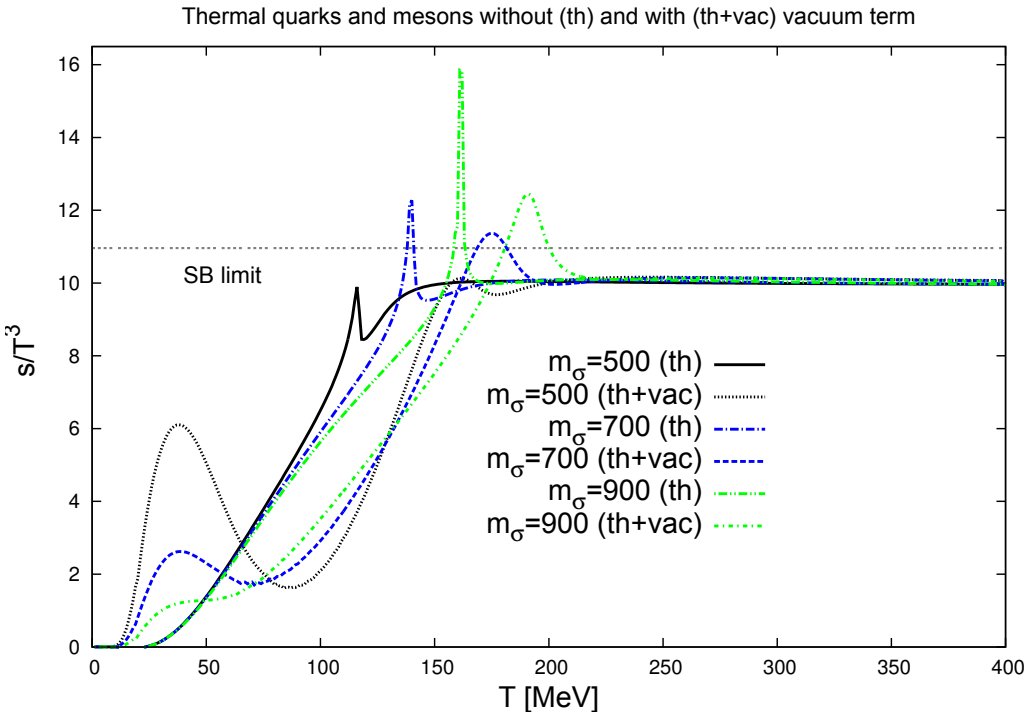

Figure 4.24: *The entropy density s divided by T^3 as a function of temperature without (denoted as "therm.") and with vacuum contribution (denoted as "vac.") for three different values of the initial vacuo sigma meson mass m_σ^{vac}. The curves show accentuated maxima at low temperature and spikes at higher temperatures.*

The entropy density divided by T^3 as a function of the temperature is shown in fig. 4.24. The curves without vacuum term rise approximately linear at low temperature. For $m_\sigma^{vac} = 500$ MeV a maximum at $T = 116$ MeV and $s/T^3 = 9.85$ can be observed, which can be traced back to the hardly visible change of slope in the pressure to T^4 ratio in fig. 4.23. The higher the vacuum sigma meson mass, the more pronounced are these slope changes, resulting in more pronounced maxima in the entropy to T^3 ratio. This occurs in all cases considered at the phase transition. These peaks arise from the fact that the pressure has a considerably change of slope at the chiral phase transition temperature, see fig. 4.23. At this point it is important to state, that the entropy density is a monotonically rising function, even if not expected when

looking at fig. 4.24. However, taking into account the vacuum contribution, the same discussion holds, only that the maxima from the pressure to T^4 curves appear in the low temperature region. The clearly visible maxima at the phase transition temperature are less spiky now as the respective increase around the phase transition temperature in the pressure to T^4 ratio. A possible explanation of having two maxima might be that the change of relativistic degrees of freedom occurs in two different temperature regions. This could go along with the increase of the pion mass at higher temperature, see fig. 4.22. Recall that the strange behaviour of the pion mass spectrum in the mesonic case, fig. 4.8, caused a similar behaviour of the respective entropy to T^3 ratio in fig. 4.10 going along with clearly visible maxima. One can interpret these pronounced peaks as an intermediate sudden increase in relativistic degrees of freedom or as an field energy contribution. Note that an entropy jump for a first order phase transition is not observed.

4.5.2. Results in the combined sector 2: Dependence on the renormalization scale

In the last section we set $F_{dr}(\bar{m}_{\sigma,\vec{\pi}}) = 0$, omitting the self energy resulting from the 2PI formalism for the mesonic sector. In this section we show that the contribution is negligible for the fields and the mass spectra, but not for the relativistic degrees of freedom. We explore the impact of having two renormalization scales, one from the quark sector Λ and one from the mesonic sector μ.

First we run the code with one value for the renormalization scale, i.e. setting $\Lambda = \mu$ and in a second approach we keep μ fixed at the value used in [43], that is $\mu = m_\sigma/\sqrt{e}$ to study what happens when the quark self energy changes. We first study the three vacuum parameters λ (eq. 4.138), m^2 (eq. 4.139) and H (eq. 4.140) as a function of the renormalization scale for $\Lambda = \mu$ and for the choice $\mu = m_\sigma/\sqrt{e}$, such as to locate the most reasonable renormalization scale value, which turns out to be the one used in the previous section,

$\Lambda = 1033$ MeV. The value of the sigma meson mass has been chosen to be $m_\sigma = 550$ MeV.

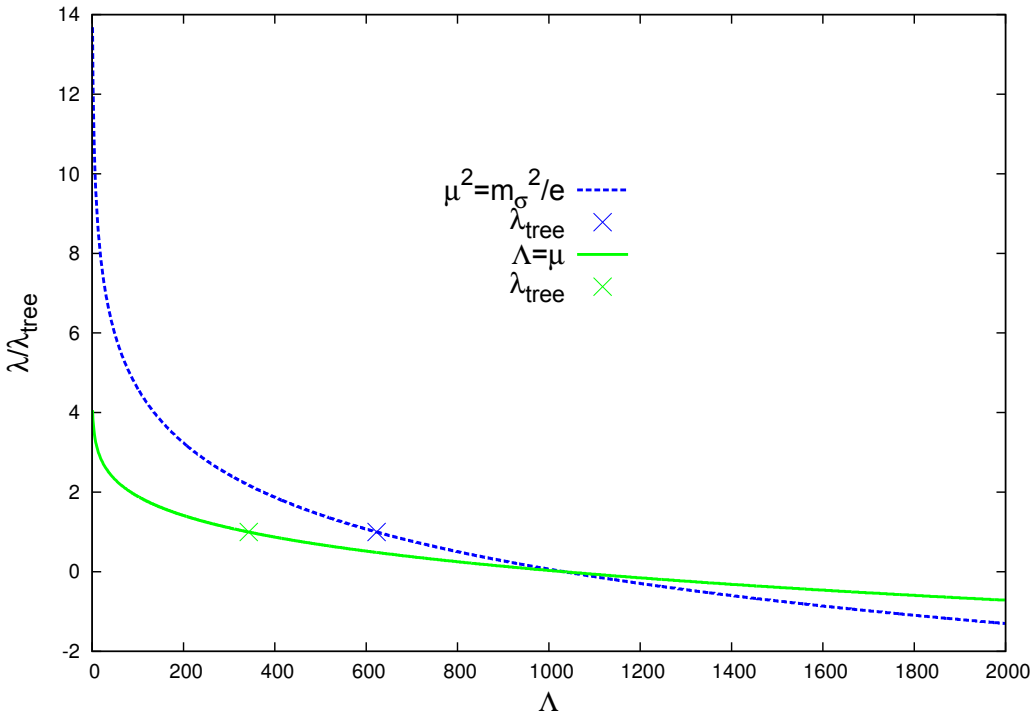

Figure 4.25: *The coupling constant λ normalized to its tree level value ($\lambda \simeq 16.64$ according to eq. 4.114) as a function of the renormalization scale parameter Λ with $\Lambda = \mu$ (continuous curve) and with $\mu = m_\sigma/\sqrt{e}$ held fixed (dotted curve). The curves intersect at $\Lambda = 1033$ MeV. The crosses mark the respective tree level value of λ.*

The renormalization scale parameter is naturally placed at the chiral scale [34, 38, 36], i.e. is of the order 1 GeV. Setting $\Lambda = \mu$ or even $\mu = m_\sigma/\sqrt{e}$ we find reasonable solutions only within the range $850 \leq \Lambda \leq 1150$ MeV, which we investigate during this section. We first calculate the vacuum parameters as a function of the renormalization scale. Fig. 4.25 shows the normalized coupling λ/λ_{tree} as a function of the renormalization scale with $\Lambda = \mu$ (continuous curve) and with $\mu = m_\sigma/\sqrt{e}$ held fixed (dotted curve). Both curves are monotonically decreasing with Λ. The tree level value for the choice $\Lambda = \mu$ is found to be located at $\Lambda = 343$ MeV, which is surprisingly close

to $\mu = m_\sigma/\sqrt{e}$ MeV. However, for the choice $\mu = m_\sigma/\sqrt{e}$ MeV the tree level value is located at $\Lambda = 623$ MeV. Note that the two curves intersect at $\Lambda = 1033$ MeV.

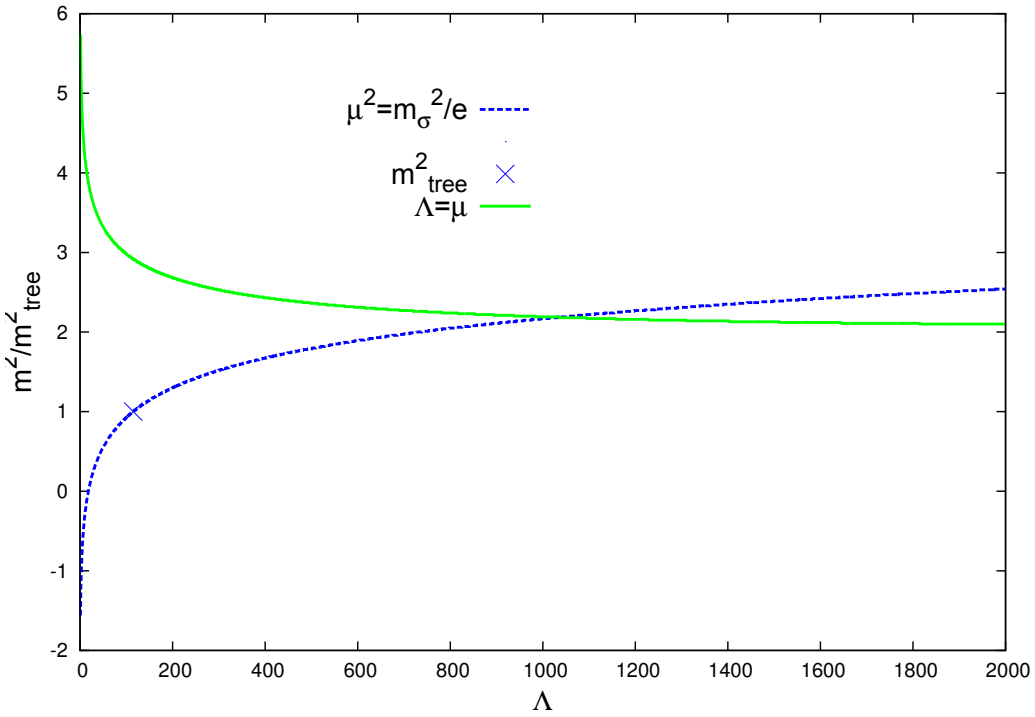

Figure 4.26: *The mass parameter m^2 normalized to its tree level value ($m^2 = -122683\text{MeV}^2$ according to eq. 4.115) as a function of the renormalization scale parameter Λ with $\Lambda = \mu$ (continuous curve) and with $\mu = m_\sigma/\sqrt{e}$ held fixed (dotted curve). The curves intersect at $\Lambda = 1033$ MeV. The cross marks the tree level value. For the case $\Lambda = \mu$ the tree level value is not reached.*

The normalized mass parameter $m^2 = -\lambda v^2$ as a function of the renormalization scale Λ is shown in fig. 4.26. Setting $\Lambda = \mu$ the curve is decreasing with Λ, but does never reach the tree level value. Setting $\mu = m_\sigma/\sqrt{e}$ MeV the curve surprisingly increases with Λ, and the tree level value is located at $\Lambda = 115$ MeV. These two cases also intersect at $\Lambda = 1033$ MeV.

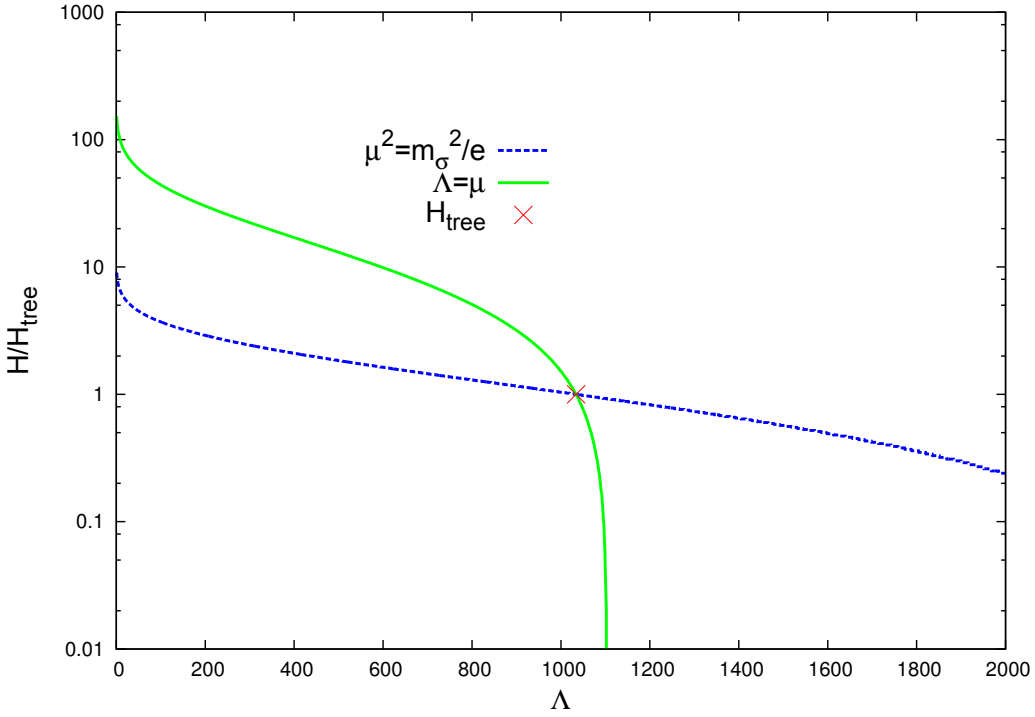

Figure 4.27: *The explicit symmetry breaking term H normalized to its tree level value ($H = 1.75 \cdot 10^6 \mathrm{MeV}^3$ according to eq. 4.116) as a function of the renormalization scale parameter Λ with $\Lambda = \mu$ (continuous curve) and with $\mu = m_\sigma/\sqrt{e}$ held fixed (dotted curve). The curves intersect at $\Lambda = 1033$ MeV. The cross marks the tree level value of $H = m_\pi^2 f_\pi$.*

The explicit symmetry breaking term, which is responsible for the mass of the pion, is shown normalized to its tree level value in fig. 4.27. The y axis is plotted in a logarithmic scale. Both cases show a decrease with Λ. The case for $\Lambda = \mu$ even becomes negative (which is not shown here), which would imply that the VEV of the sigma meson would be a negative quantity too. We relate this feature to the strange behaviour of not finding any tree level value for m^2 in fig. 4.26, and as an indication, that the choice for $\Lambda = \mu$ is not that physically reasonable. The curve for the choice $\mu = m_\sigma/\sqrt{e}$ decreases slowly with Λ. At $\Lambda = 2000$ MeV the value is at $\mathrm{H/H_{tree}} = 0.3$. The tree level value is again located at $\Lambda = 1033$ MeV.

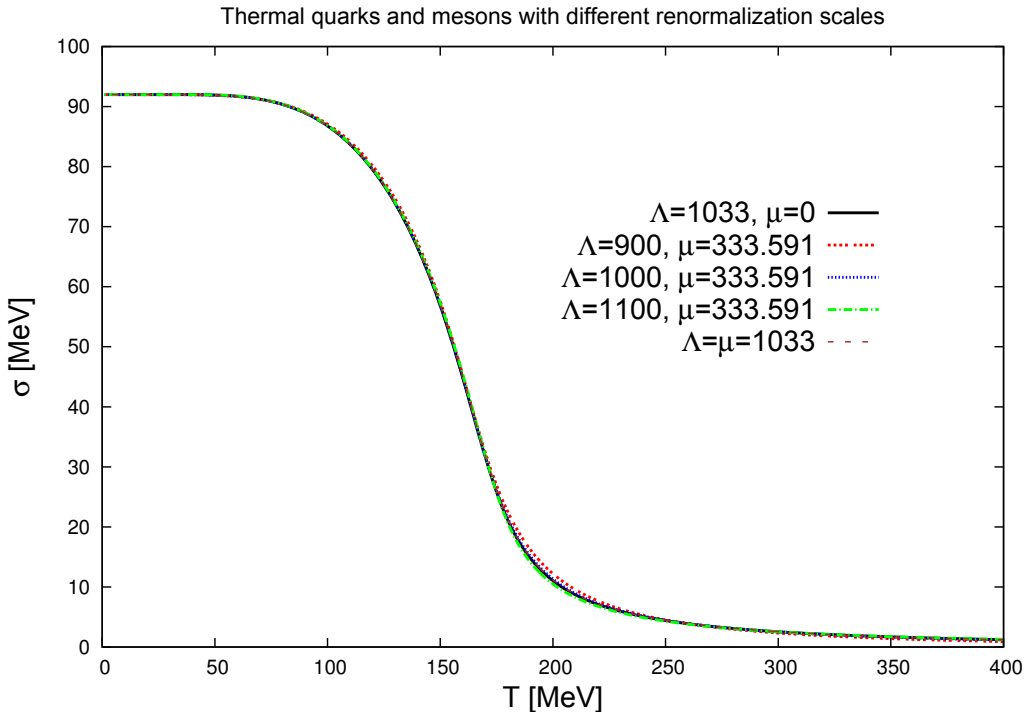

Figure 4.28: *The σ condensate as a function of temperature for the renormalization scales $\Lambda = 900, 1000, 1100$ MeV at $\mu = m_\sigma/\sqrt{e}$ held fixed and for $\Lambda = \mu = 1033$ MeV at $m_\sigma = 550$ MeV. For comparison the σ field for one fixed renormalization scale is also shown.*

The σ field for different renormalization scales is shown in fig. 4.28. For comparison the σ field for one renormalization scale with $\Lambda = 1033$ MeV and $\mu = 0$ for $m_\sigma^{vac} = 550$ MeV is also shown. The respective value of Λ has been chosen to be $\Lambda = \mu = 1033$ MeV. For the choice for μ according to [43] we choose three values of Λ. There is no notable difference in the σ field. All cases show a crossover phase transition at $T \simeq 165$ MeV. It is worth mentioning that the curves are very similar to the curves from the quark sector shown in section 4.4, demonstrating again the dominance of the quark contribution.

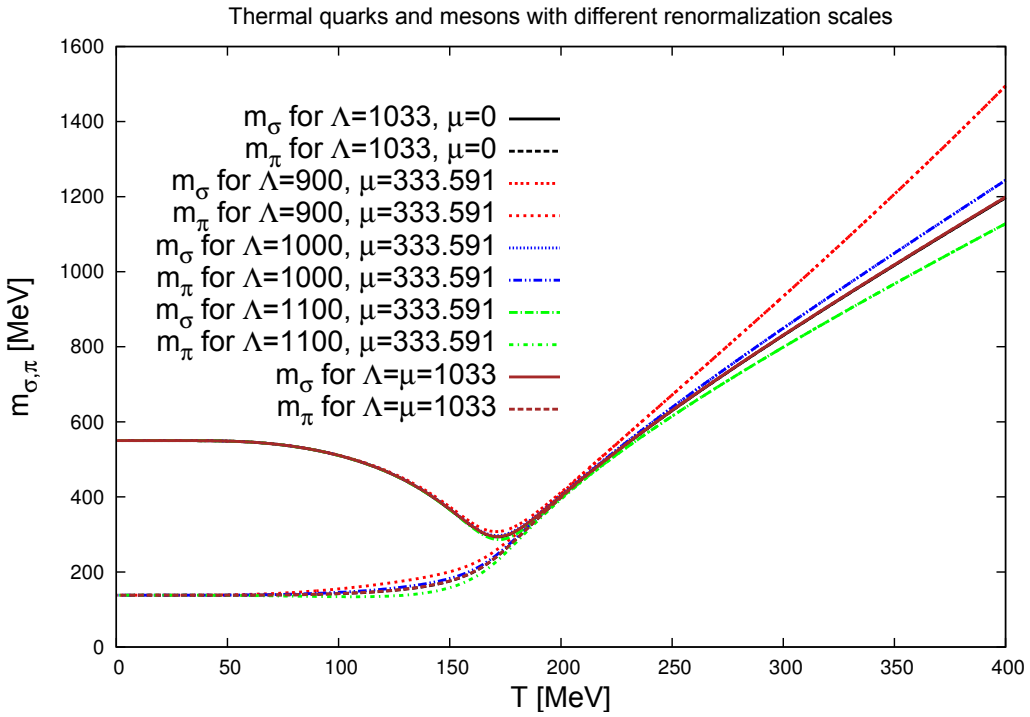

Figure 4.29: *The sigma and the pion mass spectrum as a function of temperature for the renormalization scale choices* $\Lambda = 900, 1000, 1100$ *MeV at* $\mu = m_\sigma/\sqrt{e}$ *held fixed and for* $\Lambda = \mu = 1033$ *MeV at* $m_\sigma = 550$ *MeV. For comparison the case for one fixed renormalization scale is also shown. The different curves do not show significant differences up to* $T = 250$ *MeV, where the degenerate masses of the sigma and the pion have different slopes resulting in different thermal masses at* $T = 400$ *MeV.*

The sigma and the pion mass spectrum as a function of temperature for the renormalization scale choices $\Lambda = 900, 1000, 1100$ MeV and $\mu = m_\sigma/\sqrt{e}$ held fixed, and for $\Lambda = \mu = 1033$ MeV both at $m_\sigma = 550$ MeV can be seen in fig. 4.29. For comparison m_σ and m_π for one fixed renormalization scale are also shown, i.e. for the choice $\Lambda = 1033$ MeV and $\mu = 0$. The different cases do however not show significant differences up to $T = 250$ MeV, where the degenerate masses of the sigma and the pion start having different slopes resulting in different masses at $T = 400$ MeV. For $\Lambda = 900$ MeV and $\mu = m_\sigma/\sqrt{e}$ a mass of 1.5 GeV is reached. For $\Lambda = 1000$ MeV and

Interaction type	m_σ^{vac}	Λ	μ	λ	m^2	H
Q_{th}	500	-	-	16.744	-122683	$1.75 \cdot 10^6$
Q_{th+vac}	500	-	-	42.521	-268130	$1.75 \cdot 10^6$
M_{th}	500	-	-	16.744	-122683	$1.75 \cdot 10^6$
M_{th+vac}	500	-	333.591	16.11	-90449	$2.74 \cdot 10^6$
$Q_{th} + M_{th}$	500	-	-	16.744	-122683	$1.75 \cdot 10^6$
$Q_{th+vac} + M_{th}$	550	1033	-	0.0268	-268130	$1.75 \cdot 10^6$
$Q_{th+vac} + M_{th+vac} : \Lambda = \mu$	550	1033	1033	0.013	-268148	$1.77 \cdot 10^6$
$Q_{th+vac} + M_{th+vac} : \Lambda \neq \mu$	550	900	333.591	4.583	-258959	$2.03 \cdot 10^6$
$Q_{th+vac} + M_{th+vac} : \Lambda \neq \mu$	550	1000	333.591	1.099	-265930	$1.82 \cdot 10^6$
$Q_{th+vac} + M_{th+vac} : \Lambda \neq \mu$	550	1100	333.591	-2.052	-272236	$1.62 \cdot 10^6$

Table 4.2: *The parameters λ, m^2 and H for all considered interaction cases. Thermal quarks are labeled Q_{th}, including the vacuum term in the quark sector is labeled Q_{th+vac}. The thermal mesons without vacuum term are labeled M_{th} and with vacuum term M_{th+vac}. The thermal approach combining quarks and mesons without vacuum term is labeled $Q_{th} + M_{th}$. For these cases the sigma meson mass is $m_\sigma^{vac} = 500$ MeV. The combination of both sectors with vacuum term only in the quark sector is labeled $Q_{th+vac} + M_{th}$, and with vacuum term in both sectors $Q_{th+vac} + M_{th+vac}$. Here $m_\sigma^{vac} = 550$ MeV for the different choices of the renormalization scale.*

$\mu = m_\sigma/\sqrt{e}$, $\Lambda = 1033$ MeV and $\mu = 0$ and for $\Lambda = \mu = 1033$ MeV the masses are around 1.2 GeV. The highest value of $\Lambda = 1100$ MeV at fixed μ results in a mass of ~ 1.1 GeV.

The pressure divided by T^4 as a function of of temperature for the renormalization scale choices $\Lambda = 900, 1000, 1100$ MeV at $\mu = m_\sigma/\sqrt{e}$ held fixed and for $\Lambda = \mu = 1033$ MeV at $m_\sigma = 550$ MeV are represented in fig. 4.30. All curves show the same kind of extrema at relatively low temperature, especially the maximum at $T = 50$ MeV, which are not shifted in temperature when changing the renormalization scale.

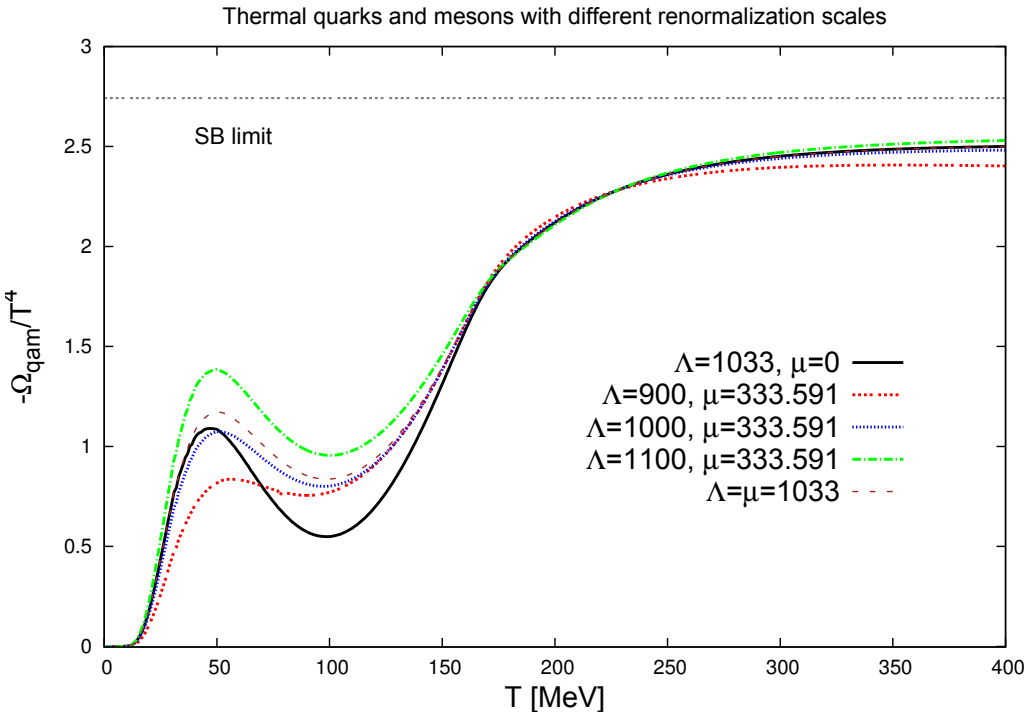

Figure 4.30: *The negative of the potential, i.e. the pressure, divided by* T^4 *as a function of of temperature for the renormalization scale choices* $\Lambda = 900, 1000, 1100$ *MeV at* $\mu = m_\sigma/\sqrt{e}$ *held fixed and for* $\Lambda = \mu = 1033$ *MeV at* $m_\sigma = 550$ *MeV. For a better comparison the* p/T^4 *curve for one renormalization scale is also shown. The different curves do show the same kind of extrema at relatively low temperature as in fig. 4.23.*

This particular behaviour is the same as seen in fig. 4.23. The extrema are a result from the mesonic sector only, where the inclusion of the mesonic self energy leads to no significant changes when ignoring its contribution. For comparison the p/T^4 course for one renormalization scale, that is $\Lambda = 1033$ MeV and $\mu = 0$ at $m_\sigma^{vac} = 550$ MeV, is also shown. The maximum is located within the same region as for two renormalization scales, whereas the minimum is shifted to a considerably lower value of p/T^4. To emphasize is, that this feature originates only from the inclusion of the self energy from the mesonic sector. All the curves, apart from the curve with the parameter choice $\Lambda = 900$ MeV and $\mu = m_\sigma/\sqrt{e}$, which is slightly lower, reach the same

limit at high temperatures.

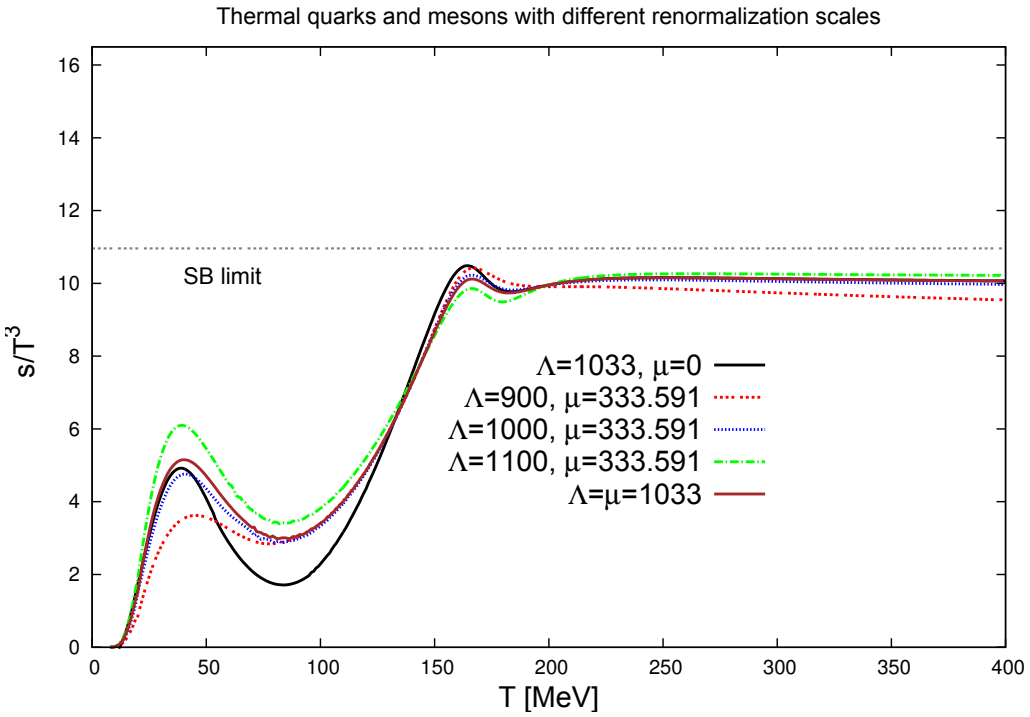

Figure 4.31: *The entropy density divided by T^3 as a function of of temperature for the renormalization scale choices $\Lambda = 900, 1000, 1100$ MeV at $\mu = m_\sigma/\sqrt{e}$ held fixed and for $\Lambda = \mu = 1033$ MeV at $m_\sigma = 550$ MeV. For a better comparison the s/T^3 curve for one renormalization scale is also shown. The different curves do show the same kind of extrema at relatively low temperature as in fig. 4.24 where the self energy of the mesons were not taken into account.*

Since the pressure in fig. 4.30 does not show any steep increase, the entropy density in fig. 4.31 has no spikes. All the curves show two maxima, one at $T \simeq 50$ MeV and a smaller one around the phase transition at $T \simeq 168$ MeV. The minimum for the case of only one renormalization scale is located at a considerably lower value of s/T^3 than for the case of two renormalization scales, indicating again the influence of the mesonic self energy.

Table 4.2 shows the explicit values of λ, m^2 and H for thermal quarks with-

out vacuum term, labeled Q_{th} and with vacuum term, labeled Q_{th+vac}. The thermal mesons without vacuum term are labeled M_{th} and with vacuum term M_{th+vac}. The thermal approach combining quarks and mesons without vacuum term is labeled $Q_{th} + M_{th}$. For the above mentioned cases the sigma meson mass is $m_\sigma^{vac} = 500$ MeV. Table 4.2 shows furthermore these values for the combination of both sectors with vacuum term only in the quark sector $Q_{th+vac} + M_{th}$ and with vacuum term in both sectors $Q_{th+vac} + M_{th+vac}$ for different choices of the renormalization scale. Here $m_\sigma^{vac} = 550$ MeV.

As already mentioned before, the tree level values for the cases, when neglecting the vacuum term, are all equal. Since the renormalization scale Λ for the quark sector (Q_{th+vac}) cancels out, there is no impact on the three vacuum values, apart from varying m_σ^{vac} of course. In the case for thermal quarks with vacuum term the coupling constant $\lambda_r = 2.54\lambda$ and the mass term is $m_r^2 = 2.2m^2$, while the explicit symmetry breaking term H remains unaffected. The case $\mu = m_\sigma/\sqrt{e}$ for the inclusion of the vacuum contribution in the mesonic sector leads to the same tree level value for the coupling constant λ, but to a lower value of the mass term m_r^2 and a higher value of H, resulting in a increase of the pion mass at small temperatures, see fig. 4.8 and the discussion in section 4.3.

The case with one renormalization scale in the combined sector ($Q_{th+vac} + M_{th}$) for the choice $\Lambda = 1033$ MeV and $\mu = 0$ yields a value of $\lambda = 0.0268$, which is rather small compared to the other cases, m^2 and H are virtually unaffected. The conclusion is, that this feature is a result from the inclusion of the CJT formalism, i.e. the mesons influence is rather small. For a lower value of m_σ^{vac} the coupling constant would be negative, which is unphysical since the potential would yield no stable state. Choosing $\Lambda = \mu = 1033$ MeV ($Q_{th+vac} + M_{th+vac} : \Lambda = \mu$) the parameter values are similar as for one renormalization scale, indicating again the small impact of the mesonic self energy onto the fields and the mass spectra. It is apparent, that the results with renormalization scales are very similar to the pure quark case, since for a small value of λ the contribution of the mesons is nearly negligible, see also eqs. 4.141, 4.142 and 4.143.

For two different renormalization scales ($Q_{th+vac} + M_{th+vac} : \Lambda \neq \mu$) things

seem slightly different. The value for μ was held fixed at $\mu = m_\sigma/\sqrt{e}$ and Λ was varyied from $900 \leq \Lambda \leq 1100$ MeV. An increase of Λ reduces the value of the coupling λ, which gets negative at $\Lambda \geq 1050$ MeV. m^2 and H are still close to the tree level values. For $\Lambda = 900$ MeV the coupling constant λ is 4.583, resulting in degenerate masses of the sigma and the pion $\simeq 1500$ MeV at $T = 400$ MeV, see figure 4.29.

5

Finite temperature field theory - SU(3) case

Working with $N_f = 3$ considering up, down and strange quarks and three colored states[1] $N_c = 3$, our aim is to set up a chirally invariant model with quarks being the active degrees of freedom.

5.1. Noninteracting quark matter hypothesis

Before setting up our model, we briefly discuss the *noninteracting quark matter hypothesis* in the bag model [44, 45, 46]. The bag model is a phenomenological way to incorporate confinement within our description of quark matter [30]. To understand how the bag constant models confinement, one can compare the pressure of a noninteractiong gas of quarks (deconfined) with the pressure of a noninteracting gas of pions (confined) at $\mu = 0$ and $T \neq 0$. According to the equations 4.7 and 4.8 and considering the respective de-

[1] Remember the discussion in section 3.6.2, i.e. see equation 3.41

grees of freedom $\xi_q = 37$ and $\xi_m = 3$, the pressue of a noninteracting gas of pions (confined) would have less pressure and thus the noninteracting gas of quarks would be preferred for all temperatures. We know however, that at sufficently low temperatures the confined phase is preferred. The *energy penalty* correcting this is the so called bag constant B, which is substracted from the pressure of the noninteracting gas of quarks[2].
In the context of compact stars $T \ll 1$ and $\mu \neq 0$. Here too one can compare nuclear (confined) matter with quark (deconfined) matter. Hence, the introduction of a bag constant is for that case justified as well.

$$p = \sum_f p_f - B \tag{5.1}$$

$$\epsilon = \sum_f \epsilon_f + B \tag{5.2}$$

At vanishing quark mass this implies that $\epsilon_f = 3p_f$ and expressing p in terms of the energy density ϵ yields

$$p(\epsilon) = \frac{1}{3}(\epsilon - 4B) \tag{5.3}$$

This phenomenological model of confinement is called *Bag model* [47]. Note that the energy density is finite at vanishing pressure, which we will encounter again in the chapter on compact stars 6.

5.2. The SU(3) Quark Meson model

In section 4.4 the step from the Lagrangian 4.106 to the grandcanonical potential 4.107 was abbreviated. For the SU(3) case an explicit calculation will be performed. This then can easily be retraced for the performance of the much simpler SU(2) case in the previous section 4.4. Based on the results from section 4.5 we neglect mesonic contributions in the SU(3) case. The

[2] See [30] for details.

renormalization procedure will be performed in section 5.7.

Based on QCD, an effective model must doubtless implement features of QCD:

- Color symmetry as will be discussed in section (3.6.2):
  All the states in the model have to be color neutral, this feature is guaranteed, since the transmitting mesons are $\Psi\bar{\Psi}$ states.

- Flavor symmetry as will be described in section (3.6.3):
  This symmetry is exact only in the limit of vanishing quark masses, and needs to be considered in any effective theory based on QCD.

- Spontaneous breaking of chiral symmetry as discussed in the forthcoming section (3.6.5):
  Due to a non-vanishing vacuum expectation value of the quark condensate $< \Psi\bar{\Psi} > \neq 0$ chiral symmetry is spontaneously broken. This leads to the emergence of Goldstone bosons, in the $N_f = 2$ case these are identified as the pions, which will be present in this thesis too.

- Explicit breaking of chiral symmetry as discussed in section (3.6.6):
  Considering massive quarks, chiral symmetry is explicitly broken. The model therefore contains terms proportional to the quark masses.

- The *chiral anomaly* term[3] generates the mass splitting between Pions and the η'-meson, whose mass is far to high for being an usual Goldstone boson.

In the following, an appropriate Lagrangian will be presented, and its different terms and to which symmetry(-breaking) they refer to, will be described in detail. The $N_f = 3$ Lagrangian[38, 48, 49] including vector mesonic inter-

[3]The determinant in equation 5.4

actions reads

$$\begin{aligned}\mathcal{L} &= \sum_{\alpha}\left(\bar{\Psi}_n\left(i\not{\partial}-g_\alpha\hat{m}\right)\Psi_n+\bar{\Psi}_s\left(i\not{\partial}-g_\alpha\hat{m}\right)\Psi_s\right)\\ &+ \mathrm{tr}(\partial_\mu\Phi)(\partial^\mu\Phi)^\dagger-\lambda_1[\mathrm{tr}(\Phi^\dagger\Phi)]^2-\lambda_2\mathrm{tr}(\Phi^\dagger\Phi)^2\\ &- m_0^2(tr(\Phi^\dagger\Phi))+tr[\hat{H}(\Phi+\Phi^\dagger)]+c\left(\det(\Phi^\dagger)+\det(\Phi)\right)\\ &- m_v^2tr(V^\dagger V)\end{aligned} \tag{5.4}$$

5.3.
$\mathcal{L}$: The fermion contribution

The part of the Lagrangian modelling the fermionic contribution reads

$$\mathcal{L}_{F_{n,s}} = \sum_{\alpha}\left(\bar{\Psi}_n\left(i\not{\partial}-g_\alpha\hat{m}\right)\Psi_n+\bar{\Psi}_s\left(i\not{\partial}-g_\alpha\hat{m}\right)\Psi_s\right) \tag{5.5}$$

where the sum represents a flavor independent Yukawa type coupling for the fields involved $\alpha = \sigma_n, \sigma_s, \vec{\omega}, \vec{\rho}, \vec{\phi}$. The indices n and s represent the flavour f considered: n=nonstrange (up and down quarks) and s=strange (strange quarks). The nonstrange-strange decoupled Lagrangian in terms of the involved fields then reads

$$\mathcal{L}_{F_{n,s}} = \bar{\Psi}_n\left(i\not{\partial}-g_\omega\gamma^0\omega-g_\rho\vec{\tau}\gamma^0\rho-g_n\sigma_n-ig_\pi\vec{\tau}\gamma^5\vec{\pi}\right)\Psi_n \tag{5.6}$$

$$+ \bar{\Psi}_s\left(i\not{\partial}-g_s\sigma_s-g_\phi\gamma^0\phi\right)\Psi_s \tag{5.7}$$

with γ^0 being the time component of the Dirac matrices according to equation 3.13. Note that in the following the vectorial character of $\vec{\omega}, \vec{\rho}, \vec{\phi}$ is implied, so that the notation will be ω, ρ, ϕ.

5.4.
$\mathcal{L}$: The meson contribution

The meson contribution modelling the interaction as an exchange of mesons (instead of gluons) of the Lagrangian reads

$$\begin{aligned} \mathcal{L}_{mes} &= \mathrm{tr}(\partial_\mu \Phi)(\partial^\mu \Phi)^\dagger - \lambda_1[\mathrm{tr}(\Phi^\dagger \Phi)]^2 - \lambda_2 \mathrm{tr}(\Phi^\dagger \Phi)^2 \qquad (5.8) \\ &- m_0^2(tr(\Phi^\dagger \Phi)) + tr[\hat{H}(\Phi + \Phi^\dagger)] + c\left(\det(\Phi^\dagger) + \det(\Phi)\right) \\ &- m_v^2 tr(V^\dagger V) \qquad (5.9) \end{aligned}$$

where the derivative term represents the kinetic of the fields. The terms containing λ_1 and λ_2 model partially the spontaneous breaking of the symmetry and are responsible for the generation of the masses of the scalar- and pseudoscalar condensates, since $< \bar{\Psi}|\Psi > \neq 0$. The explicit symmetry breaking pattern has to be modelled via the matrix

$$\hat{H} = \begin{pmatrix} \frac{h_n}{2} & 0 & 0 \\ 0 & \frac{h_n}{2} & 0 \\ 0 & 0 & \frac{h_s}{\sqrt{2}} \end{pmatrix} \qquad (5.10)$$

where h_f is proportional to the mass of the appropriate quark flavor

$$h_n = f_\pi m_\pi^2 \qquad (5.11)$$

$$h_s = \sqrt{2} f_K m_K^2 - \frac{h_n}{\sqrt{2}} \qquad (5.12)$$

m_K being the mass of the kaon and f_K the corresponding decay constant, see also [38, 48, 4, 49].

The determinant term including the constant[4] c describes the $U(1)_A$ anomaly, i.e. controlls the far to high mass of the η' meson.

$m_v^2 tr(V^\dagger)V$ generates the masses of the vector meson contribution. In the three flavor case it is more convenient to work with the matrices explicitly

[4] Not to be messed up with the speed of light c - which however has been set to $c^2 = 1$.

rather than with the SU(3) representation in terms of generators [4, 49][5]. Note however, that for the derivation of the renormalized vacuum parameters (see the forthcoming section 5.7.1) the generator representation is chosen due to reasons of convenience.

$$S_{ij} = \frac{1}{\sqrt{2}}\bar{\Psi}_j\Psi_i \tag{5.13}$$

$$P_{ij} = \frac{1}{\sqrt{2}}\bar{\Psi}_j i\gamma^5\Psi_i \tag{5.14}$$

where S denotes the scalar and P the pseudoscalar current. The indices i,j represent the flavor states up, down and strange. The composed matrix with all elements then is

$$\Phi_{ij} = S_{ij} + iP_{ij} \tag{5.15}$$

$$S = \frac{1}{\sqrt{2}}\begin{pmatrix} \frac{\sigma_n+a_0^0}{\sqrt{2}} & a_0^+ & K_s^+ \\ a_0^- & \frac{\sigma_n-a_0^0}{\sqrt{2}} & K_s^0 \\ K_s^- & \bar{K}_s^0 & \sigma_s \end{pmatrix} \tag{5.16}$$

$$P = \frac{1}{\sqrt{2}}\begin{pmatrix} \frac{\eta_n+\pi_0}{\sqrt{2}} & \pi^+ & K^+ \\ \pi^- & \frac{\eta_n-\pi^0}{\sqrt{2}} & K^0 \\ K^- & \bar{K}^0 & \eta_s \end{pmatrix} \tag{5.17}$$

Both together form

$$\Phi = S + iP = \frac{1}{\sqrt{2}}\begin{pmatrix} \frac{\sigma_n+a_0^0}{\sqrt{2}} & a_0^+ & K_s^+ \\ a_0^- & \frac{\sigma_n-a_0^0}{\sqrt{2}} & K_s^0 \\ K_s^- & \bar{K}_s^0 & \sigma_s \end{pmatrix} + \frac{i}{\sqrt{2}}\begin{pmatrix} \frac{\eta_n+\pi_0}{\sqrt{2}} & \pi^+ & K^+ \\ \pi^- & \frac{\eta_n-\pi^0}{\sqrt{2}} & K^0 \\ K^- & \bar{K}^0 & \eta_s \end{pmatrix}$$

or more compact

$$\Phi = \frac{1}{\sqrt{2}}\begin{pmatrix} \frac{(\sigma_n+a_0^0)+i(\eta_n+\pi_0)}{\sqrt{2}} & a_0^+ + i\pi^+ & K_s^+ + iK^+ \\ a_0^- + i\pi^- & \frac{(\sigma_n-a_0^0)+i(\eta_n-\pi^0)}{\sqrt{2}} & K_s^0 + iK^0 \\ K_s^- + iK^- & \bar{K}_s^0 + i\bar{K}^0 & \sigma_s + i\eta_s \end{pmatrix} \tag{5.18}$$

[5] For an overview on the calculation involving the generators see for instance [50, 51]

and respectively the complex conjugate

$$\Phi^\dagger = \frac{1}{\sqrt{2}} \begin{pmatrix} \frac{(\sigma_n + a_0^0) - i(\eta_n + \pi_0)}{\sqrt{2}} & a_0^+ - i\pi^+ & K_s^+ - iK^+ \\ a_0^- - i\pi^- & \frac{(\sigma_n - a_0^0) - i(\eta_n - \pi^0)}{\sqrt{2}} & K_s^0 - iK^0 \\ K_s^- - iK^- & \bar{K}_s^0 - i\bar{K}^0 & \sigma_s - i\eta_s \end{pmatrix} \tag{5.19}$$

In the scalar- and pseudoscalar sector we will restrict ourselves to the scalar fields σ_n and σ_s and a pionic contribution[6]. The matrix Φ then reads

$$\Phi = \frac{1}{\sqrt{2}} \begin{pmatrix} \frac{\sigma_n + i\pi_0}{\sqrt{2}} & i\pi^+ & 0 \\ i\pi^- & \frac{\sigma_n + i\pi^0}{\sqrt{2}} & 0 \\ 0 & 0 & \sigma_s \end{pmatrix} \tag{5.20}$$

and respectively

$$\Phi^\dagger = \frac{1}{\sqrt{2}} \begin{pmatrix} \frac{\sigma_n - i\pi_0}{\sqrt{2}} & -i\pi^+ & 0 \\ -i\pi^- & \frac{\sigma_n - i\pi^0}{\sqrt{2}} & 0 \\ 0 & 0 & \sigma_s \end{pmatrix} \tag{5.21}$$

5.4.1. Computation of the kinetic part

The kinetic part from equation (5.8) is then

$$\mathrm{tr}(\partial_\mu \Phi)(\partial^\mu \Phi)^\dagger = \frac{1}{2}\mathrm{tr}\partial_\mu \begin{pmatrix} \frac{\sigma_n + i\pi_0}{\sqrt{2}} & i\pi^+ & 0 \\ i\pi^- & \frac{\sigma_n + i\pi^0}{\sqrt{2}} & 0 \\ 0 & 0 & \sigma_s \end{pmatrix} \partial^\mu \begin{pmatrix} \frac{\sigma_n - i\pi_0}{\sqrt{2}} & -i\pi^+ & 0 \\ -i\pi^- & \frac{\sigma_n - i\pi^0}{\sqrt{2}} & 0 \\ 0 & 0 & \sigma_s \end{pmatrix} \tag{5.22}$$

[6] We do not consider Kaon condensation: Because of their relatively large mass, Kaons usually do not condense in compact stars.

Computing just the product of the matrices

$$\begin{pmatrix} \partial_\mu(\frac{\sigma_n+i\pi_0}{\sqrt{2}})\partial^\mu(\frac{\sigma_n-i\pi_0}{\sqrt{2}}) - \partial_\mu i\pi^+\partial^\mu i\pi^- & 0 & 0 \\ 0 & \partial_\mu(\frac{\sigma_n-i\pi_0}{\sqrt{2}})\partial^\mu(\frac{\sigma_n+i\pi_0}{\sqrt{2}}) - \partial_\mu i\pi^-\partial^\mu i\pi^+ & 0 \\ 0 & 0 & \partial_\mu\partial^\mu\sigma_s^2 \end{pmatrix}$$

And finally taking the trace, the kinetic part reads

$$\begin{aligned} tr(\partial_\mu\Phi)(\partial^\mu\Phi)^\dagger &= \frac{1}{4}\partial_\mu(\sigma_n + i\pi_0)\partial^\mu(\sigma_n - i\pi_0) + \frac{1}{2}\left(\partial_\mu\pi^+\partial^\mu\pi^-\right) \\ &+ \frac{1}{4}\partial_\mu(\sigma_n - i\pi_0)\partial^\mu(\sigma_n + i\pi_0) + \frac{1}{2}\left(\partial_\mu\pi^-\partial^\mu\pi^+\right) \\ &+ \partial_\mu\partial^\mu\sigma_s^2 \end{aligned} \tag{5.23}$$

5.4.2. Computation of the symmetry breaking contributions

The product of $\Phi\Phi^\dagger$ is

$$\Phi\Phi^\dagger = \frac{1}{2}\begin{pmatrix} \frac{\sigma_n^2+\pi_0^2+2\pi_+\pi_-}{2} & 0 & 0 \\ 0 & \frac{\sigma_n^2+\pi_0^2+2\pi_+\pi_-}{2} & 0 \\ 0 & 0 & \sigma_s^2 \end{pmatrix} \tag{5.24}$$

The mass term is easiest to compute. For the λ_1 and λ_2 term the trace has to be taken and then squared or else squared and then to take the trace in

(5.8). After computing this, the mesonic contribution reads

$$\begin{aligned}
\mathcal{V} = \; & - \frac{\lambda_1}{4}\left((\sigma_n^2+\sigma_s^2)^2 + 2\pi_0^2(\sigma_n^2+\sigma_s^2) + 4\pi_+\pi_-(\sigma_n^2+\sigma_s^2+\pi_0^2) + \pi_0^4 + 4\pi_+^2\pi_-^2\right) \\
& - \frac{\lambda_2}{4}\left((\sigma_n^2+\pi_0^2)^2 + 4\pi_+\pi_-(\sigma_n^2+\pi_0^2) + 4\pi_+^2\pi_-^2 + 2\sigma_s^4\right) && (5.25) \\
& - \frac{m_0^2}{2}(\sigma_n^2+\pi_0^2+2\pi_-\pi_+\sigma_s^2) && (5.26) \\
& + h_n\sigma_n + h_s\sigma_s + \left(\frac{\sigma_n^2\sigma_s+\pi_0^2\sigma_s}{2\sqrt{2}} + \frac{\pi_+\pi_-\sigma_s}{\sqrt{2}}\right)\cdot c - B && (5.27) \\
& && (5.28)
\end{aligned}$$

5.4.3. Computation of the vector meson contribution

The genearal matrix representation for vector mesons is

$$V^\mu = \frac{1}{\sqrt{2}}\begin{pmatrix} \frac{\omega_n^\mu+\rho^{\mu 0}}{\sqrt{2}} & \rho^{\mu+} & K^{*\mu+} \\ \rho^{\mu-} & \frac{\omega_n^\mu-\rho^{\mu 0}}{\sqrt{2}} & K^{*\mu 0} \\ K^{*\mu-} & \bar{K}^{*\mu 0} & \phi^\mu \end{pmatrix} \tag{5.29}$$

The Matrix containing the vector meson contribution to this work is

$$V^\mu = \frac{1}{\sqrt{2}}\begin{pmatrix} \frac{\omega_n+\rho^0}{\sqrt{2}} & \rho^+ & 0 \\ \rho^- & \frac{\omega_n-\rho^0}{\sqrt{2}} & 0 \\ 0 & 0 & \phi \end{pmatrix} \tag{5.30}$$

The product with the adjoint V is the square of V

$$V^2 = \frac{1}{2}\begin{pmatrix} \frac{(\omega_n+\rho^0)^2}{2} + \rho^+\rho^- & \left(\frac{\omega_n+\rho^0}{\sqrt{2}}\right)\rho^+ + \left(\frac{\omega_n-\rho^0}{\sqrt{2}}\right)\rho^+ & 0 \\ \left(\frac{\omega_n+\rho^0}{\sqrt{2}}\right)\rho^- + \left(\frac{\omega_n+\rho^0}{\sqrt{2}}\right)\rho^- & \frac{(\omega_n-\rho^0)^2}{2} + \rho^+\rho^- & 0 \\ 0 & 0 & \phi^2 \end{pmatrix} \tag{5.31}$$

Terms with ρ^+ and ρ^- can be neglected, since they do not couple to the fields due to isospin. The trace remains to be

$$tr(V^2) = \frac{1}{2}\left(m_\omega^2\omega^2 + m_\rho^2\rho^2 + m_\phi^2\phi^2\right) \tag{5.32}$$

5.5. The whole Lagrangian $\mathcal{L}$

Summing all up, $\mathcal{L} = \mathcal{L}_{mes} + \mathcal{L}_{F_{n,s}}$ the whole Lagrangian, splitted up into its containing fields, reads

$$\begin{aligned}
\mathcal{L} &= \frac{1}{4}\partial_\mu(\sigma_n + i\pi_0)\partial^\mu(\sigma_n - i\pi_0) + \frac{1}{2}\left(\partial_\mu\pi^+\partial^\mu\pi^-\right) \qquad (5.33)\\
&+ \frac{1}{4}\partial_\mu(\sigma_n - i\pi_0)\partial^\mu(\sigma_n + i\pi_0) + \frac{1}{2}\left(\partial_\mu\pi^-\partial^\mu\pi^+\right)\\
&+ \partial_\mu\partial^\mu\sigma_s^2\\
&- \frac{\lambda_1}{4}\left((\sigma_n^2+\sigma_s^2)^2 + 2\pi_0^2(\sigma_n^2+\sigma_s^2) + 4\pi_+\pi_-(\sigma_n^2+\sigma_s^2+\pi_0^2) + \pi_0^4 + 4\pi_+^2\pi_-^2\right)\\
&- \frac{\lambda_2}{8}\left((\sigma_n^2+\pi_0^2)^2 + 4\pi_+\pi_-(\sigma_n^2+\pi_0^2) + 4\pi_+^2\pi_-^2 + 2\sigma_s^4\right)\\
&- \frac{m_0^2}{2}(\sigma_n^2 + \pi_0^2 + 2\pi_-\pi_+\sigma_s^2)\\
&+ h_n\sigma_n + h_s\sigma_s + \left(\frac{\sigma_n^2\sigma_s + \pi_0^2\sigma_s}{2\sqrt{2}} + \frac{\pi_+\pi_-\sigma_s}{\sqrt{2}}\right)\cdot c - B\\
&+ \frac{1}{2}\left(m_\omega^2\omega^2 + m_\rho^2\rho^2 + m_\phi^2\phi^2\right)\\
&+ \bar{\Psi}_n\left(i\not{\partial} - g_\omega\gamma^0\omega - g_\rho\vec{\tau}\gamma^0\rho - g_n\sigma_n - ig_\pi\vec{\tau}\gamma^5\vec{\pi}\right)\Psi_n\\
&+ \bar{\Psi}_s\left(i\not{\partial} - g_s\sigma_s - g_\phi\gamma^0\phi\right)\Psi_s \qquad (5.34)
\end{aligned}$$

Note however that all terms containing a pion contribution cancel[7], because due to parity the pion does not condensate. The inclusion of a pseudoscalar current leads furthermore to difficulties when performing perturbation theory within the path integral formalism [17] and the squared pion mass would

[7] They need to be considered when taking the derivatives of course, and then be set equal zero.

become negative for temperatures below the phase transition [48]. The explicit calculation leading to these difficulties can be found in the appendix, section 8. These problems however can be circumvented via the CJT formalism, see section 4.3. As shown in section 4.2 their contribution is additive (when neglecting higher order diagrams). Because of the small influence, i.e. the domination of the quark-quark interaction obtained in the SU(2) sector (section 4.5), we choose to neglect bosonic excitations in the SU(3) case. In mean field approximation the mesonic part of the Lagrangian is however defined as its negative potential $\mathcal{L}_{mes} = -\mathcal{V}$, and is shown in vacuo in figures 5.1 and 5.2.

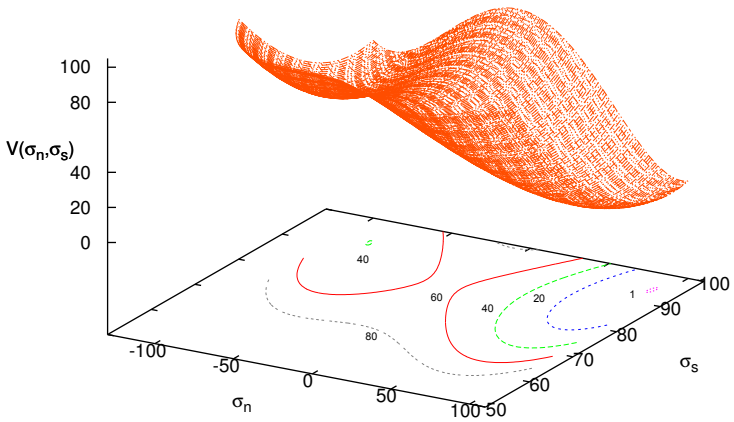

Figure 5.1: *The three dimensional potential $\mathcal{V}(\sigma_n, \sigma_s)$ and the corresponding contour lines in the nonstrange-strange plane. Because of the implementation of the explicit symmetry breaking terms it is, unlike as the mexican hat potential in figure 4.1, tilted. The minimum corresponds to the vacuum expectation value of the nonstrange and strange scalar fields.*

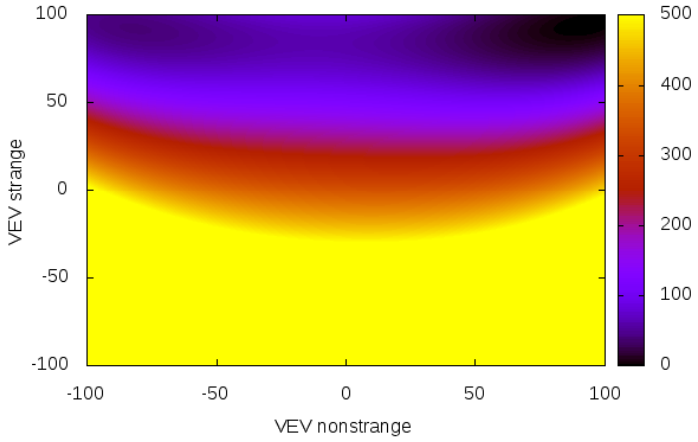

Figure 5.2: *The three dimensional potential $\mathcal{V}(\sigma_n, \sigma_s)$ as a colored contour base in the nonstrange-strange plane. The minimum, shown here in the center of the black area, corresponds to the vacuum expectation value of the nonstrange and strange scalar fields.*

5.6. The grand potential

In order to calculate the grand potential to get the desired thermodynamic quantities such as pressure and energy density, equation 5.35 known from statistical mechanics and thermodynamics can be used. In thermal equilibrium the grand potential Ω will be calculated via the partition function $\mathcal{Z}$, which is defined as a path integral over the fermionic and bosonic fields.

$$\Omega = -\frac{\ln \mathcal{Z}}{\beta} = -p \tag{5.35}$$

Low energy therorems such as the Goldstone theorem and the Ward identities are however fulfilled in mean field approximation.

5.6.1.

Path integral over the fermionic contributions

As already mentioned, in relativistic quantum mechanics fermions are described by a four-component spinor Ψ. Assuming thermal equilibrium the partition function is defined as a path-integral over the quark/antiquark and meson fields. The meson fields will be integrated out, that is: treated in mean field approximation due to the problems mentioned above. The partition function reads [38, 48, 49]

$$\mathcal{Z} = \int \mathcal{D}\bar{\Psi}\mathcal{D}\Psi e^{\left(\int_0^\beta d\tau \int_V d^3\vec{r}\mathcal{L}\right)} \tag{5.36}$$

$$= \left[\int \mathcal{D}\bar{\Psi}\mathcal{D}\Psi e^{\int_0^\beta d\tau \int_V d^3\vec{r}\left[\bar{\Psi}_n(...)\Psi_n + \bar{\Psi}_s(...)\Psi_s\right]}\right] e^{-\int_0^\beta d\tau \int_V d^3\vec{r}\mathcal{V}} \tag{5.37}$$

$$= \left[\int \mathcal{D}\bar{\Psi}\mathcal{D}\Psi e^{\int_0^\beta d\tau \int_V d^3\vec{r}\left[\bar{\Psi}_n(...)\Psi_n + \bar{\Psi}_s(...)\Psi_s\right]}\right] e^{-\beta\mathcal{V}} \tag{5.38}$$

The abbreviations

$$\bar{\Psi}_n(...)\Psi_n = \bar{\Psi}\left(i\partial\!\!\!/ - g_\omega\gamma^0\omega - g_\rho\vec{\tau}\gamma^0\rho - g_n\sigma_n - i\gamma^5\vec{\tau}\vec{\pi}\right)\Psi \tag{5.39}$$

such as

$$\bar{\Psi}_s(...)\Psi_s = \bar{\Psi}_s\left(i\partial\!\!\!/ - g_s\sigma_s - g_\varphi\gamma^0\phi\right)\Psi_s \tag{5.40}$$

are used.

In both, the nonstrange and strange sector, the integral in the exponent of the exponential function can be rewritten with a Fourier transformation. It is explicitly shown here in the nonstrange case. Since the calculation in the strange sector is completly analoguous, just the results will be given.

$$\Psi(\vec{r},t) = \frac{1}{\sqrt{V}}\sum_{n,\vec{k}} e^{i(\nu_n\tau + \vec{k}\vec{r})}\phi_n(\vec{k}) \tag{5.41}$$

Substituting equation (5.41) in equation (5.38) and performing the derivation

as told by $\not{\partial}$ gives:

$$\int_0^\beta d\tau \int_V d^3\vec{r}\frac{1}{V}\sum_{n,\vec{k}} e^{-i(\nu_n\tau+\vec{k}\vec{r})}\bar{\phi}_n(\vec{k})(\mathcal{A})\sum_{m,\tilde{k}} e^{i(\nu_m\tau+\tilde{k}\vec{r})}\phi_m(\tilde{k}) \tag{5.42}$$

where

$$\mathcal{A} = \left(-i\gamma^0\nu_n - \vec{\gamma}\vec{k} - g_n\sigma_n - i\gamma^5\vec{\tau}\vec{\pi} - g_\omega\gamma^0\omega - g_\rho\vec{\tau}\gamma^0\vec{\rho}\right) \tag{5.43}$$

Since no operator is left anymore, a rearrangement can be done

$$\int_0^\beta d\tau\frac{1}{V}\sum_{n,\vec{k}}\sum_{m,\tilde{k}}\bar{\phi}_n(\vec{k})\phi_m(\tilde{k})(\mathcal{A})\int_V d^3\vec{r}e^{-i(\nu_n\tau+\vec{k}\vec{r})}e^{i(\nu_m\tau+\tilde{k}\vec{r})} \tag{5.44}$$

then making use of the following identities known from quantum mechanics

$$\int_{-\infty}^{+\infty} e^{-iax}e^{ia'x}dV = \delta(a-a') \quad \text{and} \quad \int_{-\infty}^{+\infty} e^{-iax}e^{ia'x}dx = \delta_{aa'} \tag{5.45}$$

just one sum remains either for nonstrange $\frac{\beta}{V}\sum_{n,\vec{k}}\bar{\phi}_n\phi_n(\mathcal{A})$ and strange contributions $\frac{\beta}{V}\sum_{n,\vec{k}}\bar{\phi}_s\phi_s(\mathcal{B})$ respectively. In the strange sector

$$\mathcal{B} = \left(-i\gamma^0\nu_n - \vec{\gamma}\vec{k} - g_s\sigma_s - g_\phi\gamma^0\phi\right) \tag{5.46}$$

Replacing the equations (5.43) and (5.46) in the partition function

$$\mathcal{Z} = e^{-\beta\mathcal{V}}\int\mathcal{D}\bar{\Psi}\int\mathcal{D}\Psi e^{-\left(\frac{\beta}{\mathcal{V}}\sum_{n,\vec{k}}\left(\bar{\phi}_n(-\mathcal{A})\phi_n+\bar{\phi}_s(-\mathcal{B})\phi_s\right)\right)} \tag{5.47}$$

is what has up to now become of equation (5.38).
Now this integral is to be performed over Grassmann variables, which are of use when dealing with fermionic path integrals,

$$\int\prod_{i=1}^{n} d\bar{\eta}_i d\eta_i e^{-\sum_{i,j}\eta_i A_{ij}\eta_j} = \det A \tag{5.48}$$

so that the partition function

$$\mathcal{Z} = \frac{1}{T} e^{-\beta \mathcal{V}} \cdot \left[\det_{\gamma,f,c,k} \frac{\mathcal{A}}{T} \cdot \det_{\gamma,f,c,k} \frac{\mathcal{B}}{T} \right] \tag{5.49}$$

One remains with a determinant over four degrees of freedom. The calculation will be done step by step in the following sections.

The determinant over particle-/antiparticle contribution

The first determinant to be calculated is the determinat over γ, which represents particle and antiparticle contributions. First step is to insert the Dirac-matrices equation (3.13) explicitly in the equations (5.43) and (5.46). To not make confusion with the nonstrange index n, the Matsubara index $n \to \alpha$ has been substituted in the forthcoming

$$\tilde{\mu}_n = g_\omega \omega + g_\rho \vec{\tau} \rho \tag{5.50}$$

$$\tilde{m}_n = g_n \sigma_n \tag{5.51}$$

$$\tilde{\mu}_s = g_\phi \phi \tag{5.52}$$

$$\tilde{m}_s = g_s \sigma_s \tag{5.53}$$

Equation 5.43 then

$$\begin{aligned} -\mathcal{A} &= i \begin{pmatrix} 1_2 & 0 \\ 0 & -1_2 \end{pmatrix} \nu_\alpha + \begin{pmatrix} 0 & \hat{\sigma}_i \\ -\hat{\sigma}_i & 0 \end{pmatrix} \vec{k} \\ &+ i \begin{pmatrix} 0 & 1_2 \\ 1_2 & 0 \end{pmatrix} \vec{\tau}\vec{\pi} + \begin{pmatrix} 1_2 & 0 \\ 0 & -1_2 \end{pmatrix} \tilde{\mu}_n + \begin{pmatrix} 1_2 & 0 \\ 0 & 1_2 \end{pmatrix} \tilde{m}_n \end{aligned} \tag{5.54}$$

and the strange part from equation 5.46

$$\begin{aligned} -\mathcal{B} &= i \begin{pmatrix} 1_2 & 0 \\ 0 & -1_2 \end{pmatrix} \nu_\alpha + \begin{pmatrix} 0 & \hat{\sigma}_i \\ -\hat{\sigma}_i & 0 \end{pmatrix} \vec{k} \\ &+ \begin{pmatrix} 1_2 & 0 \\ 0 & -1_2 \end{pmatrix} \tilde{\mu}_s + \begin{pmatrix} 1_2 & 0 \\ 0 & 1_2 \end{pmatrix} \tilde{m}_s \end{aligned} \tag{5.55}$$

So that

$$-\mathcal{A} = \begin{pmatrix} i\nu_\alpha + \tilde{\mu}_n + \tilde{m}_n & \vec{\sigma}\vec{k} + i\vec{\tau}\vec{\pi} \\ -\vec{\sigma}\vec{k} + i\vec{\tau}\vec{\pi} & -i\nu_\alpha - \tilde{\mu}_n + \tilde{m}_n \end{pmatrix} \tag{5.56}$$

and

$$-\mathcal{B} = \begin{pmatrix} i\nu_\alpha + \tilde{\mu}_s + \tilde{m}_s & \vec{\sigma}\vec{k} \\ -\vec{\sigma}\vec{k} + i\vec{\tau}\vec{\pi} & -i\nu_\alpha - \tilde{\mu}_s + \tilde{m}_s \end{pmatrix} \tag{5.57}$$

The partition function for the nonstrange propagator then reads

$$\mathcal{Z} = e^{-\beta\mathcal{V}} \cdot \det_\gamma \frac{1}{T} \cdot \begin{pmatrix} i\nu_\alpha + \tilde{\mu}_n + \tilde{m}_n & \vec{\sigma}\vec{k} + i\vec{\tau}\vec{\pi} \\ -\vec{\sigma}\vec{k} + i\vec{\tau}\vec{\pi} & -i\nu_\alpha - \tilde{\mu}_n + \tilde{m}_n \end{pmatrix} \tag{5.58}$$

Using the identity [23]

$$\det_{2N\times 2N} \begin{pmatrix} A_2 & B_2 \\ C_2 & D_2 \end{pmatrix} = \det_{N\times N} (AD - BD^{-1}CD) \tag{5.59}$$

and after a bit of non-enlightening algebra the determinant $\det_\gamma A$ reads

$$\begin{pmatrix} \nu_\alpha^2 - \tilde{\mu}_n^2 + \tilde{m}_n^2 - 2i\nu_\alpha\tilde{\mu}_n + g_n(\vec{\tau}\vec{\pi})^2 + \vec{k}^2 & 0 \\ 0 & \nu_\alpha^2 - \tilde{\mu}_n^2 + \tilde{m}_n^2 - 2i\nu_\alpha\tilde{\mu}_n + g_n(\vec{\tau}\vec{\pi})^2 + \vec{k}^2 \end{pmatrix}$$

$$\begin{aligned} \det_\gamma A &= (\nu_\alpha^2 - \tilde{\mu}_n^2 + \tilde{m}_n^2 - 2i\nu_\alpha\tilde{\mu}_n + g_n(\vec{\tau}\vec{\pi})^2 + \vec{k}^2)^2 && (5.60)\\ &= (E_n^2 + (\nu_\alpha^2 - \tilde{\mu}_n^2 - 2i\nu_\alpha\tilde{\mu}_n) + \vec{\tau}^2\vec{\pi}^2)^2 && (5.61)\\ &= (E_n^2 + (\nu_\alpha - i\tilde{\mu}_n)^2 + \vec{\tau}^2\vec{\pi}^2)^2 && (5.62) \end{aligned}$$

Analogue is the calculation in the strange contribution

$$\det_\gamma B = (E_s^2 + (\nu_\alpha - i\tilde{\mu}_s)^2)^2$$

For a better overview of the rather lenghty equations, one can abbreviate

$$E_n^2 = k^2 + \tilde{m}_n^2 + (g_n\vec{\tau}\vec{\pi})^2 \tag{5.63}$$

such as

$$E_s^2 = k^2 + \tilde{m}_s^2 \tag{5.64}$$

Finally the partition function is left with but three degrees of freedom

$$\mathcal{Z} = e^{-\beta\mathcal{V}} \det_{f,c,k} \cdot \frac{1}{T^4} \left[\left(E_n^2 + (\nu_\alpha - i\tilde{\mu}_n)^2 \right)^2 \cdot \left(E_s^2 + (\nu_\alpha - i\tilde{\mu}_s)^2 \right)^2 \right] \tag{5.65}$$

The determinant over momentum space

Since the goal is to collect all momenta, the determinant over momentum space det_k becomes a sum $\sum_k$ and eventually an integral.

$$\mathcal{Z} = e^{-\beta\mathcal{V}} \det_{f,c} \cdot \frac{1}{T^4} \sum_{\alpha,\vec{k}} \left[\left(E_n^2 + (\nu_\alpha - i\tilde{\mu}_n)^2 \right)^2 \cdot \left(E_s^2 + (\nu_\alpha - i\tilde{\mu}_s)^2 \right)^2 \right] \tag{5.66}$$

At this point it is more convenient to take the logarithm of the partition function in equation (5.66) and making use of another identity

$$\ln \det A = \mathrm{tr} \ln \mathrm{A} \tag{5.67}$$

Then

$$\begin{aligned} \Omega &= -\frac{1}{\beta} \ln \mathcal{Z} \qquad (5.68) \\ &= \mathcal{V} - \frac{1}{\beta} \ln \det_{c,f} \cdot \frac{1}{T^4} \sum_{\alpha,\vec{k}} \left[\left(E_n^2 + (\nu_\alpha - i\tilde{\mu}_n)^2 \right)^2 \cdot \left(E_s^2 + (\nu_\alpha - i\tilde{\mu}_s)^2 \right)^2 \right] \\ &= \mathcal{V} - \frac{1}{\beta} \cdot tr_{c,f} \sum_{\alpha,\vec{k}} \ln \left[\left(\frac{E_n^2 + (\nu_\alpha - i\tilde{\mu}_n)^2}{T^2} \right)^2 \cdot \left(\frac{E_s^2 + (\nu_\alpha - i\tilde{\mu}_s)^2}{T^2} \right)^2 \right] \end{aligned}$$

The Matsubara frequencies $\nu_\alpha = (2n+1)^2\pi^2$ run over $-\infty \to +\infty$, and from the sum on

$$= \sum_{-\infty}^{+\infty} \ln\left[\left(\frac{E_n^2 + (\nu_\alpha - i\tilde{\mu}_n)^2}{T^2}\right)^2 \cdot \left(\frac{E_s^2 + (\nu_\alpha - i\tilde{\mu}_s)^2}{T^2}\right)^2\right] \tag{5.69}$$

$$= \sum_{-\infty}^{+\infty} \ln\left(\frac{E_n^2 + (\nu_\alpha - i\tilde{\mu}_n)^2}{T^2}\right) + \sum_{-\infty}^{+\infty} \ln\left(\frac{E_n^2 + (-\nu_\alpha - i\tilde{\mu}_n)^2}{T^2}\right)$$
$$+ \sum_{-\infty}^{+\infty} \ln\left(\frac{E_s^2 + (\nu_\alpha - i\tilde{\mu}_s)^2}{T^2}\right) + \sum_{-\infty}^{+\infty} \ln\left(\frac{E_s^2 + (-\nu_\alpha - i\tilde{\mu}_s)^2}{T^2}\right) \tag{5.70}$$

which justifies the change in the algebraic sign. Rearranging

$$(E_n^2 + (\nu_\alpha - i\mu_n)^2)(E_n^2 + (-\nu_\alpha - i\mu_n)^2) = (\nu_\alpha^2 + (E_n + \mu_n)^2)(\nu_\alpha^2 + (E_n - \mu_n)^2) \tag{5.71}$$

and substituting the Matsubara frequencies $\nu_\alpha = (2n+1)^2\pi^2$ gives[8]

$$\sum_{n=-\infty}^{\infty} \ln\left[(2n+1)^2\pi^2 + \frac{(E_{n,s} \pm \tilde{\mu}_{n,s})^2}{T^2}\right] \tag{5.72}$$

Making use[9] of another identity

$$\ln(a+b) = \int_1^{b^2} \frac{1}{\theta^2 + a} d\theta^2 + \ln(a+1) \tag{5.73}$$

and identifying $a = (2n+1)^2\pi^2$ and $b^2 = \frac{(E_{n,s} \pm \tilde{\mu}_{n,s})^2}{T^2}$ the sum then reads

$$\sum_{n=-\infty}^{\infty} \int_1^{b^2} \frac{1}{\theta^2 + (2n+1)^2\pi^2} d\theta^2 + \sum_{n=-\infty}^{\infty} \ln((2n+1)^2\pi^2 + 1) \tag{5.74}$$

[8] The calculation is shown for one case of the four terms in equation (5.70), the others are performed analoguous.

[9] Note that in finite temperature field theory certain idenities need to be known, else the calculation cannot be performed. A similar procedure took already place while deriving the vacuum contributions to the grandcanonical potential in section 4.3.1, i.e. the equations 4.57, 4.58, 4.63 and 4.64.

For further calculations of the first term the denominator has to become complex, and after another few algebraic steps including another known identity from quantum fields theory (performed in detail in [5]) one finally gets for 5.72

$$\int_1^{b^2} d\theta^2 \frac{1}{\theta}\left[\frac{1}{2} - \frac{1}{e^\theta + 1}\right] + \sum_{n=-\infty}^{\infty} \ln((2n+1)^2\pi^2 + 1) \tag{5.75}$$

The integral in equation (5.75) can be solved with $d\theta^2 = 2\theta d\theta$, substituting $\alpha = e^{-\theta} + 1$ and its derivation $\frac{d\alpha}{d\theta} = -e^{-\theta}$

$$\int_1^{b^2} d\theta^2 \frac{1}{\theta}\left[\frac{1}{2} - \frac{1}{e^\theta + 1}\right] \quad = \quad [b-1] + 2\ln(1+e^{-b}) - 2\ln(1+e^{-1}) \tag{5.76}$$

Having done this thrice[10] and replacing all relevant quantities, the grand potential now reads

$$\begin{aligned}\Omega = \mathcal{V} - \frac{1}{\beta} tr_{c,f} \sum_k & \frac{(E_n \pm \tilde{\mu}_n)}{T} + 2\ln\left(1 + e^{-\frac{(E_n \pm \tilde{\mu}_n)^2}{T^2}}\right) \\ & + \frac{(E_n \pm \tilde{\mu}_s)}{T} + 2\ln\left(1 + e^{-\frac{(E_n \pm \tilde{\mu}_s)^2}{T^2}}\right) + \tilde{\mathcal{C}}\end{aligned}$$

where

$$\tilde{\mathcal{C}} = 4 \cdot \sum_{-\infty}^{\infty} \ln\left((2n+1)^2\pi^2 + 1\right) - 1 - 2\ln(1 - e^{-1}) \tag{5.77}$$

is the appropriate constant vacuum energy pressure containing only c-numbers.

The determinant over color-and flavor space

As mentioned above, the sum $\sum_k$ becomes an integral over the whole space $\int \frac{d^3\vec{k}}{(2\pi)^3}$ in the thermodynamical limes, which finally can be rewritten as a surface integral $d^3\vec{k} \to 4\pi k^2 d\vec{k}$. What remains to be done is to calculate

[10] The explicit analytical solution of the integral can be found in my master thesis, [5].

both traces over color- and flavorspace.

$$\Omega = \mathcal{V} - \frac{1}{\beta} tr_{c,f} \int \frac{d^3k}{(2\pi)^3} \left[\frac{E_{n,s} \pm \tilde{\mu}_{n,s}}{T} + 2\ln\left(1 + e^{-\frac{E_{n,s}\pm\tilde{\mu}_{n,s}}{T}}\right)\right] \quad (5.78)$$

$$= \mathcal{V} - \frac{3}{\beta} tr_f \int \frac{d^3k}{(2\pi)^3} \left[2\frac{E_{n,s}}{T} + 2\ln\left(1 + e^{-\frac{E_{n,s}\pm\tilde{\mu}_{n,s}}{T}}\right)\right] \quad (5.79)$$

$$= \mathcal{V} - \frac{3}{\pi^2\beta} tr_f \int k^2 dk \left[\frac{E_{n,s}}{T} + \ln\left(1 + e^{-\frac{E_{n,s}\pm\tilde{\mu}_{n,s}}{T}}\right)\right] \quad (5.80)$$

The trace over color space just yields a factor three in equation (5.78). Choosing as base τ_3 (see equation (3.14)) and splitting up equation (5.50) in its flavor content gives

$$\tilde{\mu}_{up} = \tilde{\mu}_u = g_\omega\omega + g_\rho\rho \quad (5.81)$$

$$\tilde{\mu}_{down} = \tilde{\mu}_d = g_\omega\omega - g_\rho\rho \quad (5.82)$$

$$\tilde{\mu}_{strange} = \tilde{\mu}_s = g_\phi\phi \quad (5.83)$$

where equation (5.83) is equal to equation (5.52). The use of equation (5.67) collects all terms relevant in flavor space and what finally remains is the grand canonical potential for finite temperature

$$\Omega = \mathcal{V} - \frac{3}{\pi^2\beta} \int_0^\infty k^2 dk \cdot \mathcal{N} \quad (5.84)$$

where $\mathcal{V}$ is the negative of equation (5.34)

$$\mathcal{V} = \frac{\lambda_1}{4}\left((\sigma_n^2 + \sigma_s^2)^2\right) + \frac{\lambda_2}{8}\left(\sigma_n^4 + 2\sigma_s^4\right) + \frac{m_0^2}{2}(\sigma_n^2 + \sigma_s^2)$$
$$- h_n\sigma_n - h_s\sigma_s - \frac{c\sigma_n^2\sigma_s}{2\sqrt{2}} - \frac{1}{2}\left(m_\omega^2\omega^2 + m_\rho^2\rho^2 + m_\phi^2\phi^2\right) + B^{1/4}$$

and where $B^{1/4}$ is a vacuum pressure term named bag constant[11]. The in-meduim part

$$\begin{aligned}\mathcal{N} &= \ln\left(1+e^{-\beta(E_n+\tilde{\mu}_u)}\right)+\ln\left(1+e^{-\beta(E_n-\tilde{\mu}_u)}\right)\\ &+ \ln\left(1+e^{-\beta(E_n+\tilde{\mu}_d)}\right)+\ln\left(1+e^{-\beta(E_n-\tilde{\mu}_d)}\right)\\ &+ \ln\left(1+e^{-\beta(E_s+\tilde{\mu}_s)}\right)+\ln\left(1+e^{-\beta(E_s-\tilde{\mu}_s)}\right)\end{aligned} \tag{5.85}$$

or in terms of flavor

$$\begin{aligned}\mathcal{N} &= \ln\left(1+e^{\frac{-E_n+\mu_u-g_\omega\omega-g_\rho\rho}{T}}\right)+\ln\left(1+e^{\frac{-E_n-\mu_u+g_\omega\omega+g_\rho\rho}{T}}\right)\\ &+ \ln\left(1+e^{\frac{-E_n+\mu_d-g_\omega\omega+g_\rho\rho}{T}}\right)+\ln\left(1+e^{\frac{-E_n-\mu_d+g_\omega\omega-g_\rho\rho}{T}}\right)\\ &+ \ln\left(1+e^{\frac{-E_s+\mu_s-g_\phi\phi}{T}}\right)+\ln\left(1+e^{\frac{-E_s-\mu_s+g_\phi\phi}{T}}\right)\end{aligned} \tag{5.86}$$

The vacuum values for the parameters λ_1, λ_2, m_0^2, c, h_n and h_s are again fixed at tree level[12].

Note that the divergent vacuum term still present in equation 5.80 has been neglected in equation 5.84. Its inclusion will be discussed in section 5.7.

Note furthermore, that the calculation of the equation of state for compact stars in the forthcoming section 6 is generally performed at $T = 0$. The appropriate approximation procedure has been performed during my master thesis [5] and shall therefore not be shown here again.

[11] Motivated by the MIT-Bag model, see for instance [1, 2], and as well as from the constant vacuum energy term which is left from the calculation of the Matsubara frequencies, equation 5.77.

[12] Although the computation is somewhat more extensive, the SU(2) section 4 can be seen as a guideline for their derivation. A more detailled treatment of the tree level parameters in mean field approximation can be found in my Master thesis [5] or in [38, 48]. In the following section upon renormalization 5.7 the vacuum parameters are explicitely derived. This calculation can also easily be backtraced to the parameter determination in mean field approximation.

5.6.2.
The Lepton contribution

Since the lepton contribution decouples from the quark grand canonical potential it can be treated separately. Its computation follows the same rules and only the result shall be given here. Worth mentioning is that the lepton-antilepton contribution has but another prefeactor compared to the in-medium part of equation 5.84, since (for instance) no colour charge appears.

$$\Omega_e = -\frac{2}{\beta}\int \frac{d^3k}{(2\pi)^3}\ln\left(1+e^{-\frac{E_{k,e}\pm\mu_e}{T}}\right) \tag{5.87}$$

with $E_{k,e} = \sqrt{k^2+m_e^2}$ and μ_e as the electron chemical potential.

5.7.
Renormalization

Like in the SU(2) case performed for the quark sector[13] the implementation of the vacuum term in the SU(3) case reads also

$$\Omega^{vac}_{\bar{q}q} = \int \frac{dk^3}{(2\pi)^3}E_k \qquad \rightarrow \qquad \Omega^{dr}_{\bar{q}q} = -\frac{N_c N_f}{8\pi^2}\tilde{m}_f^4\ln\left(\frac{\tilde{m}_f}{\Lambda}\right) \tag{5.88}$$

which is of course the same as equation 4.120. Since 4.120 it is independent of any temperature, its contribution restricts to every tree level value. That is, the vacuum parameters change upon renormalization.

5.7.1.
The renormalized vacuum parameters

The six model parameters λ_1, λ_2, m_0^2, c, h_n and h_s are fixed by six experimentally known values [38, 48, 52]. Based upon their derivation in mean

[13] Based on the computation for the mesonic sector in section 4.3.1, which is completely analoguous for any case discussed in this thesis.

field approximation the computation including the fermion vacuum contribution can also be found in [53, 31, 54], nonetheless a few important steps are shown here. As an input the pion mass $m_\pi = 136$ MeV, the kaon mass $m_k = 496$ MeV, the pion decay constant $f_\pi = 92.4$ MeV, the kaon decay constant $f_k = 113$ MeV, the masses of the eta $m_\eta = 548$ MeV meson, the mass of the eta-prime meson $m'_\eta = 958$ MeV and the mass of the sigma meson m_σ need to be known. The mass of the sigma meson, m_σ, however is not well determined experimentally. Usually, the sigma meson, which is the chiral partner of the pion, is identified with the experimentally measured resonance $\mathrm{f}_0(500)$, which is rather broad, $400 \leq m_{f_0} \leq 600$ MeV [55, 52]. Also, in Ref. [49] it was demonstrated that within an extended quark-meson model that includes vector and axial-vector interactions, the resonance $\mathrm{f}_0(1370)$ could be identified as this very scalar state. To cover the spectrum of physical possibilities, the mass of the sigma meson adopts a rather wide range in mass, $400 \leq m_\sigma \leq 800$ MeV.

Starting point is the grand canonical potential (including an average value of the pion mass m_π)[14] from equation 5.34 at tree level, that is the potential $\mathcal{V}$ and the vacuum contribution.

$$\begin{aligned}\mathcal{V} &= \frac{\lambda_1}{4}\left[(\sigma_n^2+\sigma_s^2)^2+2\pi_0^2(\sigma_n^2+\sigma_s^2)+\pi_0^4\right]+\frac{\lambda_2}{8}\left[(\sigma_n^2+\pi_0^2)^2+2\sigma_s^4\right]\\ &+ \frac{m_0^2}{2}(\sigma_n^2+\pi_0^2+\sigma_s^2)-h_n\sigma_n-h_s\sigma_s-c\left(\frac{\sigma_n^2\sigma_s+\pi_0^2\sigma_s}{2\sqrt{2}}\right)+B \qquad (5.89)\\ &+ \frac{1}{2}\left(m_\omega^2\omega^2+m_\rho^2\rho^2+m_\phi^2\phi^2\right)-\frac{N_cN_f}{8\pi^2}\left(\sigma_n^2+\sigma_s^2\right)^2\ln\left(\frac{g\sqrt{\sigma_n^2+\sigma_s^2}}{\Lambda}\right)\end{aligned}$$

with the renormalization scale parameter Λ.

Similar as in the SU(2) case to determine the vacuum parameters a few derivatives are necessary to determine the unknown quantities. When in the SU(2) case equation 4.110 is needed for the explicit symmetry breaking term H, it is the same as in SU(3), only two derivatives are needed, one with respect to the nonstrange condensate σ_n, for h_n, the other with respect to

[14] Since an input parameter, the field π can not be negelcted at this point, because m_π results from the field.

the strange condensate σ_s, for h_s. The equations 4.112 and 4.113 fix the two other unknowns in SU(2), recall section 4.4, here also similar to the SU(3) case, where the second derivatives determine the known masses, which then serve as an input. In SU(3)

$$h_n = m_0^2\sigma_n - \frac{c\sigma_s\sigma_n}{\sqrt{2}} + \lambda_1\left(\sigma_n^2+\sigma_s^2\right)\sigma_n + \frac{\lambda_2}{2}\sigma_n^3 + \text{Vac.} \tag{5.90}$$

$$h_s = m_0^2\sigma_s - \frac{c\sigma_n^2}{\sqrt{2\sqrt{2}}} + \lambda_1\left(\sigma_n^2+\sigma_s^2\right)\sigma_s + \lambda_2\sigma_s^3 + \text{Vac.} \tag{5.91}$$

$$\frac{\partial^2\mathcal{V}}{\partial\pi^2} = m_0^2 - \frac{c\sigma_s}{\sqrt{2}} + \lambda_1\left(\sigma_n^2+\sigma_s^2\right) + \frac{\lambda_2}{2}\sigma_n^2 = m_\pi^2 \tag{5.92}$$

and the vacuum contribution yet to be determined. Since the pion does not condensate, but yields a contribution to the other quantities when deriving with respect to π, it does not occur anymore in the equations above. Unfortunately does the second derivative with respect to σ_n not yield the mass of the sigma meson, because, as we will see, of mixing of the mathematical fields. Furthermore the kaon mass is needed as well as the vacuum contribution. Here we remain with three unknowns, so that the corresponding second derivatives of $\mathcal{V}$ need to be performed with respect to the mathematical fields. At this point however we have only three scalar fields and neither of them corresponds to the experimentally required values, so that it is necessary to rewrite the nonstrange-strange basis in terms of the generators, i.e. the mathematical fields and idenitfy those with the physical fields so to derive $\mathcal{V}$ twice. Following [38, 48] the matrix

$$\Phi = \frac{1}{\sqrt{2}}\begin{pmatrix} \frac{(\sigma_n+a_0^0)+i(\eta_n+\pi_0)}{\sqrt{2}} & a_0^+ + i\pi^+ & K_s^+ + iK^+ \\ a_0^- + i\pi^- & \frac{(\sigma_n-a_0^0)+i(\eta_n-\pi^0)}{\sqrt{2}} & K_s^0 + iK^0 \\ K_s^- + iK^- & \bar{K}_s^0 + i\bar{K}^0 & \sigma_s + i\eta_s \end{pmatrix} \tag{5.93}$$

(see also equation 5.18) can be written as $\Phi = T_a\Phi_a = T_a(\sigma_a + i\pi_a)$ with $T_a = \frac{\lambda_a}{2}$ with λ_a as the Gell Mann matrices and $a = 1, 2, ..8$ as the nine generators of the U(3) symmetry group[15]. Rearranging the entries of 5.93

[15] The generators obey the U(3) algebra with the standard symmetric d_{abc} and antisymmetric structure constants f_{abc}

gives

$$\Phi = \frac{1}{2}\begin{pmatrix} \sqrt{\frac{2}{3}}\sigma_0 + \sigma_3 + \frac{\sigma_8}{\sqrt{3}} & \sigma_1 - i\sigma_2 & \sigma_4 - i\sigma_5 \\ \sigma_1 + i\sigma_2 & \sqrt{\frac{2}{3}}\sigma_0 - \sigma_3 + \frac{\sigma_8}{\sqrt{3}} & \sigma_6 - i\sigma_7 \\ \sigma_4 + i\sigma_5 & \sigma_6 + i\sigma_7 & \sqrt{\frac{2}{3}}\sigma_0 - \frac{2\sigma_8}{\sqrt{3}} \end{pmatrix} \tag{5.94}$$

The basis transformation from the nonstrange-strange basis to the mathematical basis is

$$\begin{pmatrix} \sigma_n \\ \sigma_s \end{pmatrix} = \frac{1}{\sqrt{3}}\begin{pmatrix} \sqrt{2} & 1 \\ 1 & -\sqrt{2} \end{pmatrix}\begin{pmatrix} \sigma_0 \\ \sigma_8 \end{pmatrix} \tag{5.95}$$

Separating the entries for the scalar and the pseudoscalar sector (see equations 5.16 and 5.17) gives the potential in terms of the mathematical fields (see [38, 48] for details). The mass matrix[16] m_{ij} is determined by the mesonic part of the potential only, since the quark contribution vanishes in the vacuum at $T = \mu = 0$. Because of isospin symmetry some entries are degenerate and furthermore $m_{08}^2 = m_{80}^2$, so that

$$m_{ij}^2 = \frac{\partial^2 \mathcal{V}}{\partial\Phi_i \partial\Phi_j} + \frac{\partial^2 \Omega_{\bar{q}q}^{dr}}{\partial\Phi_i \partial\Phi_j} = \begin{pmatrix} m_{00}^2 & \dots & m_{08}^2 \\ \vdots & \ddots & \vdots \\ m_{80}^2 & \dots & m_{88}^2 \end{pmatrix} \tag{5.96}$$

the equated matrix needs to be diagonalized for m_σ^2 and $m_{f_0}^2$ in the scalar sector and as well as m_η and m_η' in the pseudoscalar sector introducing a mixing angle θ. Eventually the mass of the kaon in the nonstrange-strange basis is

$$m_k^2 = m_0^2 - \frac{c\sigma_n}{2} + \lambda_1\left(\sigma_n^2 + \sigma_s^2\right) + \frac{\lambda_2}{2}\left(\sigma_n^2 - \sqrt{2}\sigma_n\sigma_s + 2\sigma_s^2\right) \tag{5.97}$$

[16] Remember that the second derivative of the potential yields the corresponding mass of a given particle.

which determines the axial anomaly term c

$$c = \frac{-2\left(m_k^2 - m_\pi^2\right) - \lambda_2\left(\sqrt{2}\sigma_n\sigma_s - 2\sigma_s^2\right)}{\sigma_n - \sqrt{2}\sigma_s} \tag{5.98}$$

Having performed a few algebraic steps using 5.96, m_η and m'_η read

$$\begin{aligned} m_\eta + m'_\eta &= 2m_0^2 + 2\lambda_1\left(\sigma_n^2 + \sigma_s^2\right) + \frac{\lambda_2}{2}\left(\sigma_n^2 + 2\sigma_s^2\right) + \frac{c\sigma_s}{\sqrt{2}} \\ &= 2m_\pi^2 - \frac{\lambda_2}{2}\left(\sigma_n^2 - 2\sigma_s^2\right) + \frac{3c\sigma_s}{\sqrt{2}} \end{aligned} \tag{5.99}$$

inserting 5.98 in 5.99 to eventually solve for λ_2 gives

$$\lambda_2 = \frac{m_\eta^2 + m_\eta'^2 - 2m_\pi^2 + \frac{6\sigma_s(m_k^2 - m_\pi^2)}{\sqrt{2}(\sigma_n - \sqrt{2}\sigma_s)}}{\sigma_s^2 - \frac{\sigma_n^2}{2} - \frac{(3\sqrt{2}\sigma_s^2\sigma_n - 6\sigma_s^3)}{\sqrt{2}(\sigma_s - \sqrt{2}\sigma_s)}} \tag{5.100}$$

These two parameters are equal in mean field approximation and as well as in the renormalized approach[17]. The further procedure in mean field approximation is to determine $\lambda_1(m_0^2)$ via m_σ and m_π, see [38, 48, 5] for further details. All these quantities enter in the condensate equations 5.90 and 5.91. Working in an renormalized approach however, we need to rewrite the vacuum contributing part from equation 5.89 in terms of the mathematical fields and derive according to 5.96 with respect to σ_0, σ_8. The corrections are then

$$\begin{aligned} \frac{\partial^2\Omega_{\bar{q}q}^{dr}}{\partial^2\sigma_0^2} &= \kappa\left[\left(96\sigma_0^2 - 48\sqrt{2}\sigma_0\sigma_8 + 48\sigma_8^2\right)\mathcal{W} + \frac{\mathcal{X}\left(\frac{8}{3}\sigma_0 - \frac{2\sqrt{2}}{3}\sigma_8\right)}{\mathcal{Z}}\right] \\ \frac{\partial^2\Omega_{\bar{q}q}^{dr}}{\partial^2\sigma_0\sigma_8} &= \kappa\left[\left(96\sigma_0\sigma_8 - 30\sqrt{2}\sigma_8^2 - 24\sqrt{2}\sigma_0^2\right)\mathcal{W} + \frac{\mathcal{X}\left(\frac{10}{3}\sigma_8 - \frac{2\sqrt{2}}{3}\sigma_0\right)}{\mathcal{Z}}\right] \\ \frac{\partial^2\Omega_{\bar{q}q}^{dr}}{\partial^2\sigma_8^2} &= \kappa\left[\left(48\sigma_0^2 - 60\sqrt{2}\sigma_8\sigma_0 + 150\sigma_8^2\right)\mathcal{W} + \frac{\mathcal{Y}\left(\frac{10}{3}\sigma_8 - \frac{2\sqrt{2}}{3}\sigma_0\right)}{\mathcal{Z}}\right] \end{aligned}$$

[17] This is due to the fact that the corresponding derived fields do not depend on any renormalization, i.e. they do not contribute to the vacuum.

with

$$\kappa = -\frac{N_c N_f}{72\pi^2} g^4$$

$$\mathcal{W} = 2\ln\left(\frac{g\sqrt{\frac{4}{3}\sigma_0^2 + \frac{2\sqrt{2}}{3}\sigma_0\sigma_8 + \frac{5}{3}\sigma_8^2}}{\Lambda}\right) + \frac{1}{2}$$

$$\mathcal{X} = 32\sigma_0^3 - 10\sqrt{2}\sigma_8^3 - 24\sqrt{2}\sigma_0^2\sigma_8 + 48\sigma_8^2\sigma_0$$

$$\mathcal{Y} = 50\sigma_8^3 - 8\sqrt{2}\sigma_0^3 + 48\sigma_0^2\sigma_8 - 30\sqrt{2}\sigma_0\sigma_8^2$$

$$\mathcal{Z} = \frac{4}{3}\sigma_0^2 - \frac{2\sqrt{2}}{3}\sigma_0\sigma_8 + \frac{5}{3}\sigma_8^2$$

as abbreviations. Rewriting everything according to 5.95 in terms of the physical fields, these mass corrections enter in the numerical routine to search for the vacuum parameters λ_1 and m_0^2. As already mentioned, the other quantities remain unaffected. These two parameters compensate then the vacuum contribution in 5.90 and 5.91, and reduces their values to the same as in mean field approximation.

Interesting to note is that also the grand canonical potential remains unaffected by the choice of the renormalization scale parameter Λ. This is as in the SU(2) case, remember the discussion in section 4.4.1, i.e. see equations 4.130 and 4.132, and it also has been shown in [31, 53] for the SU(3) case. In the forthcoming we will choose a value of $\Lambda = 200$ MeV to be in the Λ-QCD range, but this value affects only the vacuum parameters and not the thermodynamics or any other relevant quantity.

5.8.
Thermodynamical quantities

Having performed all necessary calculations to achieve the total grand canonical potential

$$\begin{aligned}\Omega_{tot} &= \mathcal{V} - \frac{N_c N_f}{8\pi^2}\tilde{m}_f^4 \ln\left(\frac{\tilde{m}_f}{\Lambda}\right) - \frac{3}{\pi^2\beta}\int_0^\infty k^2 dk \cdot \mathcal{N} \\ &- \frac{2}{\beta}\int \frac{d^3k}{(2\pi)^3}\ln\left(1+e^{-\frac{E_{k,e}\pm\mu_e}{T}}\right)\end{aligned} \tag{5.101}$$

and the parameter set to start with in the vacuum (previous section 5.7.1), the next step is to define the chemical potentials according to

$$\mu_i = B_i\mu_B + Z_i\mu_Z + L_i\mu_L \tag{5.102}$$

where B indicates the baryon number, Z the charge and L the lepton number of the corresponding particle. It turns out that $\mu_d = \mu_s$, apart from the vector meson contribution, and implementing these, the chemical potentials are

$$\tilde{\mu}_u = \mu_u - g_\omega\omega - g_\rho\rho + \frac{2}{3}\mu_e \tag{5.103}$$

$$\tilde{\mu}_d = \mu_d - g_\omega\omega + g_\rho\rho - \frac{1}{3}\mu_e \tag{5.104}$$

$$\tilde{\mu}_s = \mu_s - g_\phi\phi - \frac{1}{3}\mu_e \tag{5.105}$$

$$\tilde{\mu}_e = -\mu_e + \mu_L \tag{5.106}$$

The derivatives with respect to the fields need to be minimized according to

$$\frac{\partial\Omega}{\partial\sigma_n} = \frac{\partial\Omega}{\partial\sigma_s} = \frac{\partial\Omega}{\partial\omega} = \frac{\partial\Omega}{\partial\rho} = \frac{\partial\Omega}{\partial\phi} \stackrel{!}{=} 0$$

and are called Gap-equations[18] and yield the corresponding field values. With the definitions

$$f(\tilde{\mu}_f) = \frac{1}{1+e^{\beta(E_f-\tilde{\mu}_f)}} \quad \text{and } f(-\tilde{\mu}_f) = \frac{1}{1+e^{\beta(E_f+\tilde{\mu}_f)}} \tag{5.107}$$

the Gap equations read

$$\begin{aligned}
\frac{\partial\Omega}{\partial\sigma_n} &= \lambda_1\sigma_n(\sigma_n^2+\sigma_s^2) + \frac{\lambda_2}{2}\sigma_n^3 + m_{\sigma_n}^2\sigma_n - h_n - \frac{c\sigma_n\sigma_s}{\sqrt{2}} \\
&- \frac{N_cN_f}{8\pi^2}g_n^4\sigma_n^4\ln\left[\frac{g_n\sigma_n}{\Lambda}\right] \\
&+ \frac{3g_n^2\sigma_n}{\pi^2}\int_0^\infty \frac{dk\cdot k^2}{E_n}\left(f(\tilde{\mu}_u)+f(-\tilde{\mu}_u)+f(\tilde{\mu}_d)+f(-\tilde{\mu}_d)\right) \\
\frac{\partial\Omega}{\partial\sigma_s} &= \lambda_1\sigma_s(\sigma_n^2+\sigma_s^2) + \lambda_2\sigma_s^3 + m_{\sigma_s}^2\sigma_s - h_s - \frac{c\sigma_n^2}{2\sqrt{2}} \\
&- \frac{N_cN_f}{8\pi^2}g_s^4\sigma_s^4\ln\left[\frac{g_s\sigma_s}{\Lambda}\right] \\
&+ \frac{3g_s^2\sigma_s}{\pi^2}\int_0^\infty \frac{dk\cdot k^2}{E_s}\left(f(\tilde{\mu}_s)+f(-\tilde{\mu}_s)\right] \\
\frac{\partial\Omega}{\partial\omega} &= -m_\omega^2\omega + \frac{3g_\omega}{\pi^2}\int_0^\infty dk\cdot k^2\left[f(\tilde{\mu}_u)-f(-\tilde{\mu}_u)+f(\tilde{\mu}_d)-f(-\tilde{\mu}_d)\right] \\
\frac{\partial\Omega}{\partial\rho} &= -m_\rho^2\rho + \frac{3g_\rho}{\pi^2}\int_0^\infty dk\cdot k^2\left[f(\tilde{\mu}_u)-f(-\tilde{\mu}_u)-f(\tilde{\mu}_d)+f(-\tilde{\mu}_d)\right] \\
\frac{\partial\Omega}{\partial\phi} &= -m_\phi^2\phi + \frac{3g_\phi}{\pi^2}\int_0^\infty dk\cdot k^2\left[f(\tilde{\mu}_s)+f(-\tilde{\mu}_s)\right]
\end{aligned} \tag{5.108}$$

To perform calculations in mean field approximation the vacuum contributing term in the potential, equation 5.88, has to vanish, such as the respective derivations of the vacuum term in 5.108 of course. For the treatment of compact stars in the following chapter 6, not only the charge neutrality constraint

$$\sum_{i=u,d,s,e} Q_i n_i = \frac{2}{3}n_u - \frac{1}{3}n_d - \frac{1}{3}n_s - n_e = 0 \tag{5.109}$$

[18] Which is a slightly more complicated form of a Klein-Gordon equation (recall section 3.4)

where $n_i \equiv -\frac{\partial \Omega_{tot}}{\partial \mu_i}$ is the particle density of each considered species i, has to be fulfilled, but also a temperature approximation $T \to 0$ has to be done. This has been part of my master thesis and hence the $T \to 0$ calculation can be found in detail in [5, 56, 57].
The derivatives with respect to the chemical potentials (that is the corresponding particle density) and temperature (that is the entropy density) are the same quantities as in SU(2), see equations 4.2, and also known from ordinary thermodynamics. These quantities are necessary to achieve an equation of state respecting temperature effects, i.e. a **Supernova equation of state**.

5.8.1.
Electron-baryon rate

We have so far fixed all parameters which are essential to compute the respective thermodynamical quantities, given by the solutions of the Gap equations 5.108 and the implementation of charge neutrality equation 5.109. Another constraint for Supernovae is the electron-baryon rate

$$Y_e = \frac{n_e}{n_B} = \frac{3n_e}{n_u + n_d + n_s} \tag{5.110}$$

which is usually in the range $0 \leq Y_e \leq 0.5$. $Y_e = 0$ means, there are no leptons at all, $Y_e = 0.2$ corresponds to the conditions during the SN explosion and $Y_e = 0.4$ represents the situation of the massives stars core shortly before the explosion [51], see the next section 5.9 for a short illustration on Supernovae and further references on corresponding literature.

5.8.2.
Thermal evolution in the SU(3) model

In this section we present our results at finite temperature in the SU(3) Quark Meson model with- and without vacuum term.

Variation in Temperature

Figure 5.3 shows the solutions of the condensate equations 5.108 in mean field approximation, i.e. without vacuum contribution (equation 5.88).

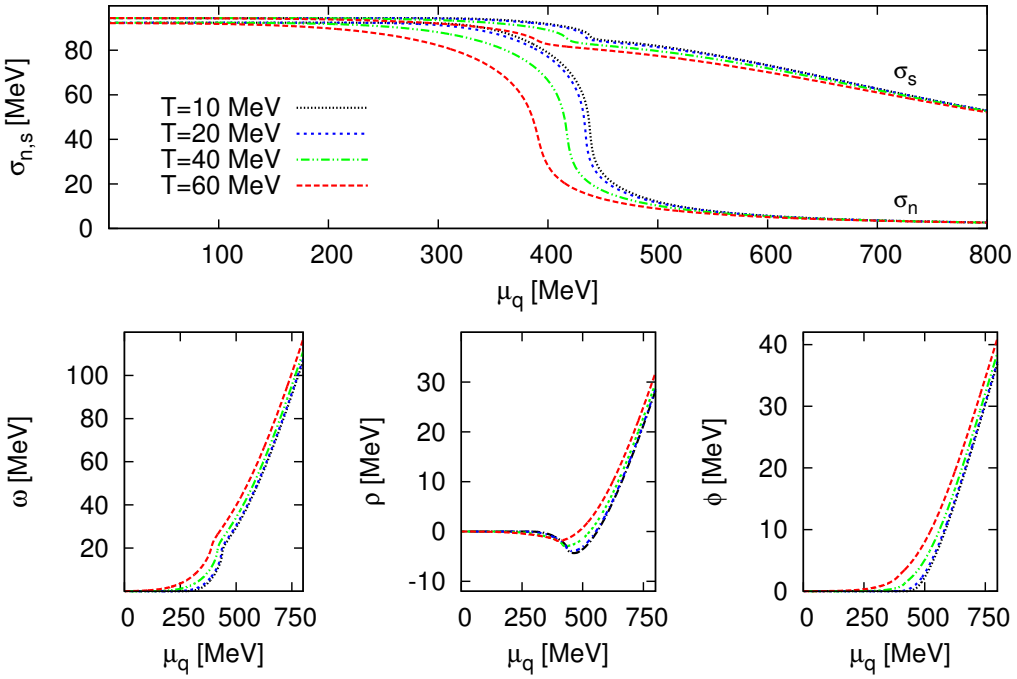

Figure 5.3: *The solutions of the condensate equations 5.108 in mean field approximation for different values of the temperature for the parameter choice* $m_\sigma = 600\ MeV$, $m_q = 300\ MeV$, $g_\omega = 3$, $B^{1/4} = 100\ MeV$ *and* $Y_e = 0.2$ *as a function of the quark chemical potential* μ_q. *The nonstrange and strange* σ *condensate are shown in the upper figure, whereas the vector fields are shown in the three lower plots.*

For larger temperature the phase transition sets in at lower values of the quark chemical potential μ_q and both scalar condensates melt away faster[19], whereas the vector fields increase with larger temperature, which can be seen in the lower three plots in figure 5.3. Figure 5.4 shows the fields as

[19]This is reasonable since QCD is expected to be restored at high chemical potential and large temperatures, therefore the scalar condensates melt away faster.

a function of the chemical potential for two different temperatures in mean field approximation and with the vacuum term.

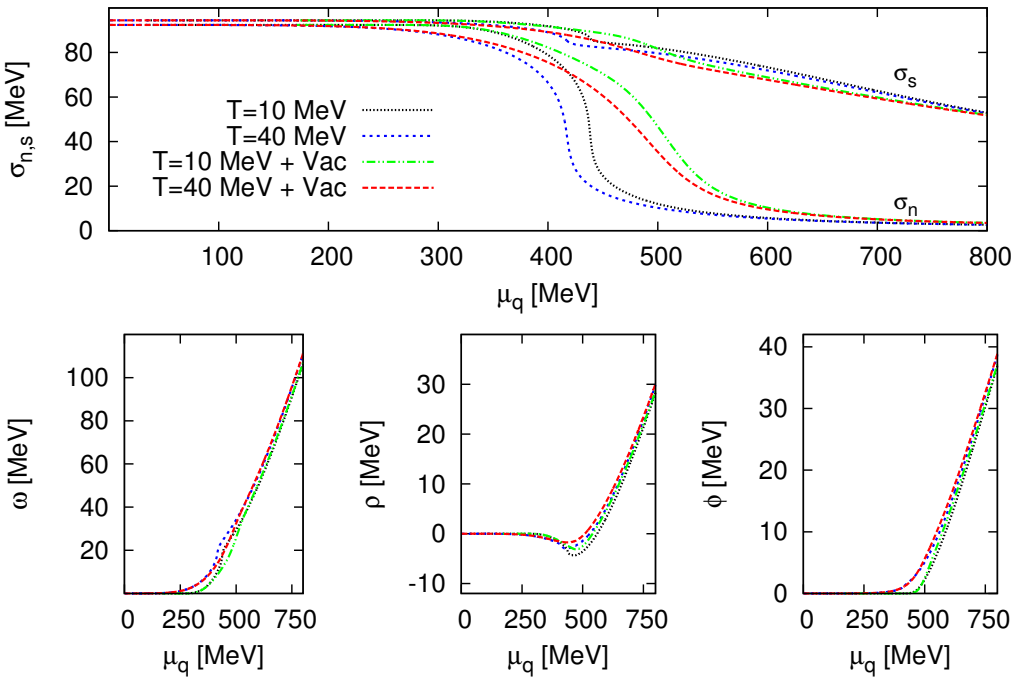

Figure 5.4: *The solutions of the condensate equations 5.108 for two different values of the temperature in mean field approximation and with the vacuum term for the parameter choice* $m_\sigma = 600\ MeV$, $m_q = 300\ MeV$, $g_\omega = 3$, $B^{1/4} = 100\ MeV$ *and* $Y_e = 0.2$ *as a function of the quark chemical potential* μ_q. *The nonstrange and strange* σ *condensate are shown in the upper figure, whereas the vector fields are shown in the three lower plots.*

Respecting the vacuum term, it can be seen that the nonstrange condensate is shifted to considerably larger values of the chemical potential, whereas the strange condensate shows hardly any influence respecting the vacuum term. The nonstrange fields reaches the chirally restored phase, whereas the strange field remains in the broken phase. This is due to the fact, that the strange quark is heavier. The repulsive vector fields change unsignificantely compared to the mean field case. This might be explained due to the fact

that the vacuum contribution in the potential, equation 5.88, just consists of contributions from the scalar sector.

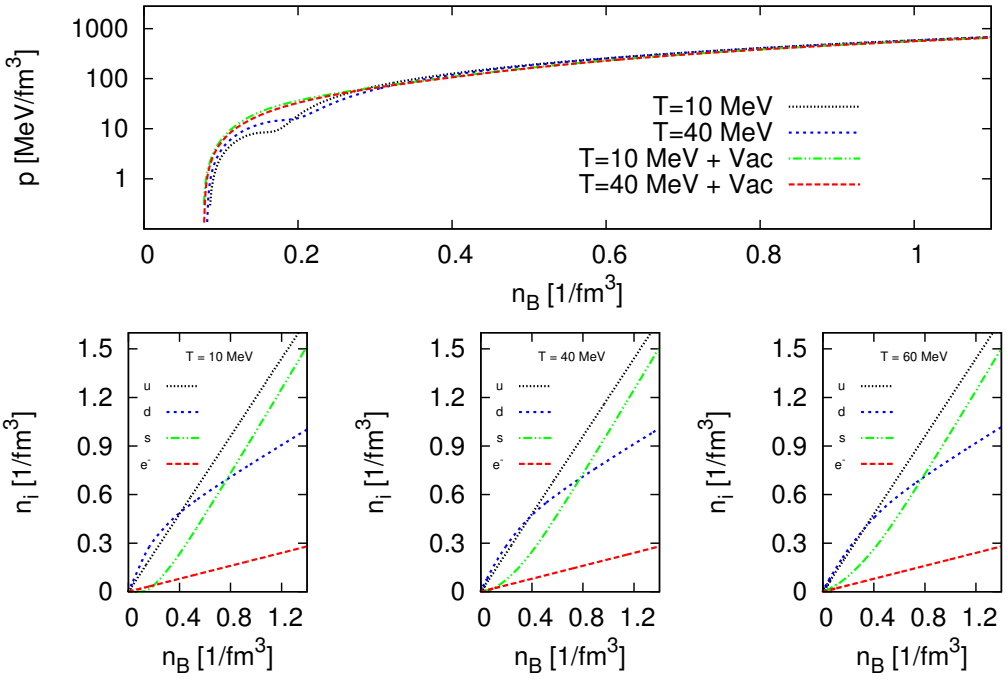

Figure 5.5: *The pressure p and the fermion densities n_i as a function of the baryon number density n_B in mean field approximation and with the vacuum term for different values of the temperature for the parameter choice $m_\sigma = 600\ MeV$, $m_q = 300\ MeV$, $g_\omega = 3$, $B^{1/4} = 100\ MeV$ and $Y_e = 0.2$. The upper plot $p(n_B)$ shows differences when respecting the vacuum contribution for two different temperatures, whereas the lower plot shows the fermion densities with the vacuum term.*

Figure 5.5 shows the pressure as a function of the baryon number density for different values of the temperature respecting and neglecting the vacuum term. The phase transition happens to be $n_B \simeq 0.18/\mathrm{fm}^3$ for any case at slightly various values of the pressure. The quark number densities are also only slightly affected by increasing the temperature. The lower plots in figure 5.5 shows the densities with the fermion vacuum contribution, where a small impact for different temperatures can be seen for low n_B. Here

the down quark density is somewhat above the up quark density for $T = 10$ MeV, corresponding to a larger negative value of the ρ field, i.e. the difference between up- and down quarks (see figure 5.3). Increasing the temperature suppresses the down quark density at small n_B. At large n_B there is however no significant change among the densities, which is also the case for $p(n_B)$, because the scalar fields reach the chirally restored phase likewise. The calculation in mean field approximation is quantitatively of the same behaviour, without a noteworthy significant change for the quark number densities.

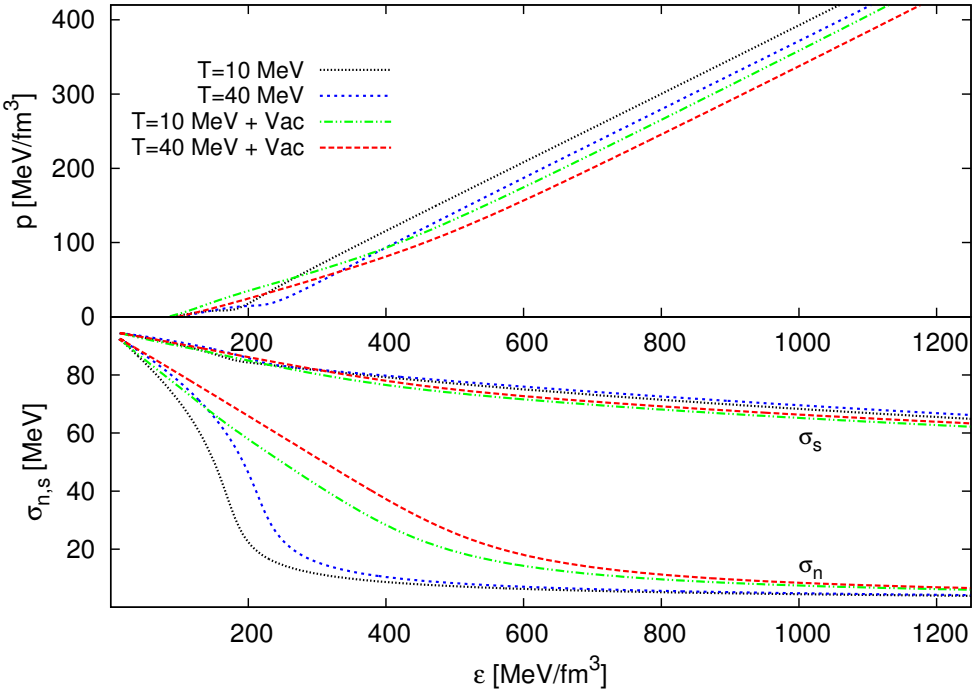

Figure 5.6: *The pressure p and the scalar condensates as a function of the energy density ϵ in mean field approximation and with the vacuum term for two different values of the temperature for the parameter choice $m_\sigma = 600$ MeV, $m_q = 300$ MeV, $g_\omega = 3$, $B^{1/4} = 100$ MeV and $Y_e = 0.2$.*

Figure 5.6 shows the pressure and the scalar fields as a function of the energy density. The EoSs with and without the fermion vacuum term (upper plot) are softer for larger temperatures, which is counterintuitive. However, this

can be explained because of the interactions considered within the system. Recall that in a nonrelativistic system p increases with temperature, in a relativistic system $p \sim \frac{\epsilon}{3}$, that is, the pressure p is independent of temperature. In our case the interactions are consequently responsible for the softening of the EoS with increasing temperature. The scalar fields as a function of the energy density underline the statement (lower plot), because the phase transition occures at a larger value of ϵ. The EoS with vacuum term show some noteworthy differences for $150 \leq \epsilon \leq 400$ MeV/fm^3. For both values of the temperature the EoS is more linear-like and cross $p = 0$ at lower values of the energy density, making the EoS stiffer in the low energy regime and softer in the high energy regime. As has been the case for $\sigma(\mu_q)$ in figure 5.4, $\sigma(\epsilon)$ changes significantely only in the nonstrange sector. The linear-like behaviour of the EoS in the low energy regime discussed above can be backtraced to the course of the nonstrange condensate as a function of the energy density, which can be seen in the lower plot in figure 5.6.

Variation in electron-baryon rate Y_e

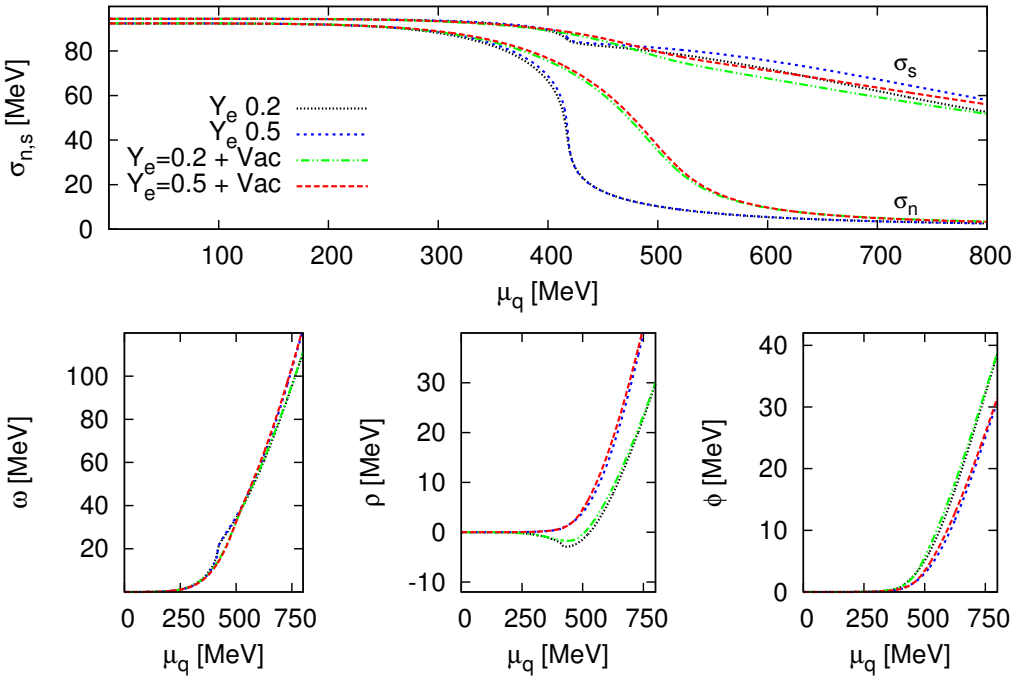

Figure 5.7: *The solutions of the condensate equations 5.108 for two different values of Y_e in mean field approximation and with the fermion vacuum term for the parameter choice $m_\sigma = 600$ MeV, $m_q = 300$ MeV, $g_\omega = 3$, $B^{1/4} = 100$ MeV and $T = 40$ MeV as a function of the quark chemical potential μ_q. The nonstrange and strange σ condensate are shown in the upper figure, whereas the vector fields are shown in the three lower plots.*

Figure 5.7 shows the behaviour of the fields in mean field approximation and with the vacuum term as a function of the chemical potential μ_q. The influence of the vacuum term is analoguous to the situation discussed for different values of the temperature, that is the phase transition is shifted to larger values of μ_q. Inclusion of the fermion vacuum contribution shifts the ρ condensate to lower values at given μ_q compared to the case when neglecting it. In the same amount the ϕ condensate is affected to somewhat larger values. The influence of the vacuum term consequently affects the

quark number densities and $p(n_B)$ in figure 5.8. However, unlike as the nonstrange field, σ_s does not reach the chirally restored phase for both cases, i.e. respecting or neglecting the vacuum term. For both cases a lower electron fraction means, that the the condensate melts away slightly faster, because of the presence of more strange quarks, which can also be seen in the lower plots in figure 5.8. The repulsive vector fields in the lower three plots in figure 5.7 underline the same statement. The nonstrange repulsive fields ω and ρ are proportional to the nonstrange quark density and thus larger for lower electron fraction, whereas the strange field ϕ is suppressed for large electron fraction. The ρ condensate is proportional to the difference between up- and down quarks. If there is a region where more down quarks then up quarks are present, its value is negative until the up quarks redominate the system again, which is consistent with the lower plots in figure 5.8.

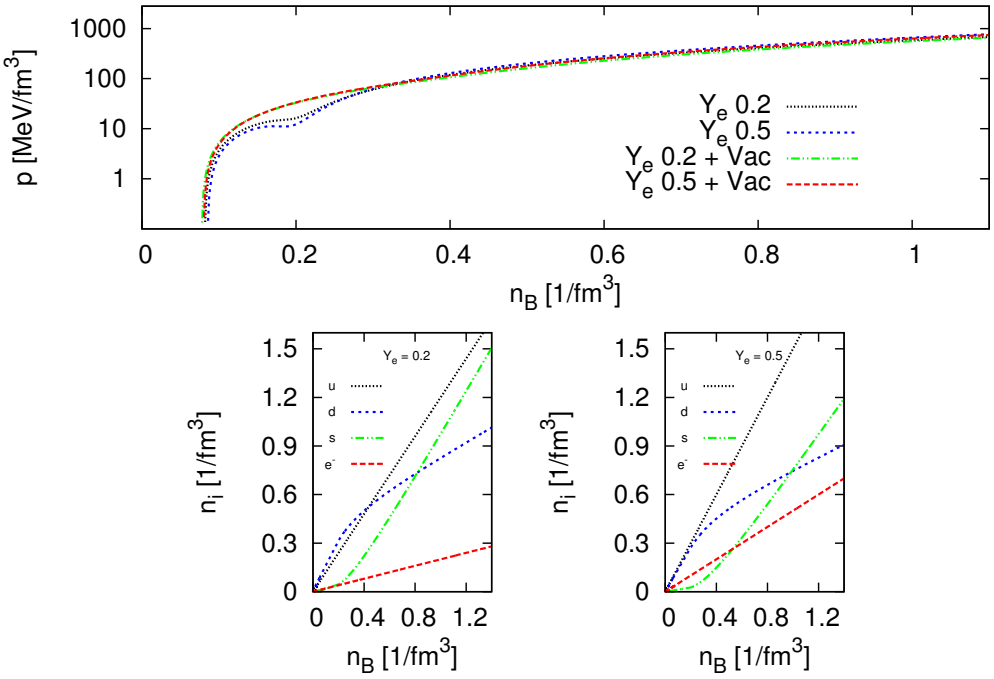

Figure 5.8: *The pressure p and the fermion densities n_i as a function of the baryon number density n_B in mean field approximation and with the vacuum term for two different values of Y_e for the parameter choice $m_\sigma = 600$ MeV, $m_q = 300$ MeV, $g_\omega = 3$, $B^{1/4} = 100$ MeV and $T = 40$ MeV. The upper plot $p(n_B)$ shows differences when respecting the vacuum contribution for two different values of Y_e, whereas the lower plot shows the fermion densities with the vacuum term.*

Figure 5.8 shows the pressure as a function of the baryon number density. As for different temperatures, $p(n_B)$ is only affected around the chiral phase transition ($n_B \simeq 0.18/\text{fm}^3$). The lower two figures show the influence of Y_e on the quark number densities respecting the vacuum term[20]. The electron fraction remains low for a low value of Y_e. For $Y_e = 0.2$ up to $n_B \simeq 0.4$ there are more down- then up quarks corresponding to a negative value of the ρ field (see figure 5.7), which couples to the isospin density. As has been the

[20] Comparing to mean field approximation the quark number densites are quantitatively the same. The down and strange change only slightly around $0 \leq n_B \leq 0.4$

case for different temperatures, there is hardly any difference for the quark number densities in mean field approximation to be seen.

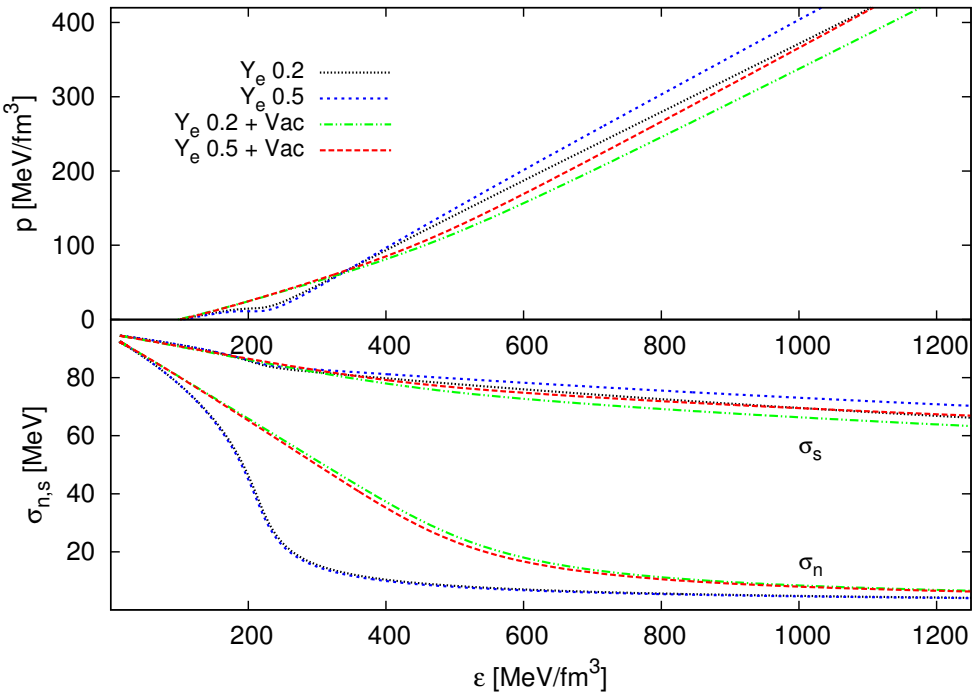

Figure 5.9: *The pressure p and the scalar condensates as a function of the energy density ϵ for two different values of Y_e in mean field approximation and with the vacuum term for the parameter choice $m_\sigma = 600\ MeV$, $m_q = 300\ MeV$, $g_\omega = 3$, $B^{1/4} = 100\ MeV$ and $T = 40\ MeV$.*

The EoS $p(\epsilon)$ is shown in the upper plot in figure 5.9. $p(\epsilon)$ is stiffer for larger Y_e in the high density regime, because the strange scalar field reaches the chirally restored phase later, see figure 5.7, i.e the electron contribution to the pressure becomes important since the strange quark is a bit more suppressed. This statement is valid in mean field approximation and as well when considering the fermion vacuum contribution. The vacuum term influences the EoS in the same manner as discussed for different temperatures: The influence of the nonstrange condensate as a function of the energy density (lower plot in figure 5.9) influences the stiffness in the low energy regime, whereas for high densites the EoS respecting the vacuum term becomes softer.

Variation of the sigma meson mass

Figure 5.10 shows the scalar and vector condensates as a function of the chemical potential in mean field approximation. For $m_\sigma = 400$ MeV a first order phase transition occurs, whereas for larger values of the sigma meson mass m_σ the scalar condensates are longer in the chirally broken phase and the phase transition is smoother[21].

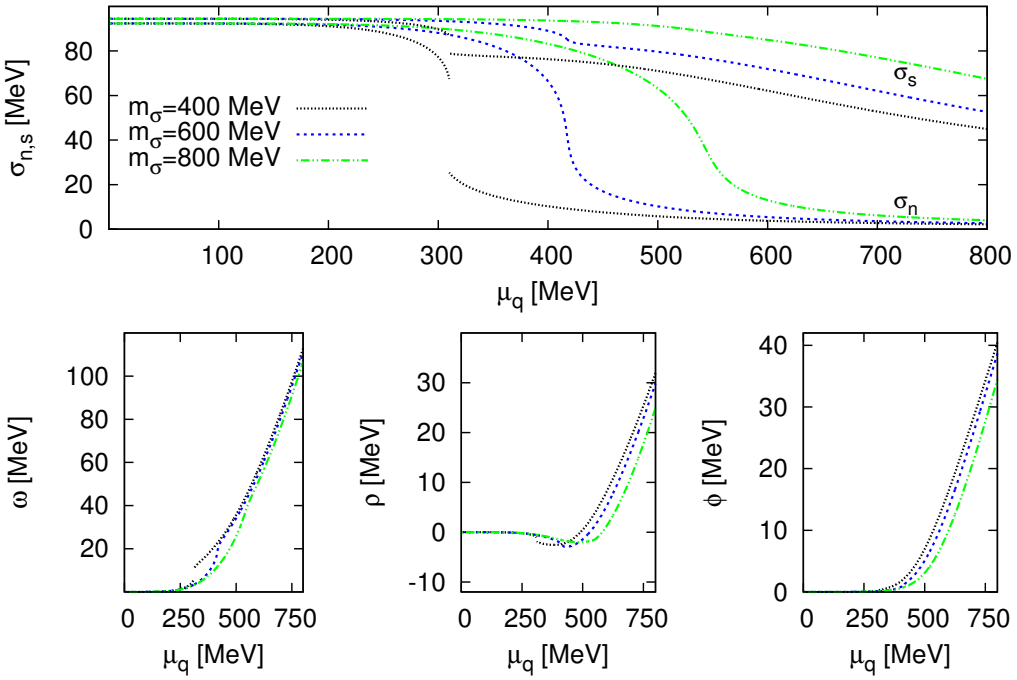

Figure 5.10: *The solutions of the condensate equations 5.108 for different values of the sigma meson mass m_σ in mean field approximation for the parameter choice $m_q = 300$ MeV, $g_\omega = 3$, $B^{1/4} = 100$ MeV, $T = 40$ MeV and $Y_e = 0.2$ as a function of the quark chemical potential μ_q. The nonstrange and strange σ condensate are shown in the upper figure, whereas the vector fields are shown in the three lower plots.*

This behaviour can be translated from the SU(2) model: The value of the

[21] As we will see, raising the repulsive vector coupling has the same influence on the fields, but stiffens the EoS, whereas for larger m_σ the EoS is softer.

sigma meson mass determines the coupling λ (recall the discussion in section 4.4 and see equation 4.112), so that a larger value of the sigma meson mass is proportional to a larger λ, i.e. more energy is needed to develop the second minimum in the potential → the phase transition is shifted to larger chemical potentials, which is analoguous in the SU(3) case, although not immediately that eyecatching.

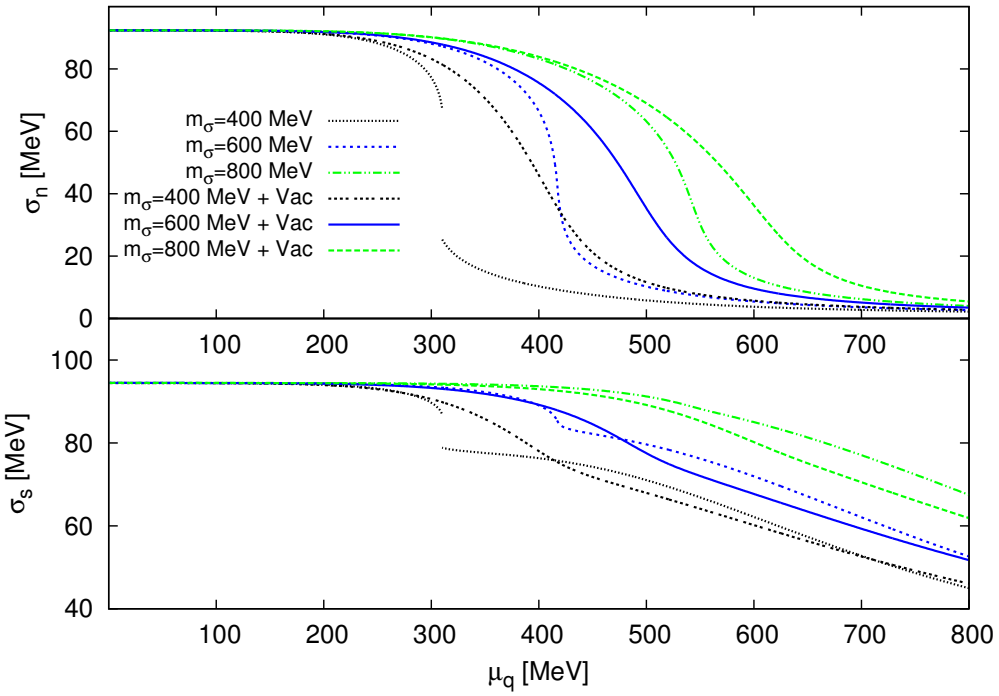

Figure 5.11: *The solutions of the condensate equations 5.108 for different values of the sigma meson mass m_σ in mean field approximation and with the vacuum term for the parameter choice $m_q = 300$ MeV, $g_\omega = 3$, $B^{1/4} = 100$ MeV, $T = 40$ MeV and $Y_e = 0.2$ as a function of the quark chemical potential μ_q.*

The incorporation of the vacuum term leads (as in any case considered so far) to a smoothening of the fields course, see figure 5.11. For $m_\sigma = 400$ MeV the first order phase transition has become a crossover. Respecting the vacuum contribution the phase transition however shifts to considerable larger values of the chemical potential, which has already been observed in the SU(2)

case as a function of the temperature, see figure 4.15 in section 4.4.2, and is therefore not surprising. The discussion in section 4.4.2 can be consultetd as a guideline for various m_σ and is also valid in the SU(3) case for running μ_q.

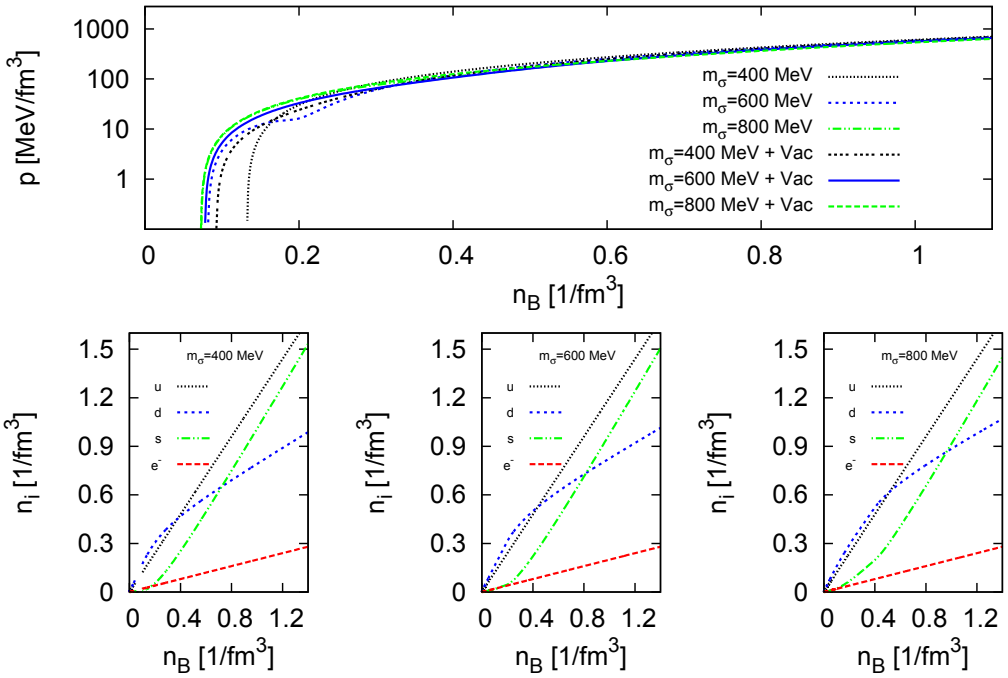

Figure 5.12: *The pressure p and the fermion densities n_i as a function of the baryon number density n_B for different values of the sigma meson mass m_σ in mean field approximation and with the vacuum term for the parameter choice $m_q = 300\ MeV$, $g_\omega = 3$, $B^{1/4} = 100\ MeV$, $T = 40\ MeV$ and $Y_e = 0.2$. The upper plot $p(n_B)$ shows differences when respecting the vacuum contribution for three different values of m_σ, whereas the lower plot shows the fermion densities with the vacuum term.*

Figure 5.12 shows the pressure as a function of the baryon number density. As in the previous discussed cases, differences occur only around $n_B \simeq 0.18/\mathrm{fm}^3$, from there on the functions degenerate. A large value of the sigma meson mass corresponds to more nonstrange quarks being present[22]. The strange

[22]This is reasonable, since the sigma meson consists of nonstrange quarks.

quark density n_s is therefore slightly suppressed, which can be seen in the lower plots in figure 5.12 and also in the behaviour of the ϕ condensate in figure 5.10.

The EoSs in mean field approximation and with the vacuum term are shown in figure 5.13. The EoSs become softer for larger m_σ, because of its influence on the vacuum parameters λ_1 and m_0^2 (recall the discussion in section 5.7.1) which are mainly responsible for the potentials depth, i.e. the minimum in the grand canonical potential. Differences occur again at low energy densities, where the vacuum term leads generally to a stiffening. At high energy densites the vacuum term respecting EoSs are softer.

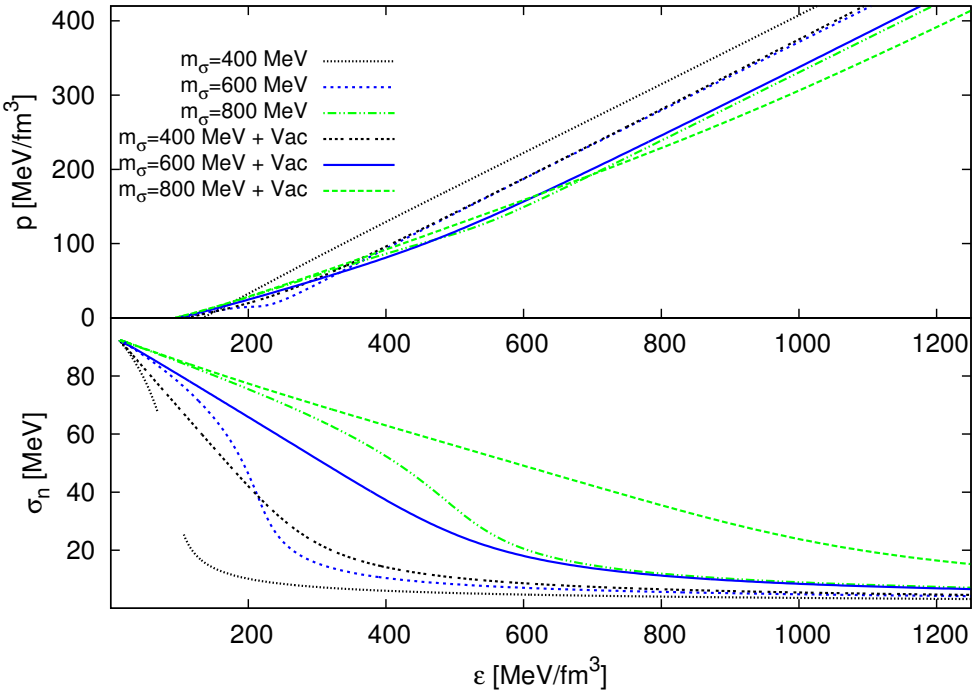

Figure 5.13: *The pressure p as a function of the energy density ϵ for different values of the sigma meson mass m_σ in mean field approximation and with the vacuum term for the parameter choice $m_q = 300$ MeV, $g_\omega = 3$, $B^{1/4} = 100$ MeV, $T = 40$ MeV and $Y_e = 0.2$.*

Variation of the repulsive coupling at $Y_e = 0.2$

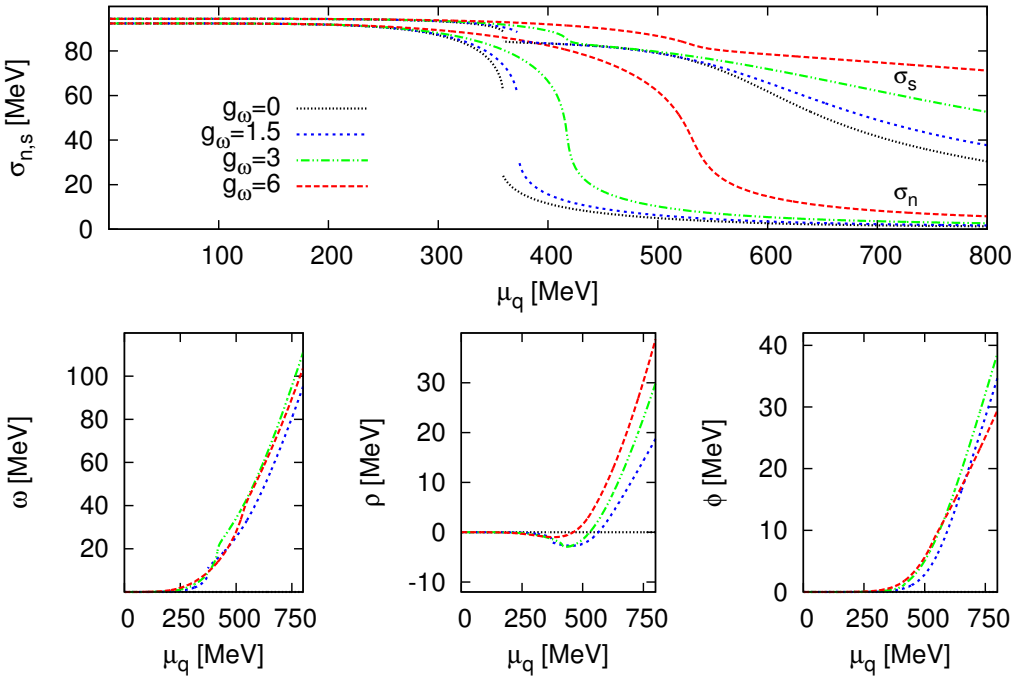

Figure 5.14: *The solutions of the condensate equations 5.108 for different values of the repulsive coupling* g_ω *in mean field approximation for the parameter choice* $m_\sigma = 600$ *MeV,* $m_q = 300$ *MeV,* $B^{1/4} = 100$ *MeV,* $T = 40$ *MeV and* $Y_e = 0.2$ *as a function of the quark chemical potential* μ_q.

Figure 5.14 shows the scalar and the vector fields as a function of the chemical potential in mean field approximation. Small values of the repulsive coupling exhibit a first order phase transition, which is not seen anymore when taking into account the vacuum term, see figure 5.15. As has been discussed before for the other parameter variations, the vector fields show hardly any influence on the vacuum term.

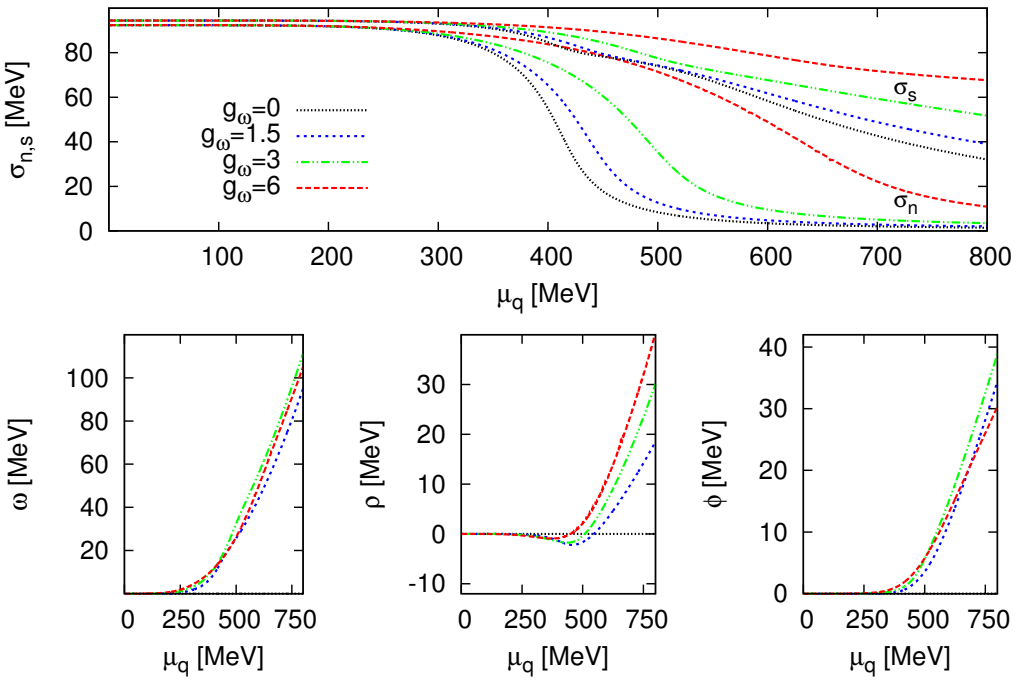

Figure 5.15: *The solutions of the condensate equations 5.108 for different values of the repulsive coupling g_ω with the vacuum term for the parameter choice $m_\sigma = 600\ MeV$, $m_q = 300\ MeV$, $B^{1/4} = 100\ MeV$, $T = 40\ MeV$ and $Y_e = 0.2$ as a function of the quark chemical potential μ_q.*

The pressure as a function of the baryon number density can be seen in figure 5.16. The first order phase transition for vanishing repulsion in mean field approximation is responsible for the jump in n_B in the upper figure, which disappears when respecting the vacuum term. The lower figures show the quark number densites. Choosing $Y_e = 0.5$ the densities would change according to the electron fraction, similar as in figure 5.8.

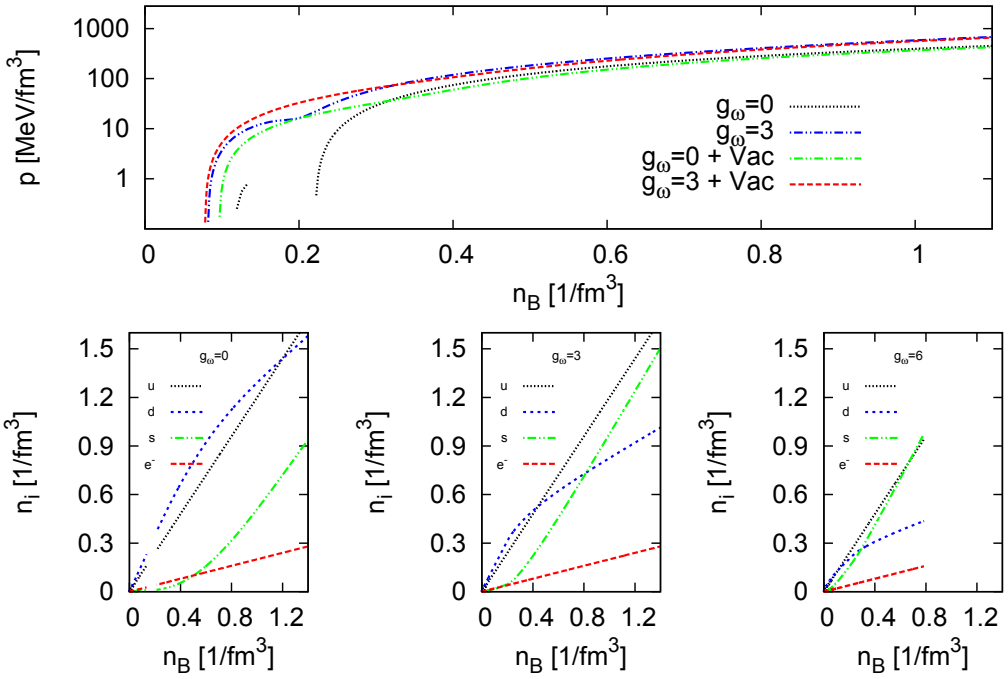

Figure 5.16: *The pressure p and the fermion densities n_i as a function of the baryon number density n_B for different values of the repulsive coupling g_ω in mean field approximation and with the vacuum term for the parameter choice $m_q = 300\ MeV$, $g_\omega = 3$, $B^{1/4} = 100\ MeV$, $T = 40\ MeV$ and $Y_e = 0.2$. The upper plot $p(n_B)$ shows differences when respecting the vacuum contribution for two different values of g_ω, whereas the lower plot shows the fermion densities with the vacuum term.*

Figure 5.17 shows the equation of state in mean field approximation (upper figure) and with the vacuum term (lower figure). Neglecting the vacuum contribution leads to a nonlinear behaviour of the EoS in the low energy regime, whereas its consideration leads to a nearly equal start at $\epsilon \leq 150\text{MeV/fm}^3$ but a splitting-up of the EoS at $200 \leq \epsilon \leq 800\text{MeV/fm}^3$, to finally degenerate again. Respecting the vacuum term leads generally to a softer EoS.

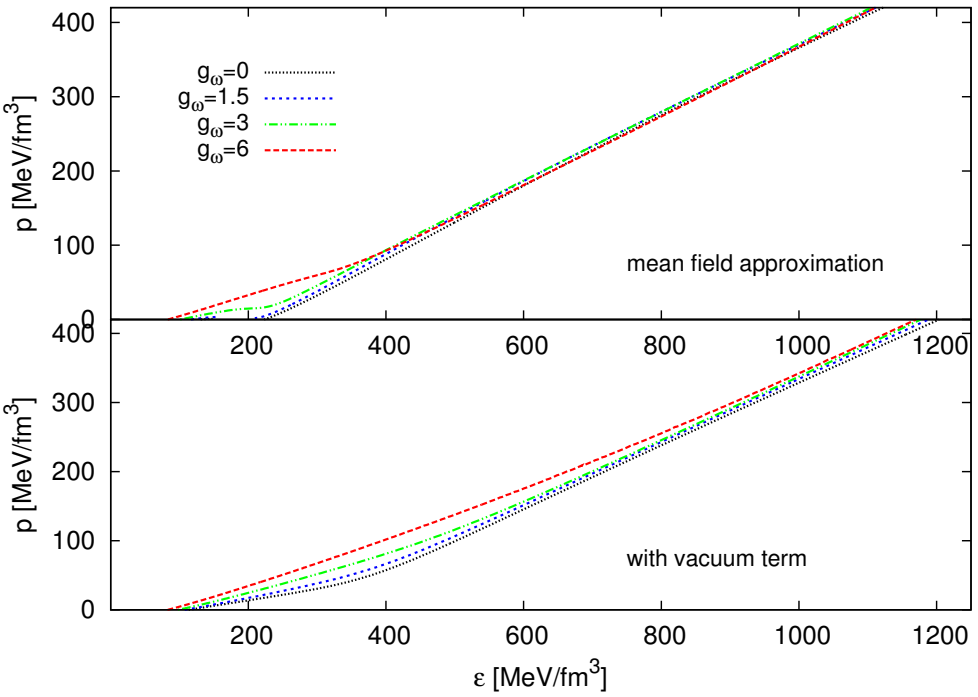

Figure 5.17: *The equation of state in mean field approximation (upper figure) and with the vacuum term (lower figure) for various values of the repulsive coupling g_ω for the parameter choice $m_\sigma = 600\ MeV$, $m_q = 300\ MeV$, $B^{1/4} = 100\ MeV$, $T = 40\ MeV$ and $Y_e = 0.2$.*

Raising the value of the electron-baryon rate in mean field approximation leads to more separated EoSs in the high energy realm. As already mentioned at the end of section 5.7.1 the grand potential is independend of any renormalization scale parameter Λ, and consequently is the equation of state. If choosing $Y_e = 0.5$ and varying the repulsive coupling, no noteworthy difference in the course of the scalar fields is detectable. The repuslive fields are however effected due to a larger electron fraction, which suppresses the ϕ-field and thereby the system has a lower strange quark density. Furthermore a larger Y_e changes the percentage of the nonstrange densities. This is not surprising due to the discussion on the variation of Y_e before and is important for the EoS, which is clearly more separated in the high energy realm for large Y_e. [58]

5.9. Supernovae

If the initial mass of an ordinary star exceeds eight solarmasses, carbon and oxygen burning starts in the core. Around this very core is a shell of helium, also fusioning. The star has a onion-like structure, since new burning processes in the core will take place, surrounded by the outer burning shells. The star largely expands and is called a *Red giant*[23]. Once iron is produced in the core, no burning process is left to generate energy to fusion even heavier elements. At some critical mass the iron core collapses and the electrons are captured by the nuclei to form neutrons. The neutrons inside this core are then degenerate just as the electrons are in a white dwarf[24]. The outer layers bounce of the ultradense and (nearly) incompressible neutron core and generate a shock wave through the red giant star, which eventually will explode in a core collapse supernova Type II.

This neutron core is called proto-neutron star and its temperature in the core is $\sim$ 10MeV. After 10.000 years the temperature cools down to 100 keV[25] mainly due to neutrino emission, and after that the stars cooling is dominated by photo emissivity. The neutrino emissivity takes place through charged (URCA process) and uncharged (Bremsstrahlung) weak interaction processes [59, 60, 61, 62, 63, 64]. Studying the temperature evolution of such proto-neutron stars, one can gain insight to the thermal conductivity, heat capacity, solid state physics of the crust and super conductivity for instance [65]. Cooling processes via neutrino emission are very sensitive to the EoS and thereby to the mass and radius of the compact star. The evolution of the star will be governed by the timescale for release of the trapped neutrinos, refered to as *deleptonization*, and the timescale for thermal cooling, which reduces the entropy to a small value[26].

[23] The most famous Red giant Beteigeuze with $20M_{\odot}$ has a radius of $\sim 1200\mathrm{R}_{\odot}$.

[24] As we will see in chapter 6, degenerate neutrons are not sufficent to explain stars with $M \geq 0.9M_{\odot}$. Repulsive interactions need to be taken into account.

[25] The temperature on the compact staars surface is about two magnitudes smaller.

[26] The different types of compact stars in chapter 6 are indeed all calculated at $T = 0 \rightarrow s = 0$, s being the entropy density.

5.9.1.

Isentropes: Constant entropy per bayron

The structure of a proto-neutron star is strongly influenced by the presence of trapped neutrinos and, to a somewhat lesser extent, by the non-zero entropy per baryon rate [66]. The de-facto evolution of the connection between entropy- and neutrinofraction is a complex subject [67], but it is common use to look for isentropes in the $T - \mu$ plane, i.e. lines of constant entropy per baryon[27].

In the outer layers of the proto-neutron star the entropy is rather large, because of the shock wave through the progenitor and neutrino trapping. This stage is hard to model via a constant entropy per baryon rate, but $s = 2$ and $Y_e = 0.4 - 0.5$ is assumed to be a good approximnation after the stars formation [68, 69].

The stage when deleptonization sets in and the entropy decreases, can be approximated with $s = 1$ and $Y_e = 0.2 - 0.3$ (or even less than 0.2). The star can be considered as cold in beta equilibrium, see equations 5.103, 5.104, 5.105, 5.106, when the neutrinos have left the star. Then $T \to 0$, i.e. $s \to 0$ and thereby $Y_e \ll 1$.

[27] Recall the discussion from section 4.1 on the entropy density s.

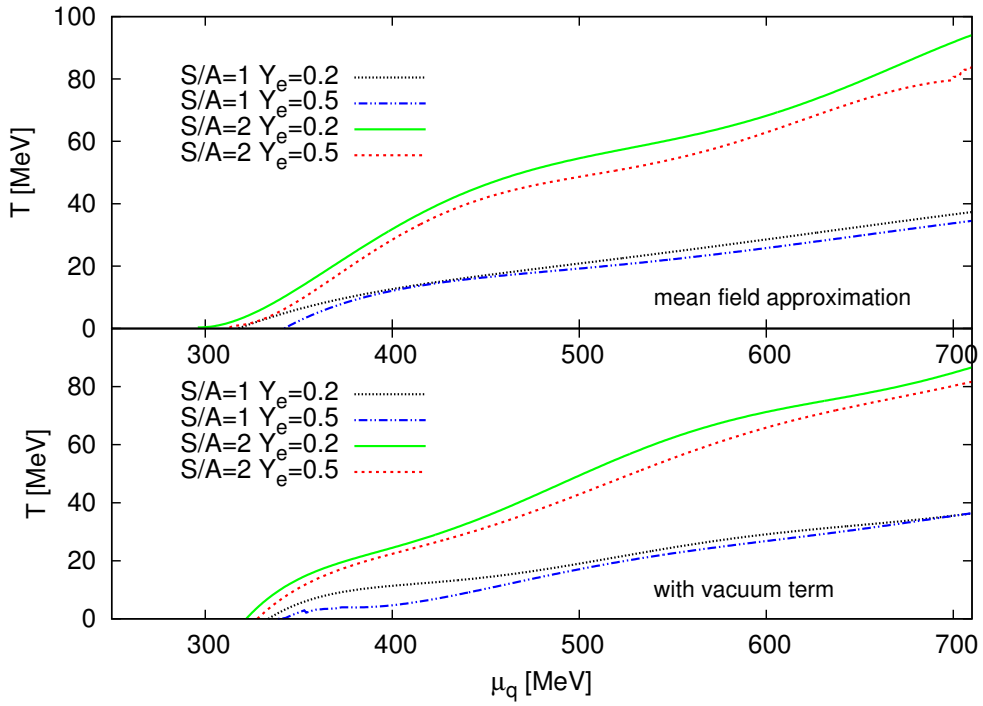

Figure 5.18: *Temperature as a function of the chemical potential for isentropes with $S/A = 1$ and $S/A = 2$ in mean field approximation (upper plot) and with the vacuum term (lower plot) for two different values of the electron baryon rate Y_e. The other parameters are $m_\sigma = 600\ MeV$, $m_q = 300\ MeV$, $g_\omega = 3$, $B^{1/4} = 100\ MeV$.*

Figure 5.18 shows lines of constant entropy per baryon (so calles isentropes) in the $T - \mu$ plane in mean field approximation and with vacuum term. As generally one can say that for $T = 0$ also $s = 0$, that is that all neutrinos have left the (proto) neutron star, and a $T \to 0$ approximation is justified. The region between the $T = 0$ axis and $S/A = 1$ indicates a boundary where the neutrinos are leaving the (proto) neutron star and above $S/A = 2$ the neutrinos are still trapped inside the proto neutron star. This statement is physically reasonable because at high temperatures and low density (i.e. low μ_q) the Supernova remnant has just formed. Increasing the density and cooling of the star via neutrino emission, decreases the entropy per baryon. Finally the star can be considered as cold and ultradense.

All curves start at $T = 0$ around $300 \leq \mu_q \leq 330$ MeV:
The region where the chiral phase transition sets in, and increase at first sight approximately linear. This linear behaviour of the isentropes can be explained with considerations from the Stefan-Boltzmann limit for the Quark Meson model, see section 4.1, just divide equation 4.5 by equation 4.6 to see that $\frac{s}{n_f} = \frac{S}{A} \propto \frac{T}{\mu}$.
As expected from the discussion above, the $S/A = 2$ curves are well above the $S/A = 1$ curves and the electron-baryon rate Y_e softens the course slightly with increasing Y_e, more noteable for $S/A = 2$ then for $S/A = 1$. The S/A development is highly related to the EoS, because the entropy and the quark densities enter in the energy density, see also the EoS for different Y_e in figure 5.9. The connection beteen EoS and S/A explains why there is more deviation of the different isentropes at low T and μ, than at larger values of T and μ. The other parameters have not only been chosen in accordance with the investigation on the fields and the corresponding EoSs in section 5.8.2, but also with the knowledge on the constraints and results in the compact star sector to be exposed in chapter 6.

6

Compact stars

The final stages of the evolution of *ordinary* stars are so called **compact stars**. The term **compact stars** illustrates that these objects are very dense compared to matter mankind usually deals with and refers to *White dwarfs*, *neutron stars* and in some sense to *black holes*. How these objects come to exist will be described in the respective following sections. However, after sufficient time a compact object will cool down, at least on nuclear scale. Once the star has dropped in temperature below an MeV[1] it is considered to be cold enough to calculate the corresponding pressure and energy density[2] in the $T = 0$ limit.

6.1. White Dwarfs

Although not that compact to be described by general relativity a white dwarf has its right to be shortly mentioned within this thesis, not only because it serves as an entrance to general relativistic effects, but also because

[1] 1eV= 11605 K

[2] Remember the discussion at the end of section 2.2.2

of interesting astrophysics behind the scenes.
The nuclear process in an ordinary star will firstly stop when all the helium is burned up to carbon, nitrogen and oxygen, so that the temperature eventually decreases. The star shrinks and so the pressure in the core increases. If the stars initial mass is $\leq 8M_{\odot}$ the gravitational pull is to weak to reach the required pressure to ignite carbon burning. The star sheds out its outer layers in a planetary nebula, and the remnant core is called *White dwarf*, whose interior consits of a degenerate gas of electrons which are responsible for the intrinsic high pressures. Because of their comparably small mass, electrons are the first particles to become degenerate. Since there are no more fusion processes, the dwarf needs a different force than thermal pressure to maintain hydrostatic equilibrium. With increasing density the electrons fill up the phase space from the lowest energy state on. Due to the Pauli exclusion principle only two electrons can occupy one energy level, i.e. the electrons sit in physical states with high momentum, that is large pressure. This counteracts the gravitational pull and the dwarf is in an equilibrium state. Above a critical mass of $\sim 1.44M_{\odot}$, the famous Chandrasekhar mass limit, even the electrons cannot prevent the star from further collapsing. Typical white dwarfs have masses around one solarmass and radii comparably to the earths radius.

6.2.
Neutron stars

The term "neutron" star refers to the remaining core with a mass $\sim 1.5M_{\odot}$ and a radius ∼12 km after a Supernova explosion type II (see section 5.9). The central density may reach several times nuclear saturation density 0.16 fm^{-3}. Although neutrons dominate the nucleonic component, some protons and electrons still exist (This is due to charge neutrality). Like for all relativistic spherically symmetric non-rotating stars, solutions for the TOV equations 2.55 and 2.62 need an appropriate EoS as an input. For each EoS, $p(\epsilon) = p(\epsilon(r))$, where p is the pressure and ϵ the corresponding energy den-

sity at a given radius r, exists a solution which is parametrized by p_c, the central pressure of the star. Figure 6.1 shows a polytropic EoS, which can be found in [70] and a density dependent EoS called DD2, to be found in [71], which we will use within the following section on hybrid stars too. The DD2 is a stiffer EoS, that is, the pressure is higher for a given energydensity.

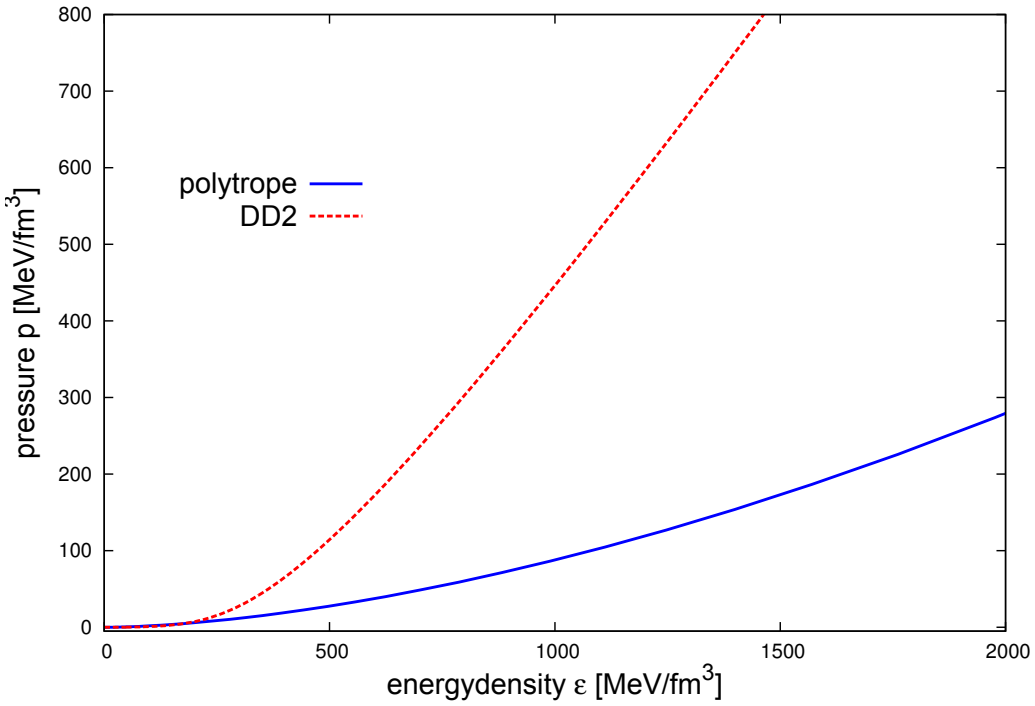

Figure 6.1: *Pressure versus energydensity: A so called equation of state. Shown here is a polytropic EoS (blue) and a hadronic matter EoS named DD2. The hadronic EoS is significantly stiffer than the polytropic one.*

These two EoS from figure 6.1 yield typical mass radius relations for neutron stars when solving the TOV equations 2.55 and 2.62.

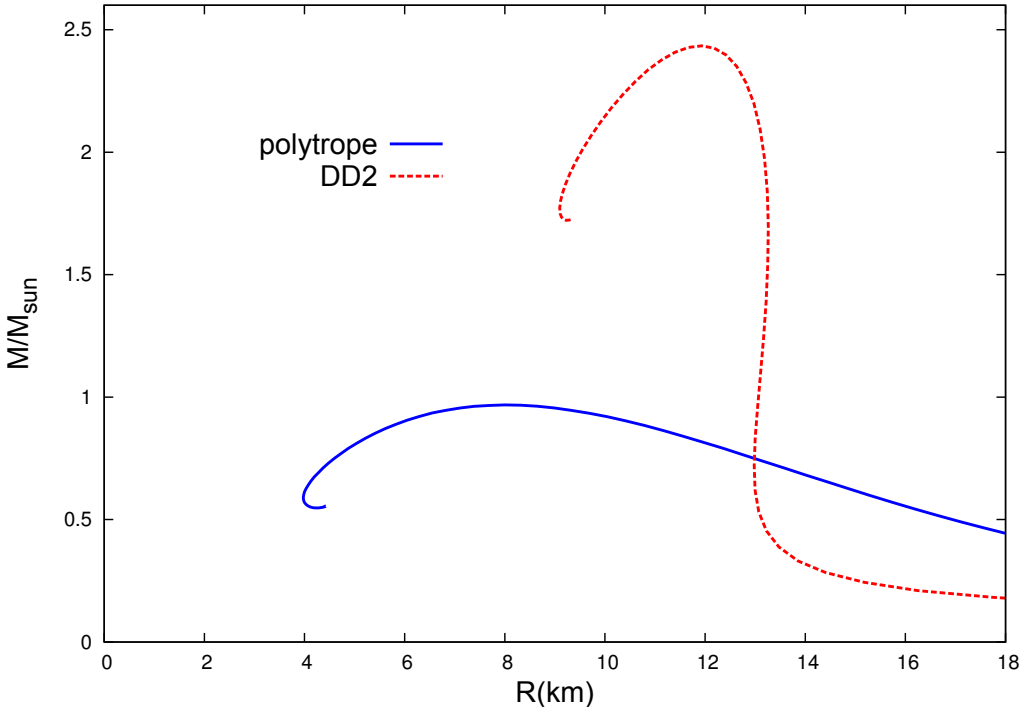

Figure 6.2: *The resulting mass radius relations for the two EoS shown in figure 6.1. The polytropic EoS yields* $\sim 1M_\odot$ *at* $\sim$ *7 km radius. The density dependend DD2 reaches up to* $\sim$ *2.4*$M_\odot$ *at a radius of* $\sim$*12 km.*

The polytropic EoS yields solutions with around one solarmass at the maximum with a radius of $\sim$ 7 km, whereas the density dependent EoS yields solutions up to 2.4 $M_\odot$ at a radius of $\sim$ 12 km[3]. The stiffer the EoS the higher the resulting maximum mass. The different slopes and other properties such as the steep increase of the DD2 mass radius relation are of tremendous importance for the stars properties and are discussed throughout the literature [72, 73, 74, 75]. The particle composition in terms of neutrons, protons and electrons for a "DD2"-star with $1.4M_\odot$ and a radius of 13.1 km is shown in figure 6.11, and discussed in greater detail within the respective section 6.3. However, a neutron stars density can reach and surpass nuclear density, that

[3]Because pulsars with $M \geq 1M_\odot$ have been observed, nuclear (or: strong) interactions need to be taken into account, i.e. the degeneracy pressure of neutrons is not sufficent to describe compact objects.

is $2.5{\cdot}10^{14}\frac{\mathrm{g}}{\mathrm{cm}^3}$ or in terms of energy density, $145\frac{\mathrm{MeV}}{\mathrm{fm}^3}$. At these super-nuclear densities it is field of research if exotic particles, such as strangeness bearing baryons, kaons or even deconfined quarks appear. In the following sections 6.3 and 6.4 some of these possible features will be investigated in greater detail.

Although this thesis does not touch the subject of black holes it has to be mentioned that for ordinary stars with $M > 20M_\odot$ even the neutrons (or the assumed exotic fermions occupying the center of the star) cannot stabilize the compact object anymore and the star collapses to a black hole.

6.3. Hybrid stars

A proto-compact star is formed in the aftermath of a supernova explosion, which is one of the most extreme events to occur in the universe. At low temperature and finite baryon density these objects contain the densest matter known to mankind, which exceeds even nuclear density ($\rho_0 \approx 2.5{\cdot}10^{14}\,\mathrm{g/cm}^3$). The recent measurements of the masses of the pulsars PSR J1614-2230 [76] and of PSR J0348+0432 [77] with $M = 2.01 \pm 0.04 M_\odot$ impose considerable constraints on the equation of state (EoS) for compact stars.

The inner regions of the most massive compact stellar objects might be occupied by a phase of quarks. In this section stable hybrid stars, i.e. compact objects with an outer layer composed of nuclear matter and with a core consisting of quark matter, will be discussed. This work has been carried out in collaboration with Matthias Hanauske and Jürgen Schaffner-Bielich and has been published in Physical Review D [57]. For the outer nuclear layer we utilize a density dependent nuclear equation of state and we use the chiral SU(3) Quark-Meson model equation of state (as been discussed in section 5) in the $T = 0$ limit with a vacuum energy pressure to describe the object's core. How to calculate the $T = 0$ limit can be found in my master thesis [5] or somewhat abbreviated described in the resulted publication [56] on pure quark stars. The appearance of a disconnected mass-radius branch emerging

from the hybrid star branch implies the existence of a third family of compact stars, so called *twin* stars. Twin stars will be subject in section 6.5 in greater detail.

The repulsive effect of the strong interaction triples the maximum obtainable mass compared to a non-interacting Fermi gas of neutrons [78]. An appropriate EoS therefore should yield solutions for compact stars with $\gtrsim 2M_{\odot}$ and illustrates likewise the importance of the incorporated interactions.

Spherically symmetric compact stars are generally described by the Tolman-Oppenheimer-Volkoff equations 2.55 and 2.62, derived in section 2.2.2.

The solutions of these equations are determined by different equations of state (EoS), and the entire collection of masses and corresponding radii is called the mass-radius relation of compact stars [70]. For each EoS, $p(\epsilon) = p(\epsilon(r))$, where p is the pressure and ϵ the corresponding energy density at a given radius r, exists a solution which is parametrized by p_c, the central pressure of the star.

Two different types of compact stars containing quark matter ought to be considered. The first one is based on the idea that the appearance of the strange quark lowers the energy per baryon and consequently forms the true ground state of nuclear matter, i.e. forms the whole star [79, 44, 46]. The resulting object is called a pure quark star, briefly discussed in the next section 6.4, and entirely discussed within the SU(3) model in [5, 56]. The second one is called a hybrid star, where a quark matter core is surrounded by an outer crust of hadronic matter, see fig. 6.3.

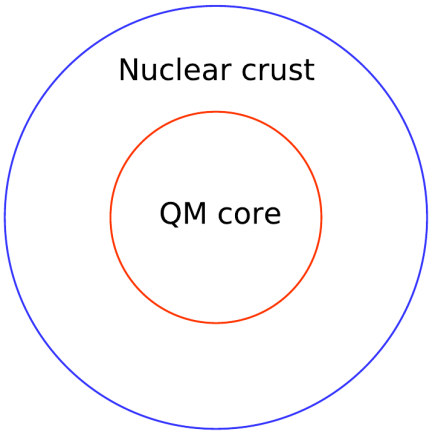

Figure 6.3: *A nuclear crust (blue circle) surrounding a quark matter core (red circle) with a sharp transition from one phase to the other: A Maxwell construction*

The transition from nuclear matter to quark matter can occur either in a mixed phase (Gibbs construction) or, assuming that there exists a first order phase transition at p_t, at a sharp transition (Maxwell construction).
Now, the particle transformations described by the EoS may influence the compressibility of the star, which can affect the stability. Is this effect significantly enough to alter the properties of the resulting compact object, i.e. give rise to a third family of degenerate stars, so called *twin* stars? These objects would again be stable at a smaller radius but similar mass as the former compact star. A possible evidence of twin stars goes along with a discontinuity in the EoS [80, 81, 82, 83, 84, 85, 86, 87, 88]. In this section we study various EoS and their solutions within the TOV equations using a Maxwell construction. A stable hybrid star configuration with $p_c \geq p_t$ is given, if the mass of the star continues to increase after the quark matter core appears [89, 90, 91]. As soon as the mass decreases with larger central pressures p_c, the configurations become unstable. If the mass then, after decreasing, increases again with larger p_c, a stable twin star configuration would have been established. This behaviour is determined by the energy discontinuity $\Delta\epsilon$ between the two EoS and the speed of sound within the

object. The works of Alford et. al [89, 90, 91] confirmed that a stable connected hybrid star branch emerges from the hadronic branch if the energy density discontinuity is less than a critical value. They used a constant speed of sound parametrization within the field correlator method for the QM EoS to provide a general framework for empirical testing and comparison. The recent observations of the $2M_{\odot}$-stars [76, 77] constraints the constant speed of sound parametrization. A stiffer HM EoS and $c_s^2 \geq \frac{1}{3}$ for the QM EoS yields solutions with star sequences $\geq 2M_{\odot}$ in their approach. We will work with a density dependent (DD2) nuclear matter EoS [71] for the outer layers of the star and a chiral SU(3) EoS derived from the Quark-Meson model (section 5) for the stars core. In the last section we found that pure quark star configurations $\geq 2M_{\odot}$ for a small parameter range exist, whereas all other solutions were hybrid stars completely built of a mixed phase of HM and QM. We scan the same parameters of the SU(3) EoS as in [56] to look for possible twin stars emerging from a stable hybrid star.

According to lattice QCD calculations, the phase transition at high baryonic densities is of first order [92, 93, 94]. Based on this assumption the transition from hadronic matter to quark matter is described via a Maxwell construction [95, 96, 97]. The quark-meson model couples mesons as mediators of the strong interaction to quarks utilizing chiral symmetry [37] via a Yukawa type coupling (Remember the discussion in section 4.4 for the SU(2) case). The coupled equations of motions of the meson fields derived from the grand canonical potential have to be solved self-consistently and determine finally the EoS. The energy density and the pressure derived from the grandcanoniocal potential in mean field approximation (Section 5.6, equation 5.84) have

to be determined for $T = 0$ and read[4]

$$\begin{aligned}
\epsilon &= \epsilon_e + \frac{\lambda_1}{4}(\sigma_n^2+\sigma_s^2)^2 + \frac{\lambda_2}{4}(\sigma_n^4+\sigma_s^4) \\
&+ \frac{m_0^2}{2}(\sigma_n^2+\sigma_s^2) - \frac{2\sigma_n^2\sigma_s}{\sqrt{2}}\cdot c - h_n\sigma_n - h_s\sigma_s + B^{1/4} \\
&+ \frac{1}{2}\left(m_\omega^2\omega^2 + m_\rho^2\rho^2 + m_\phi^2\phi^2\right) \\
&+ \frac{3}{\pi^2}\sum_{f=u,d,s}\int_0^{k_F^f} dk\cdot k^2\left(\sqrt{k_{n,s}^2+\tilde{m}^2}\right)
\end{aligned} \tag{6.1}$$

and

$$\begin{aligned}
p &= -\frac{1}{2}\left(m_\omega^2\omega^2 + m_\rho^2\rho^2 + m_\phi^2\phi^2\right) \\
&+ \frac{\lambda_1}{4}(\sigma_n^2+\sigma_s^2)^2 + \frac{\lambda_2}{4}(\sigma_n^4+\sigma_s^4) \\
&+ \frac{m_0^2}{2}(\sigma_n^2+\sigma_s^2) - \frac{2\sigma_n^2\sigma_s}{\sqrt{2}}\cdot c - h_n\sigma_n - h_s\sigma_s + B^{1/4} \\
&+ \frac{3}{\pi^2}\sum_{f=u,d,s}\int_0^{k_F^f} dk\cdot k^2\left(\sqrt{k_{n,s}^2+\tilde{m}^2} - \tilde{\mu}_f\right)
\end{aligned} \tag{6.2}$$

where the indices n=nonstrange (up- and down quarks) and s=strange quarks. For the couplings and masses of the included fields standard values are assumed. A detailed treatment on the parameters, if maybe not sufficently discussed within this thesis, can be found in [37, 38, 48, 56]. Since the properties of the reviewed hybrid stars depend only on the parameters of the quark sector, a broader overview shall be given compared to the nuclear matter parameter range. Four parameters can be varied:

1. The constituent quark mass m_q determines the scalar coupling for the nonstrange g_n and strange condensate g_s via the Goldberger-Treiman relation: $g_n = \frac{m_q}{f_\pi}$ and $g_s = g_n\sqrt{2}$, where g_s is adopted from SU(3) symmetry considerations.

2. The vector coupling is independent of the constituent quark mass, it

[4] See my Master thesis [5] for details.

will be varied in the scale of the scalar coupling, $g_\omega \sim g_n$, to study its influences in an appropriate range. The strange coupling of the ϕ-meson is fixed by SU(3) symmetry.

3. The experimentally not well determined mass of the σ-meson covers a range from 400 MeV $\leq m_\sigma \leq$ 800 MeV [4, 52].

4. The Bag constant $B^{\frac{1}{4}}$ [MeV] models the confinement and can be interpreted as a vacuum energy density term, remember section 5.1. The fields are independent of its variation, its impact is to stiffen or soften the EoS. Physically reasonable ranges within this context are 60 MeV $\leq B^{\frac{1}{4}} \leq$ 200 MeV.

6.3.1. Construction of the phase transition

At large densities hadronic matter is expected to undergo two phase transitions. The first one deconfines hadrons to quarks and gluons. Note that in a strict sense neither the deconfinement phase transition nor the chiral phase transition can be described by an order parameter based on underlying symmetries of QCD. The second one restores chiral symmetry. Yet it is an unsettled issue whether these transitions are real phase transitions or crossover transitions [98]. We will study and compare various models at ultrahigh densities to search for differences and similarities as well as their resulting predictions for compact objects, i.e. the mass-radius relation. The study of the deconfined phase transition is related to the mixed phase. It has been suggested, that the mixed phase in compact objects behaves more in accordance with the Maxwell construction than with the Gibbs construction [99, 97, 100]. Furthermore it is more likely that twin stars appear within the Maxwell construction, according to [97]. In this approach we thus utilize a Maxwell construction due to the above mentioned reasons. In refs [89, 90, 91] the QM EoS was parametrized in a relatively simple form (see eq. 6.7) and the transition from HM to QM can be constructed without any constraints

concerning the chemical potential. Our approach on the other hand needs to take into account the pressure as function of the chemical potential to find the thermodynamically justified transition pressure (see fig. 6.16 and the discussion there).

In electrically neutral stellar matter baryon number and charge have to be conserved quantities. Under this assumption the chemical potential of species i can be defined as

$$\mu_i = B_i \mu_B + Q_i \mu_Q \tag{6.3}$$

where B_i is the baryon number and Q_i the charge in units of the electron charge and μ_B and μ_Q are the baryonic and electric chemical potentials respectively. Note, that strangeness is not a conserved quantity. The phase transition from HM to QM produces a mixed phase. Now, the Gibbs condition requires that the coexisting phases have opposite charge and it might also happen that the mixed phase is energetically too expensive [97, 99]. Then the two phases are in direct contact with each other, which corresponds to a Maxwell construction, where

$$P_{HM}(\mu_B, \mu_Q) = P_{QM}(\mu_B, \mu_Q) \tag{6.4}$$

$$\mu_B = \mu_{HM} = \mu_{QM} \tag{6.5}$$

The baryon chemical potential is continuous, but μ_Q jumps at the interface of the two phases, so that the phase transition takes place if the pressure of the QM phase equals the pressure of the HM phase at a given baryo-chemical potential μ_B. The MC corresponds to constant pressure in the energy density interval of the mixed phase, whereas the pressure increases with baryon density in the GC.

However, the existence of a quark phase in a compact star requires the transition pressure to be smaller than the central pressure p_c of the star, which is valid for the MC and also for the GC.

6.3.2.
Stability Criteria

As long as the mass of the star is an increasing function of p_c the compact object will be stable. Since a hybrid star contains a QM-core, there exists a threshold value in the jump in energy density $\Delta\epsilon_c$ which determines the star's stability when the QM-core first appears.

$$\frac{\Delta\epsilon_c}{\epsilon_t} = \frac{1}{2} + \frac{3}{2}\frac{p_t}{\epsilon_t} \tag{6.6}$$

where ϵ_t and p_t are the values of the energy density and pressure at the phase transition to hadronic matter. $\Delta\epsilon_c$ is the threshold value below which there is in any case a stable hybrid star branch connected to the hadronic star branch [89, 90, 91]. For a derivation and discussion of (6.6) see [101, 80, 81, 82, 102, 83, 103, 104].
For a high value of $\Delta\epsilon$ the cusp in the MR relation is hardly detectable and in the range of $\sim 10^{-4} M_\odot$ in agreement with [104, 89, 88], i.e. shortly after the QM core appears the QM core is unable to counteract the gravitational attraction from the HM and the star becomes unstable.

6.3.3.
Results

The appearance of a QM core within a compact star is entirely determined by the transition pressure p_t and the discontinuity in the energy density $\Delta\epsilon$. If the pressure within the star lies below the transition pressure, the object would be entirely determined by the HM EoS and could not be classified as a hybrid star. The relation $\frac{\Delta\epsilon}{\epsilon_t}$ as a function of $\frac{p_t}{\epsilon_t}$ will become important in context with eq. (6.6) when investigating for connected or disconnected hybrid star branches [89, 90, 91].

Various EoS and the corresponding mass-radius relations for fixed B and different g_ω

Figure 6.4 shows the total hybrid EoS for a fixed value of the vacuum pressure B = 60 MeV while varying the vector coupling constant from $0 \leq g_\omega \leq 3$.

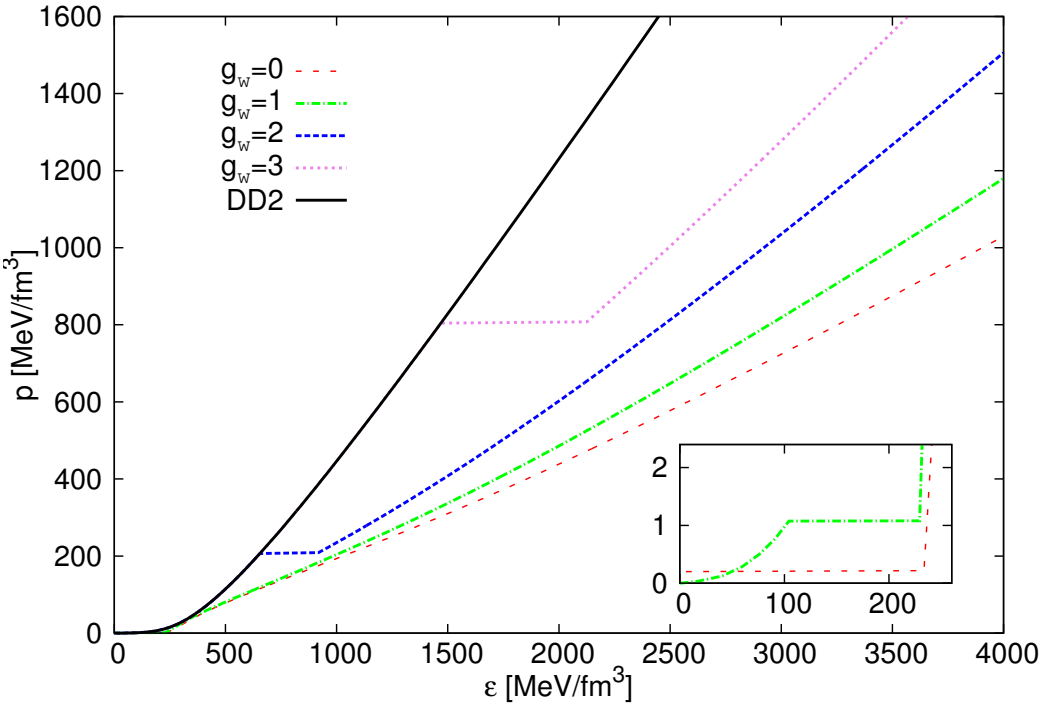

Figure 6.4: *The EoS with fixed* $B^{1/4} = 60$ *MeV while varying* g_ω *at* $m_\sigma = 600$ *MeV and* $m_q = 300$ *MeV. The inlaid figure accentuates the behaviour of the EoS for* $g_\omega = 0$ *and* $g_\omega = 1$ *which else is hardly perceivable.*

For increasing values of the repulsive coupling the transition pressure p_t increases. This is due to a higher intersection point of the hadronic EoS and the corresponding QM EoS in the $p - \mu$ plane, see fig. 6.16. Larger g_ω goes along with a stiffening in the QM EoS.
The $g_\omega = 0$ case corresponds to a transition from HM to QM at $\frac{\epsilon}{\epsilon_0} \leq 1$. A transition occurring below saturation energy density is clearly unphysical and shall therefore not be discussed any further (see upper x axis in fig 6.15).

For $g_\omega = 1$ the transition occurs at $p_t \simeq 1.05\,\mathrm{MeV/fm^3}$ and $\epsilon_t \simeq 102\,\mathrm{MeV/fm^3}$ (see inlaid figure in fig. 6.4). The discontinuity in energy density here is $\Delta\epsilon \simeq 122\,\mathrm{MeV/fm^3}$. In this case $\frac{\epsilon}{\epsilon_0} \simeq 1$, see also fig. 6.15, which corresponds to the leftmost data point on the $g_\omega = 0$ line. Note that in fig. 6.4 and in all following graphics the pure HM results are shown as a reference, denoted as "DD2".

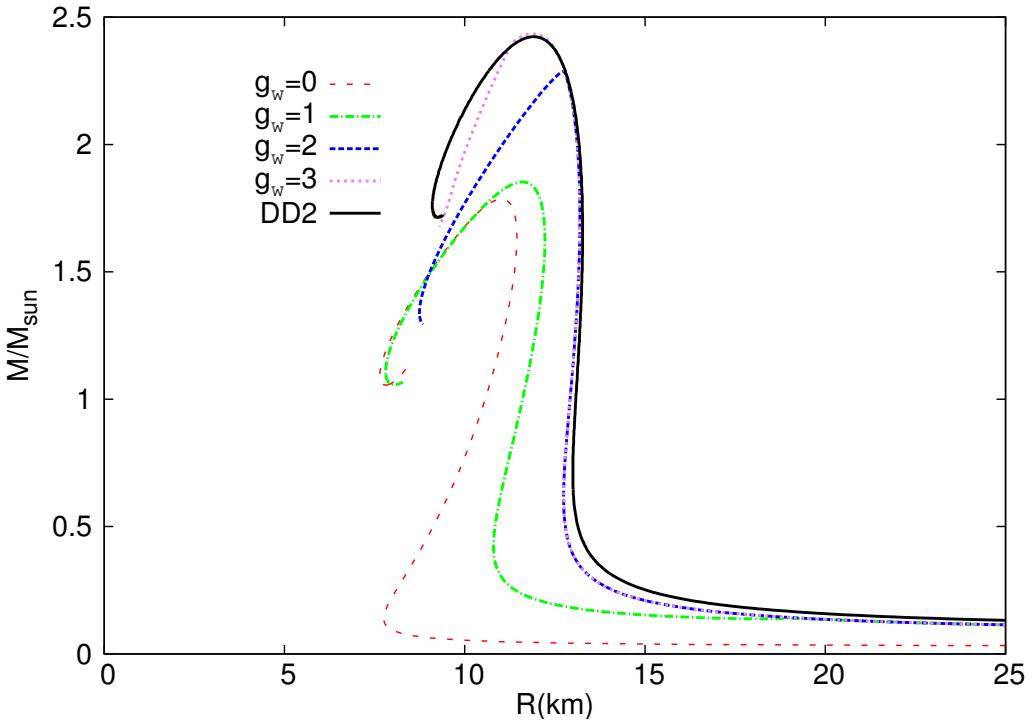

Figure 6.5: *The mass-radius relation with fixed* $B^{1/4} = 60$ *MeV while varying* g_ω *at* $m_\sigma = 600$ *MeV and* $m_q = 300$ *MeV.*

The corresponding mass-radius relation is shown in fig. 6.5. For $g_\omega = 1$ the phase transition from HM to QM does not destabilize the star for a relatively wide range in mass, i.e. the emerging QM core gets larger while the hybrid star manages to stay stable up to $\sim 1.7 M_\odot$. This behaviour is very similar to the one of the hadronic mode "DD2", but shifted to smaller masses and radii.

A repulsive coupling of $g_\omega = 2$ on the other hand results in a connected hybrid star branch hardly detectable compared to $g_\omega = 1$ and with a similar

trend as the "DD2" case, but with solutions reaching $\gtrsim 2M_{\odot}$.
For $g_{\omega} = 3$ the transition sets in at already unstable configurations for the pure nuclear matter case.

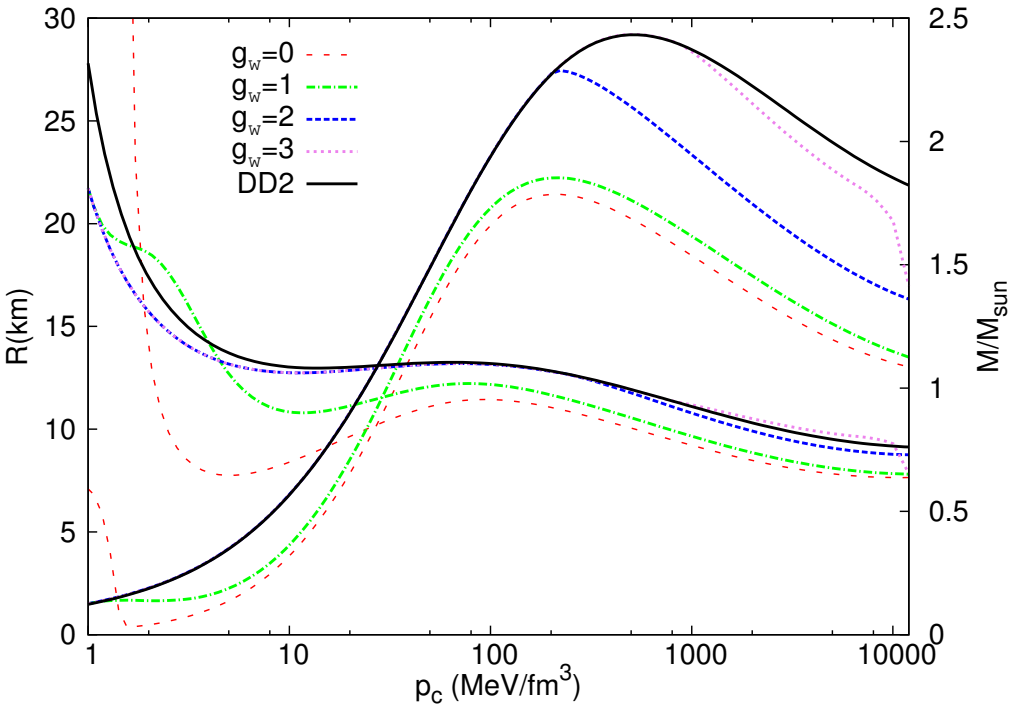

Figure 6.6: *The radius- and mass curves as function of the central pressure p_c with fixed $B^{1/4} = 60$ MeV while varying g_{ω} at $m_{\sigma} = 600$ MeV and $m_q = 300$ MeV. The curves starting in the upper left region are the radius curves whereas the curves starting on the lower left side are the mass curves.*

Figure 6.6 displays the radius- and mass curves as function of p_c with $B^{1/4} = 60$ MeV while varying g_{ω} at $m_{\sigma} = 600$ MeV and $m_q = 300$ MeV. The curves starting in the upper left region are the radius curves for a given value of g_{ω}. The curves starting on the lower left side are the mass curves. The associated x-axis in fig. 6.6 shows the pressure pertaining to both curves. The curves leave the hadronic "DD2" reference line at the respective transition pressure p_t and, still rising, yielding stable hybrid star solutions. Unstable solutions can be read off from the point where the mass decreases with increasing pressure. These features are valid for all following radius- and mass curves

as function of p_c.

Figure 6.6 substantiates the hithero discussion regarding the increase of the repulsive coupling by depicting up to which central pressure p_c the hybrid star configurations stay stable: With higher repulsive coupling, the appearing hybrid star configurations become unstable, i.e. the smaller the resulting QM core, though the masses are significantly higher.

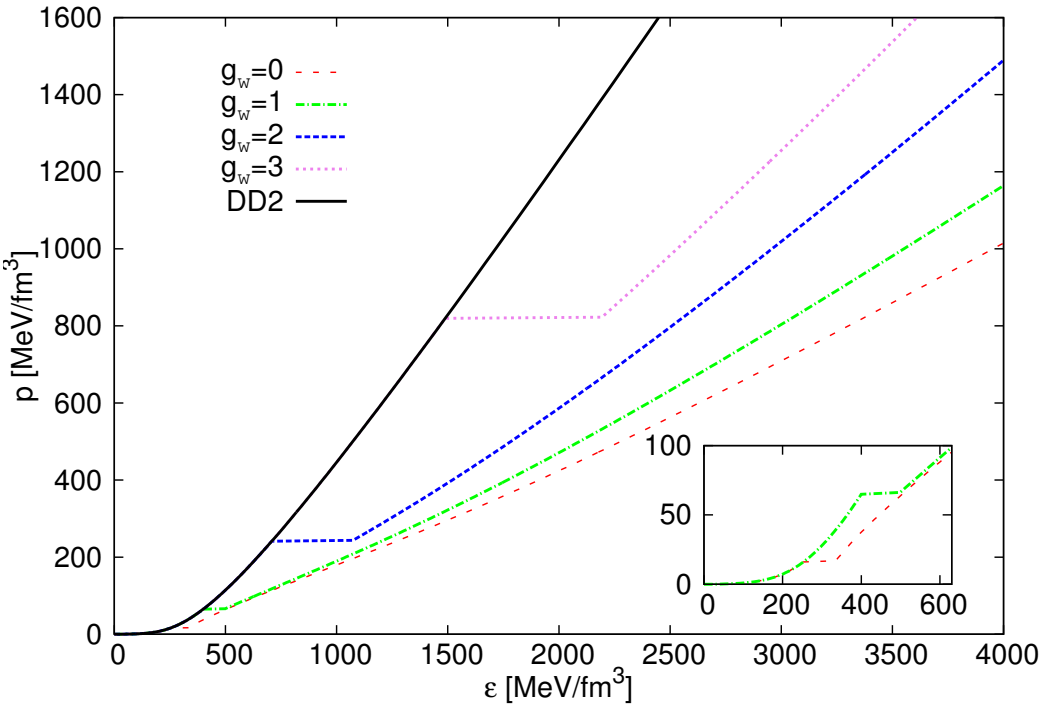

Figure 6.7: *The EoS with fixed* $B^{1/4} = 100$ *MeV while varying* g_ω *at* $m_\sigma = 600$ *MeV and* $m_q = 300$ *MeV. The inlaid figure shows the behaviour of the EoS for* $g_\omega = 0$ *and* $g_\omega = 1$.

Figure 6.7 shows the EoS for $B^{1/4} = 100$ MeV. The transition pressure increases with an associate increase of the jump in energy density. For $g_\omega = 0$ with fixed $B^{1/4} = 100$ MeV the respective values are $p_t \simeq 15$ MeV/fm^3, $\epsilon_t \simeq 230$ MeV/fm^3 and $\Delta\epsilon \simeq 90$ MeV/fm^3, see inlaid figure in figure 6.7 and see fig. 6.15 for $\frac{\epsilon}{\epsilon_0} \simeq 1.8$ respectively. For $g_\omega = 1$ and $B^{1/4} = 100$ MeV we find $p_t \simeq 75$ MeV/fm^3, $\epsilon_t \simeq 380$ MeV/fm^3 and $\Delta\epsilon \simeq 100$ MeV/fm^3 at $\frac{\epsilon}{\epsilon_0} \simeq 2.8$, see also fig. 6.15. The resulting mass-radius relations for these EoS

are shown in fig. 6.8. The symbols △ and ◯ (see figs. 6.8 and 6.9) mark the positions of two individual stars which are later discussed in greater detail.

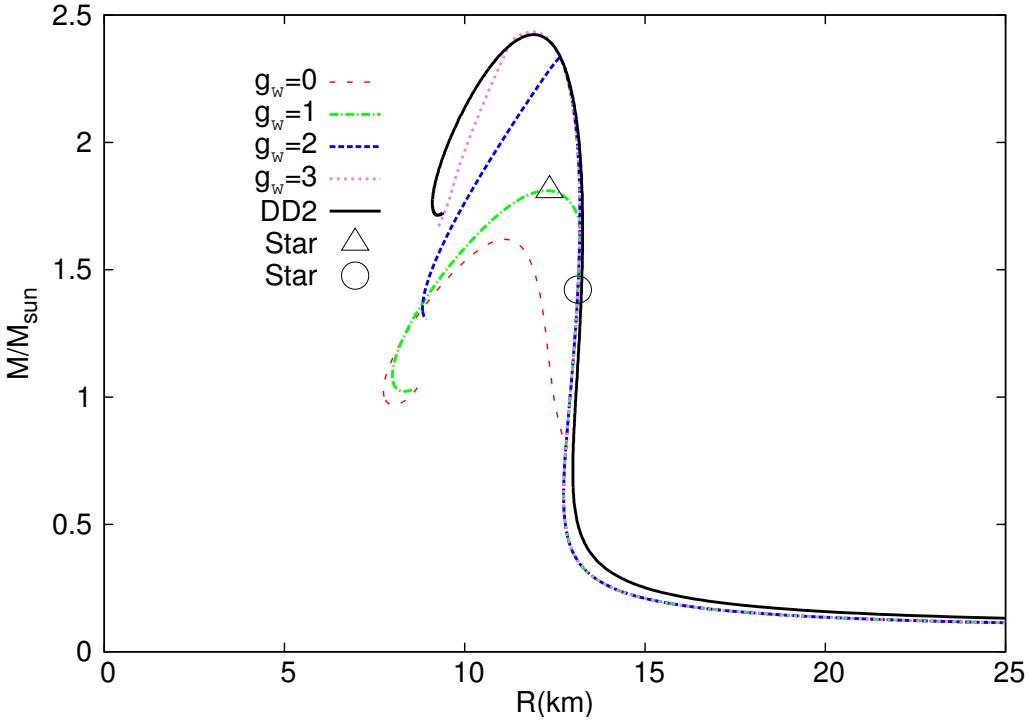

Figure 6.8: *The mass-radius relation with fixed* $B^{1/4} = 100$ *MeV while varying* g_ω *at* $m_\sigma = 600$ *MeV and* $m_q = 300$ *MeV. The symbols* △ *and* ◯ *represent two individual stars chosen from the EoS with* $g_\omega = 1$ *to discuss their individual properties.*

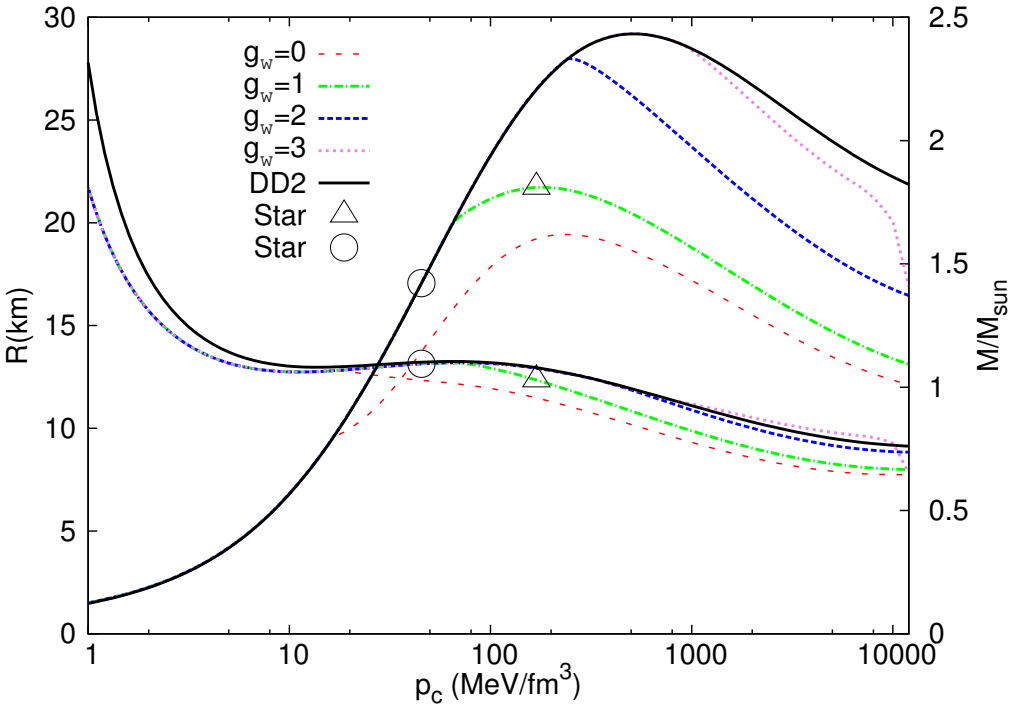

Figure 6.9: *The radius- and mass curves as function of the central pressure* p_c *with fixed* $B^{1/4} = 100$ *MeV while varying* g_ω *at* $m_\sigma = 600$ *MeV and* $m_q = 300$ *MeV. The curves starting in the upper left region are the radius curves whereas the curves starting on the lower left side are the mass curves. The symbols* △ *and* ◯ *represent two individual stars chosen from the EoS with* $g_\omega = 1$ *to discuss their individual properties.*

However, increasing further the repulsive coupling leads to hybrid star configurations, which do not support a stable QM core ($g_\omega \geq 2$). The trends of the curves obviously show differences to the $B^{1/4} = 60$ MeV parameter choice. For values of $g_\omega \leq 1$ the transition pressures for $B^{1/4} = 100$ MeV are higher compared to the $B^{1/4} = 60$ MeV case, see figs. 6.6 and 6.9. Note that for $g_\omega \geq 2$ the transition pressures change not significantly, and the appearing QM core does destabilize the configurations nearly immediately (the transition for $g_\omega = 3$ happens already in the unstable regime of the branch). The QM core for $g_\omega = 0$ appears at $\sim 0.8 M_\odot$ at a radius of ~ 12.5 km, see fig. 6.9 where the mass and radius lines leaves the hadronic "DD2" reference

line. The star does not get unstable up to $\sim 1.6 M_\odot$ at a radius of ~ 11 km. The QM core for $g_\omega = 1$ appears at $\sim 1.6 M_\odot$. The hybrid star configurations stay stable up to $\sim 1.7 M_\odot$, see figs. 6.8 and 6.9. The appearance of the QM core at $g_\omega = 1$ destabilizes the star configurations faster than in the $g_\omega = 0$ case for $B^{1/4} = 100$ MeV.

To demonstrate the particle occupation within the star configurations, we picked out two individual stars from figure 6.8 (and respective figure 6.9), marked with $\triangle$ and $\bigcirc$, whose individual properties are denoted in table 6.1.

Star	$M/M_\odot$	R	p_c	ϵ_{cent}	$\epsilon_{cent}/\epsilon_0$
$\triangle$	1.81	12.35	169.21	917.73	6.23
$\bigcirc$	1.42	13.14	45.32	351.54	2.39

Table 6.1: *The properties of the two individual stars* $\triangle$ *and* $\bigcirc$ *for the parameter choice* $B^{1/4} = 100$ *MeV*, $g_\omega = 1$, $m_\sigma = 600$ *MeV and* $m_q = 300$ *MeV. The entries display the mass in solar masses, the radius* R *of the star in km, the pressure* p_c *and the energy density* ϵ_{cent} *at the center of the star in* MeV/fm^3 *and the respective energy density in units of nuclear energy density.*

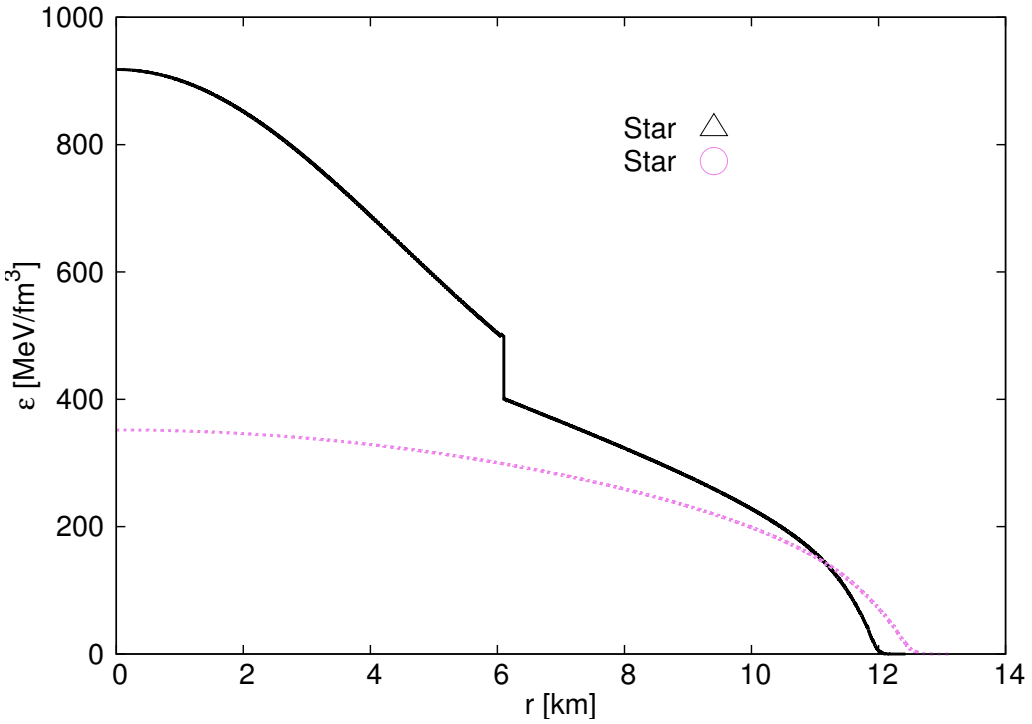

Figure 6.10: *The energy density versus radius of the two selected stars* △ *(continuous line) and* ◯ *(dotted line) from figs. 6.8 and 6.9 for the parameter choice* $B^{1/4} = 100$ *MeV,* $g_\omega = 1$*,* $m_\sigma = 600$ *MeV and* $m_q = 300$ *MeV. The phase transition for* △ *from hadronic matter to quark matter appears at* ∼*6.1 km, whereas* ◯ *is purely hadronic.*

We choose a hybrid star, marked with △, and a purely hadronic star, marked with ◯, calculated from the EoS with the parameter choice $B^{1/4} = 100$ MeV, $g_\omega = 1$, $m_\sigma = 600$ MeV and $m_q = 300$ MeV.
Figure 6.10 depicts the energy density profiles of the two stars, ranging from their center at $r = 0$ up to their surface, where $\epsilon_{cent} = 0$ and $r = R$, indicating the radius of the star. The quark matter phase for △ appears at $r \simeq 6.1$ km at $\epsilon \simeq 500$ MeV/fm^3. The respective jump in energy density is $\Delta\epsilon \simeq 100$ MeV/fm^3, which can also be seen in figure 6.7. We want to point out, that due to the used Maxwell construction of the phase transition, no mixed phase region and therefore no crystalline (pasta-like) structure [105] of mixed phase matter is present within our hybrid star model. The profile

of the star ◯ shows a continuous behaviour as the star does not reach the pressure required for quark matter to appear.
Figure 6.11 demonstrates the particle fraction of the two individual stars, plotted versus their respective radius. From the surface on at $R_{\triangle} = 12.35$ km the star △ is mainly composed of neutrons, which contribute $\sim 90\%$, and consists of an equal number of protons and electrons (due to charge neutrality), contributing $\sim 10\%$. With decreasing radius the respective hadronic particle fraction decreases, but changes are not that significantly. Yet at a radius of ~ 6.1 km, at $\epsilon_{crit} \simeq 500$ MeV/fm^3 and $p_t = 64.81$ MeV/fm^3, the phase transition from hadronic matter to quark matter takes place.

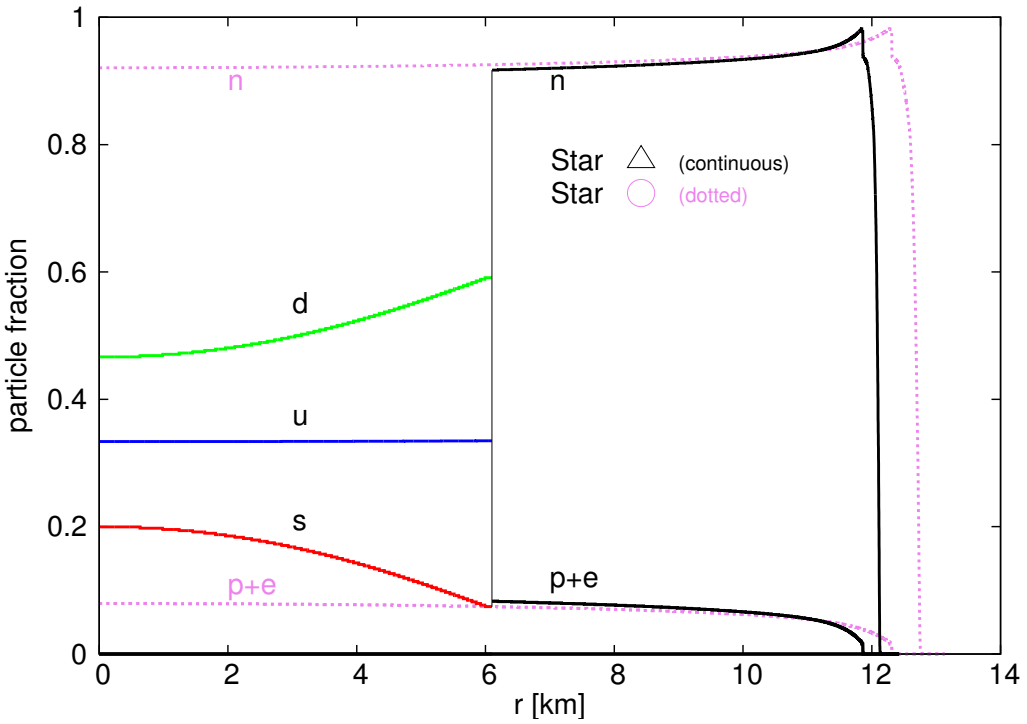

Figure 6.11: *The particle fraction versus radius of the two selected stars* △ *(continuous lines) and* ◯ *(dotted lines) from figs. 6.8 and 6.9 for the parameter choice* $B^{1/4} = 100\ MeV$, $g_\omega = 1$, $m_\sigma = 600\ MeV$ *and* $m_q = 300\ MeV$. △ *has a radius of* $R_\triangle = 12.35\ km$ *and the phase transition happens at 6.1 km. The appearing quarks form the whole star and the strange quark becomes more and more significant, and finally makes up 20 % of the star in its center. The particle composition of* ◯ *is indicated by the thin dotted lines and since the star is purely hadronic, no quarks appear. The star is mostly composed of neutrons (∼90 %) and of protons and electrons (∼10 %).*

Approaching the center of the star the contribution of the strange quark increases, while the contribution of the down quark decreases in nearly equal manner. The fraction of the up quarks stay (nearly) constant at $\sim 33\%$. The increase of the strange quark contribution can be explained with the increase in pressure approaching the center of the object [106, 107]. The particle composition of the star ◯, indicated by the thin violet dotted lines, on the other hand does not reach the required pressure for the corresponding phase

transition, $p_c = 45.323$ MeV/fm$^3 \leq p_t \leq 64.81$ MeV/fm^3, and therefore remains purely hadronic. As in the case for $\triangle$ within the shell 6.1 km$\leq r \leq R_{\bigcirc}$, the hadronic fraction, neutrons, protons and electrons, stays nearly constant.
The star is mostly composed of neutrons ($\sim$90 %), protons and electrons ($\sim$10 %).

The EoS for $B^{1/4} = 140$ MeV is shown in fig. 6.12. It shows an increase of the transition pressure p_t as expected. The discontinuity in energy density increases too, but displays a nontrivial relation to p_t which can be observed in greater detail in the phase diagram shown in fig. 6.15. The resulting mass-radius curve for $B^{1/4} = 140$ MeV is shown in fig. 6.13. A hybrid star branch appears but is hardly noticeable.

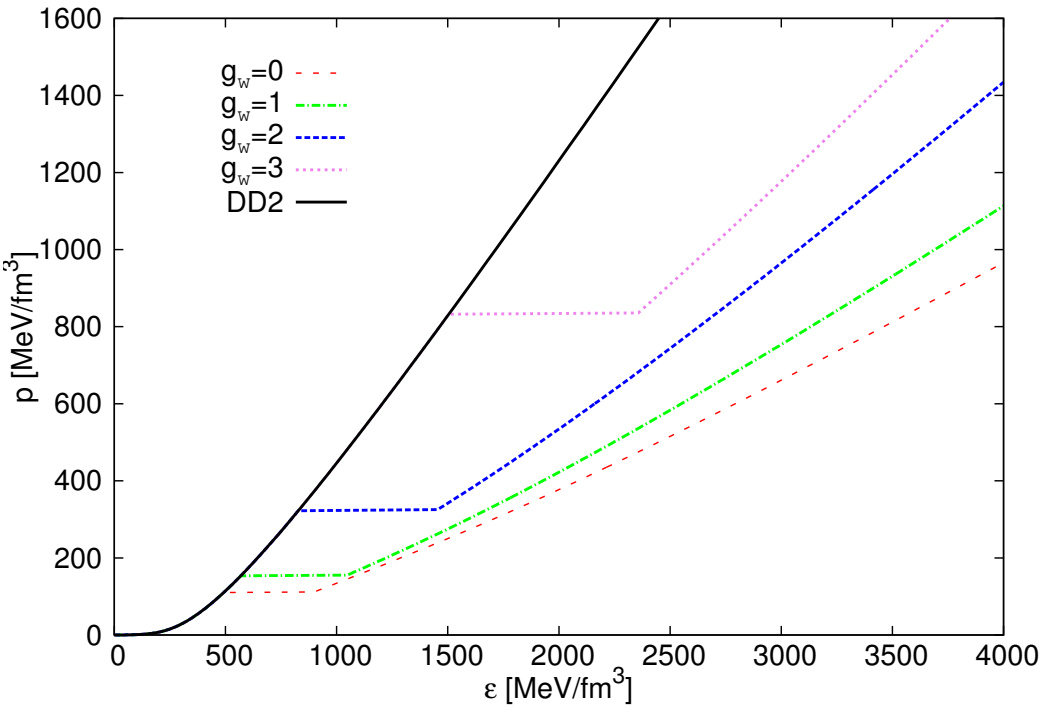

Figure 6.12: *The EoS with fixed* $B^{1/4} = 140$ *MeV while varying* g_ω *at* $m_\sigma = 600$ *MeV and* $m_q = 300$ *MeV.*

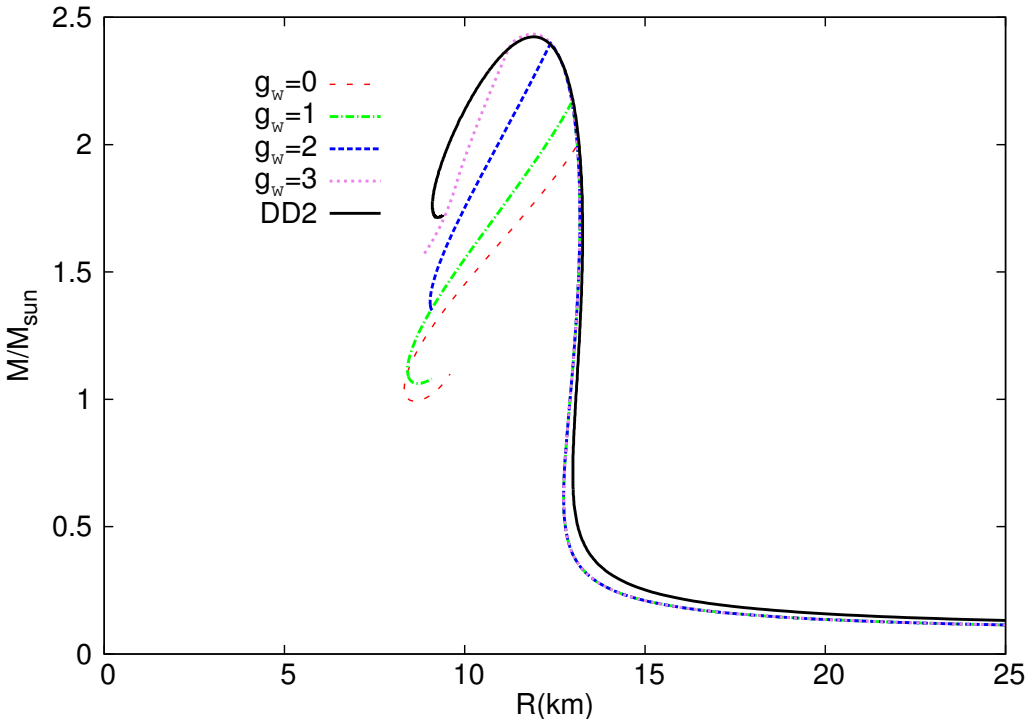

Figure 6.13: *The mass-radius relation with fixed* $B^{1/4} = 140$ *MeV while varying* g_ω *at* $m_\sigma = 600$ *MeV and* $m_q = 300$ *MeV.*

As already mentioned, the transition for a value of $g_\omega = 3$ sets in at an already unstable configuration, i.e. no stable hybrid star branch at all emerges.

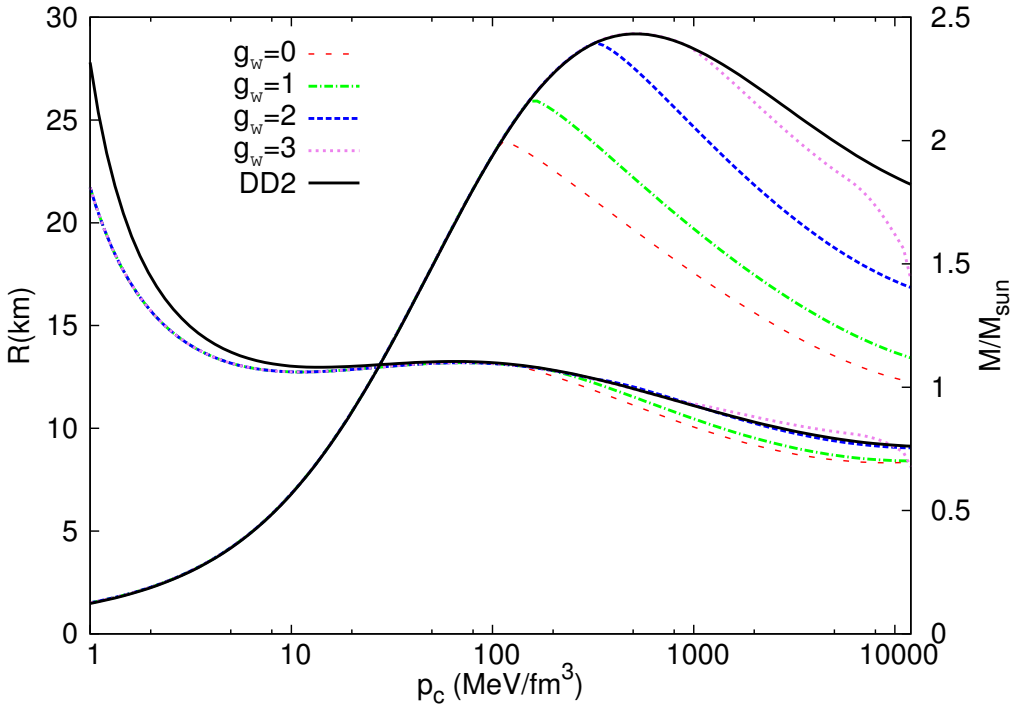

Figure 6.14: *The radius- and mass curves as function of the central pressure p_c with fixed $B^{1/4} = 140$ MeV while varying g_ω at $m_\sigma = 600$ MeV and $m_q = 300$ MeV. The curves starting in the upper left region are the radius curves whereas the curves starting on the lower left side are the mass curves.*

Fig. 6.14 shows the corresponding radius- and mass curve as function of the central pressure p_c. The hybrid star configurations follow the "DD2" curve, and become unstable nearly immediately after the appearance of the QM core. The repulsive force in the QM EoS is not strong enough to support a large hadronic mantle. The star would collapse having a too large QM core. Generally speaking: Raising the value of the vacuum pressure leads to shorter hybrid star branches, i.e. the mass difference between the maximum mass on the connected hybrid star branch and the mass of the purely hadronic star at the phase transition ($p_c = p_t$) gets smaller. The phase diagram displayed in figure 6.15 depicts the ratio of pressure to energy density at the transition of hadronic matter versus the discontinuity in energy density at the transition. The upper x axis displays the corresponding central energy density in units

of nuclear energy density $\epsilon_0 \simeq 145\ \frac{MeV}{fm^3}$.
The transition for small values of B and g_ω occurs at a too small central energy density $\frac{\epsilon_t}{\epsilon_0} \leq 1$. For large values of B and a small repulsive coupling the transition occurs at $4-10$ times nuclear saturation density. Within the range $100 \leq B \leq 140$ MeV the transition for zero repulsion stays below the constraint line, given by eqn. 6.6. It is interesting to note that all curves gather in an area at around $0.55 \leq \frac{p_t}{\epsilon_t} \leq 0.65$ and $0.4 \leq \frac{\Delta\epsilon}{\epsilon_t} \leq 0.6$ where the central energy density is ~ 10 times nuclear saturation density (even for higher values of g_ω not displayed here).

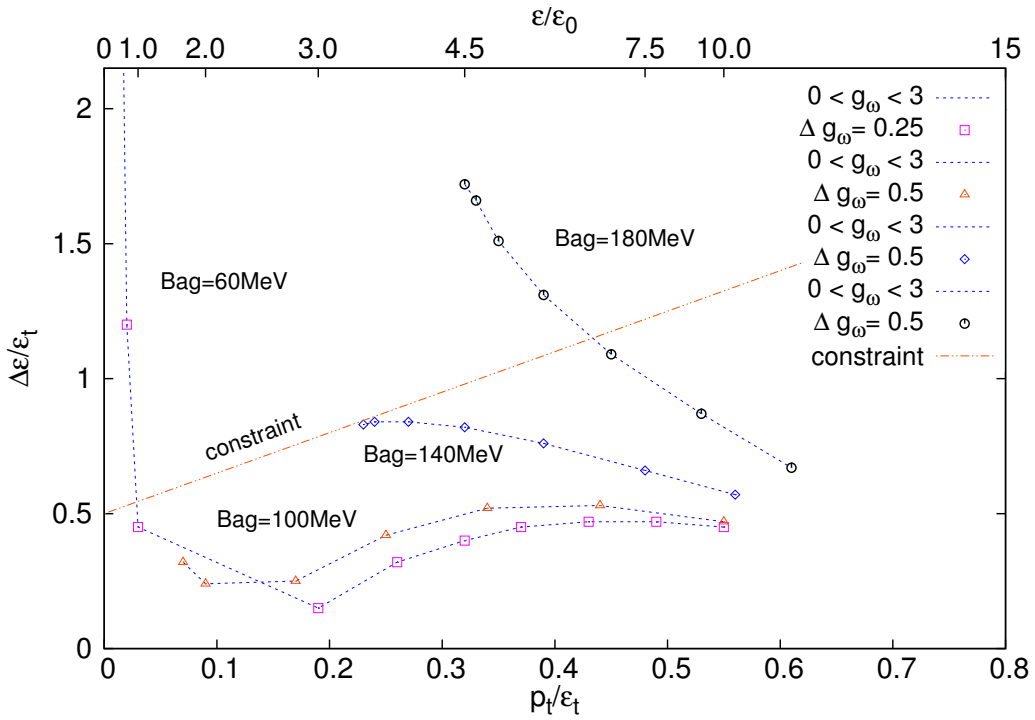

Figure 6.15: *Phase diagram for hybrid stars with fixed B while varying* $0 \leq g_\omega \leq 3$ *at constant* $m_\sigma = 600\ MeV$ *and* $m_q = 300\ MeV$. *The axes display the transition pressure* p_t *and the energy density discontinuity* $\Delta\epsilon$ *in units of the nuclear energy density at the transition* ϵ_t. *Note, that the first data point for the* $B^{1/4} = 60\ MeV$ *line (on the left) corresponds to* $g_\omega = 1$. *The following data points are incremented by* $\Delta g_\omega = 0.25$.

Figure 6.16 displays the pressure as a function of the chemical potential μ for

the parameter choice $m_\sigma = 600$ MeV, $m_q = 300$ MeV and $B^{1/4} = 100$ MeV while varying $0 \leq g_\omega \leq 3$. The intersecting point between the HM-and the QM curve indicates where the transition pressure for a given choice of parameters is located.

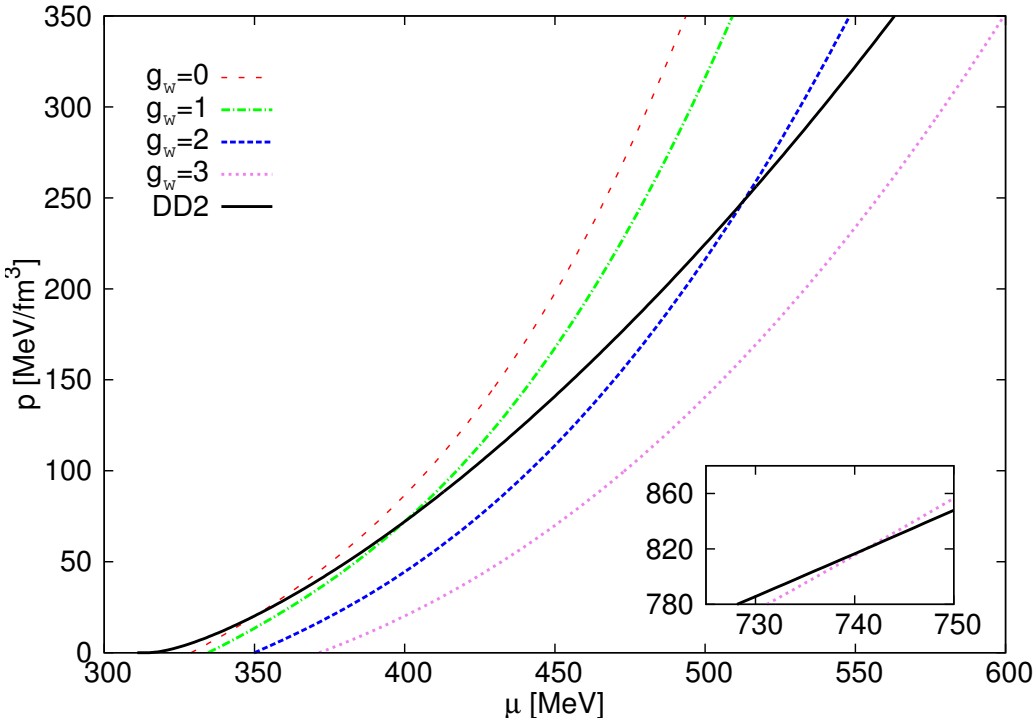

Figure 6.16: *The intersection in the pressure versus chemical potential μ plane for $0 \leq g_\omega \leq 3$ within the parameter choice $m_\sigma = 600$ MeV, $m_q = 300$ MeV and $B^{1/4} = 100$ MeV, corresponding to figs. 6.7, 6.8 and 6.9. The MC requires that from the intersecting point on the dominance in the EoS flips, which creates a QM core within the star at the corresponding pressure. The inlaid figure shows the intersection for the $g_\omega = 3$ case, which is out of the plot range.*

The intersection for $g_\omega = 0$ takes place at $p \simeq 15$ MeV/fm^3 and $\mu \simeq 355$ MeV and for $g_\omega = 1$ at $p \simeq 75$ MeV/fm^3 and $\mu \simeq 400$ MeV, see also figs. 6.7 and 6.9. It is interesting to note that within our approach a stiffer EoS has a "softer" behaviour in the $p - \mu$ plane. Due to this softening the intersection between the hadronic and the QM curve takes place at a higher pressure.

That corresponds to a transition from HM to QM at a higher energy density in terms of nuclear energy density, see figs. 6.15 and 6.21 for comparison (upper x-axis). An appearing QM core destabilizes the star quite soon, and twin star solutions are ruled out, since these require a relatively low transition pressure [94, 88].

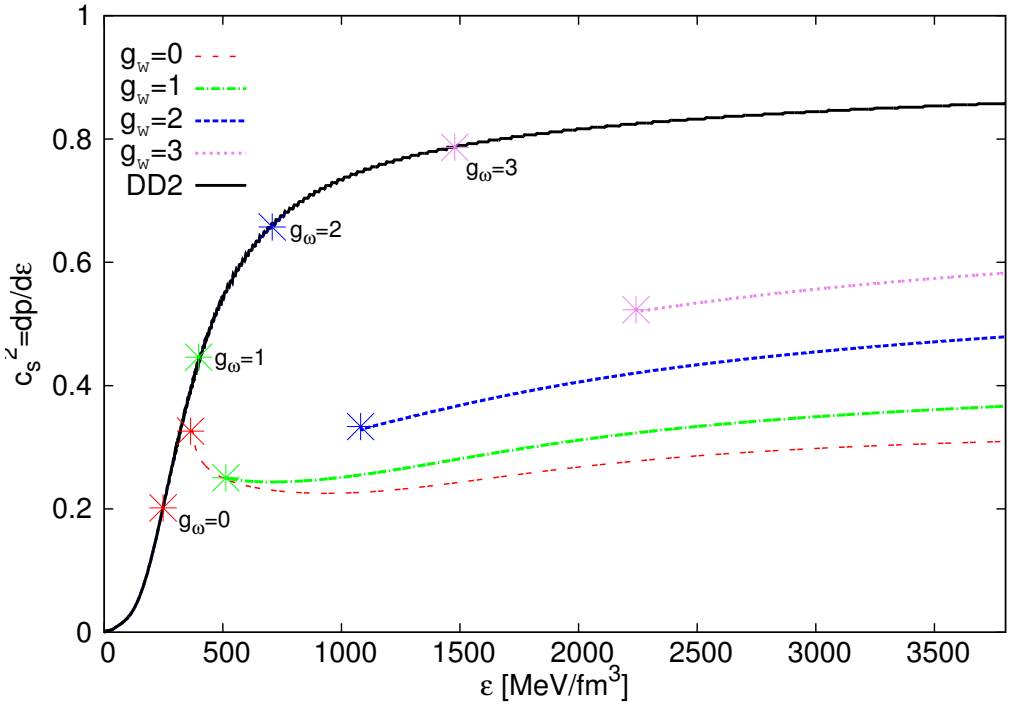

Figure 6.17: *The speed of sound* $c_s^2 = \frac{dp}{d\epsilon}$ *as a function of the energy density* ϵ *for* $0 \leq g_\omega \leq 3$ *within the parameter choice* $m_\sigma = 600$ *MeV*, $m_q = 300$ *MeV and* $B^{1/4} = 100$ *MeV, corresponding to figs. 6.7, 6.8 and 6.9. For this parameter choice the transition is marked by the symbols on the "DD2" curve.*

In fig. 6.17 we examine the speed of sound for $0 \leq g_\omega \leq 3$ within the parameter choice $m_\sigma = 600$ MeV, $m_q = 300$ MeV and $B^{1/4} = 100$ MeV, corresponding to figs. 6.7, 6.8 and 6.9. Since the Bag constant does not affect the stiffness of the EoS (it just changes the value of the vacuum pressure) the slope of theses curves for any choice of B would remain the same. Only the transition values of the energy density ϵ_t from one EoS to the other EoS would change and in equal steps of $\Delta\epsilon$.

For $g_\omega = 0$ and $g_\omega = 1$, $\Delta\epsilon \simeq 95$ MeV/fm^3, see also the discussion in the previous sections. The symbols on the "DD2" curve mark the point where the transition takes place and the stars leave the hadronic branch. The corresponding symbols on the QM lines mark then the points, where the QM core appears. As one would expect, an increase of the repulsive coupling stiffens the EoS, which is equivalent to a larger speed of sound within the medium. The $g_\omega = 0$ line saturates at $c_s^2 = \frac{1}{3}$ which is reasonable since ultrarelativistic matter without interactions saturates at $p(\epsilon) = \frac{1}{3}\epsilon$ [75, 8]. Since $g_\omega = 3$ has far too high transition pressures for hybrid- and twin stars the highest considered repulsive coupling $g_\omega = 2$ reaches $c_s^2 \simeq 0.5$. That means that all physically relevant and considered cases in this work lie within $0.3 \leq c_s^2 \leq 0.5$. This will become important in the following when we compare our results with those from Alford et. al [89, 90, 91].

Various EoS and the corresponding mass-radius relations for fixed g_ω and different Bag constant

Figure 6.18 shows the EoS at fixed $g_\omega = 0$ for various values of the Bag constant $B^{1/4}$. For increasing values of B the transition pressure p_t increases. As in the case of increasing B at fixed g_ω, increasing $B^{1/4}$ while varying g_ω leads to the same behaviour of the different EoS.

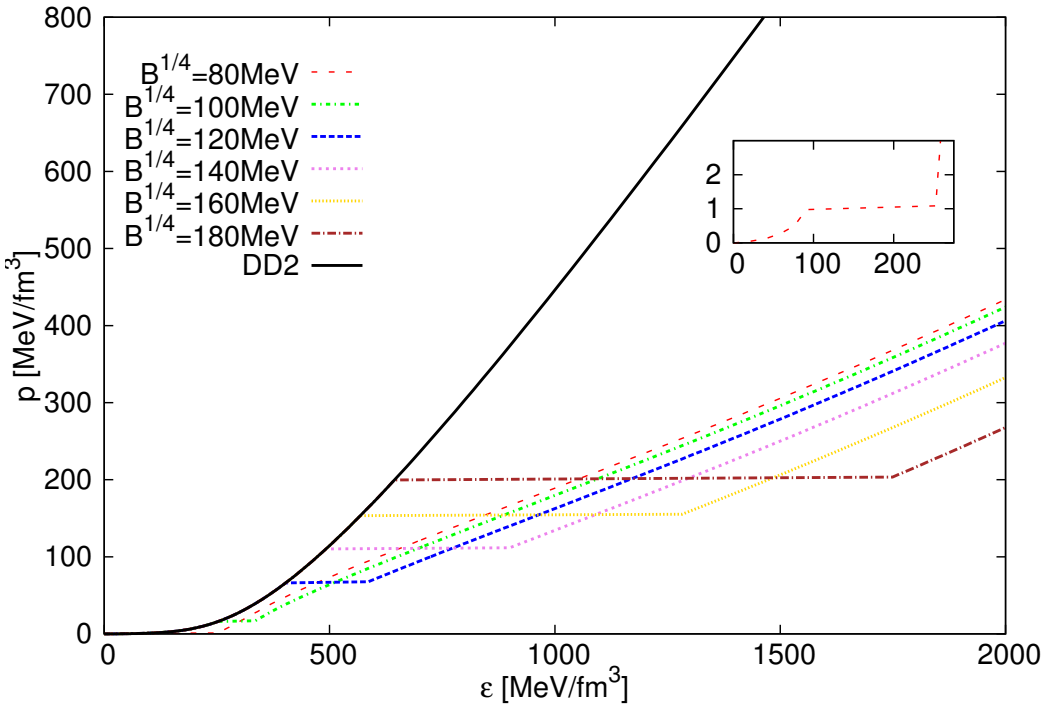

Figure 6.18: *The EoS with fixed* $g_\omega = 0$ *while varying* B *at* $m_\sigma = 600$ *MeV and* $m_q = 300$ *MeV. The inlaid figure shows the behaviour of the EoS for* $B^{1/4} = 180$ *MeV.*

For $B^{1/4} = 80$ MeV, $p_t \simeq 1$ MeV/fm^3, $\epsilon_t \simeq 92$ MeV/fm^3 and the discontinuity in energy density is $\Delta\epsilon \simeq 160$ MeV/fm^3 (see inlaid figure). For the highest chosen value of $B^{1/4} = 180$ MeV $p_t \simeq 202$ MeV/fm^3, $\epsilon_t \simeq 650$ MeV/fm^3 and $\Delta\epsilon \simeq 1100$ MeV/fm^3, i.e. the discontinuity in the energy density $\Delta\epsilon$ increases also with B. Figure 6.19 shows the mass-radius relations for $g_\omega = 0$ while varying B with $m_\sigma = 600$ MeV and $m_q = 300$ MeV. For the smallest value of $B^{1/4} = 80$ MeV the QM core appears at already $0.11 M_\odot$ at a radius of ~ 25 km (see inlaid figure), see also fig. 6.20.

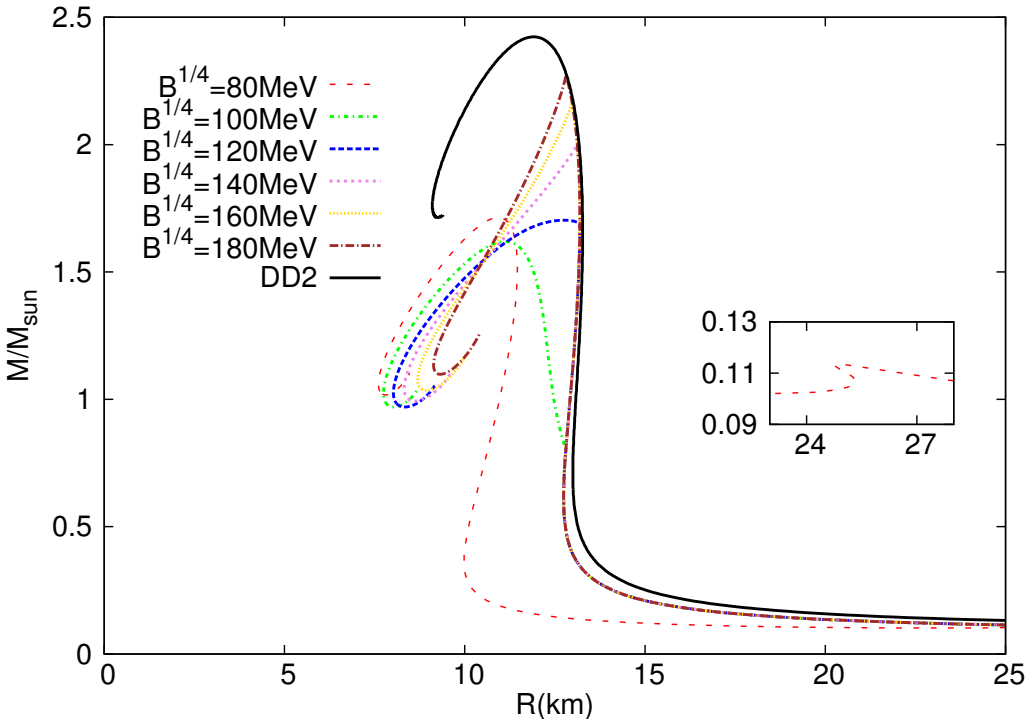

Figure 6.19: *The mass-radius relation with fixed* $g_\omega = 0$ *while varying* B *at* $m_\sigma = 600$ *MeV and* $m_q = 300$ *MeV. The inlaid figure accentuates the behaviour of the mass-radius curve for* $B^{1/4} = 80$ *MeV which else is hardly perceivable.*

The shape of the curve is similar to the pure hadronic one but shifted to slightly smaller values of mass and radius due to the appearence of the QM core. The transition from HM to QM appears at $\frac{\epsilon}{\epsilon_0} \leq 1$, see fig. 6.21. The inlaid figure displays a disconnected mass-radius branch, which is an indication for a twin star. These disconnected solutions were found up to values of $B \simeq 90$ MeV, getting harder to detect with larger B and always at physically too small transition energy densities $0.66 \leq \frac{\epsilon}{\epsilon_0} \leq 1$, see figs. 6.21 and 6.25, and shall therefore not be discussed any further.
For $B^{1/4} = 100$ MeV the transition occurs at $\frac{\epsilon}{\epsilon_0} \simeq 1.8$. The respective values are $p_t \simeq 15$ MeV/fm^3, $\epsilon_t \simeq 230$ MeV/fm^3 and $\Delta\epsilon \simeq 90$ MeV/fm^3 (see also inlaid figure in fig. 6.7, fig. 6.18 and fig. 6.20). The QM core appears at $\sim 0.8 M_\odot$ at a radius of ~ 12.5 km. The star configuration does not

get unstable up to $\sim 1.6 M_{\odot}$ at a radius of ~ 11 km, which can altogether be observed in fig. 6.20. The resulting mass-radius relation for this EoS is also shown in fig. 6.8. Higher values of the vacuum energy term B lead to much smaller hybrid star branches, hardly visible and in accordance with [89, 90, 91]. The configurations get unstable nearly immediately after the appearence of the QM core, which itself emerges at a higher mass. The case $B^{1/4} = 140$ MeV reaches $\sim 1.9 M_{\odot}$ but after the transition has set in, the star configurations get quickly unstable. These stars support, if they support, only a very small QM core and subsequently become unstable.
Interesting to note is that, when varying the vacuum pressure B, the resultant family of mass radius curves rotate clockcounterwise around a small region where all of the curves pass through, see fig. 6.19. This behaviour has already been found by Yudin et al. [108].

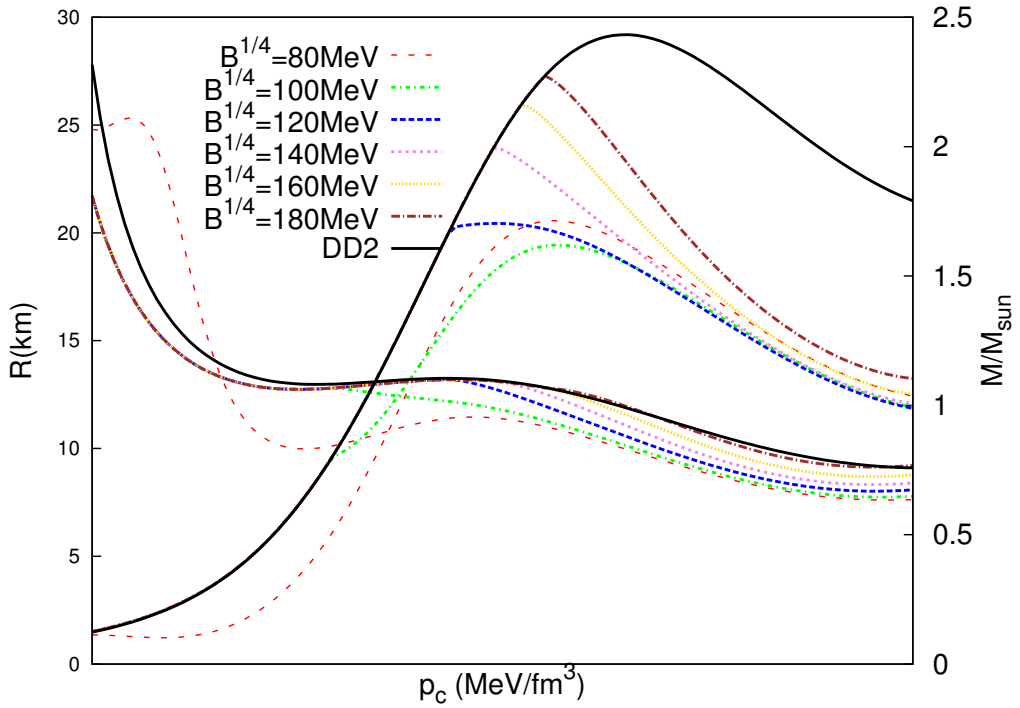

Figure 6.20: *The radius- and mass curves as function of the central pressure* p_c *with fixed* $g_\omega = 0$ *while varying* B *at* $m_\sigma = 600\ MeV$ *and* $m_q = 300\ MeV$. *The curves starting in the upper left region are the radius curves whereas the curves starting on the lower left side are the mass curves.*

However, the transition pressure rises with the increase of g_ω, which generates eventually an unstable QM core.

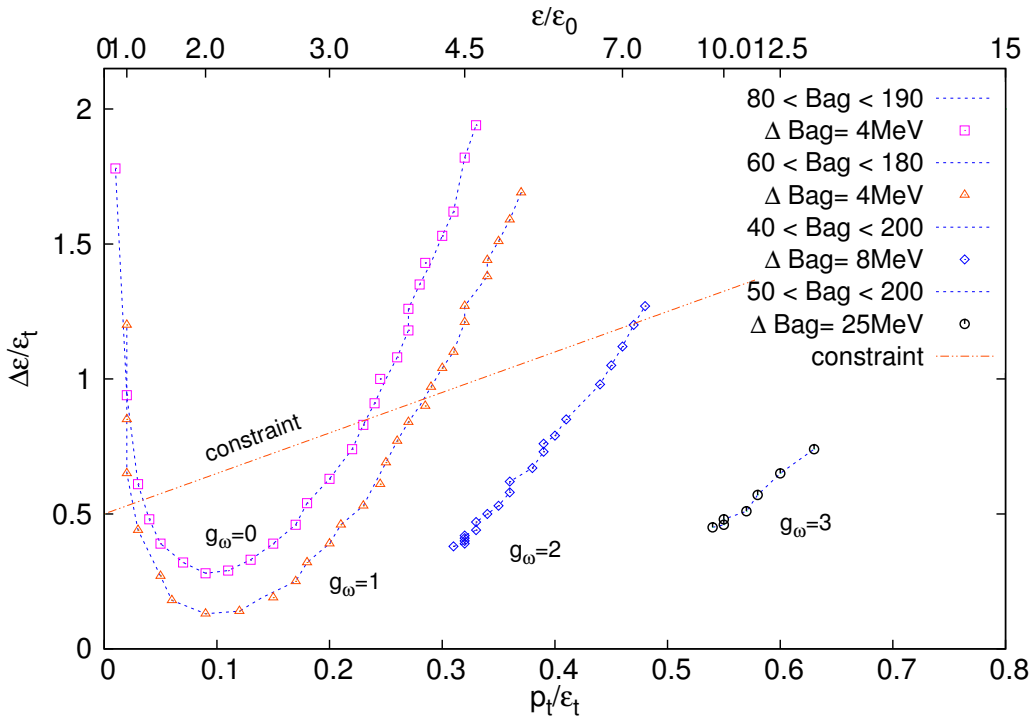

Figure 6.21: *Phase diagram for hybrid stars with fixed g_ω while varying $40MeV \leq B \leq 200\ MeV$ at constant $m_\sigma = 600\ MeV$ and $m_q = 300\ MeV$. The axes display the transition pressure p_t and the energy density discontinuity $\Delta\epsilon$ in units of the nuclear energy density at the transition ϵ_t.*

The labelling of the axes in the phase diagram for fixed g_ω in fig. 6.21 is the same as for fixed B in fig. 6.15. Generally, increasing the value of the repulsive coupling of the QM EoS leads to a higher p_t and also a larger discontinuity $\Delta\epsilon$ for a given B. The higher the repulsive force within the QM core, the higher is p_t for a QM core to appear. For the transition to occur at $2\epsilon_0$, B has to be at least 104 MeV in case of zero repulsion ($g_\omega = 0$), corresponding to the minimum of the plotted data in fig. 6.21. For $g_\omega = 1$, B has to be at least 84 MeV to be located at $2\epsilon_0$. Both cases lead to stable hybrid star configurations, shown in figs. 6.19 and 6.20 for $g_\omega = 0$.
However, both trends are parabola like, crossing the constraint line twice, whereas the $g_\omega = 2$ and the $g_\omega = 3$ case stay below the constraint (except for the choice $g_\omega = 2$ and $B \gtrsim 190$ MeV). The $g_\omega = 2$ case in the range $50 <$

$B < 200$ MeV corresponds to $4.5 \leq \frac{\epsilon_t}{\epsilon_0} \leq 7$. There a connected hybrid star branch, even if very small and hardly observable, exists up to $B \simeq 180$ MeV. The stars get unstable almost immediately after the appearance of the QM core. A higher value of B leads to transitions at already unstable mass-radius configurations. In case of even higher repulsion $g_\omega = 3$ the transition takes place at 10-14 times nuclear energy density at an already unstable mass-radius configuration. Our results match the results from [89, 90, 91].
An investigation in the phase space by variation of m_σ and m_q leads us to the conclusion that neither $\frac{\Delta\epsilon}{\epsilon_t}$ nor $\frac{p_t}{\epsilon_t}$ changes in an adequate amount to get a relatively large jump in energy density accompanied with a small transition pressure, which is an essential requirement for twin stars, see fig. 6.25. Their attractive character through varying both quantities is far weaker than the variation of g_ω and $B^{1/4}$ [109, 51, 56].

Comparison with other models

In the last section we have analyzed the parameter dependence of the resulting hybrid star properties within our HM-QM model. One main outcome of our analysis is the absence of a twin star region within the physical reasonable parameter space. Theoretically we have found a narrow parameter region where twin stars do exist ($p_t/\epsilon_t < 0.05$), however, within all of these EoSs the HM to QM phase transition appears at irrelevant low density ($\epsilon_t < \epsilon_0$). As the existence of twin stars have been found in many different kind of phase-transition scenarios, e.g. hadron-quark phase transition [110, 111, 96] (using a Maxwell- or Gibbs construction), hyperon phase transition [112], pion [113] and kaon condensation [114, 115], the question arises, what the main reason is, that we do not find twins in our model? On the one hand, in all the existing twin star models, the relevant EoS parameter region where twins occur, is always narrow and a 'parameter fine-tuning' is needed to achieve an EoS which will result in a twin star behaviour. On the other hand, we have carefully analysed the allowed parameter space in the last section and did not find a twin star solutions where $\epsilon_t > \epsilon_0$.

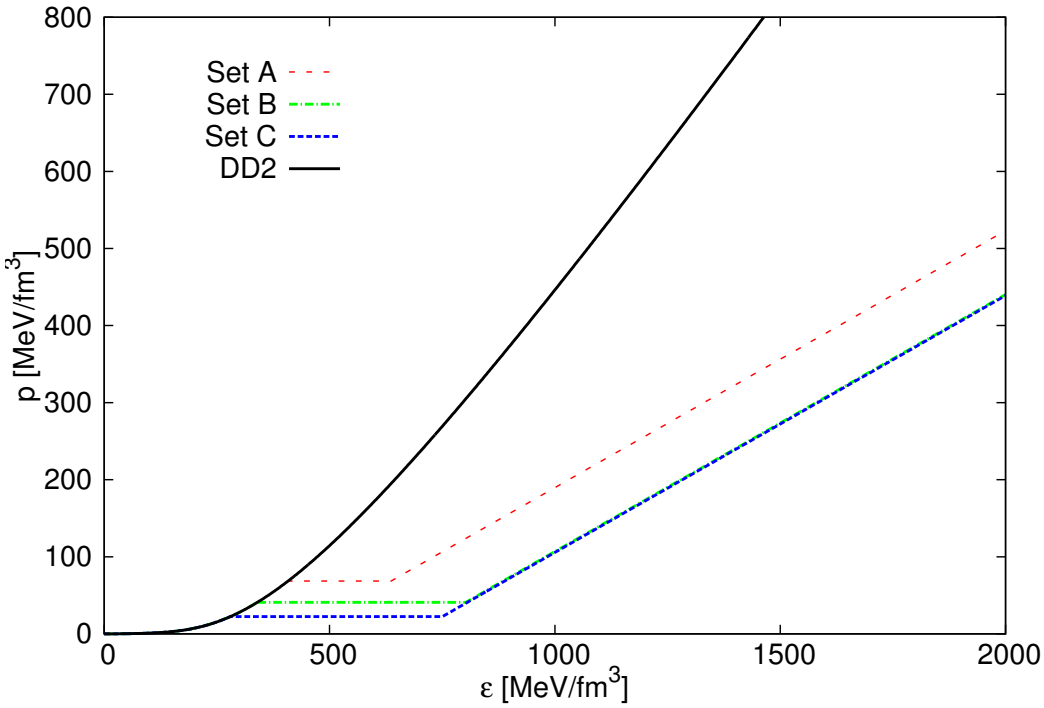

Figure 6.22: *The EoS for three different parameter sets corresponding to a QM-EoS given by eq. 6.7. The parameters of the three sets are displayed in table 6.2.*

We show that the non-existence of twin stars in our model is due to the fact that the potential twin star area lies outside of our available parameter region and therefore cannot be reached in our simulations. By constructing the phase transition within our model we are not capable to choose arbitrary values for $\Delta\epsilon$, ϵ_t and p_t (like Alford et. al [89, 90, 91]), because we need to match the HM-EoS with the QM-EoS in a consistent way, i.e. find the intersection between pressure p and chemical potential μ for the transition pressure p_t.

Star sequence	p_t/ϵ_t	$\Delta\epsilon/\epsilon_t$	M_1	R_1	M_2	R_2
● Set A	0.17	0.56	1.69	13.26	1.70	11.72
■ Set B	0.12	1.36	1.35	13.21	1.26	8.91
▲ Set C	0.08	1.68	0.96	13.05	1.20	7.90

Table 6.2: *The parameter choice for a constant speed of sound* $c_s^2 = \frac{1}{3}$ *of the three different sets of star sequences with the respective masses and radii of the corresponding branches (fig. 6.23)*

In this section we use the same density dependent DD2 EoS for the hadronic part, but we use a much simpler model for the QM sector. Similar to [89, 90, 91] we take a QM-EoS, which is parameterized by the following three values: p_t, $\Delta\epsilon$ and and c_s (constant sound speed in quark matter) and which is given by eq. 6.7. In order to construct a comparable QM-EoS with respect to our model, we have used a fixed value of $c_s^2 = 1/3$ for the following calculations. The EoS for $p > p_t$ in this simple QM model has the following form [89, 116]

$$p(\epsilon) = c_s^2\,(\epsilon - \epsilon_*) \quad , \quad \text{with: } \epsilon_* := \epsilon_t + \Delta\epsilon - \frac{1}{c_s^2} p_t \,, \tag{6.7}$$

where ϵ_* is the energy density at zero pressure. Fig. 6.22 shows the resulting EoSs for three choices of the parameters, which are given in tab. 6.2. In contrast to our model the parameters can be chosen in such a way that twin stars appear in a physically meaningful region.

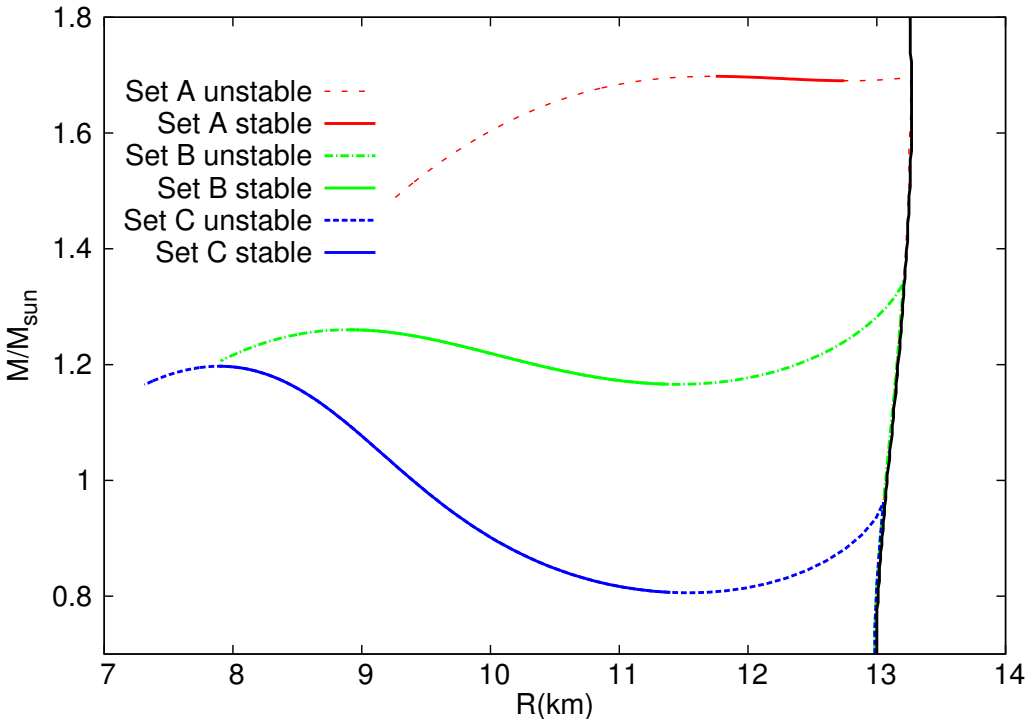

Figure 6.23: *The mass-radius relation for three different parameter sets corresponding to a QM-EoS given by eq. 6.7. The parameters of the three sets are displayed in tab. 6.2. Set C shows impressive the appearance of a second stable branch, where $M_2 > M_1$: The maximum mass of the second branch is larger than the maximum mass of the first branch. All displayed solutions are twin star solutions.*

In Figs. 6.23 and 6.24 the mass-radius relations and the radius-mass curves of the three chosen representative twin star parametrizations are displayed. The Set A mass-radius relation has been calculated by using the parameter configuration: $\Delta\epsilon/\epsilon_t = 0.56$ and $p_t/\epsilon_t = 0.168$, which is located below the constraint-line given by eq. 6.6 (see fig. 6.25). This configuration is located right at the corner of the twin star region boundary lines and the differences between the maximum masses of the first and second sequence is very small ($M_1^{max} = 1.69332 M_\odot$ and $M_2^{max} = 1.69794 M_\odot$). Set B displays a twin star where the first sequence maximum mass lies above the maximum mass of the twin star ($\Delta\epsilon/\epsilon_t = 1.36, p_t/\epsilon_t = 0.12$). The Parameter Set C curve

shows the mass-radius relation of a twin star sequence with a rather high value of $\Delta\epsilon/\epsilon_t = 1.68$ but a low value of $p_t/\epsilon_t = 0.08$. The phase transition starts at low density and the maximum mass of the first sequence is much lower than the maximum mass of the twin star sequence (see table 6.2). In this model too the neutron star sequence continuously moves to the hybrid star branch and hybrid stars with a tiny quark core are stable for a short period. The connected stable hybrid star branch is very small and difficult to recognize, as the hybrid stars get soon unstable after formation of the tiny quark core. Nonetheless twin stars somehow manage to restabilize again at a higher transition pressure.

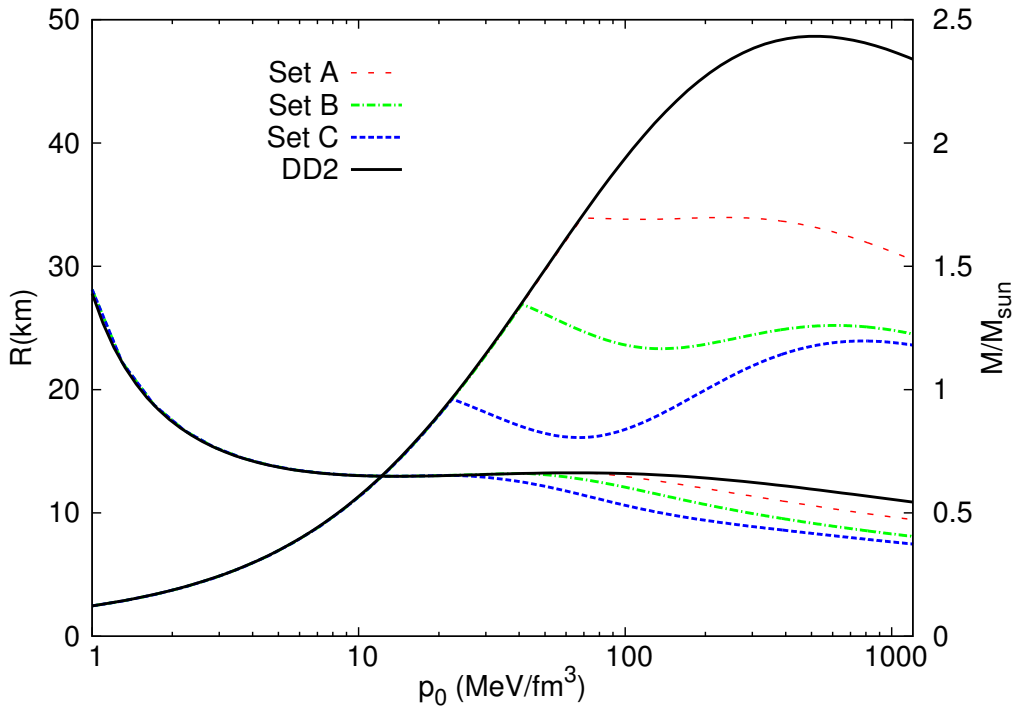

Figure 6.24: *The radius- and mass curves for three different parameter sets corresponding to a QM-EoS given by eq. 6.7. The parameters of the three sets are displayed in tab. 6.2. Set C shows the appearance of a second stable branch, where $M_2 > M_1$. All displayed solutions are twin star solutions. The curves starting in the upper left region are the radius curves whereas the curves starting on the lower left side are the mass curves.*

We do not get maximum mass values of the twin star configurations which are above the observational known value of $M = 2.01 M_{\odot}$, which means as a consequence, that all the twin star EoS are ruled out by nature.

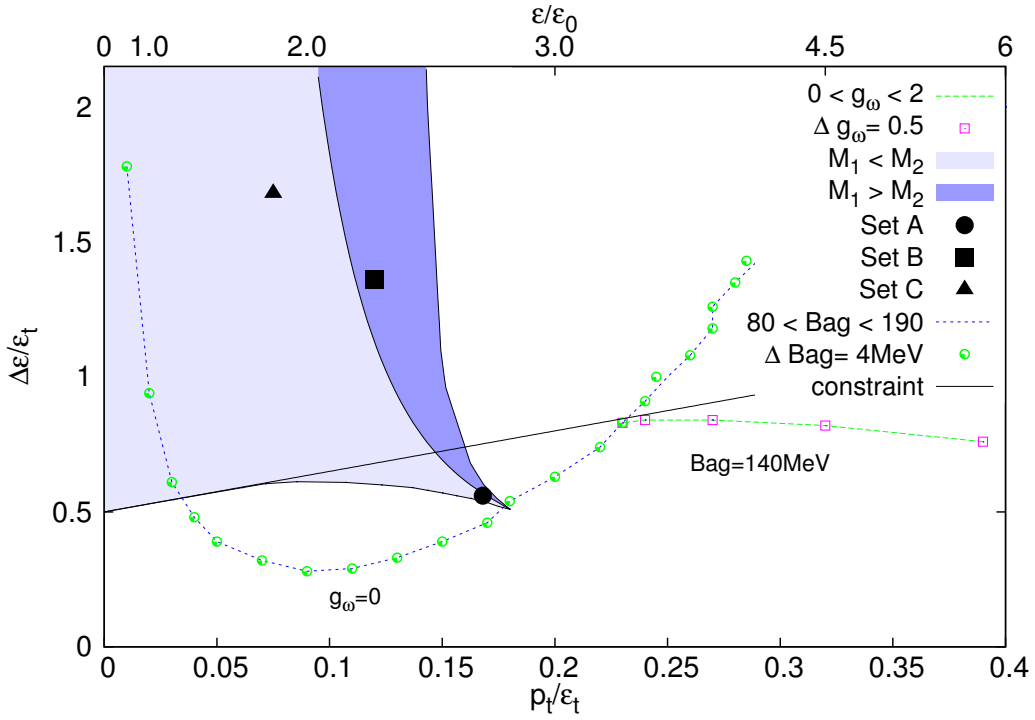

Figure 6.25: *Phase diagram for hybrid stars with the $g_\omega = 0$-line and various values of B, and $B^{1/4} = 140$ MeV at various g_ω, both with $m_\sigma = 600$ MeV and $m_q = 300$ MeV. The axes display the transition pressure p_t and the energy density discontinuity $\Delta\epsilon$ in units of the nuclear energy density at the transition ϵ_t. The shaded regions displays the twin star regions with either $M_1 < M_2$ (light blue) or $M_1 > M_2$ (blue) calculated with the QM-EoS given by eq. 6.7. The three twin star parameters sets are labelled as Set A, Set B and Set C.*

In Fig. 6.25 the twin star region in the model utilized by Alford et. al [89, 90, 91] is compared with the space of available parameters within our model. It can be easily seen that the main part of the region where twin stars exist lies out of our attainable values of $\Delta\epsilon/\epsilon_t$ and p_t/ϵ_t. Solely for irrelevant low values of p_t/ϵ_t we find a twin star area, see figure 6.19. The cusp at the

lower end of the twin star region at ($p_t/\epsilon_t = 0.18$, $\Delta\epsilon/\epsilon_t = 0.51$) overlaps in a tiny region with the curve for $g_\omega = 0$, however, we do not find any twin star in this parameter range. The radius-mass properties of hybrid stars near to the parameter region of the cusp, almost reach a twin-like structure (see e.g. the curve with $B^{1/4} = 120$ MeV in fig. 6.20). The reason for this apparent contradiction is the fact that the sound speed for $g_\omega = 0$ is not constant and slightly below the value which has been chosen to calculate the twin star area (see fig. 6.17). As pointed out in [89], a decrease of c_s^2 has the effect of scaling down the size of the twin star area and moves the cusp at the end of the twin star region upwards. Therefore, the absence of twin stars at the intersection of the cusp region is due to the energy dependence of the sound speed, resulting in an average value below $c_s^2 = 1/3$. The line between the shaded areas separates whether the mass of the first branch M_1 lies above (blue) or below (lighter blue) the mass of the second stable branch M_2. The $g_\omega = 0$ line with $B^{1/4} = 120 - 124$ MeV gets closest to the twin star region. Nevertheless, twin stars resulting from a first order phase transition could exist in nature, as other models have been constructed [117, 118] that satisfy the $M^{max} > 2.01 M_\odot$ constraint. We will see in section 6.5, that a even crossover chiral phase transition within the pure SU(3) Quark Meson model generates Twin Star solutions and that several other constraints can be fulfilled..

6.4. Quark stars

This section is a small compendium of the publication [56] based upon the my master thesis [5]. It is mentioned here mainly to the purpose of completing the discussion on compact stars, i.e. including all different considered types of stars during my studies.

Compact stars which are entirely made of quark matter, besides maybe a small layer of a crust of nuclei, are also called strange stars [119, 120]. Strange stars can only be realized in nature if strange quark matter is absolutely stable, i.e. the true ground state of matter [44, 46]. Pure quark stars based

on the simple MIT bag model could be ruled out on the basis of this measurement unless additional terms from an effective one-gluon exchange or from color-superconductivity are incorporated [121, 122]. The quark-quark interaction is, like in the case on hybrid stars 6.3, mediated by the exchange of meson fields. These interactions are conceptually different from the NJL model which considers point coupling terms between quarks. We consider scalar- and vector meson contributions to effectively model the attractive and repulsive character of the strong interaction, as has also been done in the previous section 6.3 concerning hybrid stars. The maximum masses of pure quark stars are calculated by solving the TOV equations (remember section 2.2.2) for different choices of the parameters of the SU(3) quark-meson model at $T = 0$.
The properties of quark matter have to fulfill certain conditions in order to allow for the possibility of pure quark stars.

6.4.1. Stability criteria

Normal matter, consisting of ordinary nuclei, is stable on cosmological timescales, so it does not decay to quark matter with its quark constituents of up-quarks and down-quarks. This observation requires that two flavor quark matter can not be more stable than ordinary nuclear matter, meaning that the energy per baryon has to be higher than the one of the most stable known element in nature: ^{56}Fe. We adopt a value of energy per baryon of $E/A = 930$ MeV for nuclei and add a 4 MeV correction due to surface effects of lumps of quark matter balls. Hence the critical condition for two-flavor quark matter reads

$$\left.\frac{E}{3A}\right|_{p=0} = \left.\frac{\epsilon}{n_q}\right|_{p=0} \gtrsim 311\text{MeV} \tag{6.8}$$

This condition guarantees the stability of atomic nuclei, meaning that atomic nuclei do not dissolve into their constituent quarks (Recall section 5.1).
On the other hand three-flavor quark matter, i.e. quark matter consisting of up, down and strange quarks, could be more stable than ordinary nuclei

which is the Bodmer-Witten hypothesis [44, 46]. Ordinary nuclear matter can not decay to strange quark matter, as there is a barrier between these two states of matter due to strangeness conversion via weak interactions with a corresponding conversion timescale much longer than the age of the universe. The presence of the new degree of freedom, the strange quark, in quark matter lowers the overall energy per baryon, so that this state could be energetically favorable compared to nuclear matter. Hence, the condition for absolutely stable strange quark matter of $E/A < 930$ MeV can be recast in the form

$$\left.\frac{E}{3A}\right|_{p=0} = \left.\frac{\epsilon}{n_q}\right|_{p=0} \leq 310\text{MeV} \tag{6.9}$$

In the following the physical condition for two-flavor quark matter, eq. (6.8), is denoted as the two-flavor condition (or two-flavor line in the plots) and the one for three-flavor quark matter, eq. (6.9), the three-flavor condition (or three-flavor line in the plots).

6.4.2. Results

Figure 6.26 shows as a contour plot the dependencies of the maximum mass of pure quark star configurations on the vacuum constant $B^{1/4}$ and the vector coupling constant g_ω. For $B^{1/4} = 120$ MeV and $g_\omega = 2.0$ one finds a maximum mass of about $1.6 M_\odot$. In general, smaller values of the vacuum constant B and higher values for the vector coupling constant g_ω lead to higher maximum masses.

The two-flavor line indicates the two-flavor constraint (6.8) and the three-flavor line the three-flavor constraint (6.9). In the area above the two-flavor line the condition (6.8) is fulfilled, i.e. normal matter can not decay to two-flavor quark matter as observed in nature. Hybrid star configurations, consisting of an entirely mixed phase, are located in the parameter range above the two-flavor line.

A high mass of the sigma meson seems to be necessary in order to fulfill the constraints for pure quark star configurations, i.e. equation (6.8) and (6.9),

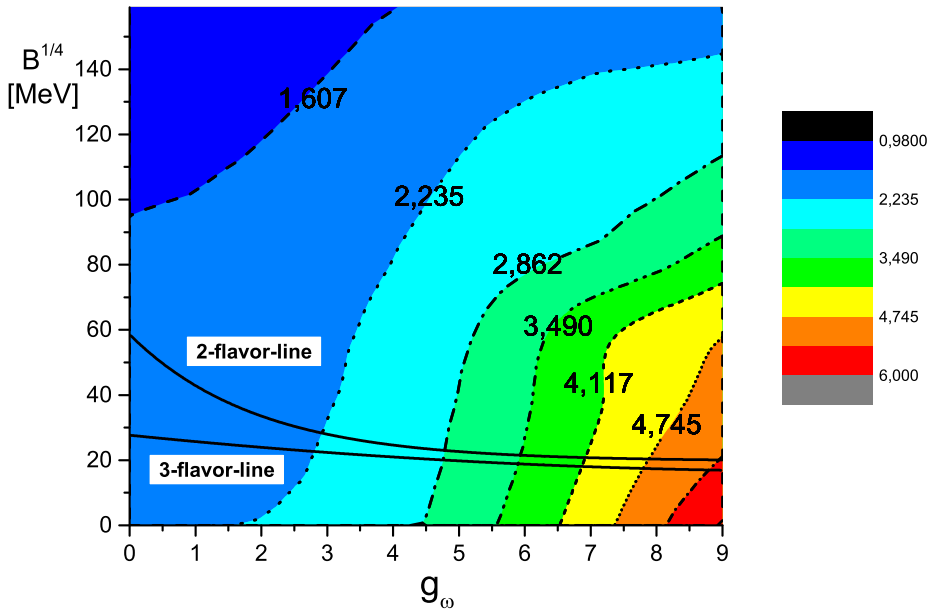

Figure 6.26: *Maximum masses for three-flavor pure quark stars in the plane of the vacuum constant B and the vector coupling constant g_ω. The two-flavor and three-flavor lines delineate the region for hybrid stars (above the two-flavor line) and pure quark stars (below the three-flavor line). Pure quark star configurations do not appear for the parameters chosen ($m_\sigma = 600$MeV and $m_q = 300$MeV).*

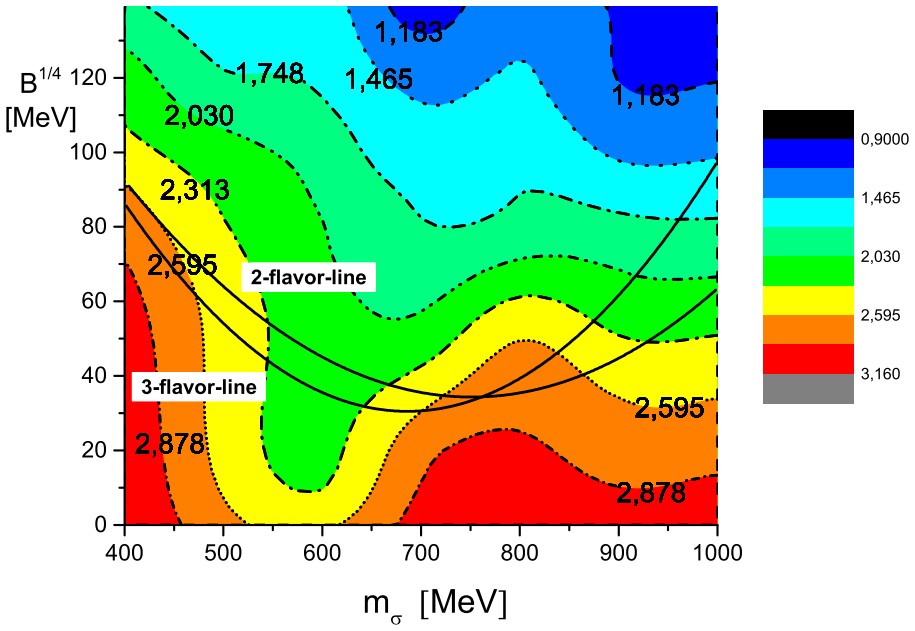

Figure 6.27: *Maximum masses and stability configurations for pure quark star configurations with a vector coupling constant of* $g_\omega = 3.0$.

in contrast to the variation of the vector coupling constant. A projection on the g_ω-m_σ-plane on the other hand (with a fixed value of $B^{1/4} = 120$ MeV) leads to a null result for pure quark star configurations due to the high value of the vacuum constant. Only a small value of the vacuum constant leads to pure quark star configurations.

The resulting maximum masses for a value of $g_\omega = 3.0$ and lines of constraints are shown in Fig. 6.27. There is an overall increase of the maximum mass as expected for a greater repulsive interaction. For $m_\sigma \geq 600$ MeV the maximum mass increases with the σ meson mass again. This behavior indicates a switch in the dominance of the scalar- and vector field contributions to the stiffness of the equation of state. Above a certain value, around $g_\omega \sim 2.75$, the repulsive fields gain on their influence on the maximum masses compared to the attractive scalar fields. A combination of $g_\omega \gtrsim 2.75$ and $m_\sigma \geq 600$ MeV leads then to higher maximum masses with increasing σ meson mass instead.

A particular behavior of the EoS has not been observed, so that most likely the higher mass of the sigma meson and its influences via λ_1, on the spontaneous symmetry breaking patterns may be responsible for that feature.
The lines of the two constraints intersect at $B^{1/4} \sim 32$ MeV and $m_\sigma \sim 760$ MeV. From this point on pure quark star configurations are realized between the two lines of constraint as discussed above. At the intersecting point at $B^{1/4} \sim 32$ MeV and $m_\sigma \sim 760$ MeV the maximum mass of the quark star would be $\sim 2.7 M_\odot$, being smaller for larger values of the σ meson mass m_σ and larger values of the vacuum constant. A pure quark star with a maximum mass of $\sim 2.0 M_\odot$ can be found at a vacuum constant of $B^{1/4} = 70$ MeV for σ meson masses between 900 MeV $\leq m_\sigma \leq 1000$ MeV.
Weissenborn et al. [122] use an extended quark bag model. Strange stars can reach maximum masses beyond $2M_\odot$ in their work if additional terms compared to the standard MIT bag model are introduced, either in the form of some effective interaction motivated from one-gluon exchange or from a large gap motivated from color-superconductivity. They found a maximum mass for a pure quark star to be at $2.54 M_\odot$, which is in the same order of magnitude as in this work.
The variation of the vector coupling constant shows the highest impact on the EoS. The higher its value, the stiffer the EoS, leading to maximum masses in excess of $2M_\odot$. The dependence of the EoS with the constituent quark mass m_q in vacuum, which fixes the scalar coupling constant, is such that the smaller m_q, the stiffer the EoS. The mass of the σ-meson studied covers a range from 400 to 1000 MeV. For a smaller mass of the σ-meson the EoS becomes stiffer. Finally, the vacuum constant does not affect the values of the meson fields, it just shifts the energy density at a given pressure. The EoS substantially stiffens when decreasing the vacuum constant so that for small values of $B^{1/4} \lesssim 40$ MeV maximum masses of up to $\geq 2M_\odot$ could easily be reached.
The stability of two-flavor and three-flavor quark matter have been checked as well, to see whether or not the model parameter space allows for physically reasonable quark matter properties in the SU(3)-flavor approach. The $2M_\odot$ limit set by the recently discovered millisecond pulsars PSR J1614-2230 [76]

and PSR J0348+0432 [77] could be reached. Having considered the stability constraints in the equations (6.8) and (6.9), most choices of the parameter space were found to be hybrid stars[5]. Nonetheless, pure quark star configurations with $\sim 2M_{\odot}$ can be realized in a small physically reasonable parameter range. A sizable additional repulsion mediated by the exchange of vector mesons as well as a nonvanishing vacuum pressure seems to be crucial to allow for maximum mass configurations of quark stars compatible with the recent pulsar mass measurements. As mentioned, a more detailled treatment on this subject can be found in [5, 56].

6.5. Twin stars

Depending on the utilized EoS a compact star might be composed of a hadronic phase (Neutron Star), a quark phase (Quark Star) or a mixed phase (Hybrid Star). Even exotic EoS's can yield possible stable solutions. In [123, 124] the authors constructed Quark Stars admixed with fermionic dark matter. However, to construct hybrid stars with a quark matter core and a hadronic shell, the EoS's decribing the two phases of ultradense matter have to be united under certain corresponding assumptions via a Gibbs- or a Maxwell construction [97, 57], remember the previous section 6.3. Depending on the microscopic properties, i.e. the EoS, a second stable branch in the mass radius relation might appear (see figure 6.23), the so called *third family* of compact stars [125, 98, 87, 126, 127, 128], which could not be found within the microscopic approach via the Maxwell construction with both utilized EoS's in the previous discussion.

This section now deals with Twin star solutions resulting from the SU(3) Quark Meson model EoS at vanishing temperature. These solutions have not been detected earlier since in [57] the parameter range has been scanned mainly for the $2M_{\odot}$-constraint at rather low g_{ω}. Twin star configurations

[5] Build of a completely mixed phase - to be distinguished from the hybrid stars discussed in section 6.3, since these are constructed with two independend phases.

however rise for large repulsive coupling and small vacuum pressure term. A Twin Star configuration resulting from one EoS has so far not been made public. Apart from the $2M_{\odot}$-constraint we furthermore impose a new constraint: The Keplerian frequency for rotating compact stellar objects.

6.5.1. Keplerian frequency: Rotating compact objects

Neutron stars are usually observed as pulsars, which are rotating compact stars. The frequency is limited by the Keplerian (or mass-shedding) frequency, which is a rotational limit obtained when the equatorial surface velocity equals the orbital speed just above the surface. Lattimer and Prakash determined an empirical formula for the mass-shedding limit for an arbitrary neutron star mass, as long as the mass is not close to the maximum mass [129]. The condition for a particle to rotate on an orbit at the stellar equator is classically

$$\Omega_c = \sqrt{\frac{M}{R^3}} \tag{6.10}$$

and it is known that the relativistic corrections lessens the classical value [8]. One can use an empirical formula including the non-rotating mass M_{nr} and radius R_{nr}, which are obtained by the TOV equations 2.55 and 2.63, rather than solve the more computationally intensive general relativistic solutions for rotating stars. In this article we follow a parametrization from Lattimer and Prakash [129]. Here

$$P_{\min} \simeq (0.96 \pm 0.03) \left(\frac{M_{\odot}}{M_{nr}}\right)^{1/2} \left(\frac{R_{nr}}{10\text{km}}\right)^{3/2} \text{ ms} \tag{6.11}$$

with M_{nr} and R_{nr} referring to the non-rotating mass and radius from the TOV equations and ν being the frequency given in milliseconds. Eq. (6.11) can be used as a rough estimate to limit masses and radii for stars made of quarks [122]. In order to constrain the allowed mass-radius for our compact

stars, we will follow previous works [129, 130] and impose that the maximum spin rate allowed is given by the most rapidly rotating pulsar observed up to now, the PSR J1748-2446ad, with a spin rate of 716 Hz [131]. Several constraints have to be fullfilled by the mass-radius relation of a compact object. In Refs. [132, 133] a rigorous causal limit for normal neutron stars has been presented independent of any other assumptions about the EoS. This sets the smallest radius possible for a given mass, being $R \geq 2.87M$ [129].

6.5.2. Influence of the Bag Constant

In order to study the possible existence of Twin Stars, we start by varying the value of the bag constant $B^{1/4}$. The change of the value of the bag constant modifies the stiffness of the EoS, and, hence, the maximum mass [46], while the meson fields are independent of this variation [2, 56, 57].
In Fig. 6.28 we show the EoS (upper plot) as well as the non-strange and strange scalar fields (lower plot) as a function of the energy density for the parameter choice $m_q = 300$ MeV, $m_\sigma = 600$ MeV, $g_\omega = 4$ and different values of the bag constant $B^{1/4}$. As expected, we find that small values of the bag constant of $B^{1/4} \sim$ 40-70 MeV stiffen the EoS, while the meson fields are unaffected by this change. The finite value for the energy density at zero pressure, typical for the EoS of self-bound stars such as strange quark stars, gets closer to zero as we reduce the value of $B^{1/4}$. As this happens, a smooth non-linear behaviour of the pressure with the energy density for $100\text{MeV/fm}^3 \leq \epsilon \leq 210\text{MeV/fm}^3$ becomes noticeable at positive pressures. This non-linearity results from a crossover-type chiral phase transition taking place in this energy range, as seen in the behaviour of the scalar fields in the lower plot of Fig. 6.28. Moreover, this non-linearity for $B^{1/4} \lesssim 100$ MeV separates two different energy-density regions with positive increasing pressure, that gives rise to the appearance of two separate stable branches in the mass-radius relation and, hence, the existence of Twin Stars, as we shall

see next.

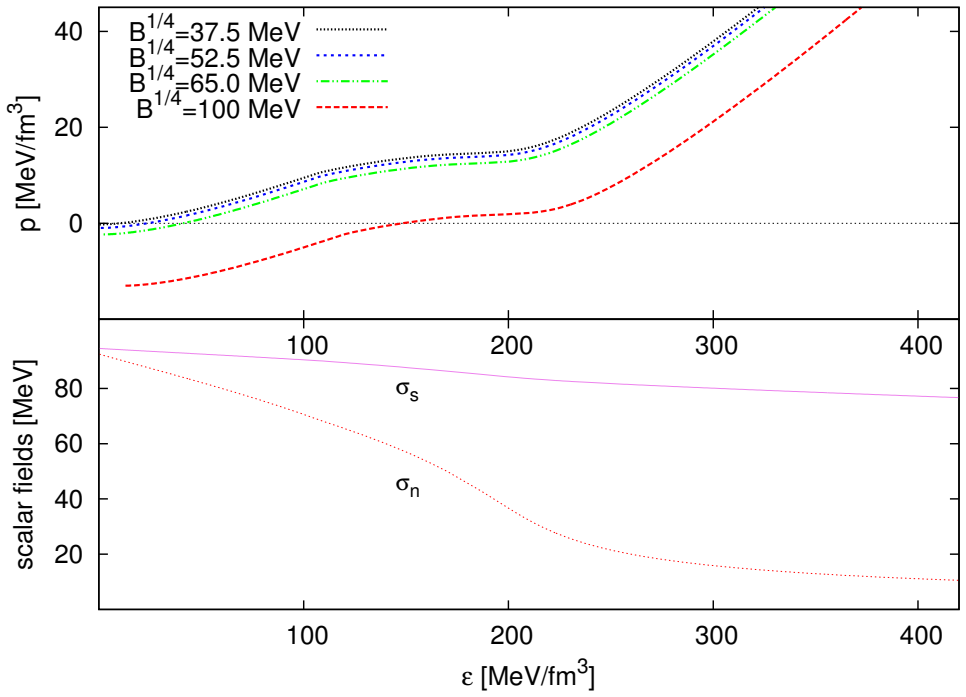

Figure 6.28: *The EoS (upper plot) and the scalar fields as a function of the energy density (lower plot) for the parameter set* $m_q = 300$ *MeV,* $m_\sigma = 600$ *MeV,* $g_\omega = 4$ *and various values of the Bag constant* $B^{1/4}$*. The Bag constant does not affect the fields, it just shifts the EoS. The chiral phase transition is crossover like and located at* $\epsilon_{cpt} \simeq 180$ *MeV, which can also be seen at the behaviour of the EoS in the same region.*

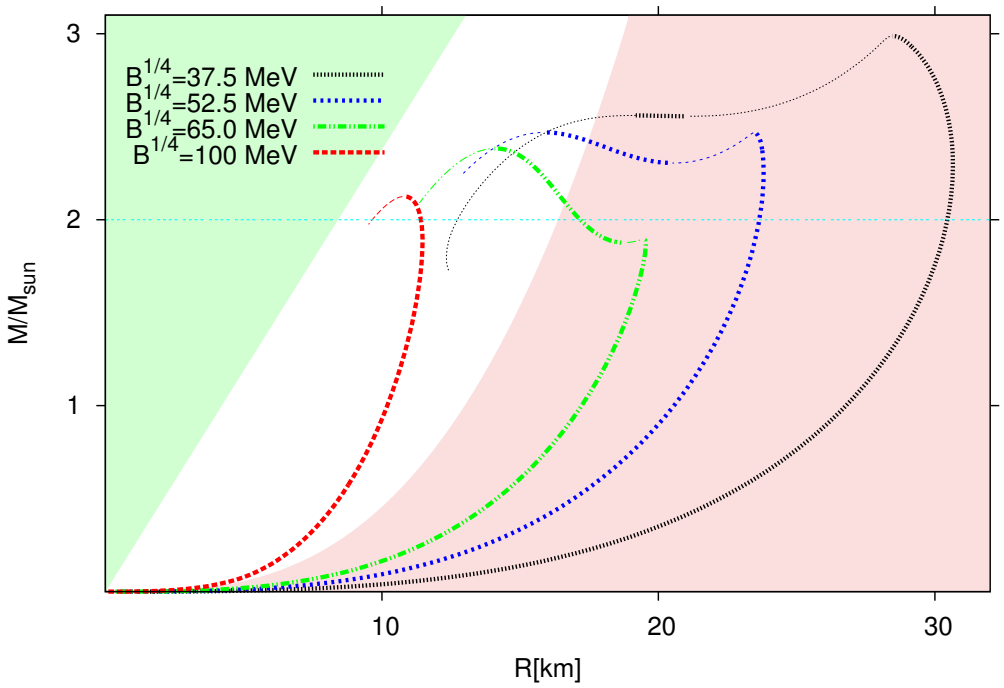

Figure 6.29: *The mass radius relation for the parameter set $m_q = 300$ MeV, $m_\sigma = 600$ MeV, $g_\omega = 4$ and various values of the Bag constant $B^{1/4}$. Lowering the values of the bag constant leads to the development of a second stable branch in the mass radius relation with relatively large radii and comparably small increment of the mass. The green shaded area in the upper left region is the causality limit, hence excluded, and the red shaded area on the right hand side is the area excluded by the millisecond pulsar PSR J1748-2446.*

The mass-radius relation for $m_q = 300$ MeV, $m_\sigma = 600$ MeV, $g_\omega = 4$ and different values of $B^{1/4}$ is depicted in Fig. 6.29. The upper left shaded region of Fig. 6.29 is excluded due to causality whereas the lower shaded area on the right-hand side is ruled out by the rotation of the millisecond pulsar PSR J1748-2446ad, as described in Sec. 6.5.1, using Eq. (6.11). The horizontal line indicates the $2M_\odot$ limit.

We first note that heavier stars with larger radii are obtained for low values of $B^{1/4}$ as compared to the $B^{1/4} = 100$ MeV case, due to the fact that the stiffness of the EoS increases. The stiffer the EoS is, the larger the masses are

and also the larger the radii become. Moreover, depending on the value of the bag constant, we find different scenarios for the mass-radius relation. The smallest value $B^{1/4} = 37.5$ MeV gives rise to two stable mass-radius branches, the Twin Star configuration. For that particular value of $B^{1/4}$, there exist two maximum masses, M_1^{max} and M_2^{max}, being $M_1^{max} \gtrsim M_2^{max}$. For the case of $B^{1/4} = 52.5$ MeV, we obtain $M_1^{max} \simeq M_2^{max}$, while for $B^{1/4} = 65$ MeV we find that $M_1^{max} \lesssim M_2^{max}$. The value $B^{1/4} = 100$ MeV does not yield to a second stable branch, thus, only one maximum mass is obtained. The values of the central pressure, central energy density, maximum mass and radius for these maxima are shown in Table 6.3.

The appearance of two separate stable branches in the mass-radius relation comes from the chiral phase transition that causes the non-linear behaviour of the EoS for values of $100\text{MeV/fm}^3 \leq \epsilon \leq 210\text{MeV/fm}^3$ (see Fig. 6.28). The physical interpretation is the following: a first branch of quark matter in a chirally non-restored phase (massive quarks) develops until the chiral phase transition sets in. After an unstable region, a new stable second branch of chirally restored quark matter (massless quarks) emerges.

We also find that, for the given values of m_σ and g_ω, the chiral phase transition is a crossover and not first order. This is in contrast to the studies on Twin Stars coming from hybrid configurations, where a first-order phase transition takes place [97]. As we increase the value of $B^{1/4}$, the phase transition is moving from the outer parts to the inner core. When the bag constant reaches values of $B^{1/4} \gtrsim 100$ MeV, the chiral phase transition is shifted to negative pressure values (Fig. 6.28) and, thus, no stable Twin Star solutions are possible, as seen in Fig. 6.29. In this case, we recover the $M \propto R^3$ relation for self-bound stars. Note that only the mass-radius branches inside the non-shaded areas are allowed by causality and the rotation of PSR J1748-2446ad, while the $2M_\odot$ limit sets a lower limit for the masses.

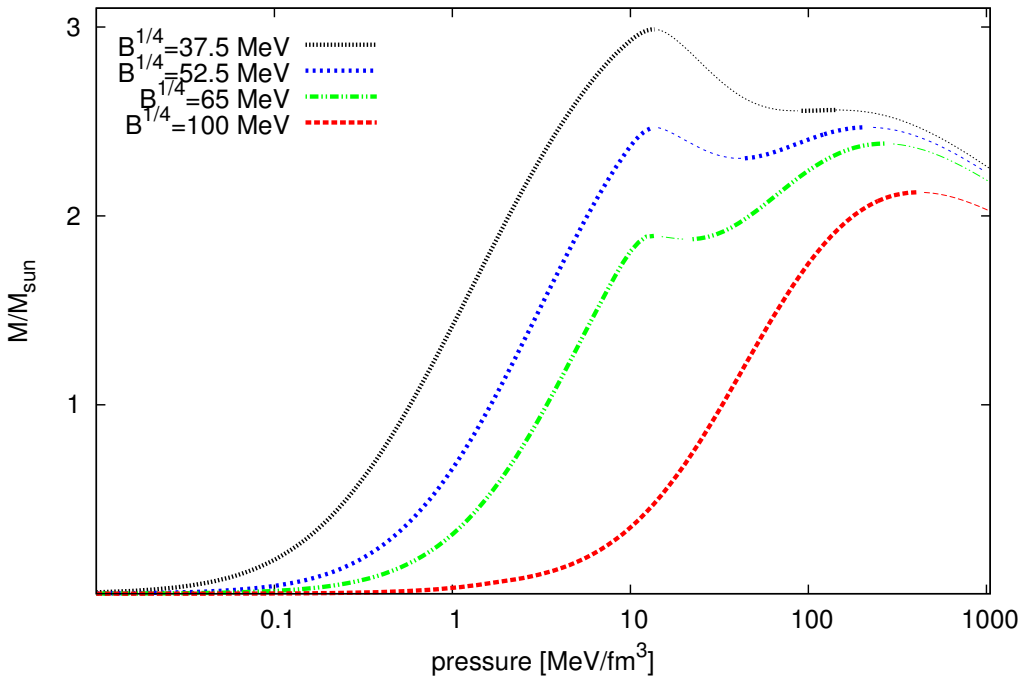

Figure 6.30: *The pressure for the parameter set* $m_q = 300\ MeV$, $m_\sigma = 600\ MeV$, $g_\omega = 4$ *and various values of the Bag constant* $B^{1/4}$. *Lowering the values of the bag constant leads to the development of a second stable branch in the mass radius relation. The configurations for* $B^{1/4} < 100\ MeV$ *become unstable at* $p \simeq 13 MeV/fm^3$ *and restablilize again for different values of* p *depending on the choice of* $B^{1/4}$.

Figure 6.30 shows the gravitational mass as a function of the central pressure. The values of the maxima in the mass radius relation and the appropriate values of the EoS are given in table 6.3.

At this stage it is pertinent to ask whether it is possible the collapse of a star in the first branch (or second family) into a star with the same mass belonging to the second branch (or third family) by introducing small perturbations that conserve the baryon number, such as compression or temperature fluctuacions. In order to assess this possibility it is necessary to show that, on the one hand, a star in the first branch has the same mass as one in the sec-

ond branch while having the same baryon number and, on the other hand, the binding energy per baryon is higher for the twin partner sitting in the second branch in order to have a more stable configuration [134].

The baryon number of the stars

The baryon number N_B of the different stars can be calculated concurrent with the gravitational mass [86], eq. 2.63. It is given as

$$N_B(r) = \frac{4\pi}{3}\int_0^r \left(1-\frac{2M(r)}{r}\right)^{-1/2} \rho_q(r) r^2 dr \tag{6.12}$$

where $\rho_q(r)$ is the quark density within the star.

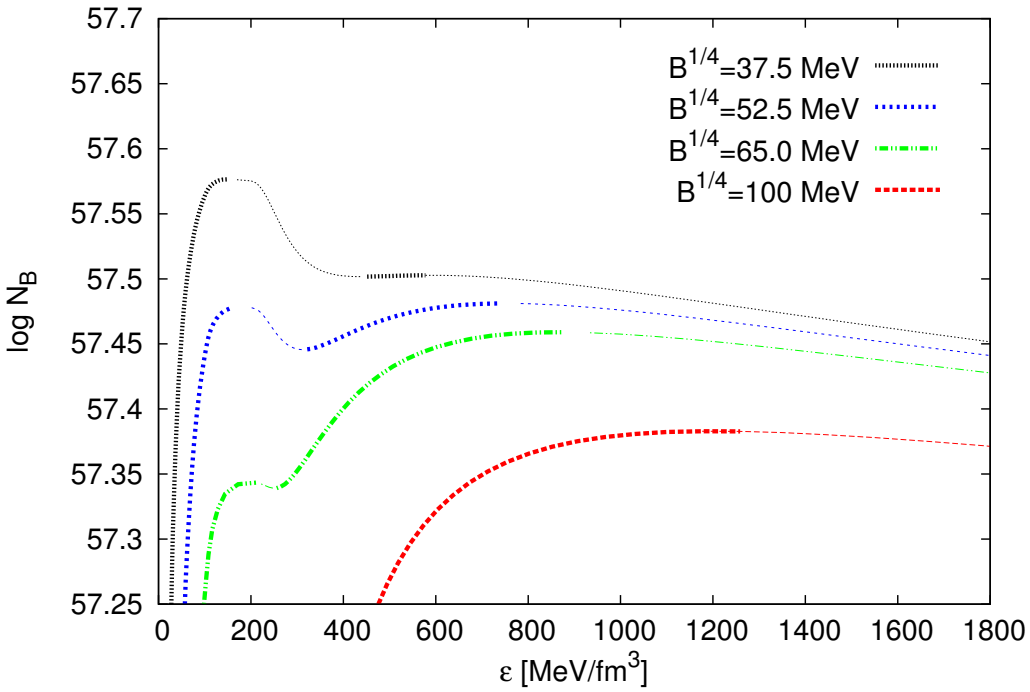

Figure 6.31: *The baryon number n_B as a function of the energy density for the parameter set $m_q = 300\ MeV$, $m_\sigma = 600\ MeV$, $g_\omega = 4$ and various values of the Bag constant $B^{1/4}$. Solid lines represent stable configurations, whereas dotted or dashed lines correspond to unstable solutions.*

Parameters			EoS $[MeV/fm^3]$		First maximum	
m_σ	$B^{1/4}$	g_ω	p(ϵ)	ϵ	$M_1/M_\odot$	R_1(km)
600	37.5	4	13.6	151.2	2.99	28.46
600	52.5	4	12.99	153.75	2.46	23.54
600	65	4	13.55	210.87	1.89	19.44
600	100	4	404.04	1176.57	2.12	10.83
Parameters			EoS $[MeV/fm^3]$		Second maximum	
m_σ	$B^{1/4}$	g_ω	p(ϵ)	ϵ	$M_1/M_\odot$	R_1(km)
600	37.5	4	141.9	577.6	2.56	19.18
600	52.5	4	209.65	736.45	2.46	15.94
600	65	4	271	873.91	2.38	14.07
600	100	4	-	-	-	-

Table 6.3: *The values of the pressure and corrsponding energy density for the values of the first and second maximum in the mass radius relation for the parameter choice* $m_q = 300$ *MeV,* $m_\sigma = 600$ *MeV and* $g_\omega = 4$ *at different values of the bag constant.*

Then, the baryonic mass is given by $M_B = N_B m_q/3$, with m_q being the constituent quark mass, and the binding energy per baryon is defined as $E_B = (M_B - M)/N_B$. Figure 6.31 shows the logarithm of the baryon number as a function of the energy density for different values of the bag constant as chosen in the above figs. 6.28, 6.29 and 6.30.

In Fig. 6.31 we show the logarithm of the baryon number as a function of the energy density for $m_q = 300$ MeV, $m_\sigma = 600$ MeV, $g_\omega = 4$ and the previously chosen values of the bag constant $B^{1/4}$. We observe that for $B^{1/4} \lesssim 100$ MeV some stars of the two stable branches have the same mass (twin partners) with the same baryon number. However, our calculations indicate that the condition for collapse coming from the binding energy is fulfilled only by the twin partners for $B^{1/4} = 52.5$ MeV. Moreover, only for $B^{1/4} = 52.5$ MeV it is possible to have few stable twin partners in the second branch that sit in the region that is not excluded by causality and rotation, as seen Fig. 6.29.

6.5.3.
Influence of the Bag Constant and the Vector Coupling Constant

In this section we vary the sigma meson mass m_σ and the vector coupling constant g_ω to locate other possible nonlinearities in the EoS.

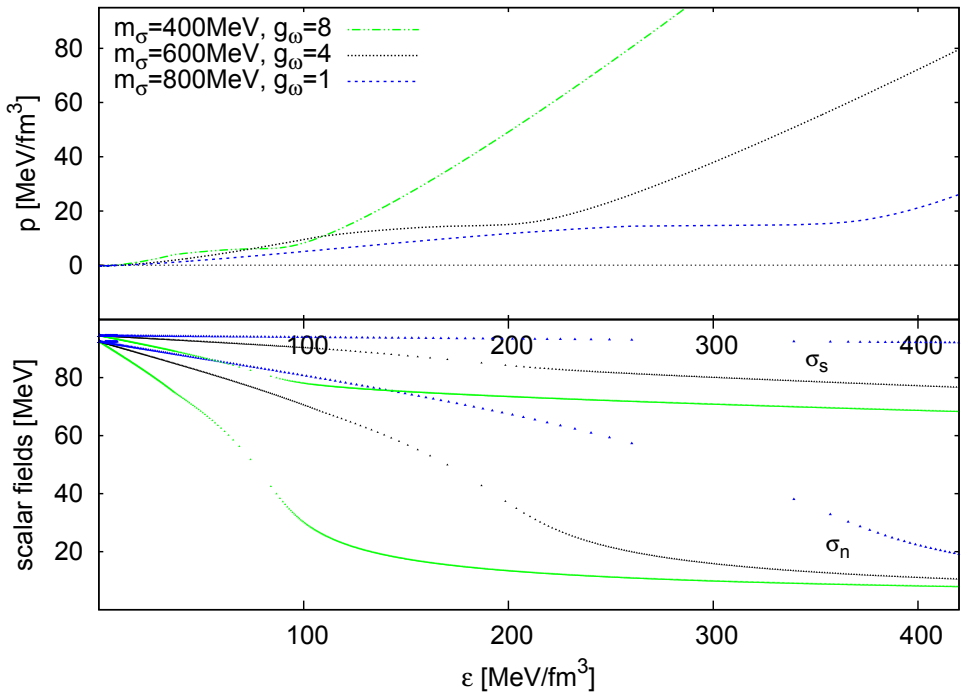

Figure 6.32: *The EoS (upper plot) and the scalar fields as a function of the energy density (lower plot) for* $m_q = 300$ *MeV,* $m_\sigma = 400 - 800$ *MeV,* $g_\omega = 1-8$ *and* $B^{1/4} = 37.5$ *MeV. The upper three curves in the lower plot are the strange scalar fields* σ_s*, and the lower lines correspond to the light quark condensate* σ_n*. Unlike as in figure 6.28 the fields are affected by a variation of* m_σ *and* g_ω*, so that the chiral phase transition differs for each parameter choice. The lower the value of* m_σ *and the higher the value of the repulsive coupling* g_ω*, the stiffer is the EoS. Since the bag constant is rather small, all nonlinearities in the EoS are located at positive pressures influencing the mass-radius relation.*

A higher mass of m_σ causes the chiral phase transition to become smoother croosover-like and the corresponding EoS gets softer. Increasing the repulsive vector coupling leads to the same trend in the fields but stiffens the EoS. Figure 6.32 shows the EoS (upper plot) and the scalar fields as a function of the energy density (lower plot). The value of the bag constant has been chosen to be $B^{1/4} = 37.5$ MeV to guarantee that the non-linearity is above

the pressure-zero axis. Note that, unlike as when varying the bag constant, the fields are affected by a variation of m_σ and g_ω (compare figure 6.28 with figure 6.32), so that the chiral phase transition differs for each parameter choice. However, for both choices, $m_\sigma = 400$ MeV where $g_\omega = 8$ and for $m_\sigma = 800$ MeV where $g_\omega = 1$ a slope like behaviour can be seen in the EoS. Note, that varying the sigma meson mass or the repulsive coupling a rather small amount causes the nonlinearities to vanish $\rightarrow$ no Twin star solutions are found anymore. The particular slope like behaviour of the EoS resulting in Twin Star solutions is found therefore in a narrower ZaTS area.
The chiral phase transition for $m_\sigma = 400$ MeV and $g_\omega = 8$ is almost a first order phase transition and located at $40\text{MeV/fm}^3 \leq \epsilon_{\text{cpt}} \leq 85\text{MeV/fm}^3$. For $m_\sigma = 600$ MeV and $g_\omega = 4$ the chiral phase transition is located at $100\text{MeV/fm}^3 \leq \epsilon_{\text{cpt}} \leq 210\text{MeV/fm}^3$, crossover like (recall the previous discussion and see also figure 6.28), whereas for $m_\sigma = 800$ MeV and $g_\omega = 1$ it is $190\text{MeV/fm}^3 \leq \epsilon_{\text{cpt}} \leq 350\text{MeV/fm}^3$ and also a crossover. The lower plot in figure 6.32 shows the scalar fields as a function of the energy density, where the transitions behaviours are more evidentely seen. The corresponding values of the pressure at the first maximum are given in table 6.4.
The nonlinearity in the EoS appears in a small window for rather small values of m_σ and a high value of the repulsive coupling g_ω, and viceversa. The corresponding Gibbs-like EoS yields small transition pressure values and corresponding (relatively) high transition energy density values, which are, following Alford et al [89, 90], important ingredients for Twin Stars to appear.

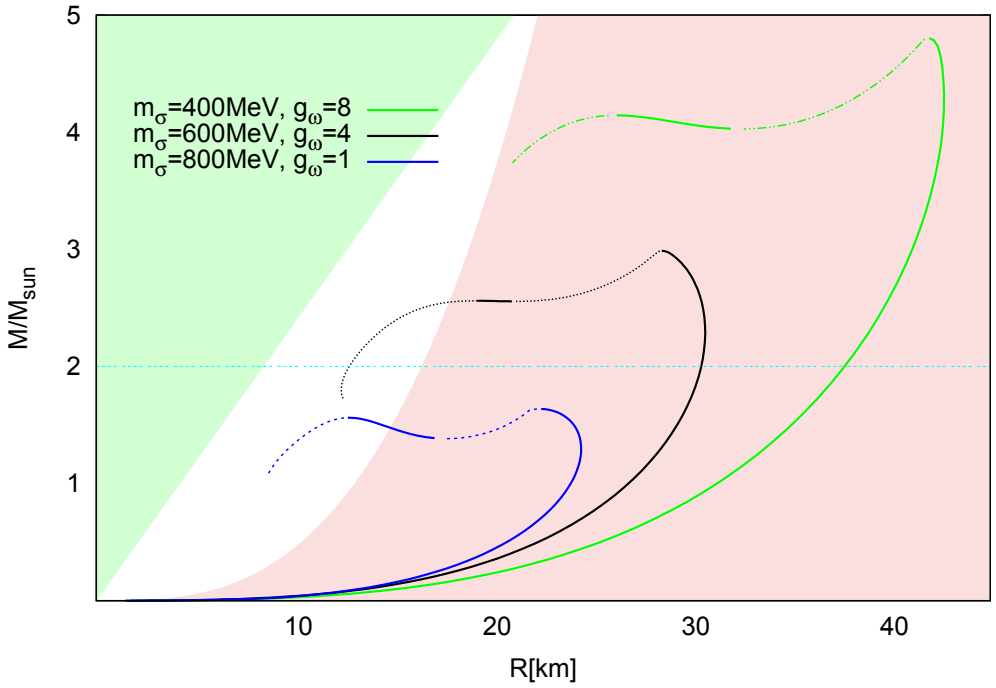

Figure 6.33: *The mass radius relation for* $m_q = 300$ *MeV,* $m_\sigma = 400 - 800$ *MeV,* $g_\omega = 1 - 8$ *and* $B^{1/4} = 37.5$ *MeV. Raising the value of* m_σ *needs smaller repulsive coupling constants for Twin Stars to develop. The masses for small* m_σ *and large* g_ω *display rather large radii and masses. As in fig. 6.29 the green shaded in the upper left region is the causality limit and the red shaded area on the right hand side is the area excluded by the millisecond pulsar PSR J1748-2446.*

The resulting mass radius relations are shown in figure 6.33. Figure 6.34 displays the gravitational mass as a function of the central pressure, where one can read of the values of the central pressure and see at which energy density the maximum mass is located. For the choice $m_\sigma = 400$ MeV and the rather high value of $g_\omega = 8$ the first maximum mass is located at $M_{max1} = 4.8 M_\odot$ and 41.94 km radius. The second stable maximum is located at $M_{max2} = 4.14 M_\odot$ and 26.19 km radius. All these star configurations are ruled out by the rotational constraint since they are located in the red shaded area.

The values for $m_\sigma = 600$ MeV have been discussed above and for $m_\sigma = 800$ MeV and $g_\omega = 1$ both maxima are located at $\sim 1.6 M_\odot$ where $r_1 = 22.39$ km and $r_2 = 12.66$ km.
As has been shown in our previous work [56], a high value of the repulsive coupling leads to a stiffer EoS resulting in very large and heavy star configurations, so that the choice for $m_\sigma = 400$ MeV and $g_\omega = 8$ is rather unphysical. Furthermore do these stars not fulfill the Keplerian frequency limit equation 6.11, as is the case for $m_\sigma = 600$ MeV, $g_\omega = 4$ and $B^{1/4} = 37.5$ MeV. Only a part of the second stable branch for the third parameter choice is within the allowed area, i.e. fulfilling all considered constraints.

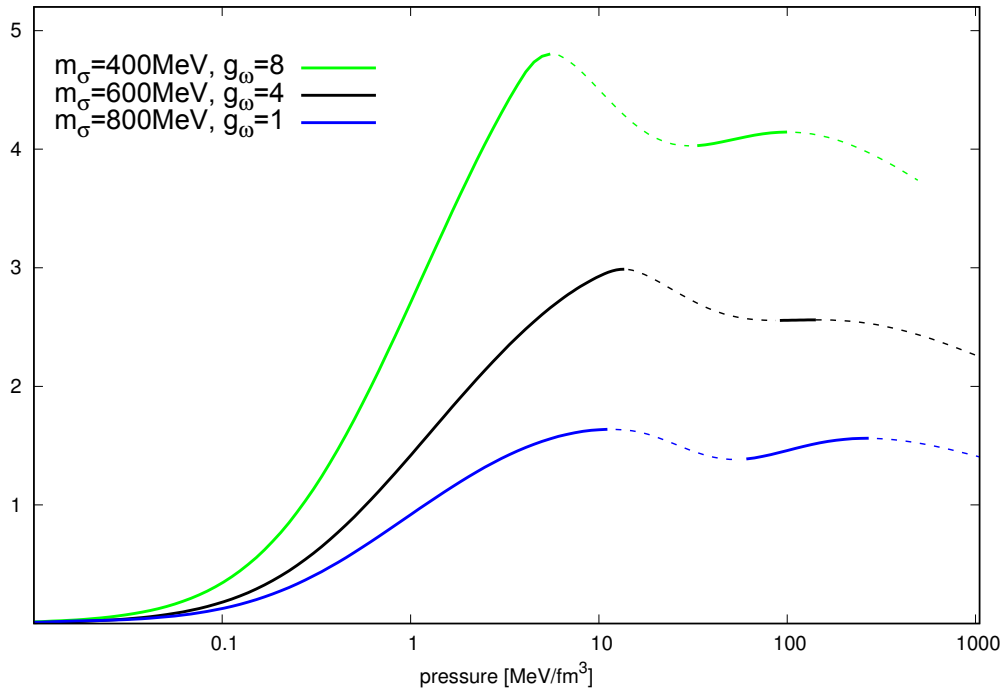

Figure 6.34: *The pressure for $m_q = 300$ MeV, $m_\sigma = 400 - 800$ MeV, $g_\omega = 1 - 8$ and $B^{1/4} = 37.5$ MeV. Raising the value of m_σ needs smaller repulsive coupling constants for Twin Stars to develop. Solid lines indicate stable solutions, whereas dashed or dotted lines represent unstable stars.*

The first maximum for $m_\sigma = 400$ MeV and $g_\omega = 8$ is found to be in the low pressure- and energy regime (see Tab. 6.4) and furthermore not fulfilling

the rotational constraint. These stars are still consisting of confined quark matter because the transition energy density is roughly 3/7 of nuclear energy density[6]. Here the second maximum should be the favoured state for a deconfined quark star.
Only for $m_\sigma = 800$ MeV the energy density at the first maximum is $1.35\epsilon_0$. Here deconfinement of (light) quarks may already have set in.

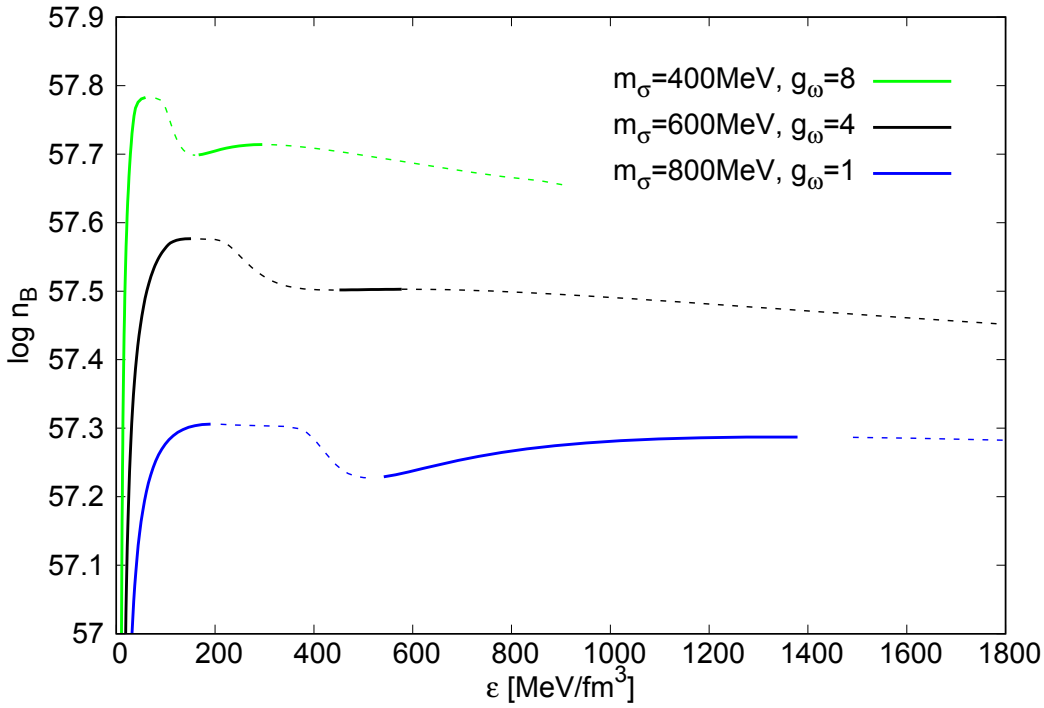

Figure 6.35: *The baryon number n_B as a function of the energy density for the parameter set $m_q = 300$ MeV, $B^{1/4} = 37.5$ MeV and $m_\sigma = 400 - 800$ MeV, $g_\omega = 1 - 8$. Solid lines represent stable configurations, whereas dotted or dashed lines correspond to unstable solutions.*

Figure 6.35 shows the logarithm of the baryon number as a function of the energy density. Only the parameter choice for $m_\sigma = 800$ MeV gives two stable stars at equal baryon number. Since the first maximum is outside the Keplerian frequency limit (i.e. in the allowed region), a star on the

[6] $\epsilon_0 \simeq 145 \frac{MeV}{fm^3}$

Parameters			EoS $[MeV/fm^3]$		First maximum	
m_σ	$B^{1/4}$	g_ω	p(ϵ)	ϵ	$M_1/M_\odot$	R_1(km)
400	37.5	8	5.51	59.09	4.80	41.94
600	37.5	4	13.6	151.2	2.99	28.46
800	37.5	1	11.10	190.82	1.63	22.39
Parameters			EoS $[MeV/fm^3]$		Second maximum	
m_σ	$B^{1/4}$	g_ω	p(ϵ)	ϵ	$M_1/M_\odot$	R_1(km)
400	37.5	8	99.85	295.42	4.14	26.19
600	37.5	4	141.9	577.6	2.56	19.18
800	37.5	1	271	1379.79	1.56	12.66

Table 6.4: *The values of the pressure and corrsponding energy density for the values of the first and second maximum in the mass radius relation for the parameter choice* $m_q = 300\ MeV$, $m_\sigma = 400 - 800\ MeV$ *and* $g_\omega = 1 - 8$ *at fixed bag constant* $B^{1/4} = 37.5\ MeV$.

second stable branch would be stable. A possible scenario might be that after a supernova explosion the proto compact object does not support the conservation of angular momentum and instead of collapsing to a black hole collapses to a star on the second maximum while conserving baryon number. It has been shown that hot compact stars have larger radii and the same mass, so that another possible explanation is that the star becomes unstable due to temperature loss and restabilizes again, remember the discussion of the EoSs at finite temperature in Section 5.8.2.

Contour areae

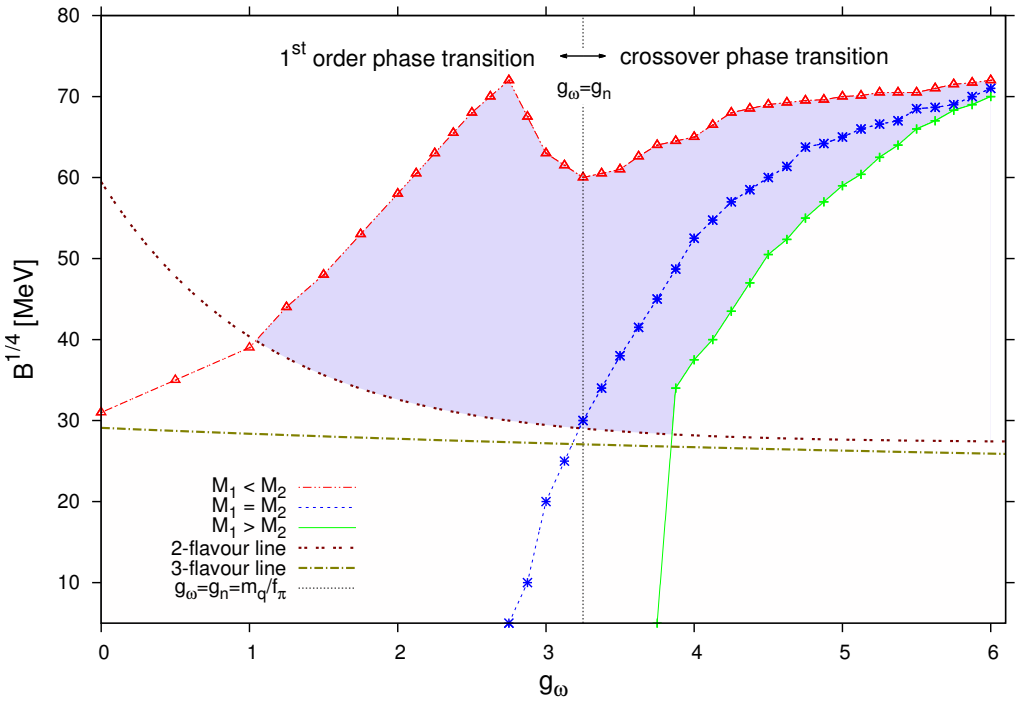

Figure 6.36: *Contour lines in the g_ω versus $B^{1/4}$ plane indicating Twin Star solutions. Two stable branches with maxima $M_1^{max} < M_2^{max}$ appear when crossing the upper line from above. The middle line indicates stars with $M_1^{max} \simeq M_2^{max}$. The lower line shows the limit where $M_1^{max} > M_2^{max}$. Above the upper line and below the lower line no Twin Stars are possible. The vertical line $g_\omega = g_n$ indicates the approximate boundary between first order- and crossover phase transitions. The two- and three flavour lines provide the stability conditions for dense matter. Twin Stars within the shaded area fullfill the stability constraints.*

Fig. 6.36 and Fig. 6.37 depict the $g_\omega - B^{1/4}$ parameter plane at $m_\sigma = 600$ MeV. By crossing the upper line from above we obtain two stable branches with two maxima being related as $M_1^{max} \lesssim M_2^{max}$. At the middle line the two stable branches have $M_1^{max} \simeq M_2^{max}$, whereas the second stable branch disappears for small values of $B^{1/4}$ and high values of g_ω below the lower line.

From Fig. 6.36 we see that, for a fixed value of $B^{1/4}$, low or high values of g_ω cause the Twin Stars disappear as there is no chiral phase transition. Moreover, the vertical line indicates the approximate boundary between first order- and crossover phase transitions, that is given by $g_\omega \sim g_n$ for $m_\sigma = 600$ MeV.

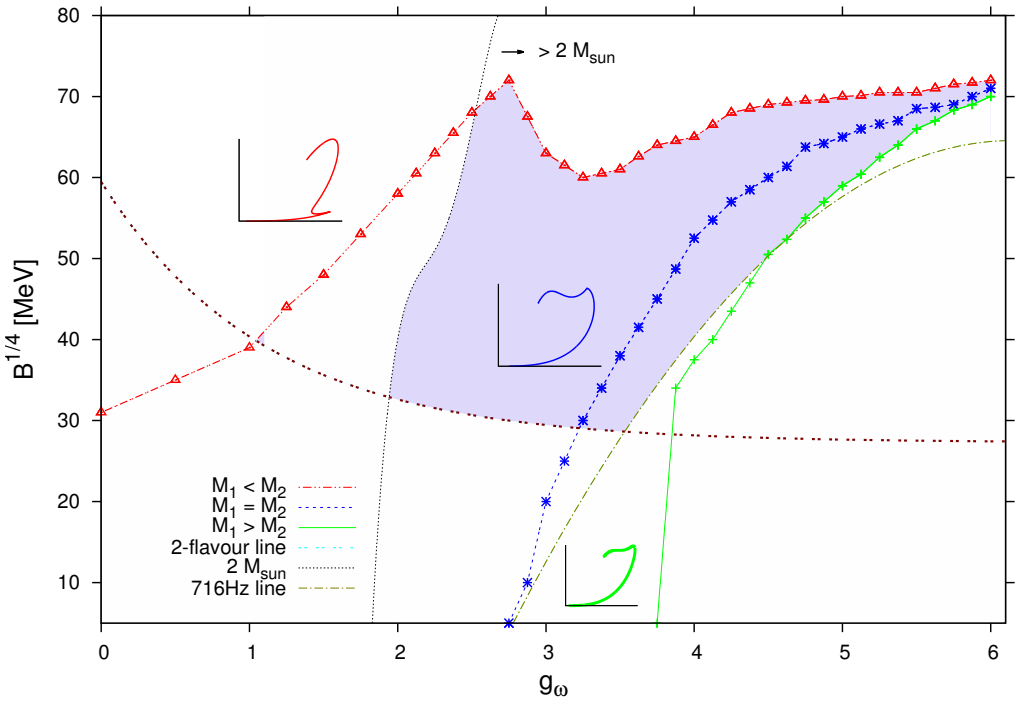

Figure 6.37: *Same contour lines in the g_ω versus $B^{1/4}$ plane indicating Twin Star solutions, as in Fig. 6.36, but including the two-flavour line, the 2 $M_\odot$ limit and also showing the region excluded by the rotation of the millisecond pulsar PSR J1748-2446ad. Twin Stars within the shaded area fullfill all these constraints.*

In Fig. 6.36 we also show the two-flavor line resulting from the stability condition of nuclear matter and the three-flavor line[7] coming from the Bodmer-Witten hypothesis of stable strange quark matter [44, 46]. On the one hand, the region above the two-flavor line indicates that two-flavor quark matter cannot be more stable than ordinary nuclear matter, meaning that the most

[7] The same lines can be seen in Fig. 6.26

stable known element in nature, ^{56}Fe, cannot decay into two-flavor quark matter. On the other hand, the area below the three-flavor line results from the Bodmer-Witten hypothesis, that assumes that strange quark matter is more stable than ordinary nuclei, remember Section 6.4 and in particular eqs. 6.8 and 6.9. Since there is no overlap between both regions, absolutely stable quark matter is not realizable.

There are further constraints to the allowed parameter range for Twin Stars coming from astrophysical observations. In Fig. 6.37 we show that, for $g_\omega \gtrsim 2$, the masses of the stars become larger than the $2M_\odot$ limit while the parameter range for Twin Star configurations lie inside the area allowed by the rotation of PSR J1748-2446ad. These Twin Stars have radii 12 Km $\lesssim R \lesssim$ 22 Km, which are larger than the recent determinations below 13 km (see the discussion in Ref. [135]).

Comparison with hybrid stars

The EoS for the values of $37.5 \leq B^{1/4} \leq 65$ MeV from figure 6.28 appear to be constructed of two EoS's via a Gibbs construction with a smooth increasing development within $100\text{MeV/fm}^3 \leq \epsilon \leq 210\text{MeV/fm}^3$ (crossover chiral phase transition), where the pressure is nearly constant $p \simeq 12\text{MeV/fm}^3$, increasing sleekly. Based on the generic results on Twin Stars by Alford et al [89, 90], also discussed in detail on our results for hybrid stars in the previous section 6.3, we are now able to investigate our obtained EoS more detailled on Twin Star solutions. Alford et al used a constant speed of sound parametrization where the transition pressure p_t, the transition energy density ϵ_t, the energy density discontinuity $\Delta\epsilon$ and the quark matter speed of sound c_s^2 act as control parameters for two EoSs, one for the nuclear crust and one for the ultradense core. Repetitive, they conclude that Twin Stars may appear for rather low p_t/ϵ_t and rather high $\Delta\epsilon/\epsilon_t$, independent of the utilized model. Recall that in this approach we are working with only one EoS, but assuming a Gibbs-constructed EoS within the chiral phase transition range for nearly constant $p \simeq 12\text{MeV/fm}^3$, we are now able to compare with the phase diagrams 6.15, 6.21 and 6.25 obtained in the previous section on hybrid stars 6.3. All our

obtained mass radius configurations showing the second stable branch have a rather low p_t and a relatively high $\Delta\epsilon$, also in accordance with our results on Twin Stars in [57] and the star configurations for $B^{1/4} = 37.5, 52, 65$ from figure 6.28 are indeed located within the Twin Star area in figure 6.25. Note however, that the quark matter speed of sound to calculate the Twin Star area in figure 6.25 has been chosen to be $c_s^2 = 1/3$ with a hadronic matter EoS for the stars outer layer and the very SU(3) Quark Meson model EoS for the stars core. As pointed out by Alford et al, an increase of the quark matter speed of sound has the effect of enlarging the size of the twin star area below the constraint line, moving the cusp in the phase diagram for hybrid stars downwards (Ref.[89] figure 4 and Ref.[57] figure 22). Comparing with figure 6.17 the quark matter speed of sound for $g_\omega = 3$ is roughly $c_s^2 = 1/2$, so that for $g_\omega = 4$ the speed of sound $c_s^2 \simeq 3/5$ so that we sure are still within the Twin Star area. We conclude that we indeed have found Twin Stars solutions, but the transition energy density of the first maximum in the mass radius relation is in the range of the chiral phase transition, indicating that the matter is to some extend still confined. The core of a quark star on the second stable branch should be made of deconfined matter up to a certain stellar radius r, i.e. the central pressure and central energy density of the star are located behind the chiral phase transition. Most stars on the second stable branch fulfill all considered constraints, so that these results may impose a collapse scenario from the first stable branch to a star on the second stable branch. Unfortunately the Bodmer Witten hypothesis, equations 6.8 and 6.9, is not fulfilled in any considered case and even if assuming different quark flavour densities, the minimum of the energy per baryon at vanishing pressure is lowest for matter in beta equilibrium.
The results considering Twin Stars have been submitted for publication in Phys.Rev.**D** [136].

7

Conclusions and Outlook

In this work, thermodynamical properties of strongly interacting matter within a chiral SU(2)- and SU(3) chiral Quark Meson model have been analysed. Both effective models describe the development of the quark masses in media via the corresponding fields through chiral symmetry, which is expected to be restored at high temperatures and/or high densities, and spontaneously broken at low temperatures and/or densities. Spontaneous and explicit chiral symmetry breaking patterns give rise to massive Goldstone bosons, which are associated with the pions. Their chiral partners, the sigma mesons, are expected to be degenerate in mass, which was what we studied and observed at large temperatures/densities.

The derivation and computation of thermodynamical quantities and properties in both cases can for instance be used to study relativistic and hydrodynamic Heavy Ion Collisions and the early universe for vanishing baryon number (SU(2)-case). They are also interesting for extreme astrophysical scenarios, such as Supernova explosions and the thermal evolution of their remnants, which has been among the topics of this thesis (SU(3)-case).

Inclusion of the zero point energy in the SU(2) model has been carried out separately for the meson sector and for the quark sector as well as in a com-

bined approach, where we learned, that the quark sector is quite dominant and that the vacuum fluctuations of the meson fields have little influence on the order parameter[1], but affect the relativistic degrees of freedom.

In the SU(3) case, the inclusion of the zero point energy in the quark sector is much more computationally complex, but, as in the SU(2) case, is also not negliable, as its influence also changes the thermodynamical quantities at finite temperatures in a nontrivial manner. Here some features of the Supernova equation of state have been studied, which look promising for further investigations for Supernovae (proto neutron stars) and also for compact star mergers.

The final chapter was dedicated to the different remnants (Compact Stars) of a Supernova explosion, which, under various assumptions and subject to several constraints, may appear. These calculations have been carried out at $T = 0$ within the SU(3) approach in mean field approximation[2].

The following detailled conclusion is therefore divided into three separate, but intimately related parts.

The importance of vacuum fluctuations

In chapter 4 we demonstrated the importance of the vacuum fluctuations within the SU(2) Quark Meson model at zero chemical potential, and furthermore included the vacuum fluctuations in the mesonic sector, where we employed the 2PI formalism (Section 4.3)[3]. For both approaches, the considerations from the mesonic sector from the quark sector (Section 4.4), were combined to an unified set of equations (Section 4.5). In the combined for-

[1] Besides being left with two renormalization scales, which, for one combined theory, is physically non warrantable [42].

[2] A future work may study compact stars in the SU(3) Quark Meson model with inclusion of the zero-point energy.

[3] In the appendix it is shown why an approach via the path integral formalism leads to difficulties, and why therefore the 2PI formalism was employed.

malism we also included the vacuum field fluctuations of quarks and mesons and varied the sigma meson mass in the range $500 \leq m_\sigma^{vac} \leq 900$ MeV. The main foci of this work were the differences in the σ field, the mass spectra and thermodynamical ratios, i.e. the relativistic degrees of freedom.

The incorporation of the vacuum fluctuations in the quark sector is independent of any renormalization scale [31, 53], and its inclusion yields similar results when changing the value of the initial vacuum sigma meson mass, namely that the chiral phase transition is shifted to higher temperatures. The impact on the masses of the sigma and the pion is similar. In all cases considered, no first-order phase transition is seen. The curves show differences around the phase transition but saturate in the Stefan Boltzmann limit at high temperatures.

In the mesonic sector the fields for different m_σ^{vac} intersect, when neglecting the vacuum term. This is not the case when including the vacuum fluctuations, which are dependent on a renormalization scale. The transition temperatures are much higher than in the quark case, e.g. in [36, 34, 38]. In most cases the degenerate masses of the sigma and the pion show a smoother rise as a function of temperature than in the quark case. Within the CJT formalism, the behaviour of the in-medium pion mass with temperature can lead to steep slopes in the p/T^4 ratio, which gives rise to peaks within the s/T^3 ratio. We conclude that the inclusion of the vacuum contribution is in both cases a small, but non-negligible correction.

Within the combined formalism we were left with the option of having two renormalization scales, one from each sector. We investigated separately the vacuum parameters λ, m^2 and H as a function of the quark renormalization scale Λ. We conclude that the main impact comes from the quark sector and that there is a tiny window around $\Lambda \sim 1$ GeV, where the results are physically reasonable. The fields and the mass spectra showed hardly any difference when varying the renormalization scale. It seems however, that the inclusion of the mesons have an influence within the temperature region $50 \leq T \leq 180$ MeV for the p/T^4 ratio, which gives rise to peaks within the s/T^3 ratio. We find that in all cases considered a chiral first order phase transition is not seen.

Ref. [137] compares the renormalized Linear sigma model with the NJL model. Like in our case a crossover transition has been found for zero chemical potential and they stress the importance of the vacuum field fluctuations to the thermodynamic properties.
In Ref. [36] the Linear sigma model including the vacuum field fluctuations, containing quark and mesonic degrees of freedom, has been utilized. The quark degrees of freedom have been integrated out and the resulting effective action was linearized around the ground state. Sigma and π mesons were described as quasiparticles and their properties were taken into account within the thermodynamic potential. Their parameter choice is similar to ours and they find a gradual decrease of the chiral condensate, which gives a crossover type transition at temperatures $150 \leq T_c \leq 200$ MeV. Also the results for the masses are very similar to our results for the masses of the sigma and the pion. Their thermodynamical ratios within the combined approach however do not show such an influence from the mesonic sector in the low temperature region. We argue that this feature comes from the utilization of the CJT formalism within our work, which is a different approach to the mesonic contribution in their approach.

A future study could implement the Polyakov loop to model the quark confinement [138, 139, 50, 32]. It would also be interesting to perform calculations for non-zero chemical potential to explore the QCD phase diagram [29] or calculations with finite isospin [50] respecting the vacuum fluctuations. The implementation of the strange quark [140, 141] and, if applicable vector mesons [142, 143], yields a model for astrophysical applications, such as for Supernovae EoSs, proto neutron stars or compact star merger, which have been studied in Chapter 5.

Strangeness, vacuum fluctuations and applications

We learned from our studies within the SU(2) approach the importance of the inclusion of the fermion vacuum term. Therefore we considered its influence when expanding to SU(3) in Chapter 5, but also compared the mean

field results. Because the main influence on the thermodynamic properties results from the quark sector, and inclusion of the meson fluctuations would make the vacuum parameter determination disproportionately difficult, we decided to neglect mesonic excitations at this point. These can however also be considered in a future work. Similar to the SU(2) case, the inclusion of the fermion vacuum term leads to a shifting of the chiral phase transition to larger chemical potentials and is also independent of any renormalization scale [31, 53].

We scanned the different parameters for the mean field approach as well as for the case when the vacuum term was included and conclude that for larger temperatures the onset of the chiral phase transition is earlier (Figure 5.3) and the EoS likewise softens at larger values of the energy density (see figure 5.6), which can be backtraced to the behaviour of the nonstrange order parameter. The strange field however is almost entirely unaffected.

Varying the electron-baryon rate hardly affects the fields (Figure 5.7), whereas the EoS is slightly stiffer for larger Y_e in the high density regime (Figure 5.9), because the strange scalar field reaches the chirally restored phase later, i.e the electron contribution to the pressure becomes important since the strange quark is slightly more suppressed.

On the other hand, low values of the sigma meson mass generate a first order phase transition in mean field approximation. The inclusion of the fermion vacuum term is influencial and means, that for every chosen value of m_σ a crossover and a smoothening in the nonstrange fields occurs (see Figure 5.11). The strange fields are hardly affected. The EoSs become stiffer (Figure 5.13) for low values of m_σ because of the influence of the (scalar) vacuum parameters. At high densities the vacuum term leads to a general stiffening of the EoS.

In the mean field approximation, the variation of the repulsive coupling g_ω leads also to a first order phase transition for low values ($g_\omega \leq 2.5$). As has been the case for different m_σ, the inclusion of the vacuum term smoothens the order parameter to a crossover phase transition, even for vanishing repulsive coupling (figure 5.14). Unlike for various values of the sigma meson mass, the EoS gets stiffer, and is more pronounced for larger values of Y_e in

the high density regime. Neglecting the vacuum term, the EoSs show significant differences in the low energy sector. Inclusion of the vacuum term extends these differences to some larger densities and the EoSs look more bulged (Figure 5.17).
The investigations on isentropes $S/A = 1$ and $S/A = 2$ lead to the conclusion, that different values of the electron baryon rate hardly change the isentropes, see Figure 5.18. The $S/A = 1$ is well below the $S/A = 2$ isentrope, which is resonable. This feature can be explained by the number of neutrinos within the proto neutron star [128]. Above $S/A = 2$ the neutrinos are still trapped inside the proto compact star whereas $S/A = 1$ indicates their escaping. At $S/A = 0$ the neutrinos have already escaped the star, which then can be considered as cold. The inclusion of the fermion vacuum term leads to a less pronounced steepening of the isentropes, with hardly any other noteable differences. We conclude that the isentropes are strongly related to the corresponding EoS, see Figure 5.9, and hence show little difference for various Y_e values.

A phase transition from hadronic matter to quark matter can eventually lead to interesting phenomenological consequences for compact stars after a core-collapse supernova [128][4]. Until now, the explosion mechanism however is working for EoSs which do not fulfill the $2M_\odot$ constraint[5]. A future work based on the results on the thermal equations of state within this Chapter and on the results of compact stars in Chapter 6 may revive the subject, because the SU(3) EoS in the mean field approximation yields solutions with $M \geq 2M_\odot$ and with two stable branches in the mass radius relation, since the explosion mechanism has recently been identified to be related with the existence of a third family of compact stars [128]. Concerning the newborn remnant of the Supernova explosion, this third family is present in the early

[4] We will study compact stars with a first order phase transition from hadronic- to quark matter in chapter 6 in section 6.3

[5] The recent measurements of the masses of the pulsars PSR J1614-2230 [76] and of PSR J0348+0432 [77] impose considerable constraints on the equation of state (EoS) for compact stars. More on the subject of constraints for compact stars can be found in chapter 6 in section 6.5.

stages of the evolution of the compact star, and absent when the star temperature is much less then the corresponding Fermi energy of the particles and fields the star is assumed to be made of[6]. The third family is a result of unusual thermal properties induced by the phase transition [66] and motivates further investigations of the SU(3) Quark Meson model at finite temperatures.

Coalescing relativistic binary systems containing compact objects are very interesting in the context of the EoS of hot and dense matter. They are likely to be important sources of detectable gravitational waves by advanced LIGO/VIRGO and KAGRA, possibly before 2020 [144, 145]. Additionally they may represent a major source of heavy r-process elements in the Universe, because they eject extremely neutron rich matter initially. Utilizing the SU(3) EoS at finite temperatures, different scenarios of compact star merger could be simulated [146, 147, 148, 145, 149, 150]. Figure 7.1 shows the temperature distributions in the x-y plane of the LS220-M132 binary, where the isocontours correspond to T =10,20,30,40 and 50 MeV. One can see that the object is not hottest in the center but in a region slightly further out (at $T = 40$ MeV), mainly because of shearing[7]. In the left panel there are two hot spots to be seen. Around these hot spots fluid elements rotate - they represent vortices. The magnetic fields generated within these vortices will become important for the future space mission NICER (Neutron star Interior Composition ExploreR) [151]. This mission aims to measure the radius of compact objects with great accuracy by using these hot spots [152].

[6] At this stage it is justified to approximate the stars temperature $T \to 0$.

[7] Hence our choice of $T = 40$ MeV as a standart parameter value in Section 5.8.2.

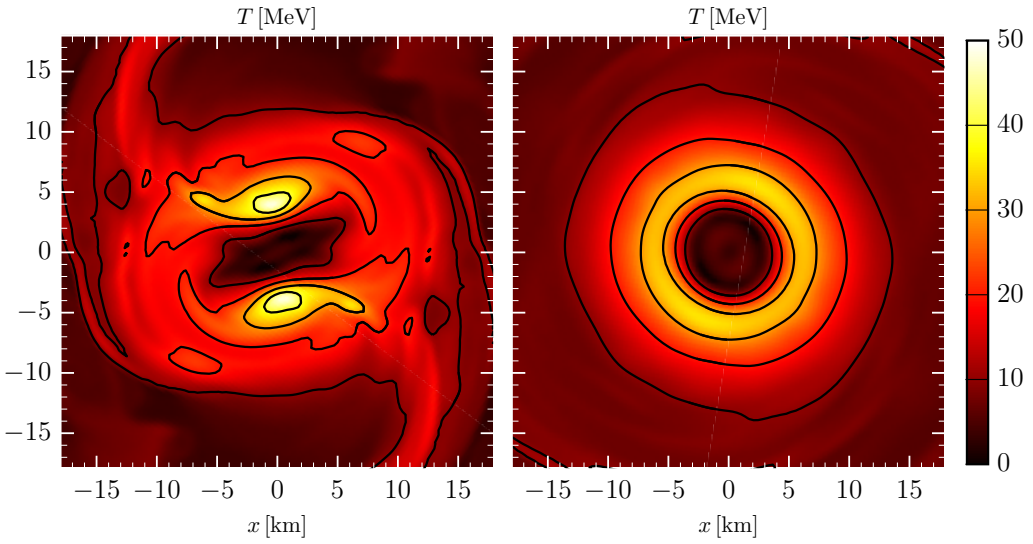

Figure 7.1: *Distributions in the x-y plane of the binary LS220-M132 at* $t = 6.71$ *ms (left) and at* $t = 23.83$ *ms (right). The isocontours correspond to* $T = 10, 20, 30, 40, 50$ *MeV. Credit: Matthias Hanauske (taken from [150]).*

The influence of the other parameters of the Quark Meson model warrants further investigation, because it would also be interesting to scan the QCD phase diagram with respect to the astrophysical constraints on compact stars [153, 154, 155]. Here the critical endpoint in the QCD phase diagram would be of tremendous importance (see also [94]).

Compact stars

In Chapter 6 various types of compact stars were discussed. Within the SU(3) approach in the mean field approximation, strange stars were already the main subject in my Master thesis. In this thesis we used the EoS to calculate Hybrid stars in order to search for Twin stars.

In the hybrid star approach we employ a density dependent hadronic matter EoS and the chiral quark matter EoS in mean fields approximation to find the phase transition from one phase to the other within compact stars. We

utilized a Maxwell construction, i.e. assume that there is a sharp transition at a given transition pressure. The transition is therefore determined consistently when the pressure in the quark phase equals the one of the hadronic phase at the same baryochemical potential. From that point on the quark matter EoS prevails with its corresponding energy density.

Within our parameter range we found stable hybrid star solutions and investigated the relation of the QM core size and the appropriate stability of the star. In the SU(3) Quark Meson model utilized for the QM EoS, four parameters can be varied, from which two of them (m_σ and m_q) have little effect on the results. We conclude that a larger repulsive coupling, g_ω, and a larger vacuum pressure, B, do not allow for a large QM core to appear but instead reach the $2M_\odot$ limit, whereas small values of both quantities generate hybrid star solutions with a corresponding, large QM core, but the configurations stay below the $2M_\odot$ constraint.

Hybrid stars with high transition pressures are hard to distinguish from pure hadronic stars because of the tiny QM core. An appearing QM core generates an additional gravitational pull on the hadronic mantle. If the core's pressure can counteract this extra pull, the star is stable. For excessively large discontinuities in energy density, the star becomes unstable since the pressure of the core is not able to counteract the extra gravitational pull [89, 90, 91].

Twin stars did not emerge as the transition pressure has to be relatively small with a large jump in energy density, which could not be satisfied within our approach. This is, among other reasons, due to the fact that the speed of sound in QM has to be relatively high, which can be accomplished by an increase of the repulsive coupling. This increase on the other hand yields transition pressures to high for twins stars to appear.

In [89] Alford et. al use hadronic EoSes based upon works from Heberler et. al [156] and Shen et. al [157]. Their QM EoS is density independent and is parametrized through p_t, ϵ_t and, assuming a constant speed of sound, c_s^2. They conclude that for stars with at least $2M_\odot$ a larger c_s^2 is advantageous, whereas for $c_s^2 = 1/3$ a larger region in the phase diagram for stars with $\geq 2M_\odot$ is excluded, which as a consequence restricts the other parameters

p_t and ϵ_t.

In a proximate work Alford et. al [90] apply the constant speed of sound parametrization to a Field-Correlator-Method calculation. The corresponding EoS is equipped with an additive density independent $\bar{q}q$-potential, corresponding to our density dependent vector coupling constant, and with a vacuum energy density term including gluon condensate contributions, analogous to the Bag constant utilized in our approach. Vacuum energy density term and Bag constant are in both cases additive, i.e. density independent. In both works the allowed region in the phase diagram for hybrid stars with more than two solar masses is shifted to high transition pressures at several times nuclear energy density ($3.5 \leq \epsilon/\epsilon_0 \leq 6.5$). The family of the Field Correlator Method EoSes (varying the two above mentioned quantities) covers only a limited region in the phase diagram due to a nearly density independent speed of sound ($c_s^2 \simeq 1/3$), whereas in our approach we achieved high transition pressures assuming a higher vector coupling constant. This feature on the other hand raises the speed of sound up to values $c_s^2 \sim 0.6$, which would leave space in the phase diagram for the other parameters p_t and ϵ_t, only we had no direct influence on them.

However, we confirm the results Alford et. al [89, 90, 91] obtained and investigate further why we were not able to find a third family (twin stars) of compact stars within a physically meaningful parameter region. The conclusion is that the chances for twins are best when the transition pressure is relatively low and the energy density discontinuity on the other hand relatively high, then an appearing QM core does not destabilize the star immediately. Likewise it gets harder to achieve the $2M_\odot$ regime. But if the discontinuity in energy density is too large, the pressure of the QM core is unable to counteract the additional downward pull and the star configurations becomes unstable.

A future work could study the interplay between the hadronic- and quark matter EoS in greater detail to work out how to achieve the appropriate proportions between pressure and discontinuity in energy density for twin stars. Furthermore kaon or pion condensation can be taken into account. The appearance of kaon condensation also depends (aside the EoS) on the

mass of the star and may significantly influence the cooling of the compact star [158, 159]. This has not been been considered within our approach.

We find that the appearance of two stable branches in the mass-radius relation and, hence, the existence of twin stars is related to the onset of the chiral phase transition in quark matter. When, instead of using two EoSs like in the approach on hybrid stars discussed above, just the SU(3) Quark Matter EoS is investigated with greater attention on the phase transition. For the analysis we vary the SU(3) parameters of the model, that is, the vacuum pressure, the vector coupling and the sigma mass. For a vacuum pressure below $B \sim 100$ MeV the EoS for quark matter exhibits a genuine transition from a chirally broken phase to a restored one and, thus, allows for the existence of twin stars.
The interplay between the vector coupling and the sigma mass is then crucial for having Twin Star solutions that fulfill causality and the stability conditions of dense matter [44, 46] as well as the astrophysical constraints coming from the rotation of the millisecond pulsar PSR J1748-2446ad [131] and the $2M_\odot$ constraint [76, 77, 160]. For $m_\sigma = 600$ MeV, twin stars fulfill the $2M_\odot$ limit for $g_\omega \gtrsim 2$ whereas values of 30 MeV $\lesssim B^{1/4} \lesssim$ 70 MeV are needed to satisfy the stability conditions of dense matter. The constraint from rotation of PSR J1748-2446ad further reduces the allowed parameter region. Smaller values of m_σ are ruled out by the rotational constraint while bigger values of m_σ imply masses below the $2M_\odot$ observations. The radii of the Twin Star configurations turn out to be above 12 Km. Recent determinations of stellar radii suggest values of 11 km [161].

Outlook

With space missions such as NICER (Neutron star Interior Composition ExploreR) [162], high-precision X-ray astronomy will be able to offer precise measurements of masses and radii, with a 1 Km resolution [152]. The discovery of two stars with the same masses but different radii could indeed

be a signal of the existence of twin stars implying the presence of a phase transition in dense matter.
A possible scenario might furthermore be, that after a supernova explosion the proto compact object does not support the conservation of angular momentum and instead of collapsing to a black hole collapses to a star on the second maximum while conserving baryon number. It has been shown that proto neutron stars have larger radii then cold neutron stars, so that another possible explanation is that the star becomes unstable due to temperature loss and restabilizes again, remember the discussion of the EoSs at finite temperature in Section 5.8.2.
Last but not least, dynamical simulations in a fully general relativistic framework including the discussed EoSs are possible. Herein, the focus could be laid on collapse scenarios of twin stars in which a star at the end of the first sequence collapses to its corresponding twin star on the second sequence. Such a collapse would be accompanied by neutrino, gamma ray and gravitational wave burst [110, 163] and in addition could explain the two-component structure in the recently observed fast radio burst FRB 121002 [164].
Another application is the implementation of our EoSs in neutron star merger simulations. In [149] it has been shown that the f_1 and f_2 frequency peaks of the emitted gravitational wave produced in the merger and post-merger phase, correlate with several EoS-dependent quantities. The impact of a twin star EoS on the spectral properties of the emitted gravitational wave and the internal structure of the produced hypermassive neutron star is an open question and the consequence involved might be observationally relevant for future gravitational wave detections.

8 Appendix

In the appendix we perform a perburbation for the scalar fields in the exponential of the Lagrangian from equation 5.33 to show explicitely that this ansatz leads to difficulties in the bosonic sector[1].
If the formalism will remind you of the fermionic case from section 5.6: This is no incident. Apart from slightly different Matsubara frequencies, you will see: The devil is found to be in the details.

The complete path integral for σ_n

Separating the Lagrangian for σ_n-contributions and sorting them by either linear, quadratic, cubic or quartic contributions, the bosonic path integral for the σ_n field will be calculated in detail in this section. Since the other mesonic fields will be calculated analogously, just the results will be given.

$$\begin{aligned} \mathcal{Z} &= \int \mathcal{D}\sigma_n e^{\left(\int_0^\beta d\tau \int_V d^3\vec{r}\mathcal{L}_{mes}\right)} \\ &= \int \mathcal{D}\sigma_n e^{\left(\int_0^\beta d\tau \int_V d^3\vec{r}\left[\sigma_n(\vec{r},t)(\mathcal{Q}_n)\sigma_n(\vec{r},t)+h_n\sigma_n(\vec{r},t)+\mathcal{O}_n^4(\sigma_n(\vec{r},t))\right]\right)} \end{aligned} \tag{8.1}$$

[1] As mentioned in section 5.5 *The whole Lagrangian*, the CJT formalism is capable of circumventing these problems.

where the index n denotes the nonstrange character.

$$\begin{aligned}\mathcal{Q}_n &= -\frac{\lambda_1}{4}\sigma_n^2\left[2{\sigma_s}^2+2{\pi_0}^2+4\pi_+\pi_-\right]-\frac{\lambda_2}{8}{\sigma_n}^2\left[2\pi_0^2+4\pi_+\pi_-\right]\\ &- \frac{m_0^2}{2}\sigma_n^2+\frac{c\sigma_s}{2\sqrt{2}}\sigma_n^2+\frac{1}{2}\partial_\mu\sigma_n\partial^\mu\sigma_n \end{aligned} \tag{8.2}$$

and the perturbative terms in 4^{th}-order are

$$\begin{aligned}\mathcal{O}_n &= -\frac{\lambda_1}{4}\left[\sigma_n^4+\sigma_s^4+2(\pi_0\sigma_s)^2+4\pi_+\pi_-(\pi_0^2+\sigma_s^2)+\pi_0^4+4\pi_+^2\pi_-^2\right]\\ &- \frac{\lambda_2}{8}\left[{\sigma_n}^4+\pi_0^4+4\pi_+\pi_-\pi_0^2+4\pi_+^2\pi_-^2+2\sigma_s^4\right]+h_s\sigma_s\\ &- \frac{m_0^2}{2}\left[\sigma_s^2+\pi_0^2+2\pi_+\pi_-\right]+\frac{c\pi_0^2\sigma_s}{2\sqrt{2}}+\frac{c\sigma_s\pi_+\pi_-}{\sqrt{2}}\end{aligned} \tag{8.3}$$

The perturbation will be expanded in Taylor series

$$exp\left(\int_0^\beta d\tau\int_V d^3\vec{r}\mathcal{O}_n^4\sigma_n(\vec{r},t)\right)\simeq 1+\int_0^\beta d\tau\int_V d^3\vec{r}\mathcal{O}_n^4\sigma_n(\vec{r},t) \tag{8.4}$$

so that

$$\mathcal{Z} \simeq \int\mathcal{D}\sigma_n e^{\left(\int_0^\beta d\tau\int_V d^3\vec{r}[\sigma_n(\mathcal{Q}_n)\sigma_n+h_n\sigma_n]\right)}\cdot\left(1+\int_0^\beta d\tau\int_V d^3\vec{r}\mathcal{O}_n^4\right) \tag{8.5}$$

$$\simeq \int\mathcal{D}\sigma_n e^{\left(\int_0^\beta d\tau\int_V d^3\vec{r}[\sigma_n(\mathcal{Q}_n)\sigma_n+h_n\sigma_n]\right)} \tag{8.6}$$

$$+ \int\mathcal{D}\sigma_n e^{\left(\int_0^\beta d\tau\int_V d^3\vec{r}[\sigma_n(\mathcal{Q}_n)\sigma_n+h_n\sigma_n]\right)}\cdot\left(\int_0^\beta d\tau\int_V d^3\vec{r}\mathcal{O}_n^4\right) \tag{8.7}$$

Equation (8.6) will be treated first. The perturbative term (8.7) will be dealt with afterwards. The fields admits a Fourier expansion similar to the fermionic case in equation 5.41.

$$\sigma_n(\vec{r},t)=\sqrt{\frac{\beta}{V}}\sum_{n,\vec{k}}e^{i(\nu_n\tau+\vec{k}\vec{r})}\sigma_n(\vec{k}) \tag{8.8}$$

Replacing the fields in the exponent and using the following abbreviation

$$\begin{aligned} -A_n &= -\frac{\lambda_1}{4}\sigma_n^2\left[2{\sigma_s}^2+2{\pi_0}^2+4\pi_+\pi_-\right]-\frac{\lambda_2}{8}{\sigma_n}^2\left[2\pi_0^2+4\pi_+\pi_-\right] \\ &- \frac{m_0^2}{2}\sigma_n^2+\frac{c\sigma_s}{2\sqrt{2}}\sigma_n^2 \end{aligned} \tag{8.9}$$

The exponent of the exponent of the path integral from equation 8.1 reads

$$\int_0^\beta d\tau\int_V d^3\vec{r}\left[\sqrt{\frac{\beta}{V}}\sum_{n,\vec{k}}e^{i(\nu_n\tau+\vec{k}\vec{r})}\sigma_n(\vec{k})(-A_n+\frac{1}{2}\partial_\mu\partial^\mu)\sqrt{\frac{\beta}{V}}\sum_{m,\tilde{k}}e^{i(\nu_m\tau+\tilde{k}\vec{r})}\sigma_m(\tilde{k})+h_n\sigma_n\right] \tag{8.10}$$

The operator $\partial_\mu\partial^\mu$ acts on the second (Fourier-)exponential function

$$\int_0^\beta d\tau\int_V d^3\vec{r}\left[\sqrt{\frac{\beta}{V}}\sum_{n,\vec{k}}e^{i(\nu_n\tau+\vec{k}\vec{r})}\sigma_n(\vec{k})(-A_n+{\nu_m}^2-\tilde{k}^2)\sqrt{\frac{\beta}{V}}\sum_{m,\tilde{k}}e^{i(\nu_m\tau+\tilde{k}\vec{r})}\sigma_m(\tilde{k})+h_n\sigma_n\right] \tag{8.11}$$

and collects two additive terms ${\nu_m}^2$ and $\tilde{k}^2$. Since there are no more operators, the sum and the exponential can be moved in their relative positions,

$$\int_0^\beta d\tau\int_V d^3\vec{r}\left[\frac{\beta}{V}\sum_{n,\vec{k}}\sum_{m,\tilde{k}}e^{i(\nu_n\tau+\nu_m\tau)}e^{i(\vec{k}\vec{r}+\tilde{k}\vec{r})}(-A_n+{\nu_m}^2-\tilde{k}^2)\sigma_n(\vec{k})\sigma_m(\tilde{k})+h_n\sigma_n\right] \tag{8.12}$$

$\nu_n\tau$, $\nu_m\tau$, $\vec{k}\vec{r}$ and $\tilde{k}\vec{r}$ are also translocated. Using the equations 5.45 one sum vanishes and we are left with ν_n and $\vec{k}$. The partition function then can be written as

$$\mathcal{Z} = \int\mathcal{D}\sigma_n e^{\left(\frac{\beta}{V}\int_0^\beta d\tau\int_V d^3\vec{r}\sum_{n,\vec{k}}\left[{\sigma_n(\vec{k})}^2(\nu_n^2-k^2-A_n)+h_n\sigma_n(\vec{r},t)\right]\right)} \tag{8.13}$$

Since being in momentum space the integration can now be performed in equation (8.13). Because of the use of equation (8.8) the expression in the brackets is diagonal already, the path integral collapses in a product of

integrals, and the algebraic sign has been changed previsitative[2].

$$\mathcal{Z} = \int \mathcal{D}\sigma_n e^{\left(\beta^2 \sum_{n,\vec{k}}\left[-(k^2+A_n+\nu_n)\sigma_n(\vec{k})^2\right]\right)} \tag{8.14}$$

$$= \int d\sigma_{n_1}(\vec{k}_1)... \int d\sigma_{n_i}(\vec{k}_i) e^{\left(\beta^2 \sum_{n}\left[-(k^2+A_n+\nu_n)\sigma_n(\vec{k})^2\right]\right)} \tag{8.15}$$

$$= \prod_{k_i} \int d\sigma_{n_i}(\vec{k}_i) e^{\left(\beta^2 \sum_{n}\left[-(k^2+A_n+\nu_n)\sigma_n(\vec{k})^2\right]\right)} \tag{8.16}$$

$$= \prod_{k_i}\prod_{\nu_n} \int d\sigma_{n_i}(\vec{k}_i,\nu_n) e^{\left(\beta^2\left[-(k^2+A_n+\nu_n)\sigma_n(\vec{k})^2\right]\right)} \tag{8.17}$$

Following [17] the formula for Riemann integrals with a constant matrix D can be obtained at this point

$$\int_{-\infty}^{+\infty} dx_1...dx_n e^{-x_i D_{ij} x_j} = \pi^{\frac{n}{2}} (detD)^{-\frac{1}{2}} \tag{8.18}$$

or else: The much easier Gauss identity for quadratic integrals

$$\int_{-\infty}^{+\infty} e^{-x^2} dx = \sqrt{\pi} \tag{8.19}$$

Equation (8.19) is easy to obtain, squaring and using polar coordinates yields

$$\int_{-\infty}^{+\infty} e^{-x^2} dx \int_{-\infty}^{+\infty} e^{-y^2} dy = 2\pi \int_{-\infty}^{+\infty} r e^{-r^2} dr \tag{8.20}$$

Substituting and deriving

$$r^2 = a \rightarrow \frac{da}{dr} = 2r = 2\sqrt{a} \tag{8.21}$$

$$= 2\pi \int_0^{r=\infty} e^{-a} \frac{\sqrt{a}}{2\sqrt{a}} da = \pi \left[-e^{-a}\right]_0^{r=\infty} = \pi \tag{8.22}$$

[2]Since $\sum_n$ runs from $-\infty \rightarrow +\infty$ its algebraic sign is of unimportance, but previsivative chosen positive

Resubstituting and taking the square gives equation (8.19). By adding a multiplicative in the exponent

$$\int_{-\infty}^{+\infty} e^{-ax^2} dx = \int_{-\infty}^{+\infty} e^{-y^2} dx \tag{8.23}$$

$$y = \sqrt{a}x \rightarrow \frac{dy}{dx} = \sqrt{a} \tag{8.24}$$

$$\rightarrow \frac{1}{\sqrt{a}} \int_{-\infty}^{+\infty} e^{-y^2} dy = \sqrt{\frac{\pi}{a}} \tag{8.25}$$

Identifying $\nu_n^2 + k^2 + A_n$ from equation (8.14) as a in equation (8.23) and logarithmise, the product becomes a sum

$$\ln \mathcal{Z} = \sum_{k_i} \sum_{\nu_n} -\frac{1}{2} \left[\ln(\beta^2(k^2 + A_n + \nu_n)) - \ln(\pi) \right] \tag{8.26}$$

Replacing $\nu_n = (2\pi n)^2$ as Matsubara frequencies and substituting $k^2 + A_n = D_n^2$

$$\ln \mathcal{Z} = \sum_{k_i} \sum_{\nu_n} -\frac{1}{2} \left[\ln(\beta^2 D_n^2 + (2\pi n)^2) - \ln(\pi) \right] \tag{8.27}$$

Now the following is obtained

$$\ln \left[(2\pi n)^2 + \beta^2 D_n^2 \right] = \int_1^{\beta^2 D_n^2} d\Theta^2 \frac{1}{\Theta^2 + (2\pi n)^2} + \ln \left[1 + (2\pi n)^2 \right] \tag{8.28}$$

First glance to the integral

$$\sum_{\nu_n} \int_1^{\beta^2 D_n^2} d\Theta^2 \frac{1}{\Theta^2 + (2\pi n)^2} \tag{8.29}$$

$$\int_1^{\beta^2 D_n^2} \frac{d\Theta^2}{4\pi^2} \left(\sum_{\nu_n} \frac{1}{\frac{\Theta^2}{(2\pi)^2} + n^2} \right) = \int_1^{\beta^2 D_n^2} \frac{d\Theta^2}{4\pi^2} \frac{2\pi^2}{\Theta} \left(1 + \frac{2}{e^{\Theta} - 1} \right) \tag{8.30}$$

where (again [17])

$$\sum_{\nu_n} \frac{1}{\frac{\Theta^2}{(2\pi)^2} + n^2} = \frac{2\pi^2}{\Theta}\left(1 + \frac{2}{e^{\Theta} - 1}\right) \tag{8.31}$$

Using $\frac{d\Theta^2}{d\Theta} = 2\Theta$, cancelling in the fraction and changing the integration limits

$$\int_1^{\beta^2 D_n^2} \frac{d\Theta^2}{4\pi^2}\frac{2\pi^2}{\Theta}\left(1 + \frac{2}{e^{\Theta} - 1}\right) = \int_1^{\beta D_n} d\Theta \left(1 + \frac{2}{e^{\Theta} - 1}\right) \tag{8.32}$$

$$= \beta D_n - 1 + 2\int_1^{\beta D_n} \frac{d\Theta}{e^{\Theta} - 1} \tag{8.33}$$

Substituting $e^{\Theta} = z$ and deriving $\frac{dz}{d\Theta} = e^{\Theta} = z$ the following integral $\int \frac{dz}{z(z-1)}$ can be solved by expansion into partial fractions

$$\frac{1}{z(z-1)} = \frac{a}{z} + \frac{b}{z-1} = \frac{a(z-1) + bz}{z(z-1)} \tag{8.34}$$

$$\rightarrow \quad az - a + bz = 1 \rightarrow z(a+b) - a = 1 \tag{8.35}$$

$$\rightarrow \quad a + b = 0 \rightarrow -a = 1 \tag{8.36}$$

$$\rightarrow \quad a = -1 \qquad\qquad b = 1 \tag{8.37}$$

The Integral then can easily be solved

$$\int \frac{dz}{z(z-1)} = \int dz \left(-\frac{1}{z} + \frac{1}{z-1}\right) = -\ln(z) + \ln(z-1) \tag{8.38}$$

$$= \ln\frac{z-1}{z} = \ln\left(\frac{e^{\Theta} - 1}{e^{\Theta}}\right) = \ln(1 - e^{-\Theta}) \tag{8.39}$$

Having solved the integral, then equation (8.28) can be rewritten

$$\ln\left[(2\pi n)^2 + \beta^2 D_n^2\right] = \beta D_n - 1 + 2\left[\ln(1 - e^{-\beta D_n}) - \ln(1 - e^{-1})\right] + \ln\left[1 + (2\pi n)^2\right]$$

and the logarithm of the partition function in equation (8.27) becomes

$$\ln \mathcal{Z} = \sum_{k_i} \sum_{\nu_n} -\frac{1}{2} \left[\ln(\beta^2 D_n^2 + (2\pi n)^2) - \ln(\pi) \right] \tag{8.40}$$

$$\ln \mathcal{Z} = \sum_{k_i} -\frac{1}{2} \beta D_n - \ln\left(1 - e^{-\beta D_n}\right) + \mathcal{C} \tag{8.41}$$

where

$$\mathcal{C} = \frac{1}{2} + \ln(1 - e^{-1}) + \ln[1 + (2\pi n)^2] + \frac{\ln(\pi)}{2} \tag{8.42}$$

The sum becomes an integral $\sum_{k_i} \to \int \frac{d^3\vec{k} \cdot V}{(2\pi)^3}$ and finally we obtain

$$\ln \mathcal{Z} = V \int \frac{d^3\vec{k}}{(2\pi)^3} \left[-\frac{1}{2} \beta D_n - \ln\left(1 - e^{-\beta D_n}\right) \right] \tag{8.43}$$

Equation 8.43 also contains a contribution from from the zero-point energy, which needs to be regularized[3]
Since the calculation of the other path integrals is analoguous to the calculation for the σ_n-field, just the abbreviations and the results will be given.

The results for the σ_s field

The partition function for the σ_s field reads

$$\mathcal{Z} = \int \mathcal{D}\sigma_s e^{\left(\int_0^\beta d\tau \int_V d^3\vec{r} \left[\sigma_s(\vec{r},t)(\mathcal{Q}_s)\sigma_s(\vec{r},t) + \mathcal{O}_s^4(\sigma_s(\vec{r},t))\right]\right)} \tag{8.44}$$

where the index s denotes the strange character and

$$\mathcal{Q}_s = -\frac{\lambda_1}{4}\sigma_s^2 \left[2{\sigma_n}^2 + 2{\pi_0}^2 + 4\pi_+\pi_- \right] - \frac{m_0^2}{2}\sigma_s^2 + \frac{1}{2}\partial_\mu \sigma_s \partial^\mu \sigma_s \tag{8.45}$$

[3] The formalism derived and applied in section 4.3.1 after solving via the CJT formalism.

and the perturbative terms in 4^{th}-order are

$$\begin{aligned}\mathcal{O}_s &= -\frac{\lambda_1}{4}\left[\sigma_n^4+\sigma_s^4+2(\pi_0\sigma_n)^2+4\pi_+\pi_-(\pi_0^2+\sigma_n^2)+\pi_0^4+4\pi_+^2\pi_-^2\right]\\ &- \frac{\lambda_2}{8}\left[({\sigma_n}^2+\pi_0^2)^2+4\pi_+\pi_-(\sigma_n^2+\pi_0^2)+4\pi_+^2\pi_-^2+2\sigma_s^4\right]+h_n\sigma_n\\ &- \frac{m_0^2}{2}\left[\sigma_s^2+\pi_0^2+2\pi_+\pi_-\right] \qquad (8.46)\end{aligned}$$

Following equation (8.8) the abbreviation for the σ_s field in the exponent reads

$$-A_s = -\frac{\lambda_1}{4}\sigma_s^2\left[2{\sigma_n}^2+2{\pi_0}^2+4\pi_+\pi_-\right]-\frac{m_0^2}{2}\sigma_s^2 \qquad (8.47)$$

after performing the derivation and having done the other steps from equation (8.11) to equation (8.26) the anew abbreviation reads $k^2+A_s=D_s^2$. Calculating further from equation (8.27) to equation (8.41), the logarithm of the partition function reads

$$\ln\mathcal{Z}=V\int\frac{d^3\vec{k}}{(2\pi)^3}\left[-\frac{1}{2}\beta D_s-\ln\left(1-e^{-\beta D_s}\right)\right] \qquad (8.48)$$

The result for the π_0 field

$$\mathcal{Z} = \int\mathcal{D}\pi_0 e^{\left(\int_0^\beta d\tau\int_V d^3\vec{r}\left[\pi_0(\vec{r},t)(\mathcal{Q}_{\pi_0})\pi_0(\vec{r},t)+\mathcal{O}^4_{\pi_0}(\pi_0(\vec{r},t))\right]\right)} \qquad (8.49)$$

where

$$\begin{aligned}\mathcal{Q}_{\pi_0} &= -\frac{\lambda_1}{4}\pi_0^2\left[2(\sigma_s^2+\sigma_n^2)+4\pi_+\pi_-\right]-\frac{\lambda_2}{8}\pi_0^2\left[2\sigma_n^2+4\pi_+^2\pi_-^2\right]\\ &- \frac{m_0^2}{2}\pi_0^2+\frac{c\sigma_s\pi_0^2}{2\sqrt{2}}+\frac{1}{2}\partial_\mu\pi_0\partial^\mu\pi_0 \qquad (8.50)\end{aligned}$$

and the perturbative terms in 4^{th}-order are

$$\begin{aligned}\mathcal{O}_{\pi_0} &= -\frac{\lambda_1}{4}\left[(\sigma_n^2+\sigma_s^2)^2+4\pi_+\pi_-(\sigma_n^2+\sigma_s^2)^2+\pi_0^4+4\pi_+^2\pi_-^2\right] \\ &- \frac{\lambda_2}{8}\left[{\sigma_n}^4+\pi_0^4+4\pi_+\pi_-\sigma_n^2+4\pi_+^2\pi_-^2+2\sigma_s^4\right] \\ &- \frac{m_0^2}{2}\left[\sigma_n^2+2\pi_+\pi_-+\sigma_s^2\right]+\frac{c\sigma_n^2\sigma_s}{2\sqrt{2}}+\frac{c\sigma_s\pi_+\pi_-}{\sqrt{2}} \end{aligned} \tag{8.51}$$

Following equation (8.8) the abbreviation for the π_0 field in the exponent reads

$$\begin{aligned}-A_{\pi_0} &= -\frac{\lambda_1}{4}\pi_0^2\left[2(\sigma_s^2+\sigma_n^2)+4\pi_+\pi_-\right]-\frac{\lambda_2}{8}\pi_0^2\left[2\sigma_n^2+4\pi_+^2\pi_-^2\right] \\ &- \frac{m_0^2}{2}\pi_0^2+\frac{c\sigma_s\pi_0^2}{2\sqrt{2}} \end{aligned} \tag{8.52}$$

after performing the derivation and having done the other steps from equation (8.11) to equation (8.26) the anew abbreviation reads $k^2+A_{\pi_0}=D_{\pi_0}^2$. Calculating further from equation (8.27) to equation (8.41), the logarithm of the partition function reads

$$\ln\mathcal{Z}=V\int\frac{d^3\vec{k}}{(2\pi)^3}\left[-\frac{1}{2}\beta D_{\pi_0}-\ln\left(1-e^{-\beta D_{\pi_0}}\right)\right] \tag{8.53}$$

The results for the π_+ and π_- fields

Since there are no quadratic terms either for π_+ field nor for the π_- field, they will be treated as an unity, or else composed as tetraquark state, this means $\pi_+\pi_-=\tilde{\pi}^2$. Having solved the calculation for the tetraquark state similar as for the σ_s and the π_0, equation 8.6 is so far ready and would lead immediately to the grandcanonical potential, when applying equation 5.35.

Technical difficulties

The problem however is the perturbation with the terms in fourth order, equation 8.7, which one cannot just drop, because they represent three- or

four legged interaction diagrams and are an important ingredients to the potential. Neglecting terms here means that the spontaneous- and explicit symmetry breaking would not be respected anymore, the potential would not feature properties like shown in figure 3.6 or like in figure 3.7.
Because there is no way in solving equation 8.7, the expansion in Taylor series leads to *technical difficulties*[4], making this approach perturbative unsolvable, This is the reason for the use of the CJT formalism as has been carried out in section 4.3.

[4] As most authors claim without showing explicitely why these difficulties appear.

9 Danksagung

Für meine Tochter Emilia Lara und mein (noch) ungeborenes zweites Kind.

Andreas Zacchi

10 Zusammenfassung

In dieser Arbeit wurden thermodynamische Eigenschaften eines *chiralen Quark Meson Modelles* mit Bag-Konstante untersucht. Das chirale Quark Meson Model beschreibt die starke Wechselwirkung über den Austausch von Mesonen, welche an die Quarkfelder koppeln, und zudem die thermische- und dichteabhängige Entwicklung der Quarkmassen im Medium über die chirale Symmetrie. Die chirale Symmetrie ist essentiell bei der Beschreibung quantenfeldtheortischer Modelle, welche die starke Wechselwirkung untersuchen. Diese Symmetrie ist im Vakuum gebrochen, was zu nicht-verschwindenden Vakuumerwartungswerten für die entsprechenden Felder führt, und welche bei hohen Dichten und/oder Temperaturen restauriert ist [38].
Zunächst wurde nur mit leichten Quarks (up und down), mathematisch: Der SU(2) Gruppe, gearbeitet. Im Anschluss wurde noch das strange quark, mathematisch: Die SU(3) Gruppe, mit einbezogen[1].

Im SU(2) Model wurde zunächst in *mean field approximation* gearbeitet, die Mesonen wurden als stationärer Hintergrund herausintegriert und nur die Quarkfelder quantisiert. Im Anschluss wurden der divergente Vakuumterm mit einbezogen. Dazu musste das Modell regularisiert und an-

[1] SU(n) bezieht sich auf die mathematische Formulierung in der Gruppentheorie, wobei S=Speziell und U=Unitär bedeutet.

schliessend renormiert werden, um sich der auftretenden Unendlichkeiten zu entledigen. Nach eingehender Untersuchung der Ergebnisse, unter anderem durch Vergleich mit Arbeiten wie [31, 53, 36], wurden dann die rein thermischen Mesonenfluktuationen studiert, anschliessend ebenfalls regularisiert und renormiert [34, 38, 29]. In beiden Ansätzen verschiebt die Nullpunktsenergie den chiralen Phasenübergang zu höheren Temperaturen, wodurch die Massen bei höheren Temperaturen entarten. Beide Ansätze wurden dann zu einem gemeinsamen Modell kombiniert, um den Einfluss der Mesonenfluktuationen auf Ordnungsparameter, Mesonenmassen und thermodynamische Grössen zu untersuchen. Das kombinierte Modell wurde ebenfalls regularisiert und renormiert, da sich durch die Hinzunahme der Mesonen die Vakuumparameter des reinen Quark Modelles nicht-trivial ändern, zudem wurde das Regularisieren und Renormieren mathematisch nachvollzogen und auf das kombinierte Modell angepasst. Nachdem mit dem kombinierten SU(2) Modell die thermodynamischen Eigenschaften, sprich: Der Verlauf des Ordnungsparameters, die Massenentartung der Pionen und Sigma Mesonen, im besonderen jedoch die relativistischen Freiheitsgrade untersucht, und mit den einzelnen Modellen verglichen, wurden, kann behauptet werden, dass sich der Einfluss der Mesonenfluktuationen in grösserem Maß auf die Thermodynamik, als auf den Ordnungsparameter und die Massen auswirkt. Die Vakuumfluktuationen der Mesonen im kombinierten Modell kann man jedoch vernachlässigen, da deren Einfluss verschwindend gering ist und man zudem mit zwei Renormierungsskalen arbeiten muss, was für eine kombinierte Theorie physikalisch unreell ist [34, 38, 42]. Diese Ergebnisse wurden zusammengefasst und können in naher Zukunft veröffentlicht werden.

Für das chirale SU(3) Quark Meson Model wurde der Formalismus der Pfadintegralmethode zu dessen Lösung herangezogen, auch hier wurde regularisiert und renormiert um den Einfluss der Nullpunktsenergie auf die Thermodynamik zu untersuchen [38, 48]. Im SU(3) Modell wurden zudem Vektormesonen mitberücksichtigt, welche die Repulsion zwischen den einzelnen Freiheitsgraden modelliert. Für das eigentliche Ziel der Arbeit, eine Supernova Zustandsgleichung aufzustellen, wurde zudem neben der Ladungsneu-

tralität noch die Elektron-Baryon Rate fixiert [51]. Verglichen mit der mean field Analysis kann man man hier auf gewonnene Erkenntnisse aus dem SU(2) Modell zurückgreifen, denn auch hier verschiebt sich durch den Einfluss der Nullpunktenergie der chirale Phasenübergang (Ordnungsparameter) zu höheren Dichten. Die Zustandsgleichung wird durch den Vakuum Term etwas softer und zeigt ein ähnliches, wenn auch leicht abweichendes, Verhalten im niederen Energiebereich. Untersucht wurde neben der Temperatur T, die Elektron Baryon Rate Y_e, die Sigma Mesonen Masse m_σ noch der Einfluß der Vektorkopplung g_ω. Besonders interessant hervorzuheben ist das Zusammenspiel von m_σ, welches bei niedrigeren Werten den Phasenübergang zu kleineren Dichten verschiebt und die Zustandsgleichung steifer werden lässt, und der repulsiven Kopplung g_ω, welche bei niedrigen Werten den Phasenübergang zu kleineren Dichten verschiebt, die Zustandsgleichung jedoch weicher werden lässt.
Aus der Zustandsgleichung konnten dann Isentropen im $T - \mu$ Phasendiagramm errechnet werden, welche in naher Zukunft Aufschluss über eine dritte Familie von kompakten Sternen[2] in Zusammenhang mit der entsprechenden Supernova Explosion geben könnte [128, 58].

Im letzten Kapitel wurde das chirale SU(3) Quark Meson Modell in mean field approximation mit Bag-Konstante und bei verschwindender Temperatur benutzt, um die Existenz von Hybridsternen, Zwillingssternen, bzw. rein aus Quarkmaterie[3] bestehender *kompakter Sterne* zu analysieren. Ausschlaggebend dafür waren die Entdeckungen des Pulsars PSR J1614-2230 [76, 160] und PSR J0348+0432 [77] mit fast $2M_\odot$. Obgleich aus Arbeiten wie etwa [74, 120, 8, 165] bekannt ist, dass ein weiterer Freiheitsgrad (die strangeness) die Zustandsgleichung weicher werden lässt, und somit die Maximalmasse, vergleichen mit zwei flavor Quarkmaterie eher senkt, so ergaben sich doch in einem relativ grossen Parameterbereich auch einige physikalisch sinnvolle Lösungen für die Existenz solch exotischer Objekte, welche die $2M_\odot$

[2] Dritte Familie von Sternen nennt man auch Zwillingssterne. Diese haben die gleiche Masse, jedoch unterschiedliche Radien.

[3] Dies war der Hauptaugenmerk in meiner Master Arbeit [5, 56].

Bedingung erfüllen.
Über die aus dem Formalismus gewonnenen Grössen Druck und Energiedichte stellten wir die Zustandsgleichung auf. Diese diente als Input für die Tolmann-Oppenheimer-Volkoff-Gleichungen, die die Masse-Radius Beziehungen kompakter Objekte über eben jene Zustandsgleichung bestimmen. Die erhaltenen Ergebnisse wurden zum Zwecke der Validität mit diversen Arbeiten verglichen [166, 122, 167], bevor eine Auswertung der erhobenen Daten stattfinden konnte.
Bereits in meiner Master Arbeit [5, 56] wurde der Einfluss der verschiedenen Parameter[4] studiert. Auf der Suche nach Twin Star Lösungen aus dem chiralen SU(3) Quark Meson Model wurde zunächst ein Modell für Hybridsterne entwickelt. In diesem diente die DD2-EoS [71] als Zustandsgleichung die Kruste des Sternes, wohingegen im inneren (bei höheren Dichten) die Quark EoS Anwendung fand. Der Phasenübergang von hadronischer zu Quarkmaterie wurde über eine Maxwell Konstruktion generiert [97]. Im untersuchten Parameterbereich fanden wir viele Hybrid Stern Lösungen, bei welchen der Einfluss des Quarkmaterie Kernes auf die Stabilität des Sternes untersucht wurde. Für relativ hohe Repulsion g_ω und hohen Vakuumdruck[5], welcher über die Bag Konstante modelliert wurde, wurde die $2M_\odot$ Grenze erreicht, allerdings ist der Quarkmaterie Kern sehr klein. Fixiert man beide Werte eher klein, erreicht man die $2M_\odot$ Grenze nicht, hat jedoch einen Quarkmateriekern, welcher bis zur Hälfte des Radius des Sternes reichen kann. Das Einsetzen des Phasenüberganges übt einen zusätzlichen gravitativen Zug auf die hadronische Kruste aus. Der Stern ist stabil, wenn der Druck der Quarkmaterie diesem zusätzlichen Zug standzuhalten vermag. Für einen zu grossen Sprung in der Energiedichte werden die Lösungen allerdings instabil, siehe dazu auch [89, 90, 91]. Zwillingssterne waren nicht unter den Lösungen, da der Übergangsdruck relativ klein sein muss, während der Energiedichtesprung eher gross sein sollte. In diesem Zusammenhang wurde der Ein-

[4] Wie auch bei der um die Temperatur erweiterten Version des Modelles wurde die repulsive Vektorkopplung g_ω, die experimentell nicht sicher bestimmte Sigma Mesonen Masse m_σ untersucht. Für die Berechnung von Masse Radius Relationen von kompakten Sternen hat sich jedoch auch die Bag Konstante als wichtiger Parameter etabliert.

[5] Nicht zu verwechseln mit dem Vakuumterm der Nullpunktsenergie.

fluss der Schallgeschwindigkeit im Medium untersucht, der für Zwillingssterne ebenfalls groß sein sollte, was aber nur mit einer hohen Repulsivität erreicht werden konnte. Dann allerdings wurden die Lösungen instabil. Diese Arbeit wurde zusammen mit Dr.Dr. Matthias Hanauske ausgeführt und die Ergebnisse veröffentlicht [57].

Das Auftreten zweier stabiler Äste in der Masse Radius Relation kann allerdings mit dem SU(3) Modell und entsprechendem chiralen Phasenübergang modelliert werden. Für einen gewissen Parameterbereich einhergehend mit kleinem Wert des Vakuum Druckes B $\leq$ 100 MeV konnten *Nicht-Linearitäten* in der Zustangsgleichung zur Lösung der TOV Gleichung beitragen. Diese Nicht-Linearitäten definieren sich über den chiralen Phasenübergang. Im Weitern ist das Zusammenspiel der Vektorkopplung und der Sigma Mesonen Masse einflussreich auf die Lösungen, welche auf Kausalität, Stabilität [44, 46] und neben der $2M_{\odot}$ Bedingung [76, 77, 160] noch auf Restriktionen vom millisecond pulsar PSR J1748-2446ad [131] untersucht wurden. Für den Standardwert $m_{\sigma} = 600$ MeV und für $g_{\omega} \gtrsim 2$ wird das $2M_{\odot}$ limit zwar erfüllt, jedoch sind Werte für den Vakuumdruck von 30 MeV $\lesssim B^{1/4} \lesssim$ 70 MeV nötig, um die Stabilitätsbedingungen zu erfüllen. Der zulässige Parameterbereich wird weiter restriktiert durch die Bedingung des Pulsars PSR J1748-2446ad. Die Radien der Zwillingssterne fallen mit mindestens 12 km verhältnismäßig groß aus, denn neuere Studien zeigen, dass die Radien bei 11 km liegen sollten [161]. Diese Arbeit wurde zusammen mit Dr. Laura Tolos gemacht und ist zum gegenwärtigen Zeitpunkt zur Veröffentlichung bei Phys.Rev.**D** eingereicht [136].

Mit Weltraummissionen wie etwa NICER (Neutron star Interior Composition ExploreR) [162] sollte die Radiusbestimmung kompakter Objekte in Zukunft bis auf einen Kilometer genau bestimmt werden können. Die Entdeckung von zwei Sternen mit der gleichen Masse und unterschiedlichen Radien wäre in der Tat ein Beweis für die Existenz von Zwillingssternen, welche dann die Theorie des Phasenüberganges in dichter Materie untermauern würde. Da das Modell Zwillingssterne zu generieren vermag, und

der Formalismus bereits auf endliche Temeraturen erweitert wurde, kann in diesem Zusammenhang eine dritte Familie von kompakten Sternen auch mit einer entsprechenden Supernova Explosion in Verbindung gebracht werden [128, 58]. Das Kollaps-Szenario eines Zwillingssternes würde weiteren Aufschluss über Neutrino-Emmissivität, Gamma-ray burster und Gravitationswellen Signale geben können [110, 154, 163]. Dynamische Simulationen in allgemein relativistischem Kontext mit den hier diskutierten Zustandsgleichungen sind bereits in Planung[6]. Eine weitere Anwendung wäre das Einbetten der Zustandsgleichung in compact star merger Simulationen [149], um Eigenschaften wie beispielsweise das Temperatur- und Dichteprofil von compact star mergern genauer zu analysieren [146, 147, 148, 145, 149, 150].

[6] Eine Zusammenarbeit mit der Arbeitsgruppe um Prof. Dr. Luciano Rezzolla, Dr. Matthias Hanauske sowie Dr. Laura Tolos und Dr. Matthias Hempel.

Bibliography

[1] G. Baym and S. A. Chin, Phys. Lett. **B62**, 241 (1976).

[2] K. Schertler, C. Greiner, and M. Thoma, (1998), arXiv:astro-ph/9801200 [astro-ph] .

[3] B.-J. Schaefer and J. Wambach, Nucl. Phys. **A757**, 479 (2005), arXiv:nucl-th/0403039 .

[4] D. Parganlija, F. Giacosa, and D. H. Rischke, Phys.Rev. **D82**, 054024 (2010), arXiv:1003.4934 [hep-ph] .

[5] A. Zacchi, *Compact stars in a SU(3) Quark Meson model, Master thesis* (Frankfurt, 2013).

[6] R. Adler, M. Bazin, and M. Schiffer, *Introduction to General Relativity* (McGraw-Hill, New York, 1965).

[7] C. W. Misner, K. S. Thorne, and J. A. Wheeler, *Gravitation* (W. H. Freeman and Company, New York, 1973).

[8] N. K. Glendenning, *Compact Stars: Nuclear Physics, Particle Physics and General Relativity* (Springer, Berkeley, 1997).

[9] T. Fliessbach, *Allgemeine Relativitätstheorie* (Spektrum, Siegen, 2003).

[10] J. Hartle, *Gravity: An introduction to Einstein's General Relativity* (Pearson, California, 2002).

[11] R. Stannard, *Relativity: A very short introduction* (Oxford university press, London, 2008).

[12] A. Ziegler, *Vorlesung: Allgemeine Relativitätstheorie, Universität Osnabrück, SS 2012* (Osnabrück, 2012).

[13] M. Blau, *Lecture notes on general relativity, http://www.blau.itp.unibe.ch/Lecturenotes.html* (Bern, 2014).

[14] C. Greiner, *Vorlesung: Allgemeine Relativitätstheorie, Goethe Universität Frankfurt, WS 2014/15* (Frankfurt, 2014).

[15] R. C. Tolman, Phys. Rev. **55**, 364 (1939).

[16] D. Griffiths, *Introduction to elementary particles* (Wiley-VCH, Portland, Oregon, 2008).

[17] J. Kapusta, *Finite-temperature Field Theory* (Cambridge University Press, Cambridge, England, 1989).

[18] L. H. Ryder, *Quantum Field Theory* (Canterbury, 1985).

[19] N. K. Glendenning and F. Weber, Astrophys. J. **400**, 647 (1992).

[20] V. Koch, Phys. Lett. B **351**, 29 (1995).

[21] S. D. Peskin, Michael, *An introduction to Quantum Field Theory* (Boulder, 1995).

[22] D. McMahon, *Quantum field theory - demystified* (Sandia NatLab, 2008).

[23] D. Rischke, *Vorlesung: Quantenmechanik II, Goethe Universität Frankfurt, SS 2012* (Frankfurt, 2014).

[24] A. Pich, in *2004 European School of High-Energy Physics, Sant Feliu de Guixols, Spain, 30 May - 12 June 2004* (2005) pp. 1–48, arXiv:hep-ph/0502010 [hep-ph] .

[25] K. e. a. Nakamura, *(Particle Data Group), J. Phys. G 37, 075021 (2010)* (PDG, 2011).

[26] M. Gell-Mann and M. Levy, Nuovo Cimento **16**, 705 (1960).

[27] J. B. Kogut, M. Stone, H. W. Wyld, S. Shenker, J. Shigemitsu, and D. K. Sinclair, Nucl. Phys. B **225**, 326 (1983).

[28] D. Parganlija, P. Kovacs, G. Wolf, F. Giacosa, and D. Rischke, AIP Conf.Proc. **1520**, 226 (2013), arXiv:1208.5611 [hep-ph] .

[29] T. K. Herbst, M. Mitter, J. M. Pawlowski, B.-J. Schaefer, and R. Stiele, Phys.Lett. **B731**, 248 (2014), arXiv:1308.3621 [hep-ph] .

[30] A. Schmitt, Lect. Notes Phys. **811**, 1 (2010), arXiv:1001.3294 [astro-ph.SR] .

[31] S. Chatterjee and K. A. Mohan, Phys. Rev. **D85**, 074018 (2012), arXiv:1108.2941 [hep-ph] .

[32] R. Stiele and J. Schaffner-Bielich, (2016), arXiv:1601.05731 [hep-ph] .

[33] J. M. Cornwall, R. Jackiw, and E. Tomboulis, Phys. Rev. **D10**, 2428 (1974).

[34] J. T. Lenaghan and D. H. Rischke, J. Phys. **G26**, 431 (2000), arXiv:nucl-th/9901049 [nucl-th] .

[35] G. Mandanici, Int. J. Mod. Phys. **A19**, 3541 (2004), arXiv:hep-th/0304090 [hep-th] .

[36] A. Mocsy, I. N. Mishustin, and P. J. Ellis, Phys. Rev. **C70**, 015204 (2004), arXiv:nucl-th/0402070 [nucl-th] .

[37] V. Koch, Int. J. Mod. Phys. **E6**, 203 (1997), nucl-th/9706075 .

[38] J. T. Lenaghan, D. H. Rischke, and J. Schaffner-Bielich, Phys.Rev. **D62**, 085008 (2000), arXiv:nucl-th/0004006 [nucl-th] .

[39] E. Seel, S. Struber, F. Giacosa, and D. H. Rischke, Phys. Rev. **D86**, 125010 (2012), arXiv:1108.1918 [hep-ph] .

[40] A. Pilaftsis and D. Teresi, Nucl. Phys. **B874**, 594 (2013), arXiv:1305.3221 [hep-ph] .

[41] N. Dupuis, Phys. Rev. **B89**, 035113 (2014), arXiv:1310.4979 [cond-mat.str-el] .

[42] D. Rischke, *Vorlesung: Quantum Field Theory, Goethe Universität Frankfurt, SS 2014* (Frankfurt, 2014).

[43] M. Grahl, E. Seel, F. Giacosa, and D. H. Rischke, Phys. Rev. **D87**, 096014 (2013), arXiv:1110.2698 [nucl-th] .

[44] A. R. Bodmer, Phys. Rev. D **4**, 1601 (1971).

[45] E. Farhi and R. L. Jaffe, Phys. Rev. D **30**, 2379 (1984).

[46] E. Witten, Phys. Rev. D **30**, 272 (1984).

[47] A. Chodos, R. L. Jaffe, K. Johnson, C. B. Thorn, and V. F. Weisskopf, Phys. Rev. D **9**, 3471 (1974).

[48] B.-J. Schaefer and M. Wagner, Phys. Rev. **D79**, 014018 (2009), arXiv:0808.1491 [hep-ph] .

[49] D. Parganlija, P. Kovacs, G. Wolf, F. Giacosa, and D. H. Rischke, Phys. Rev. **D87**, 014011 (2013), arXiv:1208.0585 [hep-ph] .

[50] R. Stiele, E. S. Fraga, and J. Schaffner-Bielich, Phys.Lett. **B729**, 72 (2014), arXiv:1307.2851 [hep-ph] .

[51] T. Beisitzer, R. Stiele, and J. Schaffner-Bielich, Phys.Rev. **D90**, 085001 (2014), arXiv:1403.8011 [nucl-th] .

[52] K. Olive *et al.* (Particle Data Group), Chin.Phys. **C38**, 090001 (2014).

[53] U. S. Gupta and V. K. Tiwari, Phys. Rev. **D85**, 014010 (2012), arXiv:1107.1312 [hep-ph] .

[54] V. K. Tiwari, Phys. Rev. **D88**, 074017 (2013), arXiv:1301.3717 [hep-ph] .

[55] M. Y. Ishida, Nucl. Phys. **A629**, 148c (1998).

[56] A. Zacchi, R. Stiele, and J. Schaffner-Bielich, (2015), arXiv:1506.01868 [astro-ph.HE] .

[57] A. Zacchi, M. Hanauske, and J. Schaffner-Bielich, Phys. Rev. **D93**, 065011 (2016), arXiv:1510.00180 [nucl-th] .

[58] O. Heinimann, M. Hempel, and F.-K. Thielemann, Phys. Rev. **D94**, 103008 (2016), arXiv:1608.08862 [astro-ph.SR] .

[59] P. Haensel and O. Y. Gnedin, Astron. Astrophys. **290**, 458 (1994).

[60] D. G. Yakovlev and C. J. Pethick, Ann. Rev. Astron. Astrophys. **42**, 169 (2004), astro-ph/0402143 .

[61] D. Page, J. M. Lattimer, M. Prakash, and A. W. Steiner, Astrophys.J.Suppl. **155**, 623 (2004), arXiv:astro-ph/0403657 [astro-ph] .

[62] R. Negreiros, V. Dexheimer, and S. Schramm, Phys.Rev. **C85**, 035805 (2012), arXiv:1011.2233 [astro-ph.HE] .

[63] D. Blaschke, H. Grigorian, D. Voskresensky, and F. Weber, Phys.Rev. **C85**, 022802 (2012), arXiv:1108.4125 [nucl-th] .

[64] A. Sedrakian, Astron.Astrophys. **555**, L10 (2013), arXiv:1303.5380 [astro-ph.HE] .

[65] P. S. Shternin, D. G. Yakovlev, C. O. Heinke, W. C. Ho, and D. J. Patnaude, Mon.Not.Roy.Astron.Soc. **412**, L108 (2011), arXiv:1012.0045 [astro-ph.SR] .

[66] M. Prakash, I. Bombaci, M. Prakash, P. J. Ellis, J. M. Lattimer, and R. Knorren, Phys. Rept. **280**, 1 (1997), arXiv:nucl-th/9603042 [nucl-th] .

[67] J. A. Pons, S. Reddy, M. Prakash, J. M. Lattimer, and J. A. Miralles, Astrophys. J. **513**, 780 (1999), astro-ph/9807040 .

[68] M. Hempel, G. Pagliara, and J. Schaffner-Bielich, Phys. Rev. **D80**, 125014 (2009), arXiv:0907.2680 [astro-ph.HE] .

[69] M. Hempel, T. Fischer, J. Schaffner-Bielich, and M. Liebendoerfer, Astrophys. J. **748**, 70 (2012), arXiv:1108.0848 [astro-ph.HE] .

[70] I. Sagert, M. Hempel, C. Greiner, and J. Schaffner-Bielich, Eur.J.Phys. **27**, 577 (2006), arXiv:astro-ph/0506417 [astro-ph] .

[71] S. Typel, G. Röpke, T. Klähn, D. Blaschke, and H. H. Wolter, Phys. Rev. **C81**, 015803 (2010), arXiv:0908.2344 [nucl-th] .

[72] N. K. Glendenning, Phys. Lett. **114B**, 392 (1982).

[73] N. K. Glendenning, Astrophys. J. **293**, 470 (1985).

[74] N. K. Glendenning, Z. Phys. A **326**, 57 (1987).

[75] S. L. Shapiro and S. A. Teukolsky, *Black Holes, White Dwarfs, and Neutron Stars: The Physics of Compact Objects* (John Wiley & Sons, New York, 1983).

[76] P. Demorest, T. Pennucci, S. Ransom, M. Roberts, and J. Hessels, Nature **467**, 1081 (2010), arXiv:1010.5788 [astro-ph.HE] .

[77] J. Antoniadis, P. C. Freire, N. Wex, T. M. Tauris, R. S. Lynch, M. H. van Kerkwijk, M. Kramer, C. Bassa, V. S. Dhillon, T. Driebe, J. W. T. Hessels, V. M. Kaspi, V. I. Kondratiev, N. Langer, T. R. Marsh, M. A. McLaughlin, T. T. Pennucci, S. M. Ransom, I. H. Stairs, J. van Leeuwen, J. P. W. Verbiest, and D. G. Whelan, Science **340**, 6131 (2013), arXiv:1304.6875 [astro-ph.HE] .

[78] J. Zdunik and P. Haensel, Astron.Astrophys. **551**, A61 (2013), arXiv:1211.1231 [astro-ph.SR] .

[79] N. Itoh, Prog.Theor.Phys. **44**, 291 (1970).

[80] B. Kämpfer, Phys. Lett. **101B**, 366 (1981).

[81] B. Kämpfer, J. Phys. A **14**, L471 (1981).

[82] B. Kämpfer, Astron. Nachr. **303**, 231 (1982).

[83] B. Kämpfer, J. Phys. A **16**, 633 (1983).

[84] B. Kämpfer, Astron. Nachr. **304**, 167 (1983).

[85] B. Kämpfer, Phys. Lett. **153B**, 121 (1985).

[86] N. K. Glendenning and C. Kettner, Astron. Astrophys. **353**, L9 (2000), astro-ph/9807155 .

[87] K. Schertler, C. Greiner, J. Schaffner-Bielich, and M. H. Thoma, Nucl. Phys. **A677**, 463 (2000), arXiv:astro-ph/0001467 [astro-ph] .

[88] D. Blaschke and D. E. Alvarez-Castillo, (2015), arXiv:1503.03834 [astro-ph.HE] .

[89] M. G. Alford, S. Han, and M. Prakash, JPS Conf.Proc. **1**, 013041 (2014).

[90] M. G. Alford, G. Burgio, S. Han, G. Taranto, and D. ZappalÃ , (2015), arXiv:1501.07902 [nucl-th] .

[91] M. G. Alford and S. Han, (2015), arXiv:1508.01261 [nucl-th] .

[92] Z. Fodor and S. D. Katz, JHEP **03**, 014 (2002), arXiv:hep-lat/0106002 .

[93] Z. Fodor, PoS **CPOD07**, 027 (2007), arXiv:0712.2930 [hep-lat] .

[94] D. Alvarez-Castillo and D. Blaschke, (2013), arXiv:1304.7758 [astro-ph.HE] .

[95] N. K. Glendenning, Phys.Rev. **D46**, 1274 (1992).

[96] A. Bhattacharyya, S. K. Ghosh, M. Hanauske, and S. Raha, astro-ph/0406509 (2004).

[97] A. Bhattacharyya, I. N. Mishustin, and W. Greiner, J.Phys. **G37**, 025201 (2010), arXiv:0905.0352 [nucl-th] .

[98] K. Schertler, S. Leupold, and J. Schaffner-Bielich, Phys.Rev. **C60**, 025801 (1999), arXiv:astro-ph/9901152 [astro-ph] .

[99] T. Maruyama, T. Tatsumi, T. Endo, and S. Chiba, Recent Res.Devel.Phys. **7**, 1 (2006), arXiv:nucl-th/0605075 [nucl-th] .

[100] M. Hempel, V. Dexheimer, S. Schramm, and I. Iosilevskiy, Phys. Rev. **C88**, 014906 (2013), arXiv:1302.2835 [nucl-th] .

[101] Z. Seidov, Sov. Astron, 15 (347) (1971).

[102] B. Kämpfer, J. Phys. G **9**, 1487 (1983).

[103] Z. L. Schaeffer, R. and P. Haensel, Astron. Astrophysics, 126 (121-145) (1983).

[104] L. Lindblom, Phys.Rev. **D58**, 024008 (1998), arXiv:gr-qc/9802072 [gr-qc] .

[105] T. Maruyama, S. Chiba, H.-J. Schulze, and T. Tatsumi, Physics Letters B **659**, 192 (2008).

[106] R. Knorren, M. Prakash, and P. J. Ellis, Phys. Rev. **C52**, 3470 (1995), nucl-th/9506016 .

[107] J. Schaffner and I. N. Mishustin, Phys. Rev. C **53**, 1416 (1996), nucl-th/9506011 .

[108] A. Yudin, T. Razinkova, D. Nadyozhin, and A. Dolgov, Astronomy Letters **40**, 201 (2014).

[109] P. Ko and S. Rudaz, Phys.Rev. **D50**, 6877 (1994).

[110] I. Mishustin, M. Hanauske, A. Bhattacharyya, L. Satarov, H. Stoecker, *et al.*, Phys.Lett. **B552**, 1 (2003), arXiv:hep-ph/0210422 [hep-ph] .

[111] M. Hanauske, *GSI annual report: How to detect the QGP with telescopes* (2003) p. 96.

[112] J. Schaffner-Bielich, M. Hanauske, H. Stoecker, and W. Greiner, Phys.Rev.Lett. **89**, 171101 (2002).

[113] B. Kämpfer, J.Phys. **A14**, L471 (1981).

[114] S. Banik, M. Hanauske, D. Bandyopadhyay, and W. Greiner, astro-ph/0406315 (2004).

[115] S. Banik, M. Hanauske, and D. Bandyopadhyay, J.Phys. **G31**, S841 (2005), arXiv:nucl-th/0412110 [nucl-th] .

[116] J. Zdunik and P. Haensel, Astronomy & Astrophysics **551**, A61 (2013).

[117] S. Benic, D. Blaschke, D. E. Alvarez-Castillo, T. Fischer, and S. Typel, Astron.Astrophys. **577**, A40 (2015), arXiv:1411.2856 [astro-ph.HE] .

[118] V. Dexheimer, R. Negreiros, and S. Schramm, Phys.Rev. **C91**, 055808 (2015), arXiv:1411.4623 [astro-ph.HE] .

[119] P. Haensel, J. L. Zdunik, and R. Schaeffer, Astron. Astrophys. **160**, 121 (1986).

[120] C. Alcock, E. Farhi, and A. Olinto, Astrophys. J. **310**, 261 (1986).

[121] F. Ozel, D. Psaltis, S. Ransom, P. Demorest, and M. Alford, Astrophys.J. **724**, L199 (2010), arXiv:1010.5790 [astro-ph.HE] .

[122] S. Weissenborn, I. Sagert, G. Pagliara, M. Hempel, and J. Schaffner-Bielich, Astrophys.J. **740**, L14 (2011), arXiv:1102.2869 [astro-ph.HE] .

[123] G. Narain, J. Schaffner-Bielich, and I. N. Mishustin, Phys. Rev. **D74**, 063003 (2006), arXiv:astro-ph/0605724 [astro-ph] .

[124] P. Mukhopadhyay and J. Schaffner-Bielich, Phys. Rev. **D93**, 083009 (2016), arXiv:1511.00238 [astro-ph.HE] .

[125] U. H. Gerlach, Phys.Rev. **172**, 1325 (1968).

[126] S. Banik and D. Bandyopadhyay, Phys.Rev. **D67**, 123003 (2003), arXiv:astro-ph/0212340 [astro-ph] .

[127] S. Banik and D. Bandyopadhyay, Phys. Rev. C **64**, 055805 (2001), astro-ph/0106406 .

[128] M. Hempel, O. Heinimann, A. Yudin, I. Iosilevskiy, M. Liebendoerfer, and F.-K. Thielemann, Phys. Rev. **D94**, 103001 (2016), arXiv:1511.06551 [nucl-th] .

[129] J. M. Lattimer and M. Prakash, Phys. Rept. **442**, 109 (2007), astro-ph/0612440 .

[130] J. M. Lattimer and M. Prakash, Science **304**, 536 (2004).

[131] J. W. T. Hessels *et al.*, Science **311**, 1901 (2006), astro-ph/0601337 .

[132] S. Koranda, N. Stergioulas, and J. L. Friedman, Astrophys. J. **488**, 799 (1997), arXiv:astro-ph/9608179 [astro-ph] .

[133] N. K. Glendenning, Phys. Rev. D **46**, 4161 (1992).

[134] N. K. Glendenning, *Compact Stars — Nuclear Physics, Particle Physics, and General Relativity*, 2nd ed. (Springer, New York, 2000).

[135] M. Fortin, J. L. Zdunik, P. Haensel, and M. Bejger, Astron. Astrophys. **576**, A68 (2015), arXiv:1408.3052 [astro-ph.SR] .

[136] A. Zacchi, L. Tolos, and J. Schaffner-Bielich, (2016), arXiv:1612.06167 [astro-ph.HE] .

[137] O. Scavenius, A. Mocsy, I. N. Mishustin, and D. H. Rischke, Phys. Rev. **C64**, 045202 (2001), arXiv:nucl-th/0007030 .

[138] C. Sasaki, B. Friman, and K. Redlich, Phys.Rev. **D75**, 074013 (2007), arXiv:hep-ph/0611147 [hep-ph] .

[139] B.-J. Schaefer, J. M. Pawlowski, and J. Wambach, Phys.Rev. **D76**, 074023 (2007), arXiv:0704.3234 [hep-ph] .

[140] F. Karsch, E. Laermann, and A. Peikert, Nucl. Phys. **B605**, 579 (2001), arXiv:hep-lat/0012023 [hep-lat] .

[141] F. Karsch, E. Laermann, A. Peikert, C. Schmidt, and S. Stickan, in *Strong and electroweak matter. Proceedings, Meeting, SEWM 2000, Marseille, France, June 13-17, 2000* (2000) pp. 180–185, arXiv:hep-lat/0010027 [hep-lat] .

[142] G. W. Carter, P. J. Ellis, and S. Rudaz, Nucl. Phys. **A618**, 317 (1997), arXiv:nucl-th/9612043 [nucl-th] .

[143] G. W. Carter, P. J. Ellis, and S. Rudaz, Nucl. Phys. **A603**, 367 (1996), [Erratum: Nucl. Phys.A608,514(1996)], arXiv:nucl-th/9512033 [nucl-th] .

[144] T. Fischer, I. Sagert, G. Pagliara, M. Hempel, J. Schaffner-Bielich, T. Rauscher, F.-K. Thielemann, R. Kappeli, G. Martinez-Pinedo, and M. Liebendörfer, Astrophys. J. Suppl. **194**, 39 (2011), arXiv:1011.3409 [astro-ph.HE] .

[145] J. A. Faber and F. A. Rasio, Living Rev. Rel. **15**, 8 (2012), arXiv:1204.3858 [gr-qc] .

[146] R. Oechslin, K. Uryū, G. Poghosyan, and F. K. Thielemann, Mon. Not. R. Astron. Soc. **349**, 1469 (2004).

[147] R. Oechslin and H. T. Janka, Phys. Rev. Lett. **99**, 121102 (2007), astro-ph/0702228 .

[148] A. Bauswein, R. Oechslin, and H.-T. Janka, Phys. Rev. **D81**, 024012 (2010), arXiv:0910.5169 [astro-ph.SR] .

[149] K. Takami, L. Rezzolla, and L. Baiotti, Physical Review D **91**, 064001 (2015).

[150] M. Hanauske, K. Takami, L. Bovard, L. Rezzolla, J. A. Font, F. Galeazzi, and H. Stoecker, (2016), arXiv:1611.07152 [gr-qc] .

[151] F. Ozel, D. Psaltis, Z. Arzoumanian, S. Morsink, and M. Baubock, Astrophys. J. **832**, 92 (2016), arXiv:1512.03067 [astro-ph.HE] .

[152] A. L. Watts *et al.*, Rev. Mod. Phys. **88**, 021001 (2016), arXiv:1602.01081 [astro-ph.HE] .

[153] I. Sagert, M. Hempel, G. Pagliara, J. Schaffner-Bielich, T. Fischer, A. Mezzacappa, F.-K. Thielemann, and M. Liebendörfer, Phys. Rev. Lett. **102**, 081101 (2009), arXiv:0809.4225 [astro-ph] .

[154] S. Schettler, T. Boeckel, and J. Schaffner-Bielich, (2010), arXiv:1010.4857 [astro-ph.CO] .

[155] T. Fischer, D. Blaschke, M. Hempel, T. Klahn, R. Lastowiecki, M. Liebendörfer, G. Martinez-Pinedo, G. Pagliara, I. Sagert, F. Sandin, J. Schaffner-Bielich, and S. Typel, Phys. Atom. Nucl. **75**, 613 (2012), arXiv:1103.3004 [astro-ph.HE] .

[156] K. Hebeler, J. Lattimer, C. Pethick, and A. Schwenk, Phys.Rev.Lett. **105**, 161102 (2010), arXiv:1007.1746 [nucl-th] .

[157] G. Shen, C. J. Horowitz, and S. Teige, Phys. Rev. **C83**, 035802 (2011), arXiv:1101.3715 [astro-ph.SR] .

[158] T. Maruyama, H. Fujii, T. Muto, and T. Tatsumi, Phys. Lett. **B337**, 19 (1994).

[159] H. Fujii, T. Maruyama, T. Muto, and T. Tatsumi, Nucl. Phys. **A597**, 645 (1996).

[160] E. Fonseca *et al.*, Astrophys. J. **832**, 167 (2016), arXiv:1603.00545 [astro-ph.HE] .

[161] F. Ozel and P. Freire, (2016), 10.1146/annurev-astro-081915-023322, arXiv:1603.02698 [astro-ph.HE] .

[162] Z. Arzoumanian, K. C. Gendreau, C. L. Baker, T. Cazeau, P. Hestnes, J. W. Kellogg, S. J. Kenyon, R. P. Kozon, K.-C. Liu, S. S. Manthripragada, C. B. Markwardt, A. L. Mitchell, J. W. Mitchell, C. A. Monroe, T. Okajima, S. E. Pollard, D. F. Powers, B. J. Savadkin, L. B. Winternitz, P. T. Chen, M. R. Wright, R. Foster, G. Prigozhin, R. Remillard, and J. Doty, in *Space Telescopes and Instrumentation 2014: Ultraviolet to Gamma Ray*, SPIE, Vol. 9144 (2014) p. 914420.

[163] D. Alvarez-Castillo, M. Bejger, D. Blaschke, P. Haensel, and L. Zdunik, arXiv preprint arXiv:1506.08645 (2015).

[164] D. Champion, E. Petroff, M. Kramer, M. Keith, M. Bailes, E. Barr, S. Bates, N. Bhat, M. Burgay, S. Burke-Spolaor, *et al.*, arXiv preprint arXiv:1511.07746 (2015).

[165] J. Schaffner-Bielich, Nucl.Phys. **A835**, 279 (2010), arXiv:1002.1658 [nucl-th] .

[166] S. Weissenborn, D. Chatterjee, and J. Schaffner-Bielich, Phys.Rev. **C85**, 065802 (2012), arXiv:1112.0234 [astro-ph.HE] .

[167] I. Sagert, G. Pagliara, M. Hempel, and J. Schaffner-Bielich, J.Phys. **G35**, 104079 (2008), arXiv:0808.1049 [astro-ph] .